FLUID DYNAMICS AND HEAT TRANSFER IN THE SUBMERGED INJECTION OF GASES INTO LIQUID METALS FOR REFINING

A thesis presented for the degree of Doctor of Philosophy in the University of London

by

CRISPIN JOHN DOBSON

John Percy Research Group
Department of Metallurgy
and Materials Science,
Imperial College of Science
and Technology

London SW7 2BP

September, 1984

ABSTRACT

In model studies, hydrogen and nitrogen have been injected both horizontally and vertically upward into a pool of water 2 m deep, through nozzles varying from 3 mm to 12 mm in diameter. Gas flowrates ranged from Ø.Ø1 to Ø.16 m^3/s (at STP). In order to obtain very high nominal gas velocities and low values of the ratio of gas/liquid density, investigations were also carried out in a vacuum chamber using a nozzle of Ø.15 mm. The behaviour was recorded using a high speed camera. Dimensionless groups have been used to classify the observed regimes.

A study of the tuyere pressure/flowrate characteristics was carried out on an industrial 8 tonne AOD converter. Pressure transducers were placed at several positions in the core and shroud lines. Shroud flowrates were measured with an orifice meter. An accelerometer was used to measure furnace vibration. The influence of accretion presence on pressure and flowrate and refractory wear is discussed. An experimental tuyere with a narrower shroud gap was installed and monitored. A detailed analysis of tuyere pressure drops was carried out in the laboratory, including the use of artificial accretions.

Submerged injection of oxygen through a nitrogen shrouded tuyere into a silver melt containing 25% lead and 2% copper was investigated as a possible process technology for cupellation. On the laboratory scale 15 kg of silver was

refined to 99% purity in 30 minutes without the aid of added flux. Operation under constant supply pressure was more successful in terms of refractory wear around the tuyere than by attempting to operate under constant flow.

A model for heat transfer and pipe-like accretion formation around an annular tuyere has been developed to calculate accretion shapes. A mathematical formulation for the steady-state has been solved by the finite difference method, using a relaxation technique. The influences of all the processing parameters, such as superheat, on the accretion shape and temperature distribution round the tuyere were evaluated using the model.

ACKNOWLEDGEMENTS

The author is indebted to Dr D G C Robertson for supervision and assistance throughout the course of this work. I am grateful also to the SERC for the award of a research scholarship and to Britannia Refined Metals for the loan of materials.

I extend my thanks to past and present members of both teaching staff and students of the John Percy Group, especially Dr L Farias, for many interesting and helpful discussions. I wish to express my gratitude for the technical assistance provided by the technicians, particularly Messrs Willis, Neve, Andrews, Scott and Russell. Thanks are due to Mr J Rossdale and Mr P Henry for the excellent photographic productions.

Finally, I wish to express my appreciation to Miss S Johnstone for her patient efficiency in typing this manuscript and for the moral support throughout the period of study.

LIST OF CONTENTS

Page

ABSTRACT 2

ACKNOWLEDGEMENTS 4

LIST OF CONTENTS 5

LIST OF FIGURES 10

LIST OF TABLES 16

CHAPTER 1 INTRODUCTION 17

CHAPTER 2 PHYSICAL MODELLING OF SUBMERGED GAS INJECTION 21

2.1 Introduction 22

2.1.1 Previous work 22

2.1.2 Present approach 31

2.2 Experimental 33

2.2.1 Deep pool gas injection 33

2.2.2 Calibration of film speed and camera control 35

2.2.3 Reduced top pressure injection 39

2.2.4 Pressure transducers 41

2.2.5 Reduced top pressure gas injection 42

2.3 Results and their interpretation 42

2.3.1 Deep pool - horizontal injection 42

2.3.2 Deep pool - vertically upward injection 46

2.3.3 Reduced top pressure injection 48

2.4 Discussion 54

2.4.1 Dimensionless group classification of jet

behaviour 54

2.4.2 Bubbling/Jetting (B/J) transition 55

2.4.3 Validity of model work in representing industrial systems 58

2.5 Conclusions 60

2.6 Further work 61

CHAPTER 3 AOD TUYERE PRESSURE/FLOWRATE CHARACTERISTICS 62

3.1 Introduction 63

3.1.1 The argon oxygen decarburization process 63

3.1.2 Wiggin Steel and Alloys 8 tonne AOD converter gas supply 64

3.1.3 The tuyeres 65

3.1.4 Meltshop practice 66

3.1.5 Accretion control 69

3.2 Experimental 70

3.3 Results 72

3.3.1 Pressure and flow measurements 72

3.3.2 Pressure/flowrate characteristics in model accretions 76

3.3.3 Narrow annular gap tuyere 76

3.3.4 Refractory wear 87

3.4 Discussion 91

3.5 Conclusions 93

3.6 Further work 94

CHAPTER 4 CUPELLATION OF SULVER-LEAD BULLION BY SUBMERGED INJECTION OF OXYGEN THROUGH A NITROGEN SHROUDED TUYERE 96

4.1 Introduction 97

4.1.1 Present approach 98

4.1.2 Projected full-scale converter 99

4.1.3 Proposed model converter 103

4.2 Experimental 103

4.2.1 Apparatus 103

4.2.2 Procedure 110

4.3 Results and their interpretation 115

4.3.1 Impurity removal 115

4.3.2 Gas supply 128

4.3.3 Tuyere and refractory wear 129

4.4 Discussion 133

4.4.1 Laboratory model 133

4.4.2 Pilot-plant 135

4.5 Conclusions 137

4.6 Further work 137

CHAPTER 5 HEAT TRANSFER CALCULATIONS FOR PIPE-LIKE ACCRETION FORMATION AROUND A SUBMERGED ANNULAR GAS INJECTION TUYERE 139

5.1 Introduction 140

5.2 Previous work 141

5.3 Present approach 142

5.4 Modelling of heat transfer around a tuyere 143

5.5 Formulation 145

5.6 Calculation and data 150

5.7 Results 161

5.8 Discussion 171

5.8.1 Accretion growth model 172

5.8.2 Heat transfer in gas channel 172

5.8.3 Growth mechanism 173

5.8.4 Gas temperature 173

5.8.5 Reactive gas 181

5.9 Tuyere failure mechanisms 192

5.10 Conclusions 195

CHAPTER 6 SUMMARY AND CONCLUSIONS 198

APPENDIX A.1 CHOKED FLOW AND JETS FROM CHOKED NOZZLES 203

A.1.1 Introduction 204

A.1.2 Previous work 205

A.1.3 Present approach 208

A.1.4 Experimental apparatus 210

A.1.5 Experimental procedure 213

A.1.6 Results and interpretation 215

A.1.7 Discussion 221

A.1.8 Choked submerged gas jet phenomena 222

APPENDIX A.2 NOZZLE METERING 226

APPENDIX A.3 OXYGEN CONTENT IN THE MELT 231

APPENDIX A.4 FORTRAN PROGRAM REFRAC9 234

LIST OF SYMBOLS 239

REFERENCES 245

List of figures

Figure		Page
Fig.2.1	Dimensionless bubble volume as a function of Froude Number for different systems (after Farias[17]).	27
Fig.2.2	Apparatus for high injection rate in the deep pool.	34
Fig.2.3	High pressure injection apparatus. Dimensions in mm.	35
Fig.2.4	Nozzle with pressure transducer.	35
Fig.2.5	Camera remote control and timing circuits.	38
Fig.2.6	Apparatus for reduced top pressure gas injection.	38
Fig.2.7	Nozzle mounting and pressure transducer.	40
Fig.2.8	Horizontal hydrogen injection into water.	44
Fig.2.9	Comparison of vertical injection systems.	45
Fig.2.10A	Horizontal hydrogen injection into water under reduced top pressure.	50
Fig.2.10B	Detached bubble growth	
Fig.2.11	Hydrogen injection under reduced top pressure.	52
		57
Fig.3.1	Gas supply system.	67
Fig.3.2	Tuyere assembly with dimensions.	67
Fig.3.3	Typical blowing practice. Measured pressures.	77
Fig.3.4	Tuyere assembly for pressure-drop analysis.	77
Fig.3.5	Pressure drops in WSA tuyere.	80

Fig.3.6	Mass flux density as a function of accretion 'openness' for a constant supply pressure of air.	84
Fig.3.7	Supply pressure as a function of accretion 'openness' for constant mass flux density.	85
Fig.3.8	8 tonne AOD showing tuyere and slag line erosion after a campaign.	87
Fig.3.9	Newly lined AOD showing accretions in both tuyeres.	90
Fig.4.1	Schematic of proposed process converter.	101
Fig.4.2	Experimental apparatus.	109
Fig.4.3	Tuyere assembly and position relative to the crucible.	105
Fig.4.4	Gas supply system for constant flow runs.	108
Fig.4.5	Constant flowrate orifice calibration with core tube in position.	108
Fig.4.6	Silver-lead and silver-copper systems.	111
Fig.4.7	Melt content and temperature change - run P.	116
Fig.4.8	Melt content change - run A.	116
Fig.4.9	Melt content and temperature change - run B.	117
Fig.4.10	Melt content change - runs D, DD.	118
Fig.4.11	Melt content change - run E.	119
Fig.4.12	Melt content change - run F.	120
Fig.4.13	Melt content change - run H.	121

Fig.4.14 Pressure transducer output variation with time and accretion condition. 130

Fig.4.15 Tuyere refractory wear patterns observed after each run. 130

Fig.4.16 Sectioned tuyeres. 132

Fig.5.1 Heat transfer zone, incorporating the annular tuyere. 143

Fig.5.2 Section of cylindrical region for heat transfer calculations. 144

Fig.5.3 Mesh point representation of annular tuyere. 150

Fig.5.4 Resetting of thermal boundary layer. 150

Fig.5.5 Flowchart indicating solution of moving accretion boundary problem. 152

Fig.5.6 Finite difference representation of fixed interface. 154

Fig.5.7 Effect of changing core gas flowrate. 162

Fig.5.8 Variation of accretion shape and gas exit temperature with melt superheat (Q_{core} = Ø.ØØ2, Q_{sh} = Ø.Ø13 m^3/s). 164

Fig.5.9 Variation of accretion shape with thermal conductivity of refractory (Q_{core} = Ø.ØØ2, Q_{sh} = Ø.Ø13 m^3/s). 165

Fig.5.1Ø Effect of accretion/gas heat transfer coefficient variation on accretion height. Reduction step. 167

Fig.5.11 Effect of accretion/gas heat transfer coefficient variation on accretion height. Reactive gas. 167

Fig.5.12 Variation of accretion shape and gas temperature with thermal conductivity of accretion. 168

Fig.5.13 Variation of accretion shape with shroud gas properties (k_{acc} = 4 W/mK, k_{CH_4} = Ø.31 W/mK, $_{CH_4}$ = 4.134 x $1Ø^{-5}$ kg/sm, $_{CH_4}$ = Ø.196 kg/m^3, C_p = 219Ø kg/mol.K, ΔT_s = 1ØØ^{o}C). 170

Fig.5.14 The effect of a single tube tuyere. 170

Fig.5.15 Schematic of accretion structure. 174

Fig.5.16 Schematic of bubble growth around a tuyere. 175

Fig.5.17 Effect of melt superheat, gas/accretion heat transfer coefficient and accretion thermal conductivity on gas exit temperature. 175

Fig.5.18 Simplified gas/accretion/molten metal heat transfer region. 180

Fig.5.19 Transient growth of a gas bubble in molten iron. 183

Fig.5.2Ø Variation in bubble radius and oxygen volume fraction during growth. 189

Fig.5.21 Gas/liquid interfacial temperature and thickness of thermal boundary layer thickness during bubble growth. 189

Fig.5.22 Effective superheat of gas/liquid interface radiating to accretion. 190

Fig.A.1.1 Simple replaceable convergent-divergent nozzle. 209

Fig.A.1.2 Momentum flowrate measurement apparatus. 209

Fig.A.1.3 Nozzle 6 - convergent type. 214

Fig.A.1.4 Jet velocity measurement apparatus. 214

Fig.A.1.5 Nozzle gas flow calibration. 216

Fig.A.1.6 Comparison of momentum flowrate for each nozzle at x = 10 mm. 216

Fig.A.1.7 Momentum flowrate variation with supply pressure as a function of nozzle to plate separation. 218

Fig.A.1.8 Centre line stagnation pressure and Mach number versus dimensionless distance as a function of supply pressure. 220

Fig.A.1.9 Decrease in jet centre line velocity with distance from nozzle. 220

Fig.A.1.10 Froude number versus gas/liquid density ratio assuming adiabatic and frictionless flow through a small nozzle. 224

Fig.A.1.11 Ratio of momentum to buoyancy force variation with ratio of gas/liquid density for convergent-divergent and convergent nozzles. 235

Fig.A.2.1 Convergent metering nozzle. 228

Fig.A.3.1 The oxygen probe. 233

List of Tables

Table		Page
Table 2.1	Summary of horizontal injection runs.	43
Table 2.2	Summary of vertical injection runs.	43
Table 2.3	Summary of horizontal hydrogen injection runs under reduced top pressure.	49
Table 2.4	Summary of vertical hydrogen injection runs under reduced top pressure.	49
Table 3.1	Summary of procedure in the different campaigns.	71
Table 3.2	Results.	73
Table 4.1	Experimental conditions.	112
Table 4.2	Results.	122
Table 4.3	Oxygen utilization.	127
Table 5.1	Material properties.	159
Table 5.2	Gas injection conditions.	160
Table A.1.1	Nozzle dimensions.	211
Table A.1.2	Nozzle flow characteristics.	211

CHAPTER 1

INTRODUCTION

CHAPTER 1

INTRODUCTION

High productivity in pyrometallurgical processes involving gas/metal reactions requires an efficient gas/liquid contacting technique. The most successful method is the submerged injection of gas into liquid metal, providing a large gas/liquid surface area for chemical reactions and sufficient kinetic energy for stirring. The gas stream breaks up some distance from the jet orifice, so that ideally, the region of high reaction rate can be projected into the bath, avoiding too severe refractory wear problems.

The first commercially successful process incorporating submerged gas injection was developed by Bessemer in 1860[1]. Later blister copper was produced utilizing a similar method in the Great Falls and Pierce-Smith converters. With the advent of cheap bulk oxygen after World War Two and the introduction of Savard and Lee tuyeres in 1966[1], experimentation in submerged oxygen blowing has resulted in the development of several successful processes, such as the Quiet Basic Oxygen Process (Q-BOP)[2] for steelmaking and the Argon Oxygen Decarburisation Process (AOD)[3] for stainless steelmaking. In these tuyeres oxygen is blown through a central core tube and a hydrocarbon or inert gas is blown through the annular passage between a coaxial outer pipe around the central one. Shrouding of the oxygen jet in this way leads to accretion formation[4]

(called 'mushrooms' in the Q-BOP and 'knurdles' in the AOD). Localized tuyere attack is very much reduced. Further examples of the use of submerged gas injection are in transfer vessels where it is used for stirring, alloying and desulphurisation operations[5]. In the non-ferrous field bottom injection has been employed on the pilot scale[6] in silver-lead-copper bullion cupellation with great success.

Process metallurgists interested in fundamental fluid dynamic behaviour of such systems have been obliged to begin their investigations on aqueous models using non-reactive gases. Some work has been done at low flow rates in iron-carbon alloys[7] and at higher flowrates in mercury [8,9]. No work on fluid dynamic behaviour has been done on reactive gases.

Much of the work reported in the literature has concentrated on establishing whether high blowing rate converters (Q-BOP, AOD) operate in a bubbling or jetting regime and the effects this could have on refractory erosion and gas break-up. There exists, however, some disagreement over the conditions necessary to achieve jetting. Furthermore, there is very little information available in the literature[10,11,12] concerning the formation of accretions of frozen metal on the ends of tuyeres and their effect on the injected gas behaviour.

Present approach

The purpose of this study has been to establish an understanding of how a gas behaves on injection into a liquid. Gas flowrates were extended to simulate AOD conditions and the effect of varying the gas/liquid density ratio was also investigated. The author and a colleague were invited by INCO (Europe) to assist in the determination of whether accretions could be detected during a blow of their Wiggin Steel and Alloys (WSA) AOD vessel. Experiments were carried out to determine the pressure-flow characteristics of the WSA tuyere in the plant and in the laboratory. A laboratory study was commissioned by Britannia Refined Metals (BRM) to investigate submerged injection of oxygen through an annular tuyere into a silver-lead-copper melt as a possible process technology for cupellation. A computer model has been developed to describe heat transfer and accretion formation round an annular tuyere to calculate accretion shapes.

This thesis has been divided into four main chapters, each intended as a self-contained unit for readers with specific interests. Chapter 2 contains the work on physical modelling of submerged gas injection, Chapter 3 the AOD plant measurements, Chapter 4 the cupellation investigation and Chapter 5 the computer modelling of accretion formation.

CHAPTER 2

PHYSICAL MODELLING OF SUBMERGED GAS INJECTION

CHAPTER 2

PHYSICAL MODELLING OF SUBMERGED GAS INJECTION

2.1 INTRODUCTION

The principal objective of submerged gas injection is to create an extended interface between the melt and the injected gas. An important visualisation of the dispersion process may be obtained through isothermal model studies. Information on growth, separation and disintegration of the gas-filled envelopes that form at the tuyere can be obtained both simply and conveniently. Physical modelling in, for example, gas/water systems allows observation of the jet break up and classification of the physical behaviour of the gas. The objective of this study is to combine information on nozzle gas flow characteristics with the submerged gas jet observations to enable classification of the gas behaviour for different systems.

2.1.1 Previous work

In the early 1960's a theory was advanced by Davidson and Schuler[12] to calculate the volume of bubbles forming in an inviscid liquid at a submerged orifice. A force balance (buoyancy = liquid inertia) was taken from which the bubble volume at detachment could be calculated as

$$V_b = A\, Q^{6/5} g^{-3/5} \qquad (2.1)$$

They assumed that the bubble grew radially from a point source, leading to a proportionality constant of A = 1.378. Ten years later Wraith[13] observed that bubbles are really hemispherical during the early stages of growth and proposed a smaller proportionality constant of A = 1.Ø9. He then verified Equation 2.1 experimentally for the air/water system at relatively low flow rates (Ø.8 - 11.3 Nl/sec). In a later study[14] on downward lancing of air into water at low flowrates the equation was once again verified.

Bubble volumes at higher flowrates, however, were found to be[15] significantly lower than those predicted by Equation 2.1. Wraith and Chalkley[15] proposed that the gas momentum flowrate (F_M) was an important consideration at high flowrates, assisting buoyancy in lifting the bubble thus decreasing its volume at detachment. Their experimental investigations demonstrated that the ratio of momentum to buoyancy forces alone could account for the observed deviation from Equation 2.1 for vertically upward injection. The momentum flow rate was expressed as $F_M = Q^2 \rho_g / \pi r_o^2$ and the buoyancy force, $F_B = V \rho_l g$, was defined in terms of flowrate (Q) by using the bubble volume at detachment from Equation 2.1 and so

$$F_B = A Q^{6/5} g^{2/5} \rho_l \qquad (2.2)$$

The ratio $F_M/F_B = N_I$ was referred to as the Injection Number,

$$N_I = C(Q^2/(r_o^5 g))^{2/5} \rho_g/\rho_l \qquad (2.3)$$

where $$C = (2^2 \pi A^5)^{-1/5} \qquad (2.4)$$

Wraith assumed the constant C to be equal to unity. However, when C is included, Equation 2.3 has the advantage of representing the exact ratio F_M/F_B and predicts N_I values slightly lower than those reported by Wraith and his followers[16,17].

In a recent publication Nilmani and Robertson[16] solved the equation of motion of a growing bubble following the logic of Wraith. Their force balance was expressed as

Buoyancy force + Momentum force = Liquid inertial force

$$V_b(\rho_l - \rho_g)g + \rho_g u_o^2 \dot{A}_o = d/dt(K_e M(ds/dt)) \qquad (2.5)$$

where M is the virtual mass and K_e varies with bubble shape. If ρ_l is very much greater than ρ_g and $(K_e M)$ is assumed equal to $(11/16)\rho_l V_b$, integration of Equation 2.5 twice with respect to time, with initial conditions:
at t = Ø, ds/dt = Ø and s = Ø, gives

$$t_d^{5/3} + (4/\pi g)\ (\rho_g/\rho_l)\ (Q/r_o^2) t_d^{2/3}$$

$$- (11/4g)\ (3Q/4\pi)1/3 = Ø \qquad (2.6)$$

t_d is the time to detachment, which is defined as the time at which the bubble displacement s equals the bubble radius R.

Utilizing the Davidson and Schuler theory to provide a reference bubble formation time ($t_d = V_b/Q$), Equation 2.6 can be rewritten as

$$t_{dref} = A(Q/g^3)^{1/5} \qquad (2.7)$$

Writing Equation 2.6 in terms of dimensionless time $t_d^* = t_d/t_{dref}$ yields

$$t_d^{*5/3} + (const)(\rho_g/\rho_l)(Q^2/gr_o^5)^{2/5} t_d^{*2/3} - 1 = \emptyset \qquad (2.8)$$

Equation 2.8 shows that t_d^* is a function of F_M/F_B only and confirms the experimental observations of Wraith et al.[15]. Gas behaviour in actual converters can therefore be predicted from laboratory models using this unique scaling parameter.

A disadvantage of this approach is that the actual bubble volume cannot be determined directly from F_M/F_B without first calculating the reference volume. Farias[17] has solved this problem by considering that the bubble volume (V_b) depends on the following variables at high flowrates

$$V_b = f(\rho_g, \rho_l, u_o, g, r_o)$$

He combined the variables into the three following dimensionless groups,

$$V_b/r_o^3 = f(u_o^2/r_o g, \rho_g/\rho_l) \qquad (2.9)$$

The functional relationship between the groups can be obtained by setting

$$t_d = V_b/Q, \quad Q = u_o \pi r_o^2$$

Equation 2.6 can then be written in terms of the dimensionless groups as

$$(V_b/r_o^3)^{5/3} + 12.56(\rho_g/\rho_l)(u_o^2/r_o g)(V_b/r_o^3)^{2/3}$$

$$- 16.84(u_o^2/r_o g) = 0 \qquad (2.10)$$

Farias solved this equation by trial and error and plotted the results in Figure 2.1. Also shown is the Davidson and Schuler line[12] obtained by neglecting the momentum term in equation 2.6. From reference 12

$$V_b = 1.378\ Q^{6/5} g^{-3/5}$$

and so

$$(V_b/r_o^3)^{5/3} = 16.84(u_o^2/r_o g)$$

which is independent of ρ_g/ρ_l.

It can be seen from Figure 2.1 that as the Froude Number increases the dimensionless bubble volume increases more slowly than predicted by Davidson and Schuler. Experiments

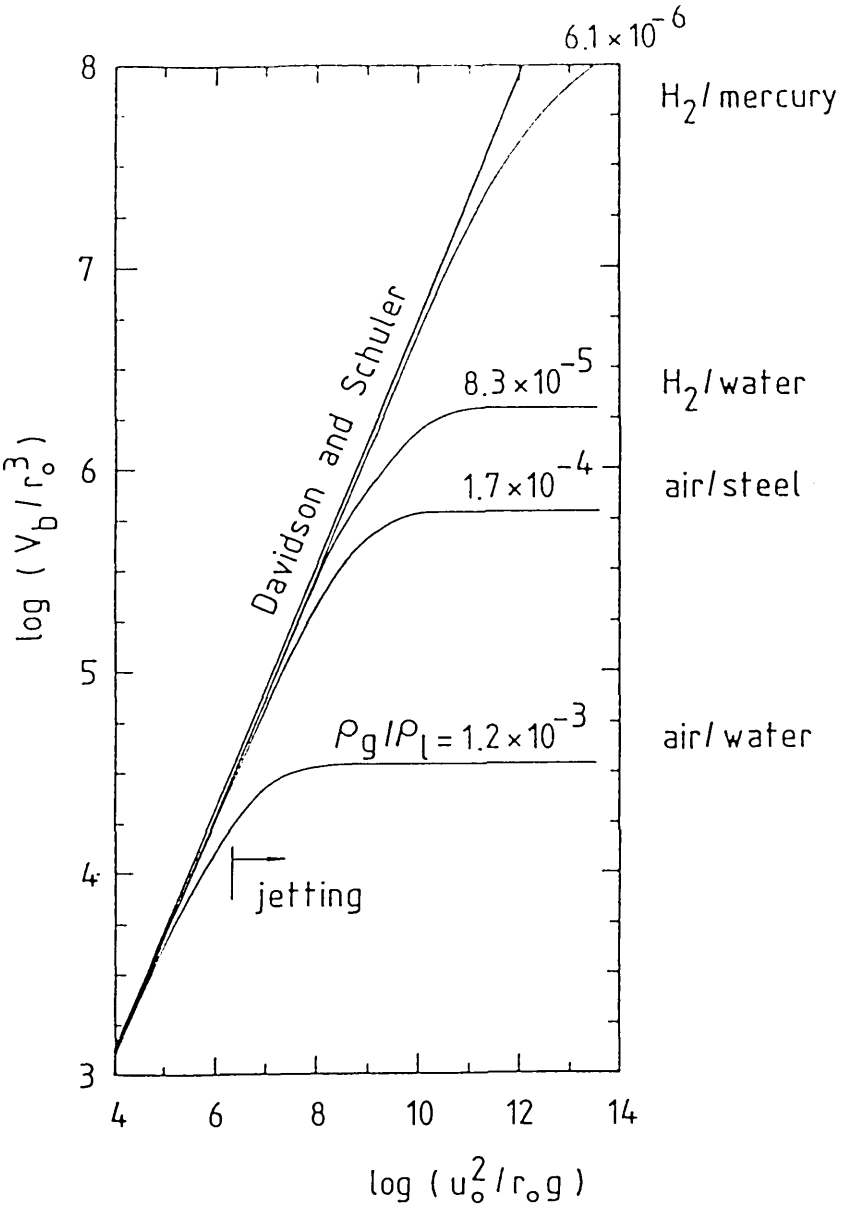

Fig.2.1 Dimensionless bubble volume as a function of Froude Number for different systems (after Farias[17]).

carried out in air-water systems by Nilmani and Robertson[16] and in air-mercury systems by Wraith and Chalkley[15] have verified this result. With further increase in Froude Number a transition in gas behaviour occurs as bubbling ceases and 'jetting' takes place instead. The smaller ρ_g/ρ_l the larger N_{Fr} required for the transition. This latter result is in qualitative agreement with the experiments of Hoefele and Brimacombe[18] on horizontal injection systems.

The main assumption of Wraith's Injection Number analysis is that the momentum force acts effectively on the centre of a homogeneous growing bubble. This is generally the case for systems of F_M/F_B less than about Ø.Ø7.

Early work on air-water systems by Themelis et al.[19] and by Turkdogan[2Ø] showed that at high injection velocities steady jets formed. Such jets, consisting of a collection of tiny bubbles, have the characteristic that the volume concentration of gas (VCG) , at an instant, drops smoothly along the jet trajectory. At any position in the jet VCG remains constant with time (actually, it may vary slightly at a high frequency). This is in direct contrast with the situation where large bubbles form. Here the instantaneous VCG is not a smooth function of position along the "jet" path and the VCG for a given position would vary a large amount at low frequency (the bubbling frequency at positions near the tuyere tip).

The distinction between the two different regimes mentioned

above has not yet been taken up during investigations of the characterization of the transition from bubbling to jetting. More interest has been shown in the gas behaviour in the immediate vicinity of the orifice. Mori[21,22] has advanced a particularly precise definition that jetting occurs when gas ceases to spread laterally across the nozzle (nozzle diameter = jet diameter). Such conditions were reported to occur when the nozzle exit velocity becomes sonic, irrespective of nozzle size or liquid density.

A classification of injection regimes has been proposed by Hoefele and Brimacombe[18] who chose the modified Froude Number ($N_{Fr}' = (u_o^2/d_o g)(\rho_g/\rho_l)$) and the gas to liquid density ratio (ρ_g/ρ_l). Their definition of jetting is the situation in which "the liquid is prevented from washing against the tuyere tip by the continuing presence of gas". A transition from bubbling to jetting occurs in a given gas-liquid system (ρ_g/ρ_l) on increasing N_{Fr}'. The critical N_{Fr}' to achieve jetting being higher for lower ρ_g/ρ_l systems.

Recently McNallan et al.[23,24] have introduced a classification of injection regimes. Their definition of jetting was defined roughly the same way as Mori, but with consideration of the steadiness of the "walls of the jet cone". A transition between regimes was suggested to occur at a fixed value of mass flux density of 400 $kg/m^2 sec$.

For the air-water system, Hoefele and Brimacombe's criterion disagrees with Mori's sonic velocity proposal. The N_{Fr}'

corresponding to the sonic velocity in air (at room temperature) for a nozzle of 3.2 mm diameter is about 2 orders of magnitude above the critical N_{Fr}' reported by Hoefele and Brimacombe.

The contrast between McNallan's classification and Brimacombe's proposal is that there is a large over-estimation in the necessary N_{Fr}' to achieve jetting predicted by McNallan for all gas-water systems.

However, once the difference in definitions is acknowledged better agreement may be found. This must necessarily be the case since the criteria are all based on valid experimental data.

The real differences in the various predictions start showing at extremely low ρ_g/ρ_l values. Work in such systems in necessary to assess the validity of the criteria. Nilmani[16] obtained ρ_g/ρ_l values as low as 4×10^{-6} by operating with hydrogen at reduced top pressure. The velocities were very nearly sonic and bubbles were still spreading at the nozzle plane.

In most of the work done on modelling gas jets water has been used as the liquid, mainly because of its transparency, which allows gas behaviour to be analysed visually by filming.

Irons and Guthrie[7] injected gas into molten iron where behaviour was observed using X-ray photography. The

technique was limited to low flowrates where surface tension forces play a role in holding the bubble to the tuyere. These forces are probably negligible at higher flow rates. Nitrogen behaviour and nozzle blocking in molten cast iron were also investigated by Davis and Magny[25] using an X-ray fluoroscopy technique.

A novel technique to study opaque systems has been developed by Mori et al.[26] whereby the jets are photographed from the bottom through a transparent window. This technique is specially suited to study gas spread at the bottom plate around the tuyere tip but it does not help to visualize the overall jet behaviour. A half slice tuyere technique, where a half tuyere was attached to a transparent wall, was more useful to study behaviour in mercury[16,17].

2.1.2 Present approach

Most of the work carried out to classify the bubbling/jetting transition has concentrated on gas injection into water or mercury under atmospheric pressure at relatively low flowrates through small tuyeres (Nilmani[16] used a maximum $Q = 5 \times 10^{-3}$ m^3/s at STP and $r_o = 3.1$ mm). In this work hydrogen and nitrogen were injected both horizontally and vertically upward into a pool of water 2 m deep through nozzles varying from 3 mm to 12 mm in diameter. Gas flowrates ranged from 0.01 to 0.16 m^3/s at STP, thus obtaining parity of scale and flowrate with some industrial converters. Included in the experimental procedure was the facility to precisely measure the dynamic

tuyere pressure and to correlate this data with bubble images from a high speed camera.

In addition, experiments were carried out in a smaller tank in order to investigate the bubbling/jetting transition at low values of gas density by observing the behaviour of hydrogen injected into water under a reduced top pressure. To obtain the highest possible gas velocities and low values of the ratio of gas/liquid density and bubbles small enough in relation to the tank size, the experiments were carried out in a vacuum chamber using a convergent nozzle of Ø.17 mm diameter. This nozzle was operated with large driving pressures and was always choked. Experimental investigations to measure momentum flowrates and velocities of jets discharging from choked nozzles are described in Appendix 1, where the results indicate the use of a simple convergent nozzle with a sonic exit velocity is appropriate.

The observed gas jet behaviour is classified in terms of the ratio of momentum to buoyancy forces (F_M/F_B). Evaluation of the momentum force assumes the velocity of the gas at the nozzle exit is sonic (as measured in Appendix 1)

$F_M = u_e \dot{m}$

and the buoyancy force is given by Equation 2.2

As a final note, large values of (F_M/F_B) are difficult to obtain at low downstream pressures because buoyancy forces dominate the gas behaviour (also demonstrated in Appendix 1).

2.2 EXPERIMENTAL

2.2.1 Deep pool gas injection

This work was carried out in the first year of the author's course of study in co-operation with L.Farias[17]. The work constituted part of his Ph.D thesis.

For the high gas flowrate work (Q = Ø.Ø1 to Ø.15 m^3/sec) the expected bubble size was very large. A 2 m deep pool with windows, in the Civil Engineering Department of Imperial College, was used in this part of the work. The injection equipment and photographic arrangement are shown in Figure 2.2. A battery of 3 H_2 cylinders was used to supply the gas at a sustained pressure (past the controller) of 1Ø-25 bar (abs). When air was injected, the compressed-air supply line of the Department (8 bar (abs)) was connected directly to the orifice meter (Figure 2.3). Two concrete blocks each weighing 5ØØ N (under water) were laid on the gas pipe to hold it in position.

The tuyeres were of 3.2, 6.35 and 12.6 mm diameter. Two pressure transducers of suitable range (Section 2.2.4) were attached: one to the tuyere itself (as in Figure 2.4) beneath the water, and the other to the pipe 6 metres upstream of the tuyere tip. The signals from T_1 and T_2 were recorded simultaneously with a Southern Instruments chart recorder (UV recorder). The gas flowrate was monitored by instrumenting the gas supply lines with an orifice meter (see Figure 2.3) with the advantage that pressures for

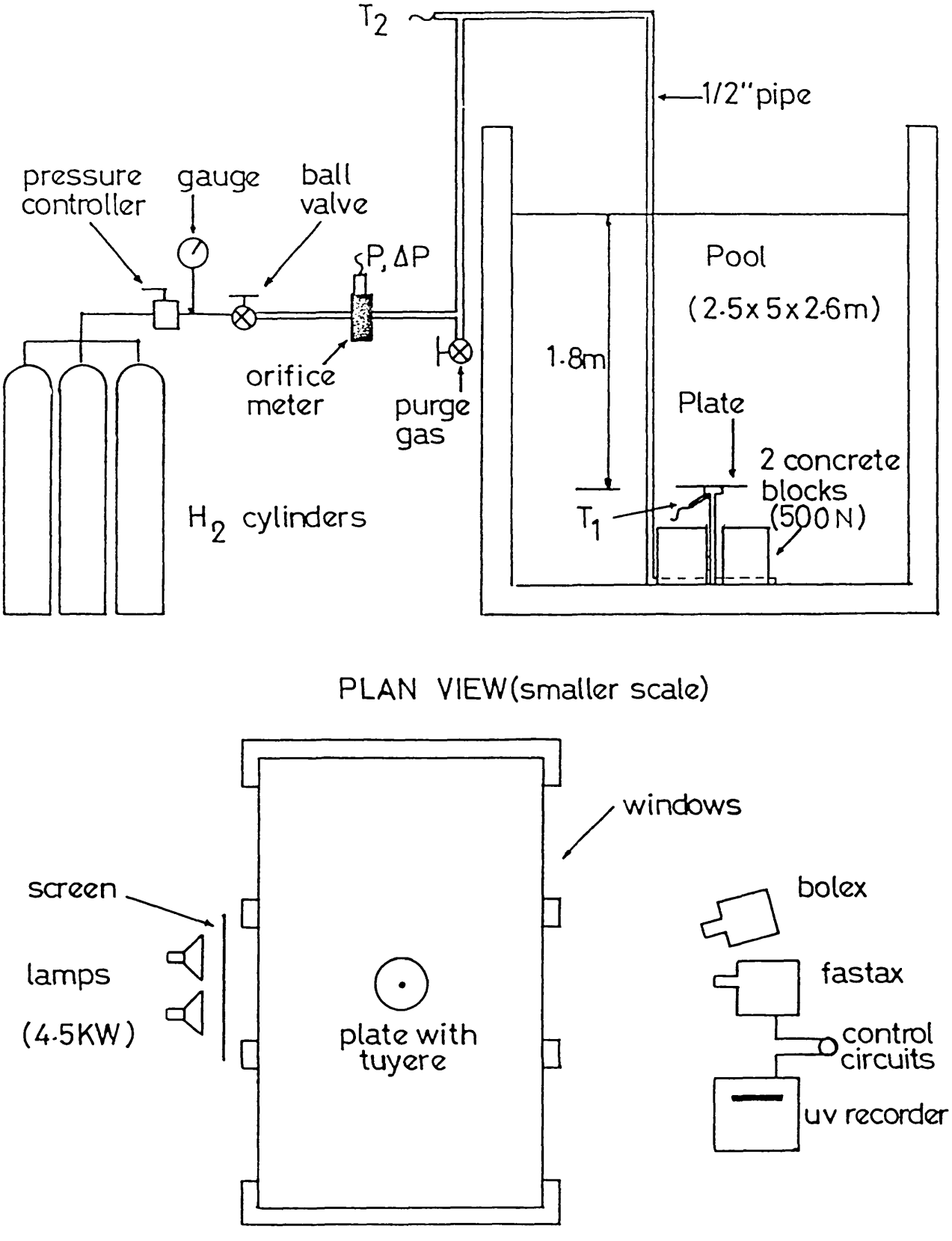

Fig.2.2 Apparatus for high injection rate in the deep pool.

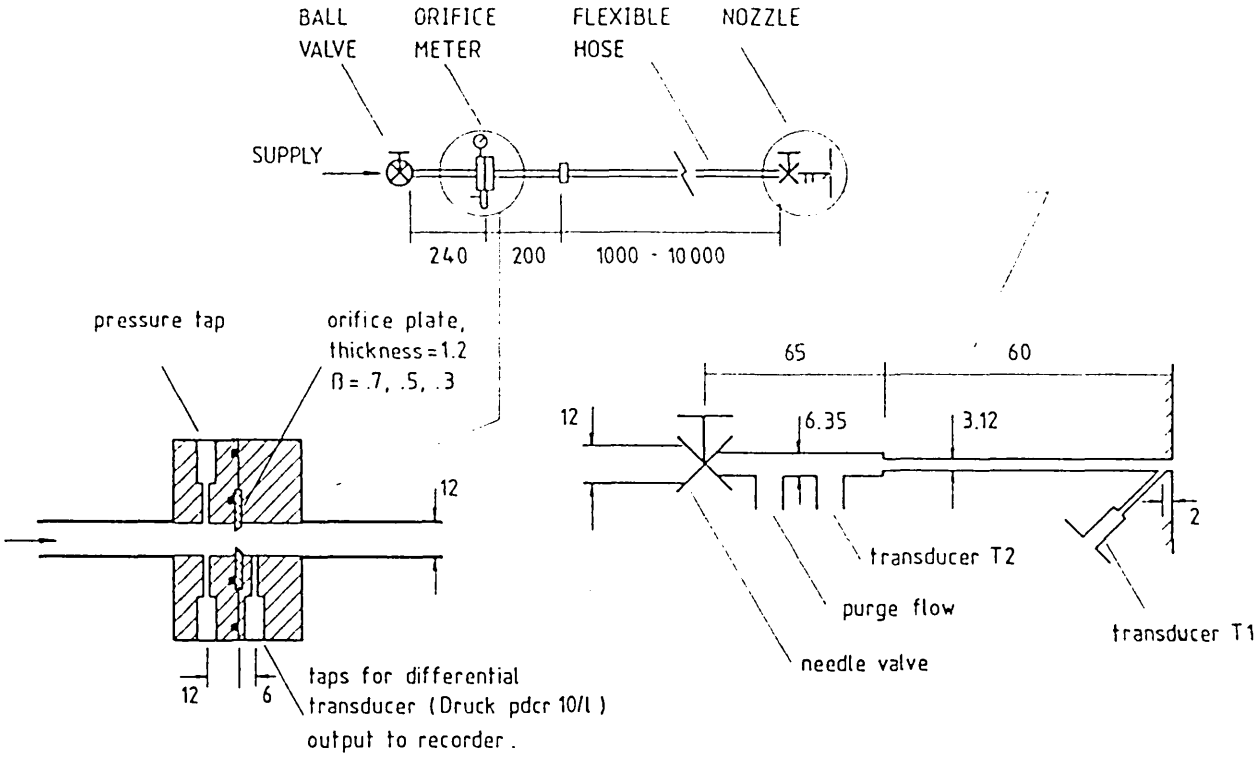

Fig.2.3 High pressure injection apparatus. Dimensions in mm.

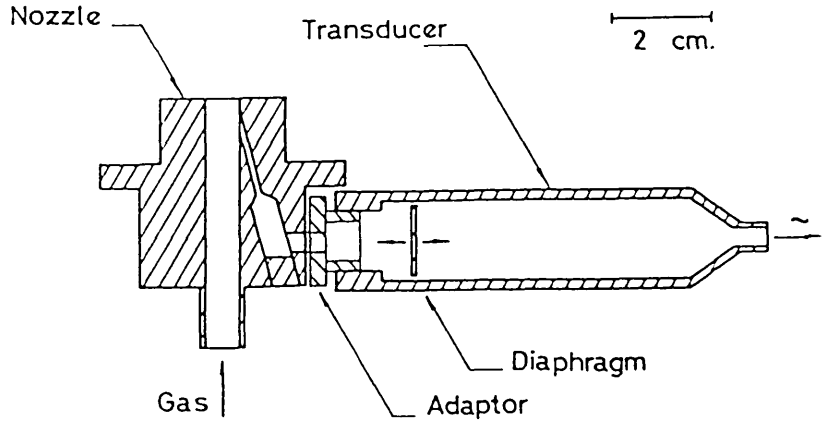

Fig.2.4 Nozzle with pressure transducer.

flowrate calculation could be recorded electrically on a chart recorder.

Events close to the tuyere were photographed with a Fastax (V,WF4ST) high speed camera equipped with Wollensak 25 mm f2.3 lens. The film used was a 16 mm Ilford HP5 type 782 (400 ASA) in 100 ft lengths. The aperture of the lens was frequently f5.6. Back light illumination was provided by Phillips photo flood lamps (500 W) and a diffuser screen.

The lower inflammability limit for H_2 in the presence of air is 4%. Operating at the highest flowrates for 15 seconds (the duration of one run) would only release 2.25 m^3 of H_2 into the lab. Doing 5 runs in a day and assuming all the H_2 remained in the laboratory of volume 9000 m^3, the concentration of H_2 would be minute. However, special precautions were taken to ban any naked lights and localized pockets of H_2 were prevented by ventilating the area around the pool.

2.2.2 Calibration of film speed and camera control

Accurate calibration of the film speed in the Fastax camera enabled time between events to be evaluated, and controlling the time of a run economized on the quantity of film used. (The actual electrical circuits used in the deep pool work for synchronizing the high speed films and the pressure traces were more complicated than reported here[17]. The synchronization circuits have been omitted from this description, leaving only the timing and remote control

circuits).

The high speed camera had a neon lamp which was used for timing (see Figure 2.5). The voltage applied across the lamp was a sine wave of known frequency that made it fire each time the voltage reached a positive and a negative peak. Distinct exposures were left on the edge of the film from which the time between two frames could easily be calculated as follows:-

$$\Delta t = \Delta F/2f\ \Delta N \text{ (sec)} \qquad (2.14)$$

where ΔF = number of frames between two frames of interest
f = driving frequency of the lamp (c/sec), and
ΔN = number of frames between two consecutive starts of the timing mark.

It is important to note that the neon light made exposures which were placed 5 frames ahead of the imaging position on the driving sprocket. The camera motors were operated by remote control through a double pole timer relay that switched them on for a preset time (see Figure 2.5).

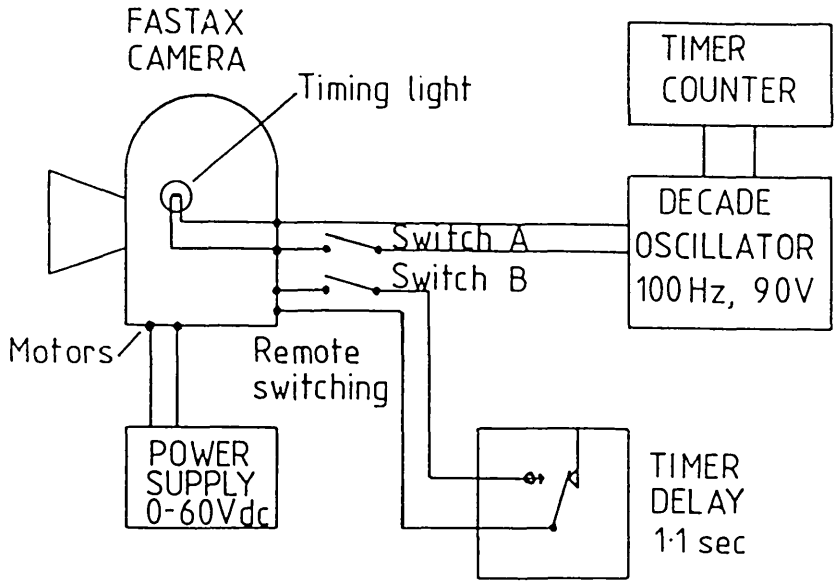

Fig.2.5 Camera remote control and timing circuits.

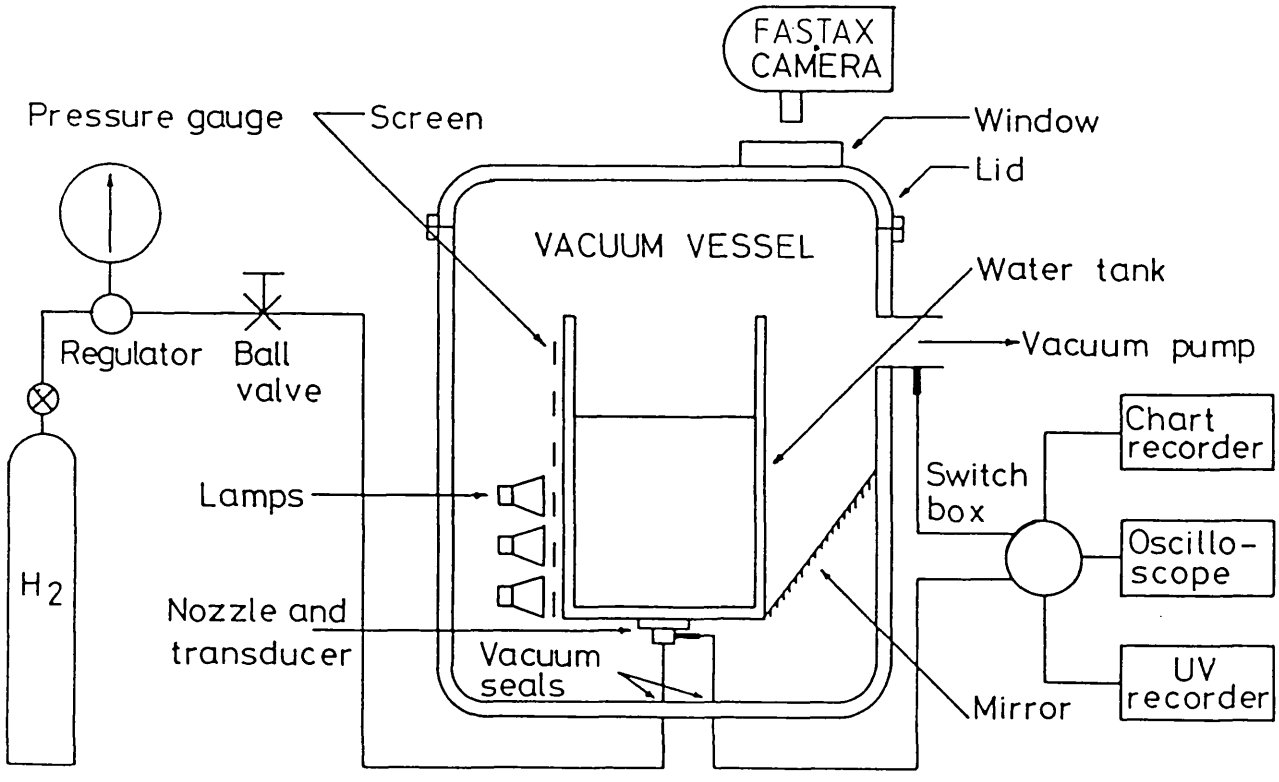

Fig.2.6 Apparatus for reduced top pressure gas injection.

2.2.3 Reduced top pressure gas injection

The experimental set-up for the low gas density and high nominal gas velocity work is shown in Figure 2.6. The 'Perspex' water tank (60 x 40 x 80 cm), mounted on a "Handy-Angle" framework, had the facility to take flush nozzles (shown in Figure 2.7 instrumented with a transducer) in the bottom for vertical injection or in the side for horizontal injection. Different nozzle configurations and sizes could be easily screwed into the nozzle mounting. Nozzle design criteria are discussed in Appendix 1. Equation 2.1 predicts the necessity for very small nozzle diameters (0.174 mm was used) to keep bubble size small enough in relation to the tank size when experiments were carried out under a low pressure.

The gas flowrate was monitored by always operating the nozzle under choked conditions. The principles of nozzle metering are discussed in Appendix 2. Any particular flowrate could be selected by setting the pressure controller to a particular value between 0-100 bar (abs) chosen from a previous calibration (Appendix 1).

Initially the signals from the pressure transducers in Figure 2.6 were recorded simultaneously on either the U V recorder, oscilloscope or chart recorder. With experience, it was found that the pressure drop between the pressure regulator and the transducer was negligible, and the exact pressure could be easily read directly from the gauge. Similarly, a gauge indicating vacuum pressure was just as

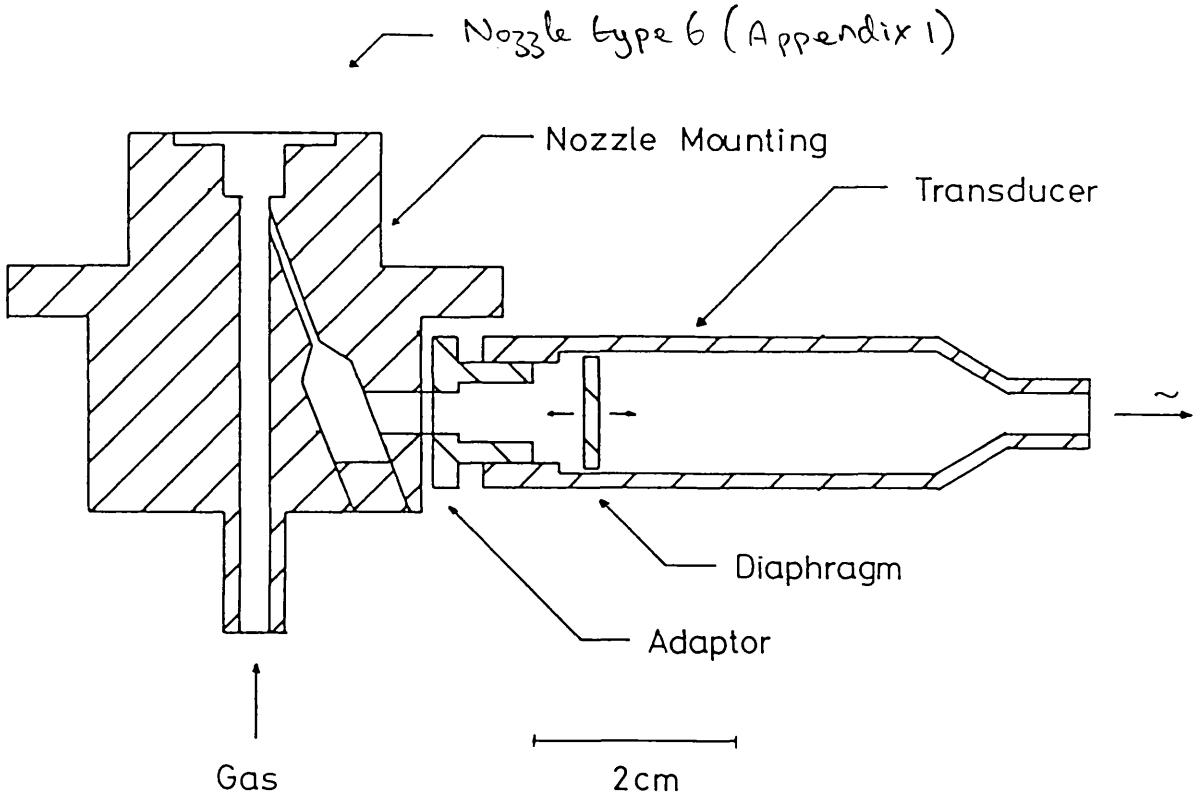

Fig.2.7 Nozzle mounting and pressure transducer.

accurate, after calibration with a mercury manometer, as the pressure transducer.

The events close to the tuyere were photographed with the high speed camera (Fastax), while in the early runs a conventional speed camera (Bolex) was used.

The vacuum tank was manufactured by EFCO EDWARDS and could be pumped by a rotary vacuum pump down to 10 mm Hg. Any vacuum pressure down to this limit could be selected by either closing a valve to the pump on evacuation or by bleeding air into the vessel. Due to the large volume of the vacuum vessel compared to that of injected gas, even at the highest flowrates, the vacuum pressure remained almost constant throughout a run. The vacuum vessel interior was accessible by removing the lid with an overhead crane. The lid contained a port for a 1/2" thick glass window. Electrical connections to the transducer and lights were made by installing ceramic-sealed electrical connecters into a plate at the bottom of the vacuum tank.

2.2.4 Pressure transducers

The transducers used in this work were manufactured by Bell and Howell and were of ranges 0-3, 0-10 and 0-100 bar (abs). At the higher injection pressures the signals went off the scales and back-off circuits were used to preserve a high sensitivity in the UV recorder.

2.2.5 Reduced top pressure gas injection

Every time a set of experiments was to be made the water tank was filled with tap water to a seal depth of 40 cm. A small gas purge was maintained to keep the tuyere clear. The vessel lid was placed in position with the window directly above the mirror. The vessel was then evacuated to 10 mm Hg and left for 24 hours to allow degassing of the water. The Fastax camera, previously focussed, was set so as to reach a framing rate of 2000 fps in about 1 second (the aperture was frequently f5.6). The timing light frequency was set to 100 Hz.

When the camera was set and the required vacuum pressure established the following rapid sequence was initiated by establishing the gas flow (usually hydrogen). Switch "A" in Figure 2.5 was closed to start the timing light, and switch "B" was closed to energize the relay. The camera was kept on for 1.1 s. This gave 4 takes per 100 ft roll of film, thus economizing on film. It was considered that 10 to 20 bubbles per take was an adequate sample. The hydrogen flow was then immediately switched off.

2.3 RESULTS AND THEIR INTERPRETATION

2.3.1 Deep pool - horizontal injection

The results of the experiments carried out in the deep pool are displayed in Table 2.1. Nozzle diameters ranged from 0.317 to 1.13 cm, gases were H_2 and N_2, and flowrates as

Table 2.1 Summary of horizontal injection runs

RUN	Gas	Tuyere pipe diam. (cm)	Q_{STP} m^3/s	F_g/F_B x 10^2	N_{Fr} x 10^{-6}	G kg/s m^2
P44	H_2	.317	.113	56.4	54.4	1200
P45	"	"	.099	50.9	54.4	1055
P46	"	"	.036	22.5	54.4	382
P39	"	.635	.107	13.3	27.17	280
P47	"	.317	.0167	12.3	54.4	179
P40	"	.635	.055	7.81	27.17	144
P41	"	"	.0213	3.7	7.16	56
P35	"	1.13	.12	3.4	7.08	74
P36	"	"	.086	2.7	3.68	54
P37	"	"	.047	1.6	1.09	29
P38	"	"	.021	0.85	0.22	13
P29	N_2	"	.0325	17.7	0.524	290
P30	"	"	.026	14.7	0.389	233
P31	"	"	.0116	7.8	0.067	104

Table 2.2 Summary of vertical injection runs

RUN	Gas	Tuyere pipe diam. (cm)	Q_{STP} m^3/s	F_g/F_B x 10^2	N_{Fr} x 10^{-6}	G kg/s m^2
P15	H_2	.317	.163	75.3	54.4	1727
P17	"	"	.14	66.7	54.4	1482
P18	"	"	.075	40.6	54.4	796
P21	"	.635	.134	15.1	27.2	333
P23	"	"	.166	13.5	27.2	288
P23	"	"	.044	6.12	26.8	108
P12	"	1.13	.135	3.81	9	84
P8	"	"	.106	3.14	5.6	66
P7	"	"	.076	2.39	2.86	47
P13	"	"	.079	2.35	2.72	46
P16	N_2	.317	.0097	115.2	3.89	1483
P27	"	.635	.035	75.5	3.89	1256
P28	"	"	.0118	31.4	3.89	421
P3	"	1.13	.026	14.4	.336	233
P2	"	"	.0074	5.3	.027	66
P1	"	"	.0023	2	.003	20

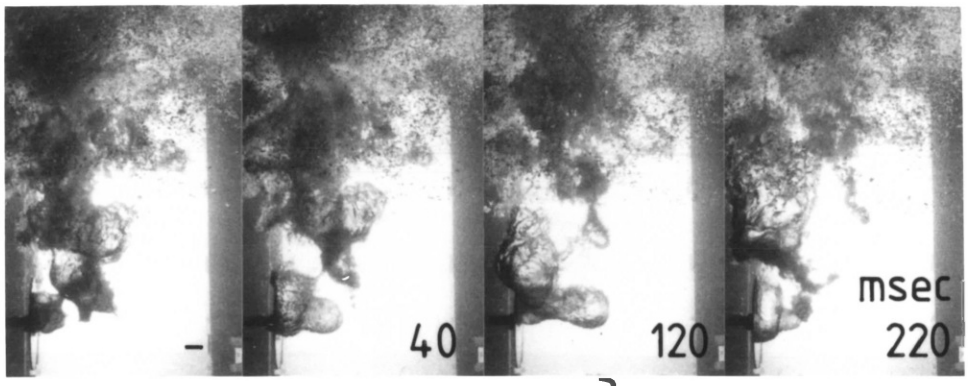

RUN P36. $d_0 = 1{\cdot}13$ cm, $Q = 0{\cdot}086\ m^3/s$, $F_M/F_B = 0{\cdot}027$

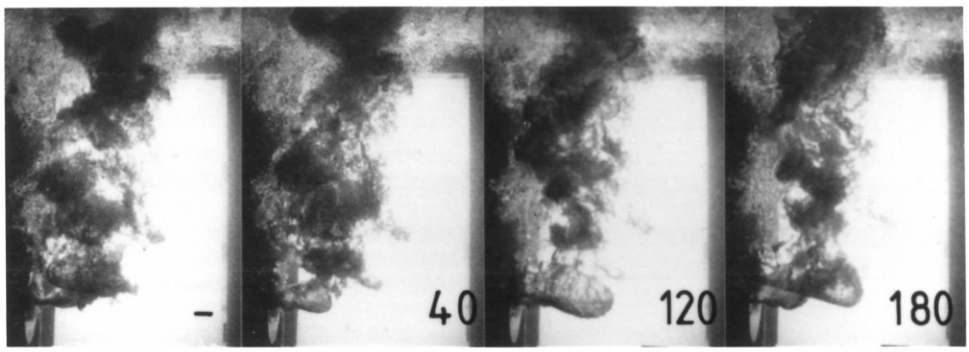

RUN P40. $d_0 = {\cdot}635$ cm, $Q = 0{\cdot}055\ m^3/s$, $F_M/F_B = 0{\cdot}078$

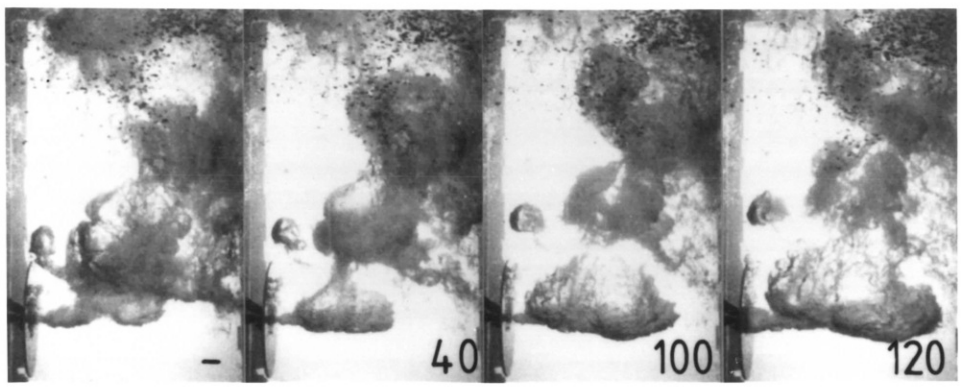

RUN P45. $d_0 = {\cdot}317$ cm, $Q = 0{\cdot}099\ m^3/s$, $F_M/F_B = 0{\cdot}51$

Fig 2·8 Horizontal HYDROGEN injection into water.

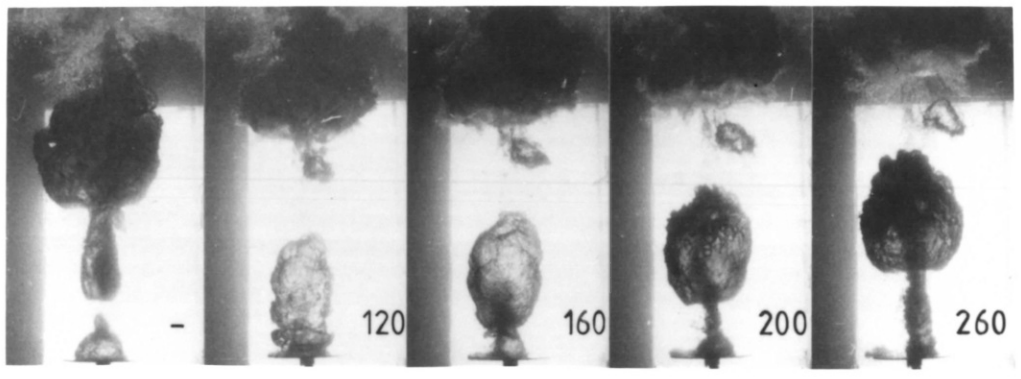

A)

RUN P7. d_o=1·13 cm, Q=0·076m^3/s, F_M/F_B=0·024

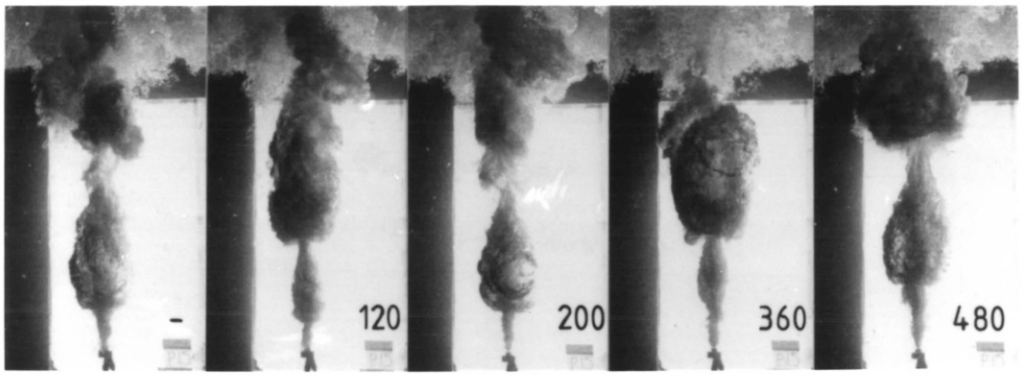

B)

RUN P15. d =·317 cm, Q=0·163m^3/s, F_M/F_B=0·75

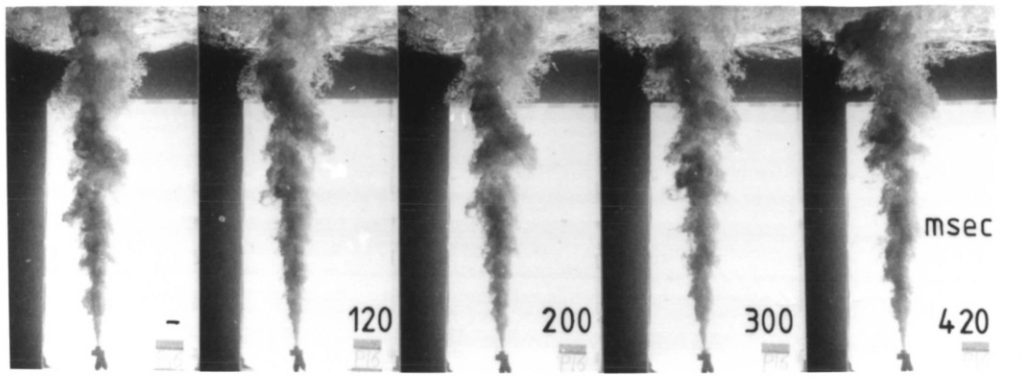

C)

RUN P16. d_o=·317 cm, Q=0·0097m^3/s, F_M/F_B=1·15

Fig. 2.9 Comparison of vertical injection systems.

high as Ø.1 m^3/sec were used.

On examining the gas behaviour on the films, at F_M/F_B less than Ø.Ø7 (for both gases) the gas bubbles grew attached to the wall in a manner similar to bubbles formed by vertical nozzles. By increasing F_M/F_B beyond Ø.11 gas bubbles grew detached from the wall. But an important difference between the two gases was observed. N_2 formed "true" jets for F_M/F_B greater than Ø.11 as there was little spread across the orifice and the jet consisted of a fine dispersion of bubbles. The jet trajectory was in good agreement with the calculations of Themelis et al.[19]. Some intermittent bursts occurred at the tuyere but did not usually represent actual bubble growth[27]. When the gas velocity was above choking conditions the bursts were present at a much lower frequency. During hydrogen injection, as F_M/F_B was increased beyond Ø.11, gas stopped spreading sideways in the nozzle plane. Instead an extremely elongated bubble that looked like a jet developed. Rapid radial expansion of the "jet" took place a few centimetres downstream of the nozzle and a bubble began to form, being fed constantly by the "jet". Large bubbles grew in about Ø.15 s and rose under the influence of buoyancy until they left another expanding "jet" behind for the next bubble to feed on. Bubbles growing attached to and detached from the wall are shown in Figure 2.8.

2.3.3 Deep pool - vertically upward injection

Table 2.2 contains the experimental results of the vertical

injection runs. Gas behaviour was very similar to that in horizontal injection, the transition of regimes occurring at about the same F_M/F_B range of Ø.Ø7 - Ø.11. The same differences as in Section 2.3.1 were observed between N_2 and H_2 jets for F_M/F_B above Ø.11. At very high flowrates hydrogen still forms big bubbles detached from the nozzle, connected to the orifice by a small jet. Figure 2.9 depicts N_2 and H_2 jets.

A typical run in which the flowrate was as large as Ø.Ø76 m^3/s through a large nozzle (1.13 cm diameter) is shown in Figure 2.9A. As soon as the bubble rose and detached from the plate the next rapidly expanding envelope caught up with it and pierced a hole at the bottom. This sent a fine spray of minute droplets into the rising bubble, causing it to lose transparency, seen in Figure 2.9A as a sudden darkening of the bubble. In this context the bubbles can be considered as a two phase mixture within a homogenous liquid.

A nitrogen jet flowing from a choked nozzle is shown in Figure 2.9C. Occasional gas bursts at the tuyere were observed. A possible mechanism to account for this is given by Aoki[27]. The gas leaves the nozzle at a pressure higher than ambient. In adjusting to ambient pressure, expansion shock waves originate at the nozzle exit. These (oblique) waves intersect to produce cyclic changes in pressure which last for a few nozzle diameters until they are damped out by friction. Experimental investigations have confirmed the expected damped pressure oscillation. Where the pressure is at a local minimum it is possible for the surrounding liquid

to flow in and pinch the jet, originating the pulses or "back-attack". One way of avoiding this problem is by using a slot-shaped nozzle which gives a flattened jet. Then it is easy for the gas to flow around any local restriction imposed by liquid drawn in.

2.3.3 Reduced top pressure injection

Hydrogen gas injection into water under top pressure of 5Ø torr results in a gas density downstream as low as 5.5 x $1Ø^{-3}$ kg/m^3. With increasing downstream pressure three main effects were found.

a) The jet started shrinking in its radial dimension.
b) Break-up of the jet started nearer to nozzle.
c) Total agitation of the bath was reduced.

These effects can be understood in terms of the smaller volume of gas injected.

Horizontal injection

A summary of horizontal injection runs is given in Table 2.3 comprising experiments carried out in the small tank under reduced top pressure. The nozzle diameter was Ø.174 mm and hydrogen was the injected gas.

Examination of the films showed that at F_M/F_B less than Ø.Ø7 the bubbles grew and rose up attached to the wall (when the momentum force is 7% or less than that of the buoyancy

J = Bubble detached

B = Bubble attached

Table 2.3 Summary of horizontal hydrogen injection runs under reduced top pressure

RUN	Tank P mmHg	Q_{STP} x 10^4 m^3/s	ρ_g/ρ_l x 10^5	F_M/F_B x 10^2	N_{Fr} 10^{-8}	G kg/sm^2	Behav -iour
V37	760	13.71	8.77	14.8	9.94	5208	J
V36	400	13.7	11.75	6.87	"	"	B/J
V19	200	13.64	2.49	104	"	5182	B
V33	100	13.71	1.37	1.3	"	5208	B
V32	50	13.7	0.81	0.57	"	"	B
V30	760	11.02	8.77	15.5	"	4297	J
V24	400	10.97	4.73	7.18	"	4168	B/J
V18	200	10.97	2.49	3.13	"	"	B
V11	100	8.29	1.37	1.36	"	"	B
V34	200	5.48	2.49	3.31	"	3151	B
V29	760	5.55	8.77	17.8	"	2137	J
V23	400	5.48	4.73	8.23	"	2089	B/J
V39	200	5.48	2.49	3.6	"	2083	B
V10	100	5.48	1.37	1.6	"	"	B
V38	50	2.74	0.81	0.68	"	"	
V28	760	2.78	8.77	20.5	"	1068	J
V9	100	2.81	1.37	1.79	"	1057	B
V3	50	1.39	0.81	0.78	"	1068	
V27	760	1.39	8.79	23.5	"	534	J
V21	400	1.39	4.73	10.9	"	531	B/J
V14	200	1.39	2.49	4.73	"	521	B
V8	100	1.39	1.37	2.06	"	"	B
V2	50	1.39	0.81	0.89	"	"	B
V26	760	0.36	8.77	30.73	"	139	J
V20	400	0.41	4.73	13.9	"	156	B
V13	200	0.34	2.49	6.3	"	130	B
V7	100	0.37	1.37	2.7	"	141	B
V1	50	0.37	0.81	1.17	"	141	B

Table 2.4 Summary of vertical hydrogen injection under reduced top pressure

RUN	Tank P mmHg	Q_{STP} x 10^4 m^3/s	ρ_g/ρ_l x 10^5	F_M/F_B x 10^2	N_{Fr} 10^{-8}	G kg/sm^2	Behav -iour
V44	760	13.7	8.83	14.8	9.94	5208	J
V43	400	13.8	4.76	6.86	"	5235	B/J
V41	100	13.7	1.37	1.3	"	5208	B
V40	50	13.7	.81	0.56	"	"	B
V48	400	10.9	4.76	7.2	"	4170	B/J
V42	200	8.29	2.51	3.31	"	3157	
V47	400	5.48	4.76	8.3	"	2083	B
V46	200	5.48	2.51	3.6	"	"	B
V45	50	5.48	.81	0.68	"	"	B

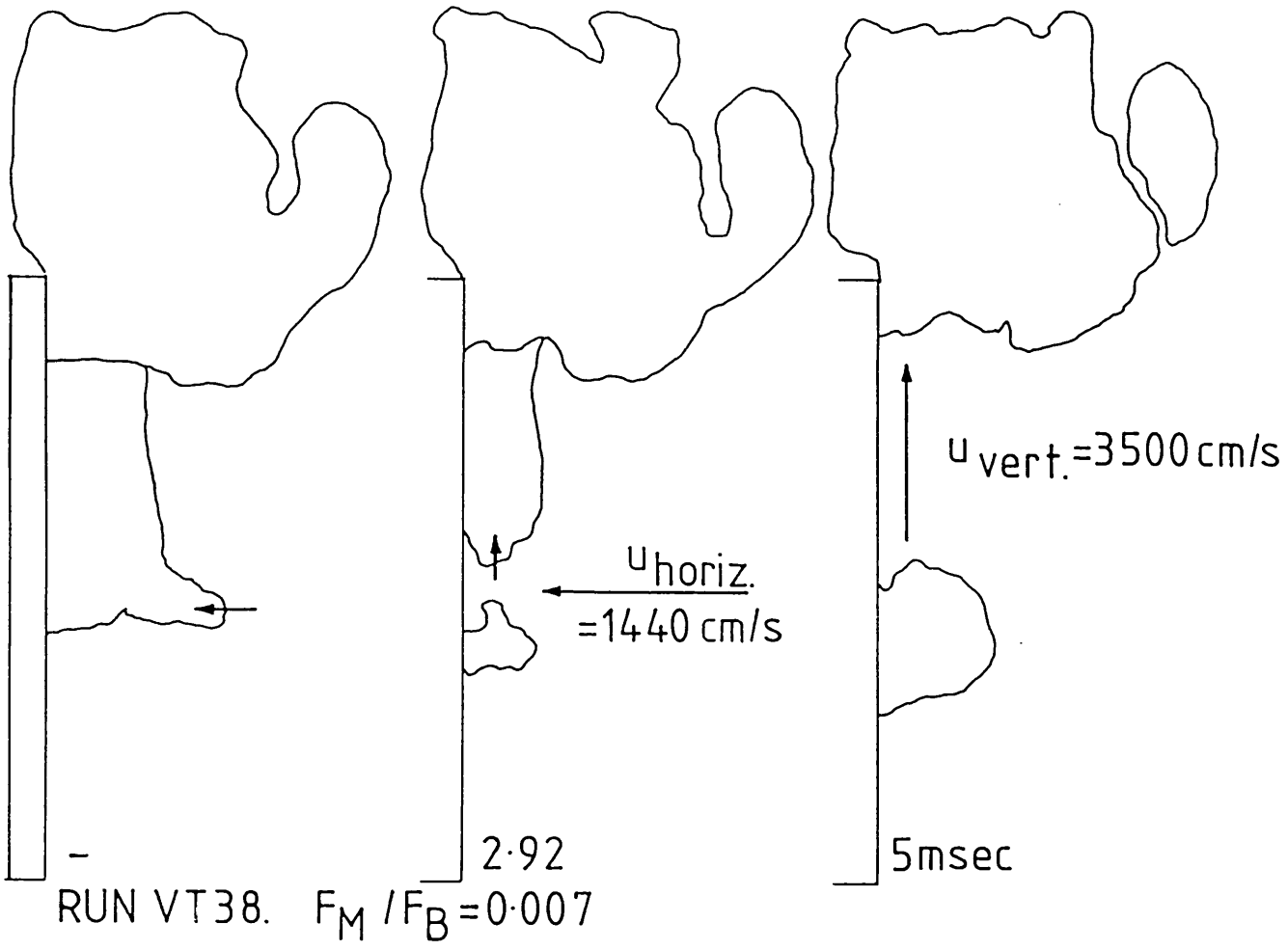

Fig.2.10 A Horizontal hydrogen injection into water under reduced top pressure.

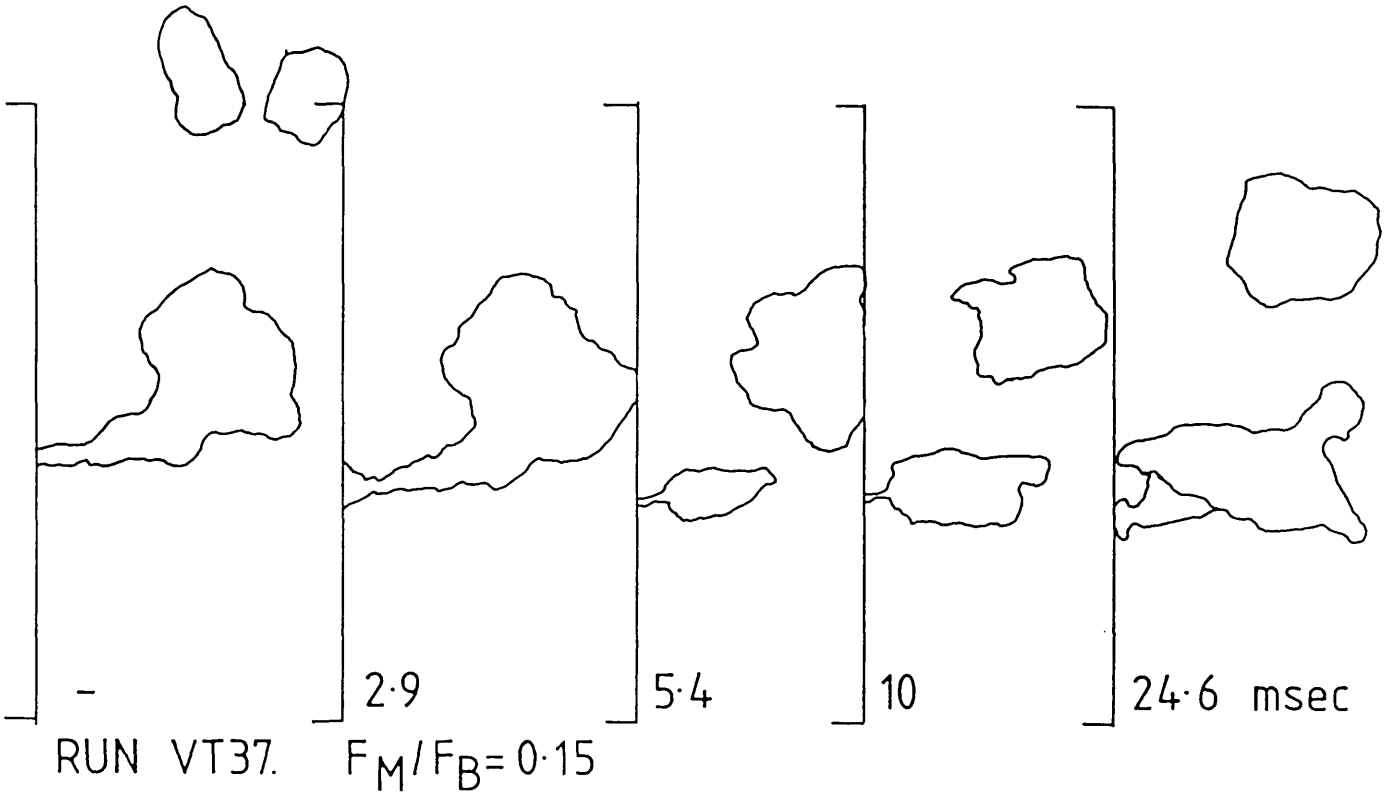

Fig.2.10B Detached bubble growth.

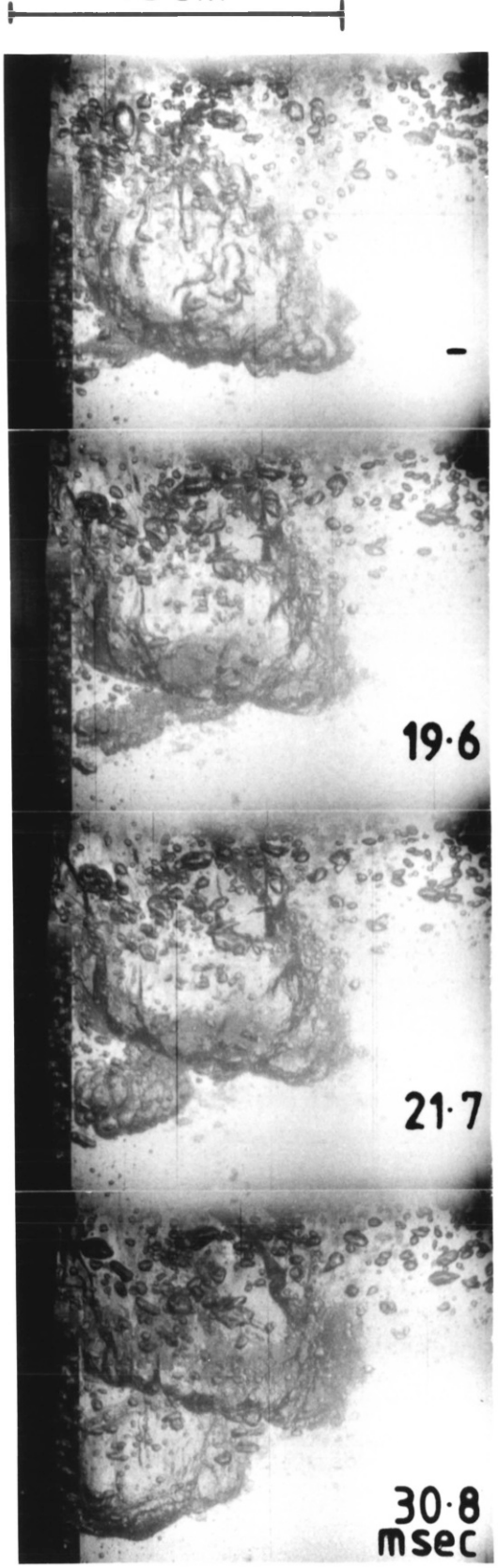

Fig. 2.11A. HYDROGEN injection under reduced top pressure. Run VT33 $F_M / F_B = 0.013$

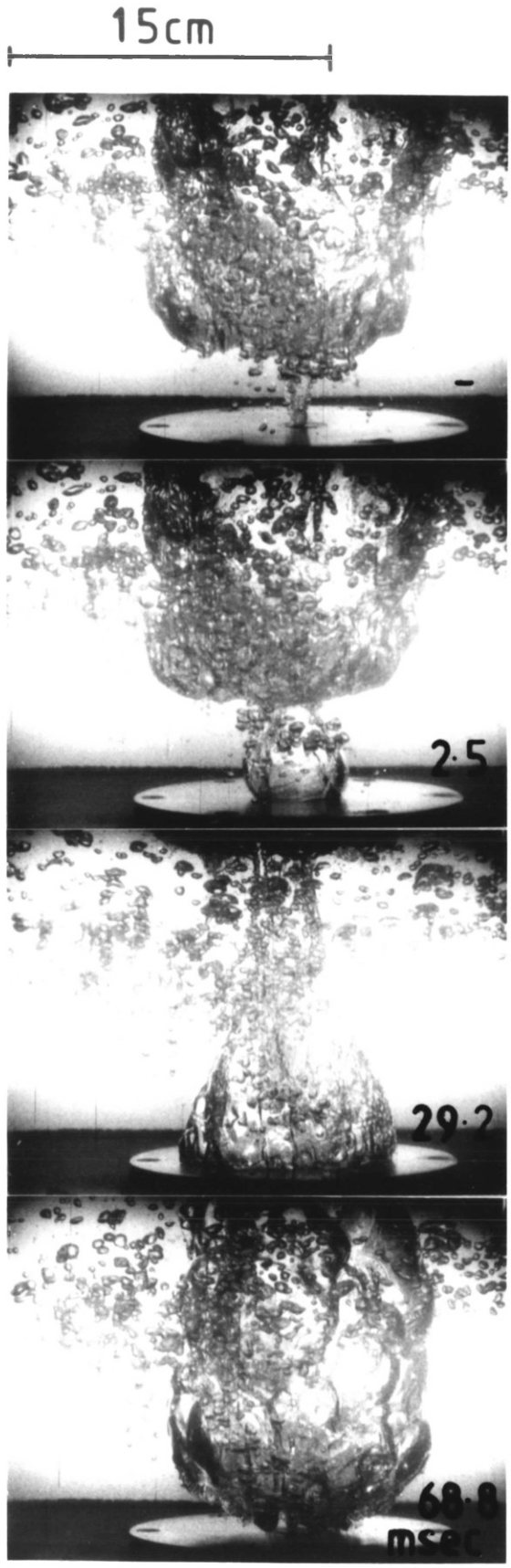

Fig. 2.11B. Run VT40 $F_M / F_B = 0{\cdot}006$

force), shown in Figure 2.10A and Figure 2.10B. As F_M/F_B is increased beyond 0.11 it was found that the gas rose up detached from the wall in a manner similar to that described in Section 2.3.1, that is a growing bubble being fed constantly by a jet, depicted in Figure 2.10B.

Vertical injection

A summary of vertical injection runs under reduced top pressure is given in Table 2.4. Results were similar to horizontal injection, transition of regimes taking place over about the same F_M/F_B range (F_M/F_B = 0.07 - 0.11).

Vertically injected bubbles are shown growing attached to the orifice plate in Figure 2.11B and subsequently rising under buoyancy.

2.4 DISCUSSION

2.4.1 Dimensionless group classification of jet behaviour

As detailed in Appendix 1 previous workers[15, 17, 18] have followed the logic of Wraith et al.[15] and classified jet break-up behaviour in terms of the Injection number (N_I). There are two inherent difficulties with this approach. Firstly, as mentioned in Section 2.1.1, the Injection number as defined by Wraith[15] does not represent the true ratio

of momentum to buoyancy forces because he left out several constants in the expression (Equation 2.3). Inclusion of Equation 2.4 allows direct comparison of the forces.

Secondly, using the nominal velocity ($u_o = Q/A_o$) in Equation 2.2 may lead to serious overestimation of the F_M/F_B value because convergent nozzle velocities can never be greater than sonic. The present approach takes sonic velocities into account in the evaluation of F_M/F_B. An important consequence of choking is that it is impossible to obtain large values of F_M/F_B at low downstream pressures, despite very large driving forces, with the result that bubbling is the predominant regime.

2.4.2 Bubbling/jetting (B/J) transition

At low values of ρ_g/ρ_l (occurring in such systems as H_2/water or Ar/steel) steady jets as defined by Themelis et al.[19], consisting of a dispersion of small bubbles, do not occur. Instead large bubbles grow at the tuyere.

Mori[21, 22] has claimed that the B/J transition occurs when the flow becomes choked and exit pressure rises above ambient. He has defined the B/J transition as the absence of gas spreading across the base of the nozzle plane. Our results show that the definition is too restrictive, since large gas envelopes can form above the nozzle plane even though there is no spreading across the nozzle plane (see Figure 2.10b). Furthermore, it is possible to achieve bubbling when the nozzle is choked if somewhat unusual

experimental conditions are chosen. For example, with say, hydrogen as the gas injected into water under a top pressure of 50 mm Hg, bubbling at the nozzle still occurs when the gas velocity is sonic as shown in Figure 2.11B. Nilmani[9] has also reported bubble spreading at the nozzle with hydrogen injection under reduced top pressure, and with hydrogen into mercury where injection velocities were very nearly sonic.

The McNallan criterion[23] for the conditions at the B/J transition is that once a mass flux density (G) of 400 kg/sm^2 is exceeded for a given system, jetting conditions will prevail. His definition of jetting is similar to that proposed by Mori but with an additional reference to the steadiness of the walls of the jet cone. Examination of Figure 2.11B reveals that bubbling (gas spread over the nozzle plane) still occurs even though G is as large as 1380 kg/sm^2.

Hoefele and Brimacombe[18] have analysed the B/J transition in terms of a jetting behaviour diagram, a plot of the modified Froude number and gas/liquid density ratio. Their definition of jetting was that "liquid is prevented from washing against the tuyere tip by the continuing presence of gas". The transition between regimes was reported to occur at a critical N_{Fr}' for a given ρ_g/ρ_l. The critical N_{Fr}' being higher for low ρ_g/ρ_l than for high ρ_g/ρ_l.

It is considered that the best criterion for the B/J transition is whether the gas spreads across the nozzle or

not, as defined by Mori[21, 22]. The condition quoted[21, 22] as necessary to achieve jetting is the attainment of sonic velocities at the nozzle exit. However, to call H_2 behaviour at F_M/F_B greater than Ø.11 jetting is highly misleading in some respects. The lack of fragmentation of H_2 bubbles forming at the nozzle leads to very poor gas-liquid contact compared with air jets. The phenomenon of lack of gas expansion very close to the tuyere in choked nozzles observed by Mori[21, 22] in the air-mercury and here in the H_2-water system at very high flowrates might best be described as a "local-jet" and is not indicative of the overall behaviour.

A more general approach to classifying the behaviour of the injected gas is taken here, following the logic of Farias[17] and Wraith et al.[15], and does not specify a B/J transition. Instead the extent of separation of the bulk of the gas from the tuyere plane is specified and this works equally well for both horizontal and vertically upward injection. The transition from bubble growth attached to and growth detached from the nozzle plane is determined by the ratio of momentum to buoyancy forces F_M/F_B. As reported earlier the transition takes place at F_M/F_B = Ø.Ø7 - Ø.11, ie. when the momentum force is 7 - 11% of the buoyancy force at bubble separation.

One great advantage is that our criterion and that of Brimacombe are independent of scale for a given ρ_g/ρ_l. Brimacombe's conditions are roughly consistant with that proposed above. In the air-water system there is absolute

agreement, but for lower values of ρ_g/ρ_l Brimacombe's conditions underestimate the necessary N_{Fr}' for jetting.

The real differences in the various predictions show at extremely low ρ_g/ρ_l values. The present work, investigating behaviour at ρ_g/ρ_l values as low as 8×10^{-6}, showed the conditions proposed by both Mori and McNallen to be incorrect.

2.4.3 Validity of model work in representing industrial systems

The complexity of industrial systems makes comparison with laboratory models a very controversial issue. The injection gas is usually reactive and relatively cold. Accretions of frozen metal (see Chapter 5) may exist at the tuyere tip and large quantities of solid scrap may be present in the bath.

If there is a hot zone, where reactive gas comes into contact with liquid metal, the effective superheat of metal adjacent to the tuyere will be much higher than the nominal superheat given by $(T_b - T_m)$ (see Section 5.8.5).

There is little information on the fluid dynamic behaviour of very reactive gas jets in liquids. This results in unreliable scale up data from non-reactive models to the Q-BOP. However, processes such as the AOD, ladle injection and copper converting, where a significant proportion of the injected gas is inert, may be better understood in terms of laboratory models.

Accretion formation further complicates injected gas behaviour. Accretions are generally porous[28] but in some cases they may be pipe-like[29], representing an effective extension of the tuyere. In these latter circumstances results from clean tuyeres should be applicable.

The behaviour of real systems may be predicted, bearing these restrictions in mind, by first calculating the bubble volume as

$$V_b = Q\ t_b,\ t_b = f(F_M/F_B,\ Q,\ g)$$

If F_M/F_B and Q are kept the same in the model as in the prototype then V_b should be equal in both systems. In this situation

$$r_o(\text{model}) = r_o(\text{prot.})((\rho_{gm}/\rho_{gp})(\rho_{lp}/\rho_{lm}))^{1/2}$$

If H_2/water is used to represent Ar/steel, then

$$r_o(\text{model}) = 0.6 r_o(\text{prot.})$$

Figure 2.8B is for flow conditions similar to some AOD practices ($200 m^3/hr$, r_o=5.5 mm (I.D. of shroud)). Bubbles wash over the nozzle plane approximately 600 times a minute and rise attached to the wall behaving much as if they had been vertically injected. High rates of refractory wear in this area can occur as a result of this washing action. Large shear stresses are set up and have been shown by Ballal and Ghosh[30] to be important in the erosion process. Further,

rapid rates of thermal cycling of the refractory may cause it to spall. The problem is compounded by the release of the exothermic heat of reaction. Altering the jet conditions to those shown in Figure 2.8C may improve the severe wear problem by moving the rear edge of the jet and the ignition zone away from the inside wall of the converter.

2.5 CONCLUSIONS

1) The bubbling/jetting transition can best be described in terms of the ratio of momentum to buoyancy forces (F_M/F_B). For all horizontal systems for F_M/F_B less than Ø.Ø7 the gas bubbles grew in a manner similar to bubbles injected vertically, attached to the wall. This latter observation may be relevant to the very severe wear observed in the brick above the tuyere in the AOD process. For F_M/F_B greater than Ø.11 the gas bubbles rose detached from the wall for horizontal submerged gas injection.

2) H_2 injection at high rates failed to produce "true" jets. Big bubbles formed away from the nozzle plane at F_M/F_B up to Ø.75.

3) At low ρ_g/ρ_l (eg. H_2/water, Argon/steel) true jets as defined by Themelis et al.[19] never occur.

4) The whole flow must be observed since even if there is no spread at the nozzle (Mori's criterion for the bubbling/jetting transition), large bubbles can form

beyond the nozzle. Furthermore, it is possible to achieve bubbling at low F_M/F_B when the nozzle is choked if somewhat unusual experimental conditions are chosen.

5) The bubbling/jetting transition criterion of McNallan and King has been shown to be inconsistant with the results of the present study.

6) It is difficult to obtain large values of F_M/F_B at low ρ_g/ρ_l values because of the nozzle choking.

2.6 FURTHER WORK

1) The use of isothermal models and inert gases is not representative of the real situation in metallurgical converters. Mixtures of a reactive gas (ammonia) and nitrogen have been injected into water at low flowrates[9]. This work needs to be extended to cover high flowrates.

2) The effect of scrap iron on the behaviour of submerged jets could be simulated by adding lumps of ice into the aqueous model. The ice could be made to sink by freezing in lead shot.

3) Flattened nozzles, as used by Aoki[27], and the effect of swirling the gas should be investigated.

CHAPTER 3

AOD TUYERE PRESSURE/FLOWRATE CHARACTERISTICS

CHAPTER 3

AOD TUYERE PRESSURE/FLOWRATE CHARACTERISTICS

3.1 INTRODUCTION

3.1.1 The argon oxygen decarburization process

The AOD process achieves decarburization of stainless steel at a CO partial pressure low enough to ensure that the gaseous product of the oxidizing reaction (CO) is eventually formed in preference to metallic oxides. The appropriate chemical reactions are:-

$$FeO + C = CO + \underline{Fe}$$

$$Cr_2O_3 + C = 3CO + \underline{2Cr}$$

The AOD process uses argon as a diluent gas as a means of reducing the CO partial pressure. Argon and oxygen are injected horizontally through submerged annular tuyeres located near the base of the vessel. Minimizing tuyere and local refractory attack depends on the presence and control of accretions of frozen metal forming at the tuyere tip. There is, at present, no means of monitoring accretion behaviour during the blow. Accretions can be observed when the vessel is tilted and the tuyeres are brought above the level of the melt.

Experimental investigations have been carried out on an 8 tonne AOD converter at Wiggin Steel and Alloys (WSA), Birmingham, with the following objectives

1) Measurement of tuyere core and shroud pressure as close as practicable to the vessel shell in the hope that these could be used to monitor accretion formation at the tuyere tip.
2) Measurement of vessel vibration in an effort to deduce bubble frequency.
3) Measurement of shroud flow to one tuyere.
4) Examination of wear patterns in the converter in an attempt to relate these to gas and liquid flow.

3.1.2 Wiggin Steel and Alloys 8 tonne AOD converter gas supply

The system for supplying the two tuyeres with gas is shown in Figure 3.1. Oxygen may be mixed with either argon or nitrogen in the core line leading to the manifold. Pure argon or nitrogen are fed to the shroud manifold. The purging gas, air, which keeps the tuyeres cold and clear when the converter is in the horizontal position, can be supplied to both the core and shroud lines from a compresser(4 bar g.).

Liquid oxygen, nitrogen and argon are stored at 17 bar g in pressure vessels. After flow through evaporators the gas is at ambient temperature by the time it reaches the supply control room.

Orifice meters OM1 and OM2, incorporating flow totalizers, and control valves CV1 and CV2 meter and control the oxygen and argon flowrates respectively. Thus the total volume of oxygen supplied to both cores is known. Some of the argon is then fed into the shroud line and is controlled by CV3. The shroud flowrate is not metered and as a result there is some uncertainty as to how much argon flows to the core. The shroud gas is supplied under constant pressure conditions as this is better for accretion size control(see Section 3.1.5).

The purge gas flows under constant pressure through the tuyeres when the converter is horizontal. The quick-shut valves QSV(1 to 3) are used in the changeover from process to purge gas. Limit switches located in the converter trunnion ring operate these valves and ensure that there is always argon flowing through the tuyeres when the vessel is in the vertical position. The operator has no indication or control over the flowrates through each individual tuyere.

3.1.3 The tuyeres

The tuyere consists of a hard drawn copper tube through which oxygen or argon/oxygen is blown. The core fits into a larger diameter shroud tube of stainless steel (type 304) and is held in position by punched indentations in the shroud tube. Argon is blown through the annular gap. The

tuyere assembly and dimensions are given in Figure 3.2. Commercial availability of different sized copper and stainless steel tubes limits the combinations suitable for tuyere manufacture and operation.

The tuyeres employed at WSA had rather large annular gaps, necessitating very large shroud gas flowrates to provide adequate cooling. For some heats (eg mild steel melts) it was impossible to obtain the specified O_2:Ar ratio of 3:1 due to the high shroud flowrate needed and the limited capacity of the oxygen supply. An experimental tuyere with a narrower annular gap (dimensions are given in Figure 3.2) was installed and monitored in this work, aimed at lowering argon consumption. Argon is a relatively expensive gas.

3.1.4 Meltshop practice

Many types of steels are manufactured at WSA. The common practice is to start the working week making low alloy melts (eg mild steel) and as the week goes on, increasing the alloying additions on each melt.

The standard operation for each melt is as follows:-

i) The air purge is switched on.

ii) The liquid metal is charged.

iii) The composition and temperature are checked.

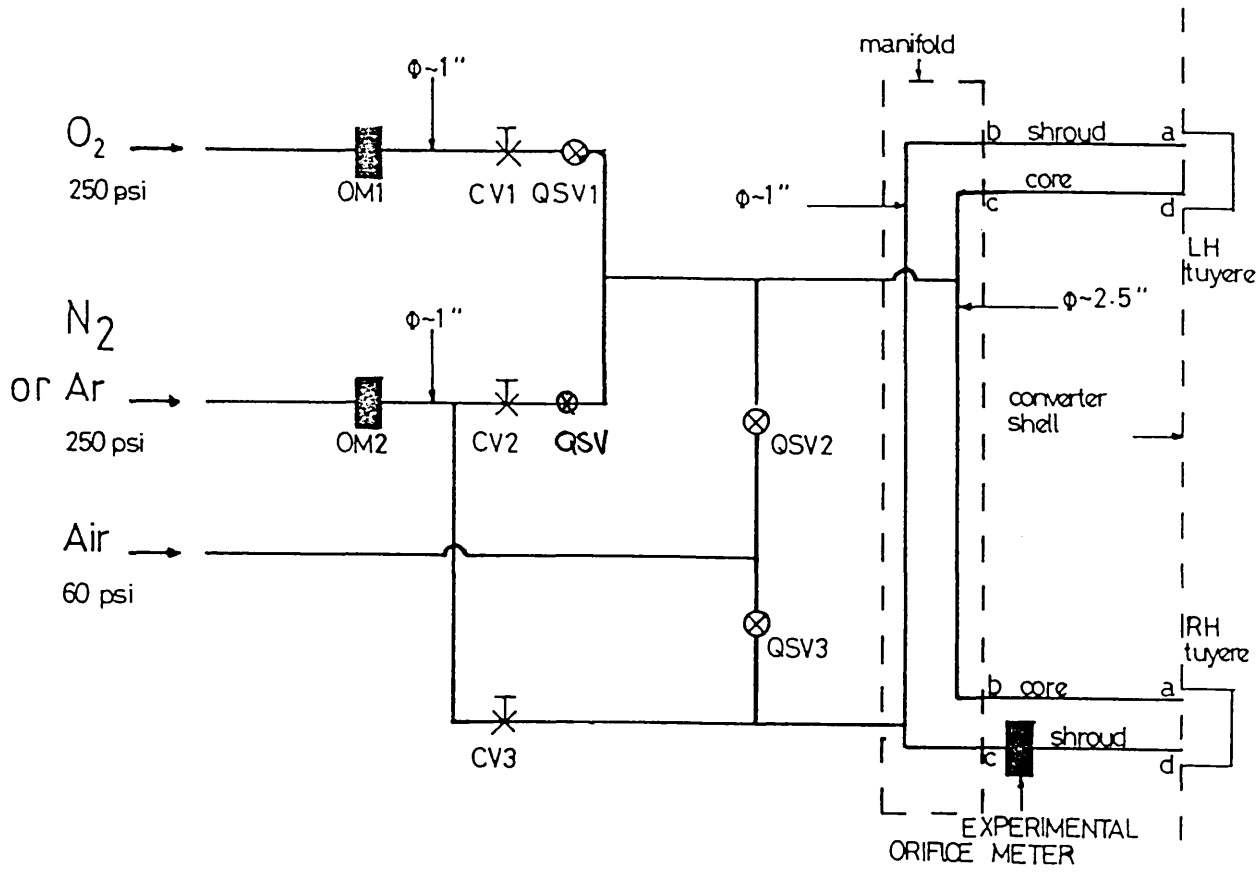

Fig.3.1 Gas supply system.

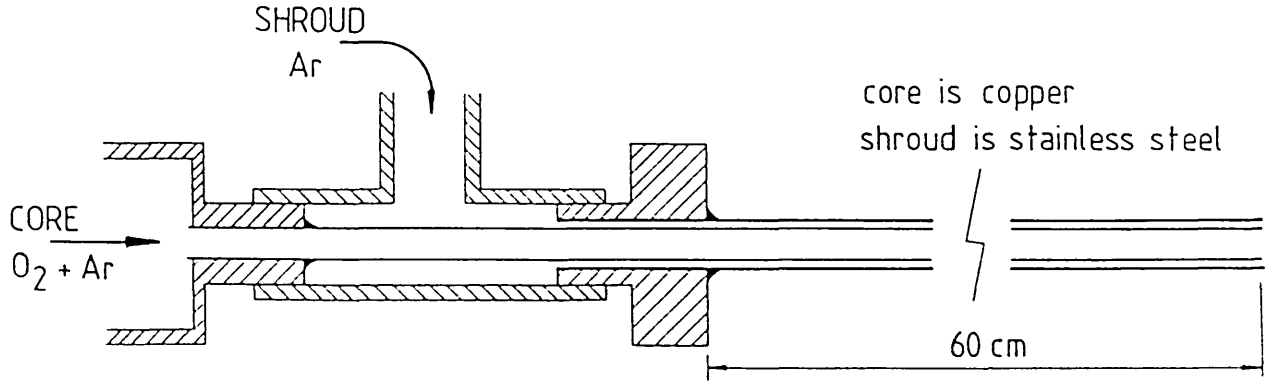

	NORMAL TUYERE	EXPERIMENTAL TUYERE	
shroud o.d.	11.11	11.11	mm
shroud i.d.	9.52	9.52	mm
core o.d.	7.94	8.48	mm
core i.d.	6.35	6.65	mm
A_s	21.67	14.70	mm^2
A_c	31.67	34.73	mm^2
A_s / A_c	0.68	0.42	

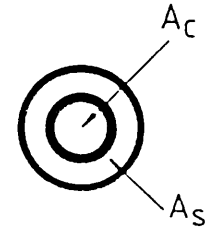

Fig.3.2 Tuyere assembly with dimensions.

iv) Some additions such as lime are made.

v) The converter is tilted to the upright position whereupon the argon flow through the core and shroud switches on automatically. Once the vessel is vertical, the O_2 flow may be switched on manually.

The amounts of O_2 and Ar flowing may be controlled manually and the shroud pressure is set by the operator. The actual practice for any given melt may vary somewhat, although generally there are three basic steps.

The liquid metal is charged at a temperature of about 1650^{o}C and a carbon content of 1 to 2% C along with some slag. In the first step the melt is refined with an oxygen to argon ratio of 1.64:1 (0.071:0.043 Nm^3/S) down to 0.4% C.

In the second step (sometimes optional) a ratio of 1:1 is used down to 0.2% C and in the third step with 1:1.64 (0.43:0.071 Nm^3/S) to lower than 0.05% C. The temperature is controlled by additions of scrap, alloys and lime so that at the end of the last step the temperature is about 1700^{o}C. After the refining period lime and ferrosilicon are added and the melt is reduced, blowing argon only. The reduction slag is skimmed off and, after sampling, the metal is tapped and cast. Sometimes further alloying or desulphurization additions will be made to obtain the required specifications. If the temperature is too low for casting, it is raised by blowing some oxygen and argon at 2:1 and

this raises the temperature by about 10°C per minute.

3.1.5 Accretion control

The optimum accretion length is believed[31] to be 1-2". It appears that accretions greater than about 3" tend to "cap-off" and become porous, which closes the main channel for gas flow, thereby increasing the radial distribution of the exitting gas. Accretions shorter than about 1" are difficult to control consistently. Further, the area of maximum heat transfer (oxygen input point) moves closer to the tuyere brick which has deleterious effects on refractory wear.

Accretions grow with increasing shroud pressure, but the shape appears to be a complex function of grade, operating temperature and processing conditions (some of these points are discussed in Chapter 5).

It is easier to form accretions when refining grades containing a high alloy content. For example stainless grades require a lower shroud pressure (50 psi) than carbon/low alloy grades (150 psi), during the first stage blow, to form an equivalent accretion size.

The tuyere is operated under constant pressure conditions because in the event of tuyere blockage by a large accretion, a constant pressure supply ensures that the flow to that particular tuyere is reduced,

and some reduction in accretion size (and therefore resistance) will occur. If a constant flowrate supply were to be employed, the accretion presenting the greatest resistance would tend to stabilize (block off) while the other grows.

3.2 EXPERIMENTAL

The gas supply and pipe-work leading to the tuyeres is shown in Figure 3.1. Bell and Howell pressure transducers (Ø-1Ø bar, abs.) were placed at several positions (marked a, b, c, d) near the tuyere entry. As many as three transducers were used simultaneously. An orifice meter, incorporating a differential pressure transducer (Ø-Ø.35 bar), was mounted on the shroud supply line to one tuyere to measure the gas flowrate. The transducer locations and experimental procedure are summarized in Table 3.1.

Certain precautionary measures had to be taken to guard against the high temperatures of the AOD vessel. Heat resistant cable was insulated by being placed inside rubber hoses covered with asbestos fabric. Plug sockets and connectors were insulated with PTFE tape and care had to be taken in positioning the pressure transducers to avoid excessive heating. In addition an asbestos skirt was fitted to the side of the converter to reduce heating by radiation and to prevent the covered hoses resting on the shell when the converter was tilted horizontally. To prevent the wires

TABLE 3.1 Summary of procedure in the different runs

Campaign (heats)	Pressure monitored *	Position of transducers (Fig.3.1)	Shroud flow monitored with orif. meter	Type of melt	Time in vessel life	Accelerometer used	Tuyere type
1 (A1-A10)	RHC,RHS LHC	bcc			middle-end		old
2 (B1-B3)	RHC,RHS	ad	at a	mild 25%Cr	end		old
3 (C1-C10)	RHC,RHS	bd	at d	mild En26 12%Cr	middle	attached permanently	old
4 (NT1-NT6)	RHC	c	at c	25%Cr 18/8	new	moveable probe	new

*
RHC = Right Hand Core
RHS = " " Shroud
LHC = Left Hand Core

burning when the pre-heater was in place, large asbestos sheets were placed in front of the hoses.

In the third and fourth campaigns an accelerometer was used to measure the vibrations of the furnace. In campaign 3 the accelerometer was screwed into the orifice meter assembly which was then attached to the tuyere. In the fourth campaign the accelerometer was fixed to the end of a 1.5 metre long rod which could be used to probe any part of the furnace.

In all cases the steady gas pressures (and pressure difference in the orifice meter) were measured on a pen-recorder; the pressure transducer and the accelerometer signals were recorded on a UV recorder.

3.3 RESULTS

Measurements were performed in four separate campaigns covering a variety of conditions. Results are summarized in Table 3.2.

3.3.1 Pressure and flow measurements

The pressure and flow measurements indicated that the tuyere operated very stably during the course of a heat. The core pressure never fluctuated more than 5% in any particular stage of the process. The shroud pressure and flow were even more stable than this.

TABLE 3.2 RESULTS

Heat	Melt type	Step	Core pressure kPa	Shroud pressure kPa	Q_{O_2} Nom m^3/s	Q_{Ar} Nom m^3/s	Q shroud per tuyere m^3/s
A1	mild	1	1172	1033	.07	.047	
		2	1172	1033	.07	.047	
		Redn.	1172	1033	0	.047	
A2	mild	2	1400	345	.058	.039	
		3	1172	345	.062	.0312	
		Redn.	828	345	0	.061	
B1	mild	3		962		.044	.0215
B2	-			780		.044	.014
				871		.044	.015
B3	25%Cr			486		.044	.01
		3		587			.014
C1	mild	3		1033			.014
C2	"			-			-
C3	"	2		1074			.019
C4	12%Cr	Redn.		851		.028	.013
C5	"			851		.031	-
NT1	25%Cr	1		426		.023	.0053
		1		496		.023	.0064
		3		567		.06	.0084
NT2	"	1		517		.023	.0076
NT3	"	1		517		.023	.0069
NT5	"	1		456		.023	.0053
NT6	stainless	1		780		.023	.0080

The core pressure in the mild steel melts was about 12 bar (176 psi) towards the end of the vessel life. In this type of heat all the argon gas goes through the shroud. The accretion was very small and had the appearance of a single hole 'nozzle'.

In the high alloy melts the core pressure increased to about 14 bar (205 psi) and the measured flow of argon through the shroud was only 40% of the total argon flow. Bigger accretions formed which had the appearance of being porous.

At first it was thought that the presence of the accretion could be detected simply by looking for fluctuations in line pressure. High frequency pressure fluctuations resulting from bubbles expanding in the liquid when they are present generally give a good idea of the gas dispersion regime[18, 33]. Any change in bubbling frequency arising from the presence of an accretion should become apparent by examining the pressure traces.

Collins and Wraith[34] have reported that the average peak to peak time in traces picked up at a tuyere discharging into molten iron decreased when an accretion was present at the tuyere tip. The suggested reason for this is that within a porous accretion each pore may act as an independent source of pulses. However, no high frequency pulsations were found in normal tuyere operation at WSA, the reason being that the gas velocities were too high for the disturbances to propagate back through the line[33]. In this situation

nothing can be said about the nature of gas behaviour at the tuyere exit.

An alternative technique used to detect bubble formation was the measurement of vessel vibration. It was found that the whole vessel, and indeed the whole shop vibrated at a frequency of about 10 Hz. This suggested that bubbling was taking place, as 10 Hz is the bubbling frequency expected in that kind of system. The measurements however were inconclusive. There was no time to carry out a proper programme of trials and the very regular measured frequency of 10 Hz could only be explained if both nozzles operated in synchronization, which is most unlikely.

The third possible way to detect accretions was by observing the relatively slow changes in core pressure that could come about from the formation and subsequent growth of the accretion producing a changing resistance to flow in the system. A typical pressure record of a heat is shown in Figure 3.3. The core pressure remained roughly steady during the plant investigations even though accretions were observed between blows. Therefore it was decided to investigate in the laboratory what the influence of an artificial accretion at the tip would be on the pressure drops across the entire length of the tuyere. This work is described in Section 3.3.2.

The results showed that for a constant mass flowrate the supply pressure dropped hyperbolically with increasing the

ratio of total area of holes in the accretion to area of the pipe (accretion 'openness'). This means that the supply pressure upstream of the accretion remains roughly constant for accretion openness greater than Ø.6. Thus if accretions in practice are fairly open it is expected that changes in their configuration would not cause significant changes in supply pressure.

Plant measurements indicated that the pressure drop through the entire supply system, from the reservoir to our measurement position, was only 3 - 5 bar. Results from laboratory studies showed that the main pressure drop is through the accretion itself, when one is present.

3.3.2 Pressure/flowrate characteristics in model accretions

The apparatus used to measure flow through artificial accretions is shown in Figure 3.4. The model tuyere was instrumented with suitable pressure transducers (Section 2.2.4) both before and after the abrupt contraction from the supply line to the core tube and also at the tuyere tip. Artificial accretions were attached to the end of the core tube. Holes were drilled radially into the accretions to increase the 'openness'.

Results of trials conducted at constant mass flowrates of oxygen ($\dot{m}$ = Ø.Ø37 kg/s) are depicted in Figure 3.5. Diameter of the holes was 1/8" (1.76 mm) and the number of holes was increased in steps of two from 6 to 14 to give a change in the total area of holes to area of the pipe (nA_h/A_p) (called

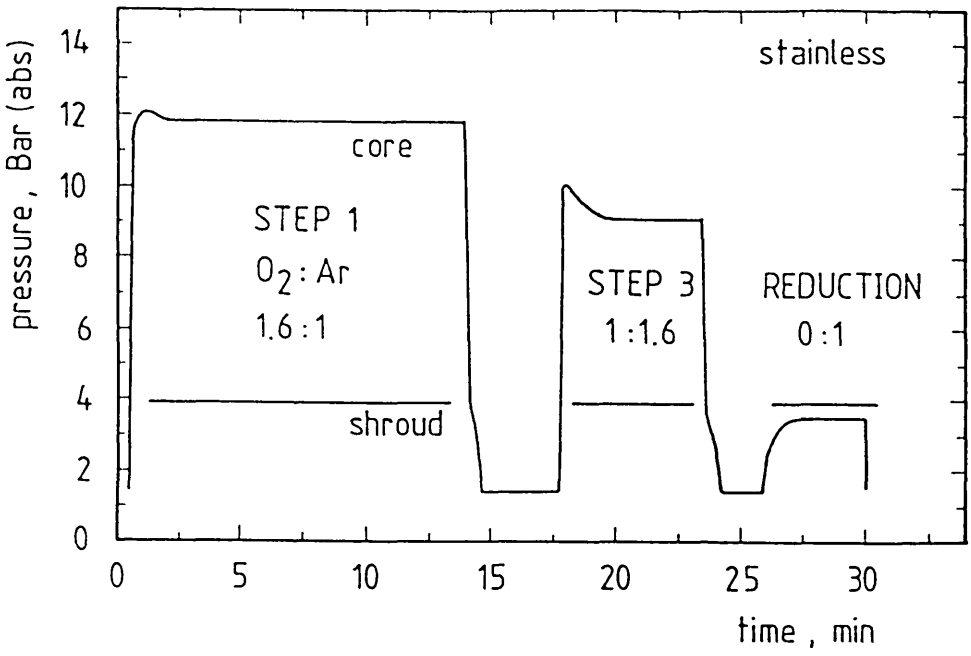

Fig.3.3 Typical blowing practice. Measured pressures.

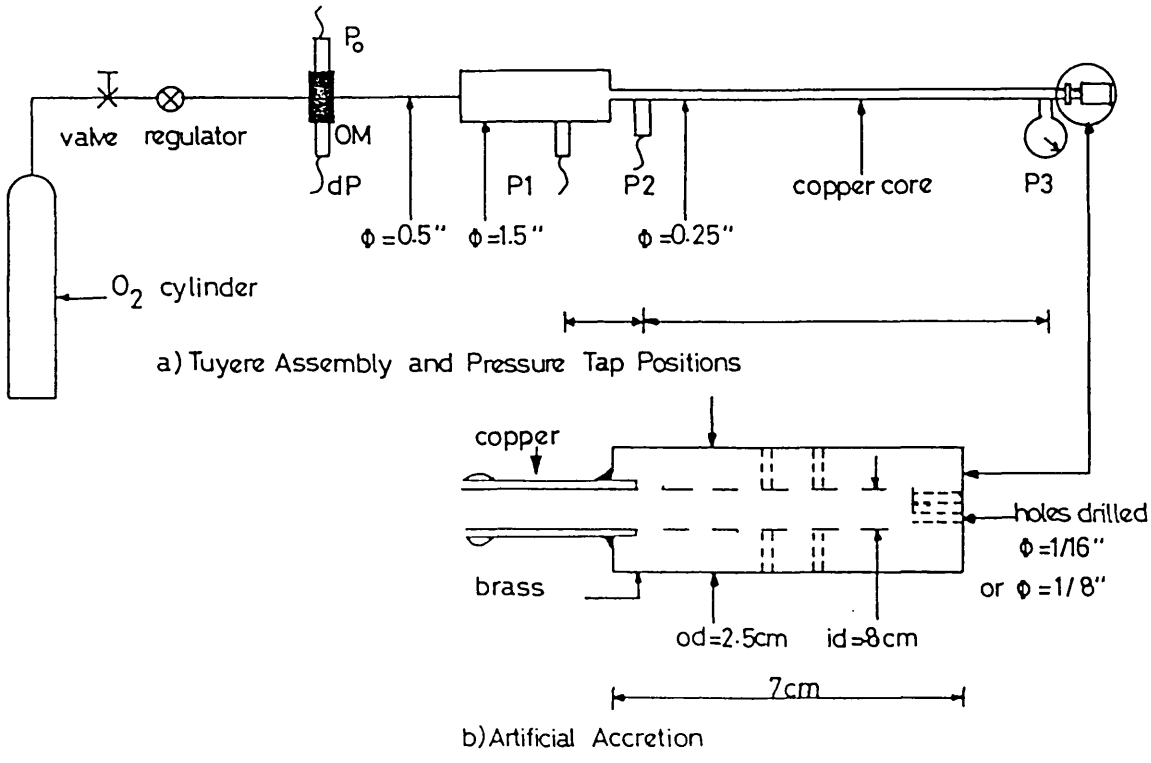

Fig.3.4 Tuyere assembly for pressure-drop analysis.

accretion openness) from 0.46 to 1.075. Results are compared with those from an open ended tuyere. In the latter case the major contribution to the pressure drop is given by friction and acceleration in the long pipe. When the accretion is present, however, the main pressure drop is through the accretion itself.

Open ended tuyere

The entry loss coefficient

$$K_L = (2\Delta P_{(1-2)} / \rho_2 G_p^2) - 1 \qquad (3.1)$$

was calculated from the data assuming frictionless adiabatic expansion of the gas through the contraction. The energy equation is thus

$$C_p T_1 = C_p T + u^2/2 \qquad (3.2)$$

and the continuity equation

$$\rho u = \dot{m}/A = G \qquad (3.3)$$

Combining Equations 3.2 and 3.3 with the perfect gas relationship

$$P = \rho RT \qquad (3.4)$$

yields the following implicit expression for the density of

the expanded gas

$$P_2 = \rho_2 R(T_1 - G_p^2 / 2C_p\rho_2^2) \qquad (3.5)$$

The K_L value calculated from Equations 3.1 and 3.5 with T_1 = 293 K was 2.5 for the open ended tuyere as well as with the accretion in position. This K_L value of 2.5 is larger than the normally reported value of Ø.5 for a square edge entrance[35]. One possible reason for the disagreement could be that the transducer tapping was placed at the throat of the vena contracta where the pressure is lower than that immediately downstream, although no attempt was made to investigate this. The gas temperature at point 2 was calculated to be Ø.976 T_1 from Equations 3.4 and 3.5 for all runs.

Hunsaker[36] outlines a method for determining the mean friction factor (f) for adiabatic flow in pipes with friction. A value of f = Ø.Ø26 was obtained for the core tube. At a Reynolds Number of 5.7 x $1Ø^5$, the friction factor value corresponds well to that of drawn tubing on a Moody diagram[35].

Effect of model accretions

Examination of Figure 3.5 reveals that the entry pressure P_1 decreases as the number of holes (n) in the accretion increase.

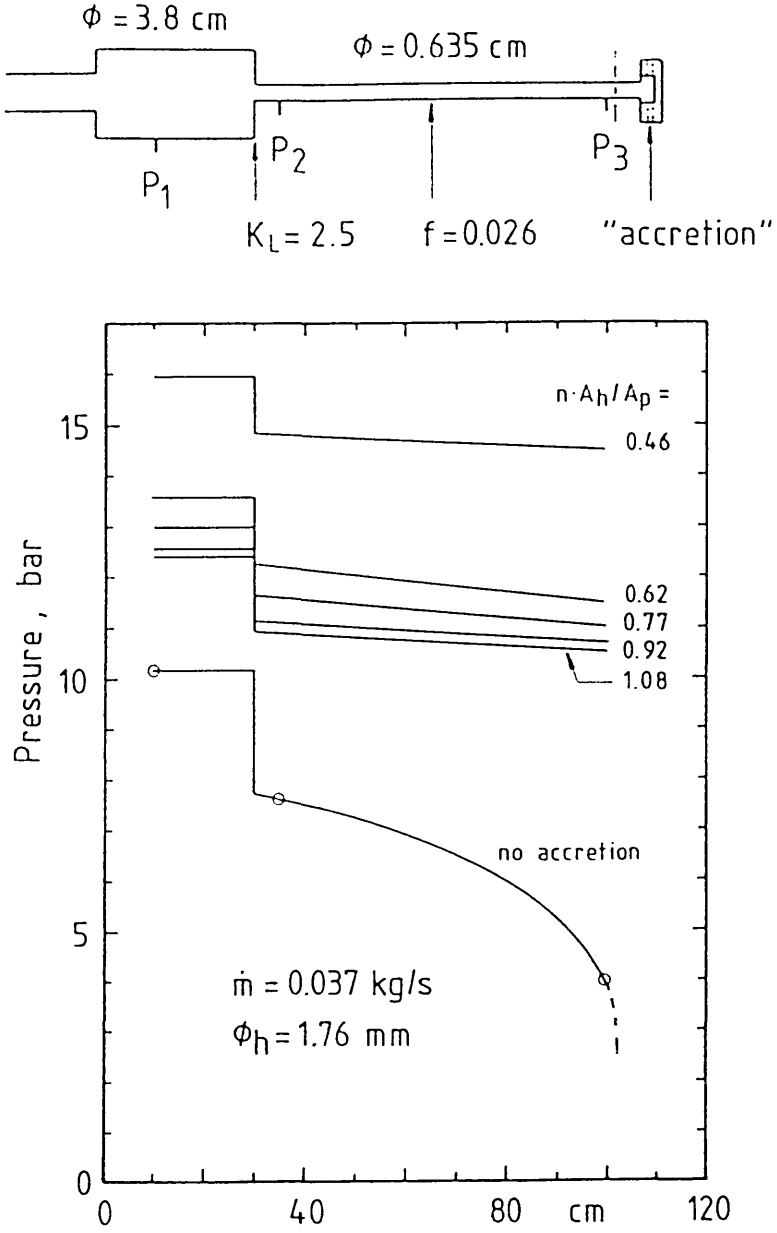

Fig.3.5 Pressure drops in WSA tuyere.

This can be understood by the following analysis. The mass flowrate per unit area through each hole can be expressed in terms of the mass flowrate per unit area of pipe as

$$G_h = (1/n)(A_h/A_p)G_p \tag{3.6}$$

At the tiny orifices the pressure loss due to entrance, acceleration and friction effects is

$$\Delta P = (K_{Lh} + fl/2D + 1)(1/n^2)(A_p/A_h)^2(G_p^2/\rho_e)(\tfrac{1}{2}) \tag{3.7}$$

ρ_e is the gas exit density just downstream of the orifice entrance and can, as a first approximation, be set equal to the density at the exit for choked flow, then

$$G_h^2/\rho_e^2 = dP/d\rho = RT_3 + (G_h^2/\rho_e^2)R/2C_p \tag{3.8}$$

from where

$$\rho_e = ((1 - R/2C_p) / RT_3)^{1/2}G_h \tag{3.9}$$

and so, the final expression for ΔP is

$$\Delta P = \frac{(K_{Lh} + fl/2D + 1) \quad T_3^{1/2}(1/n)(A_h/A_p)G_p}{2((1-R/2C_p)/R)^{1/2}} \tag{3.10}$$

The orifice exit pressure (P_e) can be evaluated from Equations 3.5 and 3.9

$$P_e = ((1-R/2C_p)R)^{1/2}(1-1/(2C_p/R-1))T_3^{1/2}(1/n)(A_p/A_h)G_p \quad (3.11)$$

Then the pressure just upstream of the accretion (P_3) would be

$$P_3 = P_e+\Delta P = (C_1+C_2)T_3^{1/2}(1/n)(A_p/A_h)G_p \quad (3.12)$$

where $C_1 = ((1-R/2C_p)R)^{1/2}(1-(2C_p/R-1)^{-1})$

and $C_2 = (K_{Lh}+fl/2D+1)/2((1-R/2C_p)(1/R))^{1/2}$

are constants for a given geometry and gas. Assuming constant temperature T_3, Equation 3.12 implies that the up stream pressure (P_3) drops hyperbolically on increasing (nA_h/A_p) for a constant value of G_p. Trials conducted at a constant P_3 for air on basically the same apparatus as in Figure 3.4 have shown that Equation 3.12 is obeyed up to an accretion openness (nA_h/A_p) of Ø.7 for artificial accretions with holes 1.57 mm and 3.Ø6 mm in diameter. The results are shown in figs 3.6. It should be noted that data for both sizes of hole lie on the same line: the mass flux would be expected to be slightly larger for the case of 3.Ø6 mm orifices since the entry loss coefficient would be less for a contraction from 6.35 to 3.Ø6 mm than from 6.35 to 1.57 mm. The gas flow conditions, however, are more complex than a simple contraction. Inherent in artificial accretion design (Figure 3.4) was a sharp bend as well as a contraction, resulting in an additional pressure loss.

Langhaar[38] calculated the increased friction losses occurring in pipe entrance lengths before a fully developed flow regime is established.

The slope of the line in Figure 3.6 enables evaluation of an 'overall loss coefficient'

$$OLC = K_{Lh} + fl/2D \qquad (3.13)$$

which contains contributions from both entry and friction losses. Applying Equation 3.12 with T_3 = 286 K (chosen arbitrarily), OLC = Ø.86 for the straight portion of the curve. Assuming 1/D is small in the orifices, then K_{Lh} = Ø.86, which is in rough agreement with the value of 1.1 quoted for mitre bends[35].

As an additional check for the case of an incompressible fluid, water was passed through the tuyere and accretions instead of gas. Results for a constant upstream pressure (P_3) showed similar behaviour to gas flow (Figure 3.6). When water is the fluid, Equation 3.12 simplifies to

$$P_3 = P_e + (OLC+1)(1/2)(1/n^2)(A_p/A_h)^2(G_p^2/\rho_w) \qquad (3.14)$$

ρ_w is constant. For constant P_3 a mass flux density - openness plot should be linear. This was confirmed up to an accretion openness of Ø.7. The overall loss coefficient was estimated to be Ø.6. Using the overall loss coefficient for gas injection (OLC = Ø.86) a plot of upstream pressure (P_3)

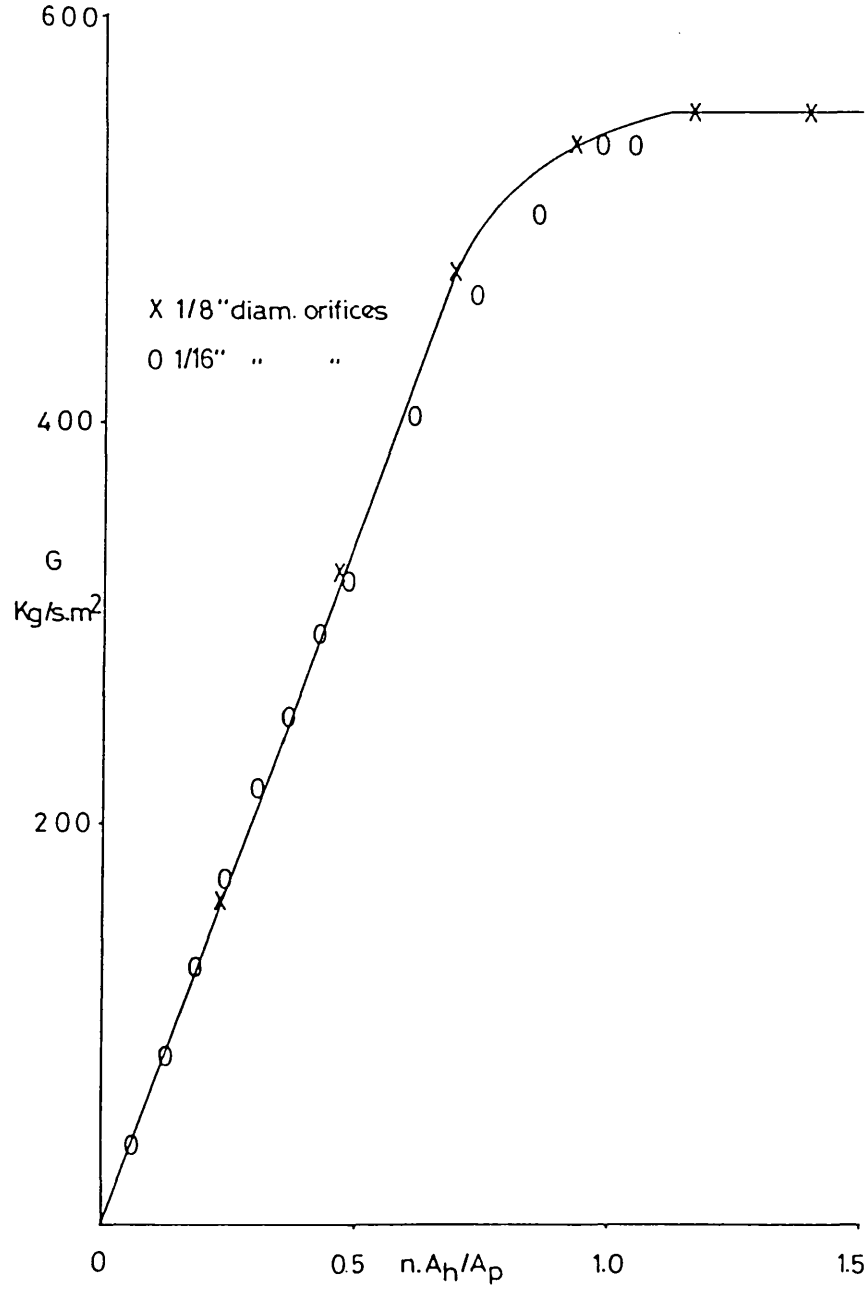

Fig.3.6 Mass flux density as a function of accretion 'openness' for a constant supply pressure of air.

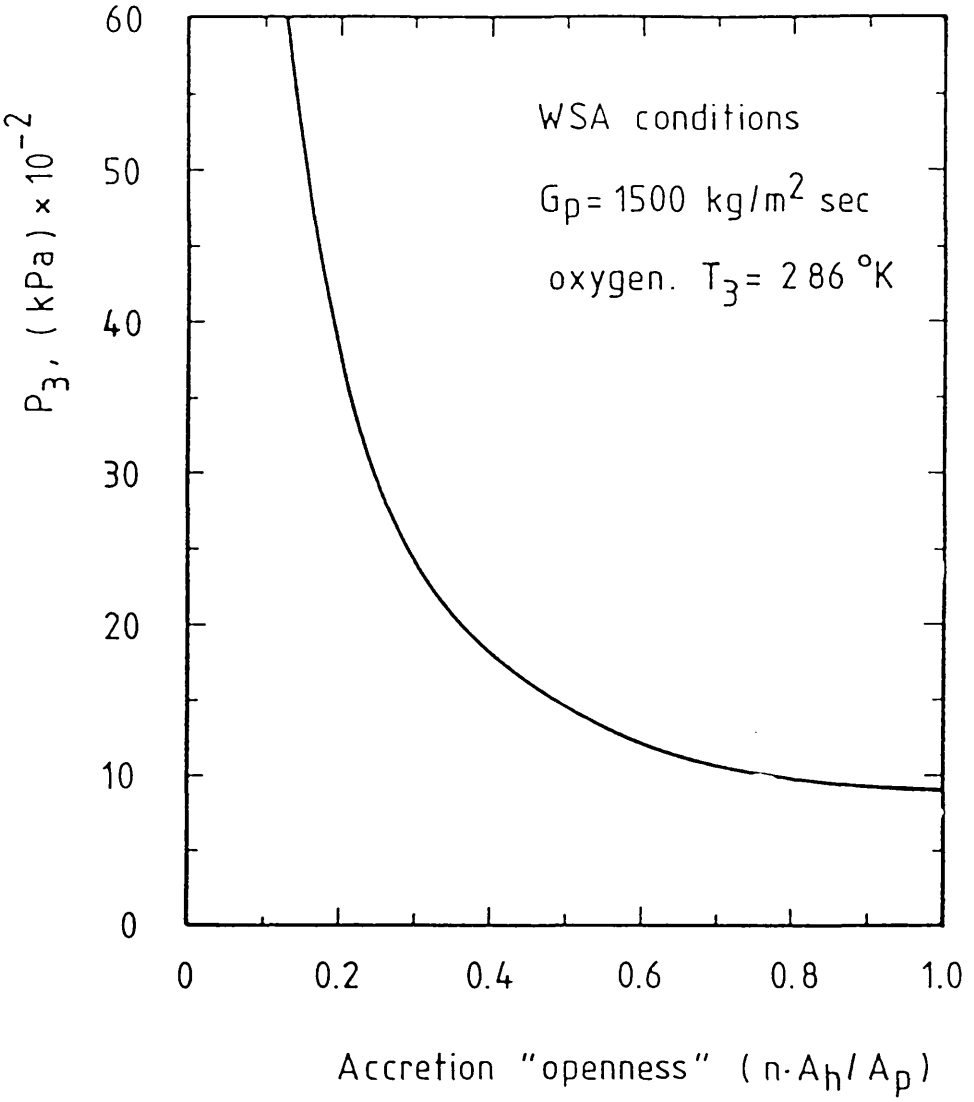

Fig.3.7 upstream pressure as a function of accretion 'openness' for constant mass flux density.

versus accretion openness can be drawn for conditions of constant mass flux density (G_p). Figure 3.7 depicts the conditions employed at WSA for an accretion of variable openness. The plot implies that if the openness value is greater than about Ø.6 then the supply pressure would not change much if the accretion were to grow and/or become more porous. This may explain why the core pressure was observed to be so steady for most of the conditions in the plant trials despite the observation of accretions between blows.

3.3.3 Narrow annular gap tuyere

A tuyere with a smaller annular gap was manufactured by hard drawing down a 3/8" OD copper tube and inserting this into the existing stainless steel shroud tube (the dimensions are given in Figure 3.2). The shroud to core area ratio (SCAR) was reduced from Ø.68 to Ø.42. This tuyere was installed in a new vessel and successful operation was monitored in some high alloy melts (25% Cr). It was possible to reduce the shroud gas velocity from 4ØØ m/s in the normal tuyere to 35Ø m/s with no apparent detriment to the cooling. The total argon flowrate was Ø.Ø234 m^3/s, with 45% going through the shroud. This represented a reduction of 5Ø% in argon consumption. A blowing ratio of 3:1 for O_2:Ar was possible in the first step due to reduced argon requirements.

Subsequently to the experimental investigations, the new tuyere was reported to have failed during a mild steel melt. It was established, however, that the overall O_2:Ar ratio

was 3:1 with no argon through the core, making conditions at the tuyere very severe. It would have been better to maintain the normal blowing ratio of 1.64:1 of O_2:Ar. Experience then may have allowed some reduction in the core argon.

The final point to mention concerns the behaviour of mild steels compared to the high alloy steels. Although the heat of reaction of Cr_2O_3 is greater than for FeO (761 KJ/mole O_2 compared to 496 KJ/mole O_2 respectively at 1550°C[39]) the iron oxide produced in the tuyere region will not tend to block further reaction as much as would the solid refractory chrome oxide. Thus rapid exothermic reaction of mild steel close to the tuyere occurs. Only approximately a 30% increase in the rate of oxide formation is needed to compensate for the less exothermic nature of iron oxidation compared to chromium oxidation. Hence, unless sufficient cooling is obtained at the tuyere in mild steel melts accretions may melt off and the tuyere could fail. This latter point is discussed in Section 5.8.4.

3.3.4 Refractory wear

Refractory erosion, particularly in the tuyere region, is a very severe problem in AOD's. The WSA converter had to be relined about every 25 heats: the reason for the bad performance was believed by the staff to be due to the large number of mild steel melts carried out where the tuyere operates virtually unprotected by accretions.

The refractory wear pattern observed at the end of the vessel campaign is shown in Figure 3.8. Tuyere region wear is generally attributed to a combination of mechanical erosion due to liquid motion, chemical attack and softening and spalling due to high temperature and thermal shock. There is some evidence that the first mechanism is predominant and may control, to a certain extent, the other two mechanisms. Laboratory tests with the hydrogen/water system at the plant flowrates, detailed in Section 2.4.2, confirm that this could be the case. Photographs of bubbles in Figure 2.8B and a similar tracing in Figure 2.10 show that gas bubbles do not separate from the wall when they grow nor when they lift upwards. The gas bubbles spread across the nozzle plane, grow to some maximum size and then collapse rapidly, approximately ten times per second. In Figure 2.10 the arrows follow the gas/liquid interface movements during the collapsing stage. In the region just above the tuyere liquid velocities were calculated to be as high as 14 m/s and 35 m/s horizontally and vertically respectively.

The large shear forces set up (measured also by Ballal and Ghosh[30]) in combination with rapid thermal cycling by bubble growth and the close proximity of elevated temperatures at the gas/liquid interface therefore lead to severe wear problems at the refractory wall. The tests reported in Figures 2.8B and 2.10 were carried out with a clean tuyere. In practice the presence of an accretion will alter the flow pattern, and in some cases make conditions

Fig. 3.8. 8 tonne AOD converter showing tuyere and slag line erosion after a campaign.

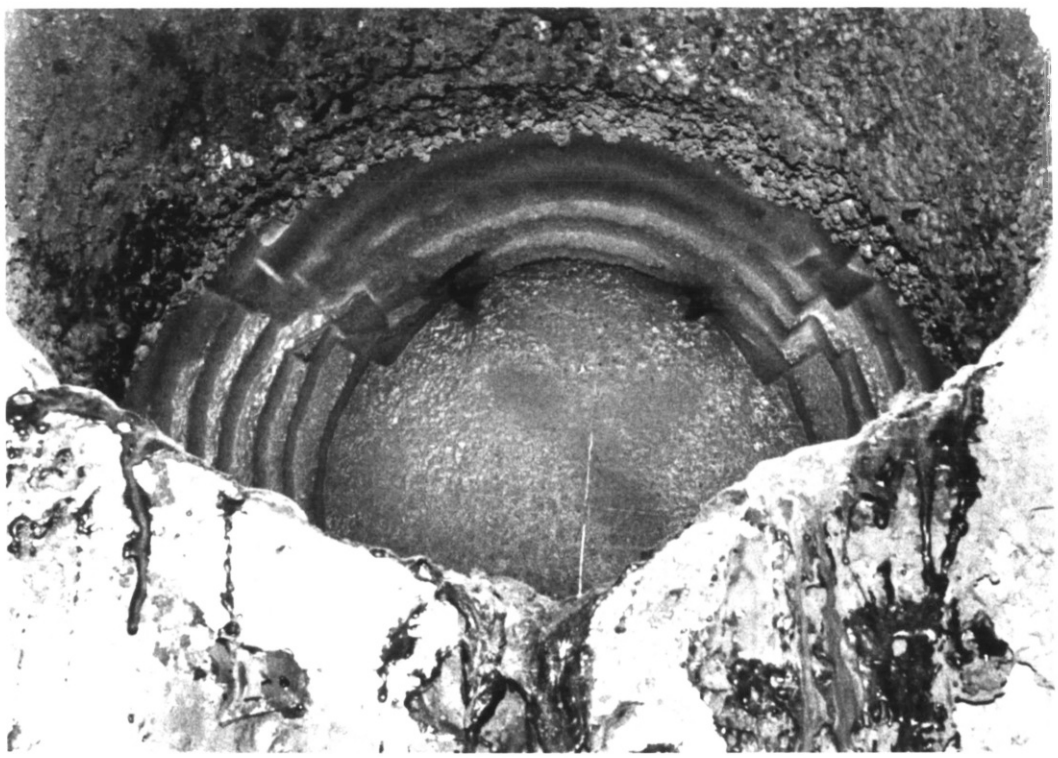

Fig. 3.9 Newly lined AOD converter showing accretion in both tuyeres.

worse by blowing gas back against the wall.

Figure 3.9 shows a unique stage in the converter life. The newly-lined vessel had only been used for a short argon stir and then emptied. Two pipe-like accretions have formed. The dark regions on the converter base directly downstream from the accretion exits result from cooling by the air purge.

3.4 DISCUSSION

On the AOD vessel at WSA it was not possible to tell whether bubbles were forming at the tuyere by monitoring the tuyere pressure/flow characteristics. The steady pressure traces observed were due to choked flow conditions at the tuyere tip and therefore pressure pulse information was unable to propagate back to the transducer. The pressure pulse technique cannot be applied to converters that operate under choked flow conditions . It is more suitable, however, for low blowing rate processes and has been used to monitor bubbling frequency in the copper and the nickel converters[18] and bottom-stirred LD's[34]. Despite these limitations, it is quite possible that bubbles still may form close to the tuyere, as detailed in Section 2.3.

Measuring the vibrations of the converter certainly indicated that bubbles may have been growing at the recognized frequency of 10 Hz. Further investigation of this technique may prove it to be applicable in understanding gas behaviour in opaque liquid systems.

Laboratory investigations of the pressure/flow characteristics of artificial accretions attached to tuyeres have shown that the major resistance to flow is presented by the accretion. Results indicate that if the accretion openness (nA_h/A_p) is greater than Ø.6 then the supply pressure will remain approximately constant despite changes in accretion geometry.

Installation of a tuyere with a narrower shroud gap enabled a 5Ø% reduction in argon consumption to be made in processing high alloy melts with no apparent detriment to the tuyere cooling. A blowing ratio of 3:1 for $Ø_2$:Ar was possible in the first stage of melt processing. Subsequent failure of the tuyere in a mild steel melt was a consequence of injecting 1ØØ% oxygen through the core with insufficient argon cooling/diluent flow. The tuyere should have been operated under less severe conditions. Furthermore, in mild steel melts any iron oxide that is produced will not tend to block further reaction as would the more refractory solid chromium oxide.

Predictions of the gas behaviour at real tuyeres from model studies should include an allowance for the presence of accretions which can markedly alter the gas flow patterns. This has been demonstrated by Leach et al.[4] in air/water models.

Mechanical erosion/corrosion plays a significant role in refractory wear in the area surrounding the accretion and in

the wall above the tuyere that may be in contact with the gas envelope. The refractory in these areas is likely to have been weakened by temperature cycling and may spall. Short term temperature cycling during bubble growth and exothermic heat generation (see Section 5.8.4) lead to rapid fluctuations in the thermal gradient at the refractory surface. Over a longer time scale the refractory surrounding the tuyere undergoes severe thermal cycling between converter blowing and idling times.

3.5 CONCLUSIONS

The pressure/flow characteristics of a gas injection tuyere were investigated in plant and laboratory trials. The following conclusions were drawn:-

1) The pressures of both shroud and core lines remained very steady throughout a particular stage during the blowing process. This implies that the resistance presented to the flow is constant. Laboratory tests show this to be the case if the accretion is fairly open (nA_h/A_p is greater than Ø.6).

2) The pressure pulse technique for flow characterization is not good for tuyeres operating under choked conditions. Thus it was not possible to make any definite statements concerning the behaviour of the gas jet.

3) It is possible to obtain adequate tuyere cooling using less shroud gas if the annular gap is decreased to maintain similar gas velocities. In the case of mild steel melts the oxygen gas should be diluted to ensure protection of the tuyere against very high temperatures in the reaction zone ahead of the tuyere.

4) Erosion patterns in the refractory around the tuyeres can be attributed to bubble motion causing large local shear stresses and rapidly fluctuating thermal gradients. Aqueous models are able to show this bubble behaviour in the vicinity of the tuyere.

3.6 FURTHER WORK

1) The pressure pulse technique was shown not to be good for classifying jet break-up behaviour when the gas injection conditions were choked. An alternative technique may be to measure the vibrations of the nozzle resulting from the forces due to rapid gas expansion during bubble growth into the liquid. Laboratory investigations could be carried out in aqueous systems by attaching an accelerometer directly behind the injection orifice. Measuring the high frequency vibrations and simultaneously filming the jet break-up may enable the behaviour of gas/metal systems to be predicted by attaching accelerometers to real converters.

2) Consumption of the shroud gas has been reduced using a tuyere with a narrower annular gap while maintaining sufficient gas velocities in the annular gap for adequate cooling protection. The use of smaller annular gaps are limited by the large driving pressures required and larger gaps by excessive gas flow for cooling. A laboratory study comparing the pressure/flow characteristics, cooling capabilities and the tube materials of tuyeres with different annular gap and core diameter configurations could be carried out in a manner similar to that described in Chapter 4. Individual experimental tuyeres could be cast into an induction furnace refractory lining and blown under reactive (lead or iron melts with an oxidizing gas) or inert (molten silver or inert gas) conditions. Examination of refractory wear and tuyere sectioning (as demonstrated in Section 4.3.3) will yield important information relating to the optimum compromise between gas savings and cooling effects. Formation, growth and structures of accretions could also be examined after the molten metal has been removed from the furnace.

CHAPTER 4

CUPELLATION OF SILVER-LEAD BULLION BY SUBMERGED GAS INJECTION OF OXYGEN THROUGH A NITROGEN SHROUDED TUYERE

CHAPTER 4

CUPELLATION OF SILVER-LEAD BULLION BY SUBMERGED INJECTION OF OXYGEN THROUGH A NITROGEN SHROUDED TUYERE

4.1 INTRODUCTION

Silver, and other noble metals, may be recovered from a wide range of residues by collecting silver in lead and subsequently oxidising the lead to leave a bullion high in silver content. At Britannia Refined Metals Limited (BRM) a proposed new process requires silver to be recovered from lead by treating bullion with zinc to produce Ag-Zn crusts. The zinc is to be volatilised from the crusts in a vacuum retort, leaving a silver alloy containing 26 wt. pct. lead and some copper. Cupellation of the melt is then to be carried out by the traditional method, where air is blown onto the surface of the alloy in a brick-lined, rectangular cupellation furnace fitted with burners. The lead oxidizes to litharge, which is also able to dissolve the copper oxides, and this slag is skimmed off periodically until the precious metal is about 98% pure.

This process has several drawbacks. Energy utilization is poor because of the relatively open construction and there is poor recovery of the heat of reaction from oxidation. The process time is long due to a relatively small interfacial area for the reaction to occur over, taking about 30 hours to cupel 8 tonnes of melt. This batch process is carried out at temperatures between 1000 - 1050 ^{0}C. The volume of waste

gas produced is large because of the high nitrogen content and material throughput is poor, with a large quantity of the precious metal retained in the process.

Two important methods utilizing submerged gas injection have been investigated to speed up the cupellation time of the alloy from the proposed vacuum retort. Firstly[42], a top blown rotary converter (TBRC) using a 1 tonne charge of 70% silver, 2% zinc and 2.5% copper has been used to oxidise the melt, but with limited success due to serious refractory erosion problems. The TBRC has also been employed[43], apparently with great success, at Degussa AG in West Germany. 6 tonnes of silver bullion containing 50% lead and 20% copper have been refined within a period of 2-3 hours with a reported refractory (magnesite bricks) life of 6000 working hours and oxygen utilization of 50%. A second and possibly more promising approach has been made by Tait et al[6], inspired by the success of bottom-blown steelmaking. They injected oxygen into the bottom of a deep-bath containing 40% lead, 30% silver and 10% copper through an annular tuyere using nitrogen as the protective shroud gas. 100kg of bullion was oxidised in 2.5 hours to give 90% silver and the refractory surrounding the tuyere seemed adequately protected by the shroud gas from high temperature and consequent erosion. About 60% of the oxygen was taken up by oxidation.

4.1.1 Present approach

The present work is an extension of that carried out by

Tait[6] and is aimed at investigating the following factors:-

a) Control of process temperature.

b) Copper refining.

c) Refractory attack.

d) Tuyere design, operation, and control of accretions.

e) Entrainment of silver prills in the slag.

f) Efficiency of oxygen utilization.

The programme of test work was initiated by designing a theoretical full-scale industrial process and then scaling down by a linear size factor of 4 so that an existing high frequency induction furnace could be used for the experimental investigation.

4.1.2 Projected full-scale converter

Gas flowrate

The proposed full-scale process has been designed to produce 1 tonne of silver at least every 12 hours. A cupellation time of 3 hours has been chosen a as a compromise:- faster cupellation would lead to splash and loss of silver prills in the slag because of the high blowing rates while slower cupellation would result in more total heat losses and greater refractory attack.

To oxidise the 370 kg of lead present with each tonne of silver would require 20 Nm^3 of oxygen. Assuming 60% utilization(6) 33 Nm^3 is required. Over a three hour period

this gives a flowrate of about 3 litres/sec. A 1/8 inch (3.17 mm) I.D. tuyere core containing oxygen (and possibly nitrogen) would be employed, along with a nitrogen or methane shroud gas. Such a tuyere would operate with a nominal velocity in the core of about 390 m/s. A pressure drop of about 9 atm (130 psig) would be necessary to "drive" this tuyere and the exact flowrate would depend on this constant pressure. The nominal velocity of the core gas is defined as the flowrate at STP divided by the cross sectional area of the core. The shrouding gas should also be supplied at up to 9 atm (130 psig) to enable determination of sufficient cooling conditions.

Furnace size

The projected furnace dimensions are shown in Figure 4.1. The tuyere would be placed in the base at a mid-radius position at the "back", giving good separation of the flow from the wall. A tilt angle of about 70^{o} would be required to remove the tuyere from the bath. This is the angle through which the converter must be tilted. Because of the tuyere position at the "back" there would be a relatively quiescent area over the surface not directly above the tuyere. Hopefully prills would settle out here. A wider shallower bath could be used, but this would increase heat losses and probably increase splashing.

Heat losses

Assuming the furnace operates at $1000^{o}C$, with 23 cm dense

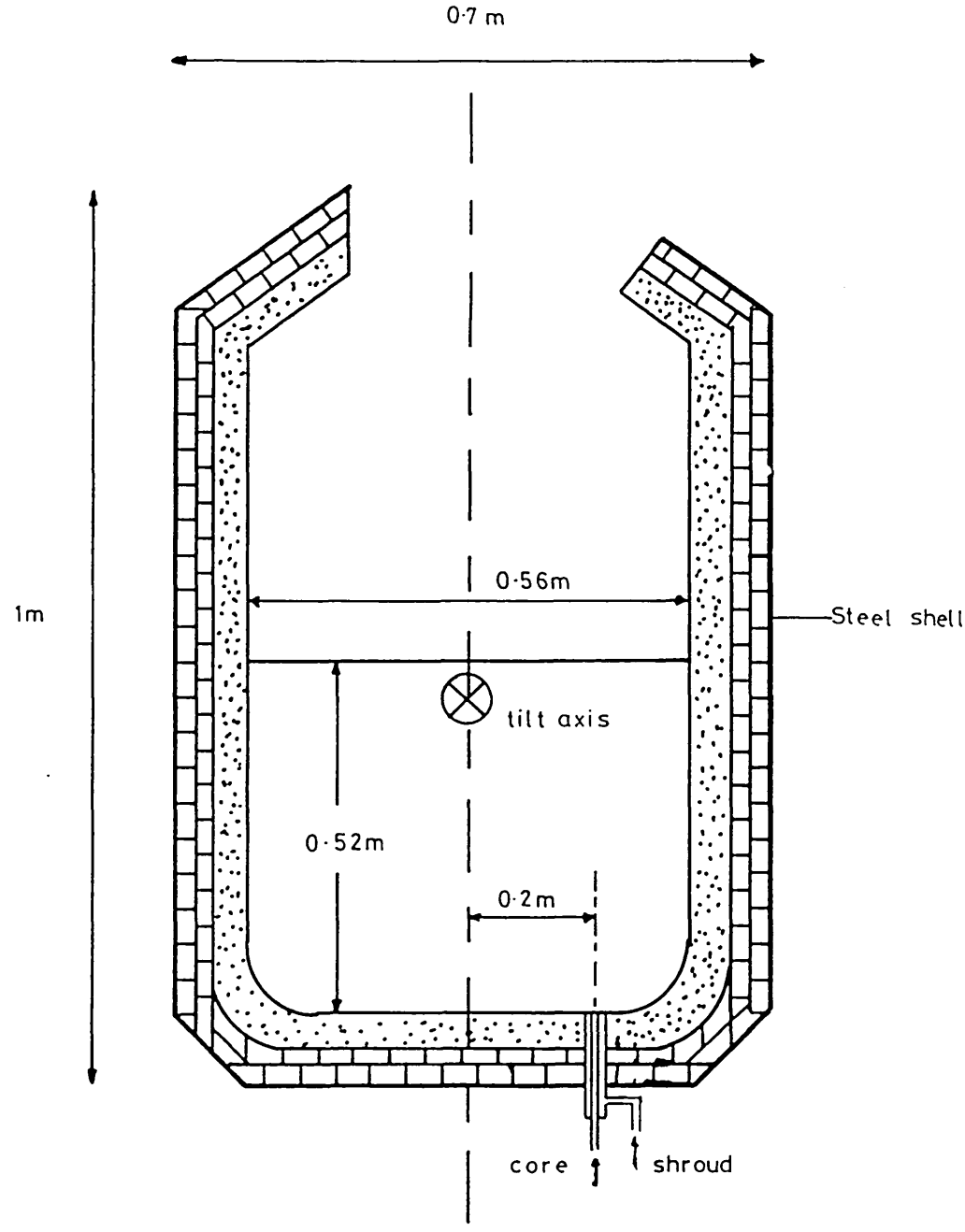

Fig.4.1 Schematic of proposed process converter.

chrome brick of conductivity 2 W/mK, and that the radiation heat loss rate from the top surface is about half the maximum possible, the estimated heat loss rate will be:-

Conduction	8 kW
Radiation	18 kW
Heating shroud gas	1 kW
Heating oxygen gas	4 kW
	31 kW

The total heat evolved as a result of the exothermic lead oxidation is 330 MJ[39]. Over the three hour period (assuming a steady rate of lead oxidation, determined by the oxygen injection rate) this gives a rate of heat release of about 30 kW. This roughly balances the heat loss rate.

Hence the process can be expected to be almost autogenous, but some heat input would be necessary to compensate for the lack of heat generation during the copper refining period when a slag flux might have to be added and the lead oxidation would be almost finished. Such possible heat inputs could be obtained by injecting fuel oils or methane through the tuyere or by utilizing a gas burner. It might be advantageous to hold the furnace with minimal or zero gas injection in the final stages to help prills to settle.

Final copper removal

This may be achieved by skimming off the main PbO slag, with the furnace tilted, after the major part of the copper has been removed, and then adding anhydrous borax as a flux for

copper oxide.

4.1.3 Proposed model converter

The high frequency induction furnace coil allows a crucible size of I.D. 15 cm. This suggests a scale factor of 4 to 1. The modelling criterion for the gas flow is that we should have the same flowrate per unit area of bath surface. This gives a gas flow of Ø.2 N litres/sec. For a charge of mass 2Ø kg this will mean a refining time of about 4Ø minutes.

To obtain good modelling of conditions at the tuyere tip both with respect to gas dispersion and accretion formation, the nozzle core should be 1.8 mm I.D. (see Section 2.4.2).

4.2 EXPERIMENTAL

4.2.1 Apparatus

The experimental apparatus is shown in Figure 4.2, and can be divided into 4 parts:-

1) The tuyere

The tuyere assembly is shown in Figure 4.3. It is generally believed that for successful and economic tuyere operation a shroud to core area ratio (SCAR) of about Ø.4 is desirable[31]. This figure is not always obtainable due to commercial availability of copper and stainless steel tubes

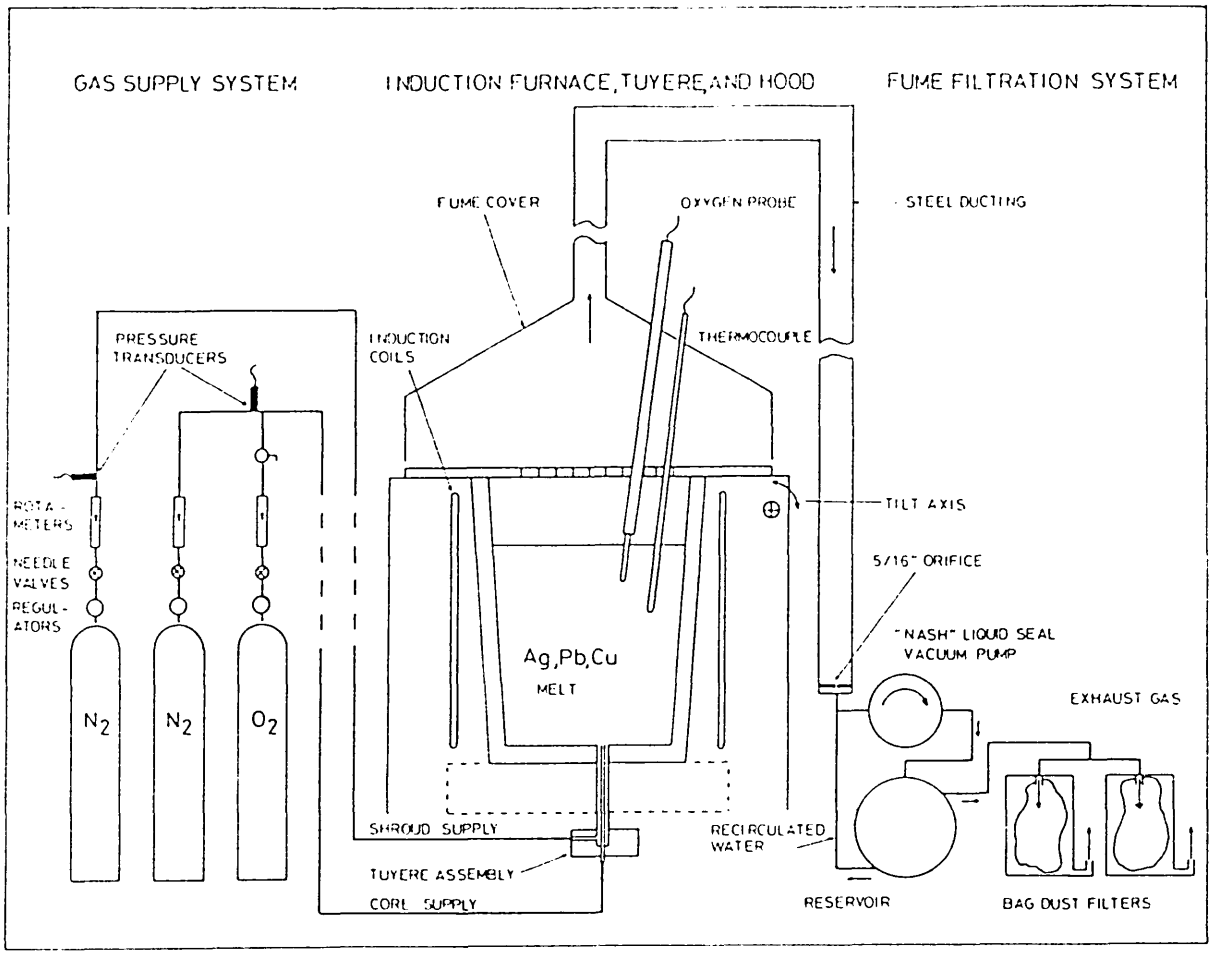

Fig.4.2 Experimental apparatus.

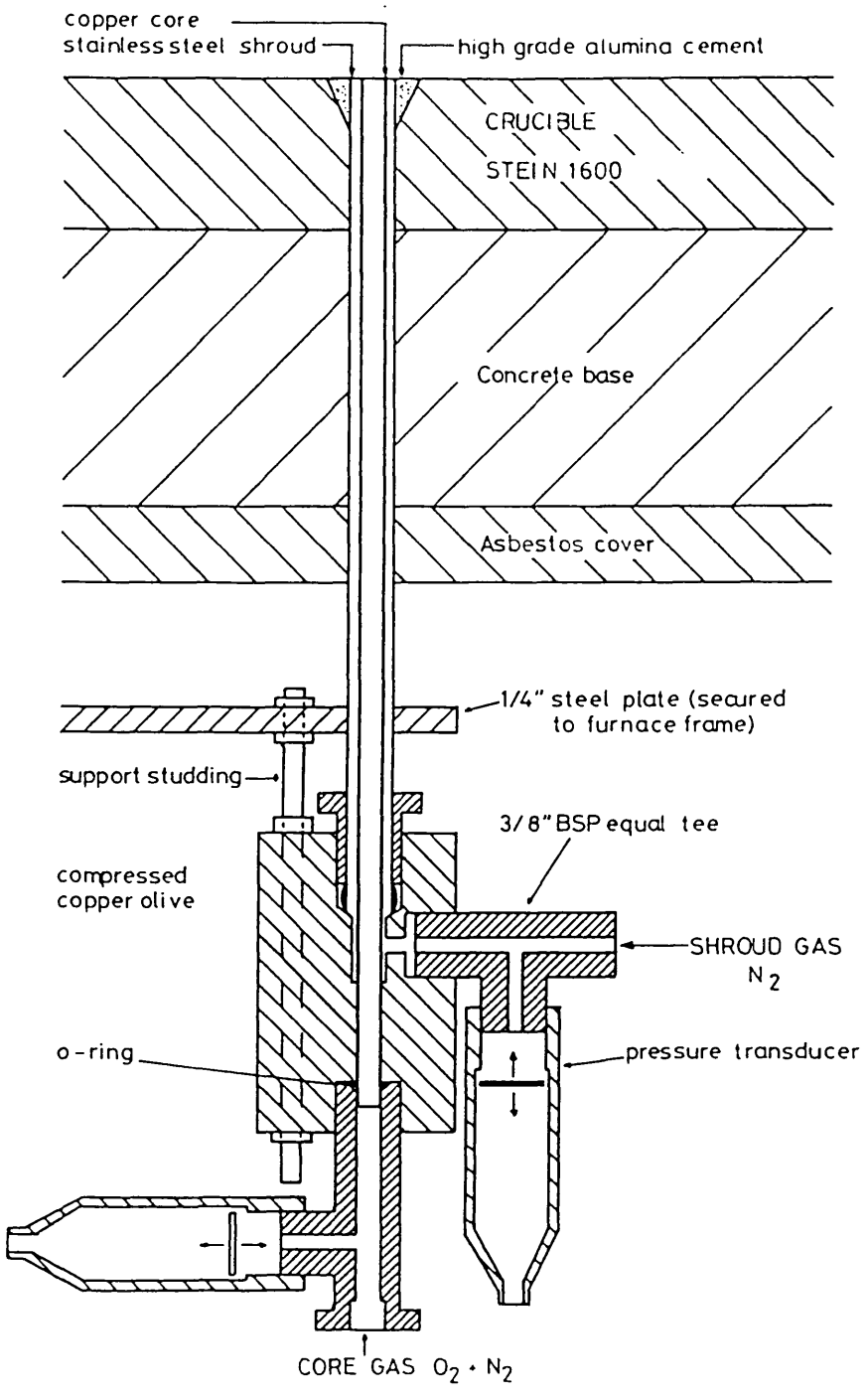

Fig.4.3 Tuyere assembly and position relative to the crucible.

at standard sizes, but it ensures that annular gas flowrates may be kept to a minimum without the requirement for high pressure gas supplies (this is of particular importance when using large amounts of expensive argon).

The tuyere consisted of a core of hard drawn copper tube through which the oxygen/nitrogen mixture was blown. The core fitted into the larger diameter tube of 2Ø S.W.G. stainless steel (Ø.91 mm, type 321) and was held concentrically by indentations punched in the shroud tube. Nitrogen was blown through the annular gap at about 4 Nl/min.

The tuyere was fitted vertically upwards through the bottom of the crucible, about 2.5 cm from the side-wall. The tuyere design was similar to that used in the steel-refining industry. The shroud flow provided an effective coolant for the refractory material in the hot zone surrounding the tuyere exit. The cooling, in addition, contolled the accretion size.

2) Gas supply system

Initially the gas flowrate was controlled under a constant supply pressure. The flowrate was measured using a rotameter to monitor the flowrate at a given pressure which was measured with a Bell and Howell pressure transducer linked to a chart recorder. The nitrogen shroud supply cylinder

pressure was set to 2 bar gauge and the flowrate set to 4 Nlitres/min with a Martonair fine control needle-valve.

The core gas supply consisted of a mixture of nitrogen and oxygen. The nitrogen supply pressure was set as before to 2 bar gauge and to a flowrate of 1 Nlitre/min. The oxygen supply pressure was 4 bar gauge and the flowrate preset to 7 Nlitres/min and then shut off with a ball-valve. The gases were connected to the tuyere by Martonair high pressure tubing.

At a later stage investigations were carried out under conditions of constant flow where an orifice of Ø.ØØ6" (Ø.13mm) was installed in the oxygen line upstream of the tuyere. Figure 4.5 shows the experimental set up for flow calibration and for the experimental trial. Figure 4.6 shows how the flowrate varies with regulated supply pressure. The required oxygen flowrate (4-5 Nl/min) was obtained by running with a regulated supply pressure of 25 bar.

This flowrate was unaffected by variation in pressure at the tuyere in the range 2 to 12 bar since the orifice plate was always choked.

3) The Furnace

The high frequency induction furnace allowed a crucible size of 28 cm high and 15 cm in diameter. Two crucible linings were used: the first was of a low grade alumina type, and the second was cast in situ using Stein 16ØØ castable

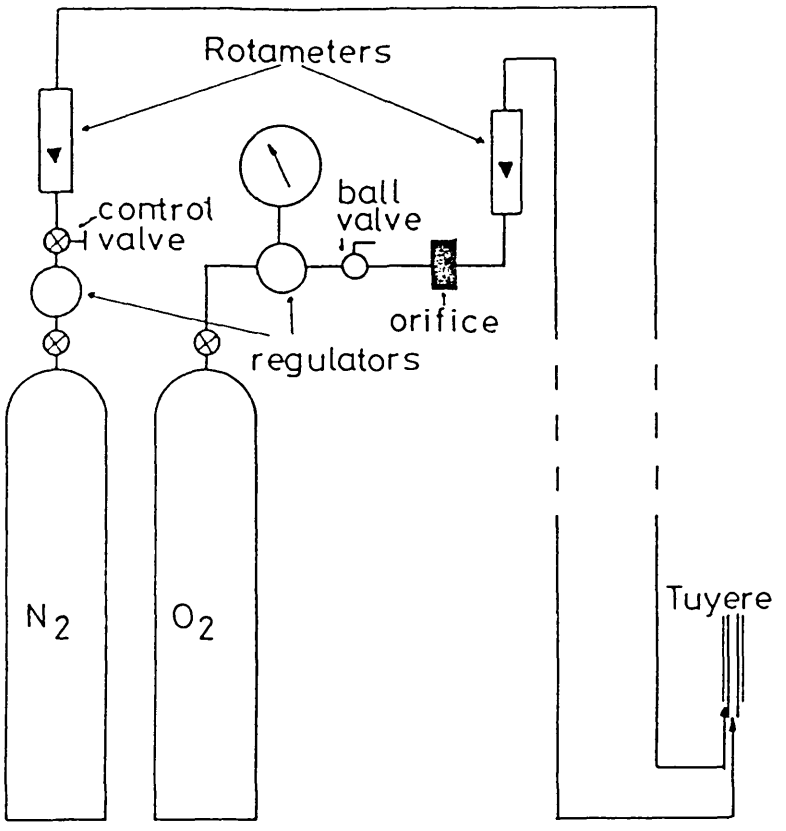

Fig.4.4 Gas supply system for constant flow runs.

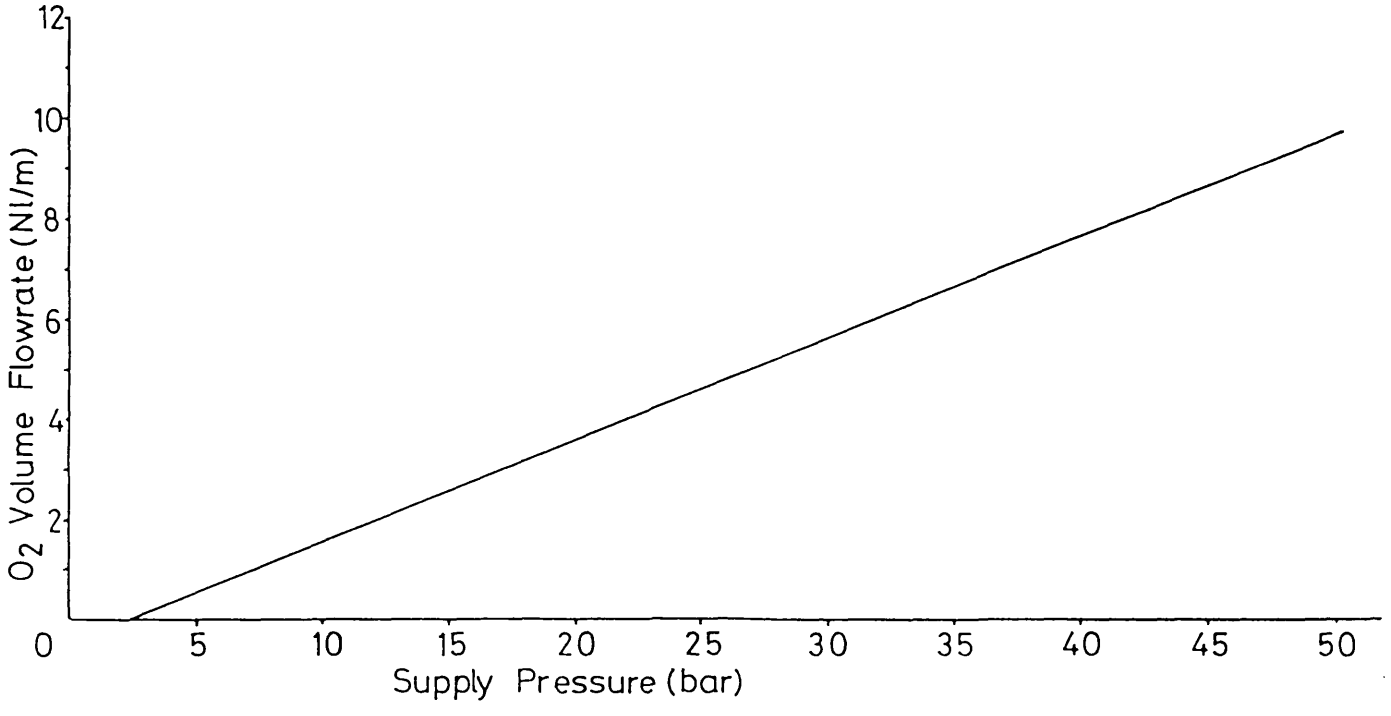

Fig.4.5 Constant flowrate orifice calibration with core tube in position.

refractory. The power input to the coils could be controlled and 15kg of silver could be melted down in one hour. The furnace was tiltable forwards but not to the extent that the tuyere could be raised above the melt surface without pouring out some of the melt. A perforated mild steel plate was placed over the crucible to reduce the heat radiated to the fume extraction hood. A chromel-alumel thermocouple in a stainless steel protective sheath was passed through the perforations. Similarly the silica glass tubes used for metal sampling were also passed through the perforations.

4) Fume control

A hood was made of stainless steel sheet to closely cover the crucible and the mild steel plate. Three holes were made in the hood: a silica glass window was used to observe the melt, and the other holes could be used for the thermocouple and metal sampling or closed when not in use. The hood was attached to 10 m of heat resistant flexible stainless steel ducting of 10.8 cm I.D. The other end of the ducting was attached to a "Nash"liquid seal vacuum pump. A 7.9 mm orifice was placed upstream of the pump in order to provide an adequate pressure drop for the pump to function in the manner of its design, pumping 11.8 scfm (330 Nlitres/minute) at 64 cm of mercury vacuum. The fume passed through the pump water, thus cooling the gas and any dust was caught in the water. The water was recirculated and the exhaust gas was taken through two vacuum cleaner bags connected in parallel to catch any fine dust that may have passed through the pump. Finally, the remaining gas was then removed from the

laboratory by the overhead extraction system.

4.2.2 Procedure

Each run was operated by carrying out the following sequence of events. The nitrogen and oxygen flowrates were set; oxygen was then turned off. 15 kg of solid silver was charged to the crucible and the induction power was switched on. When the silver was molten 5 kg of lead and Ø.5 kg of copper were added in small pieces. The radiation shield and hood were placed in position with the nitrogen still bubbling through the melt. When a steady temperature of about 3ØØ^{o}C was obtained (induction heat input = heat losses) and sufficient time had elapsed for all of the lead and copper to dissolve, the metal was sampled by sucking it up into a silica glass tube. The oxygen was then allowed to pass through the melt to begin the refining and further samples were taken with time. In the later runs the frequency of sampling was increased towards the end of the refining period when copper removal took place. The temperature and flowrates were constantly monitored until about 4Ø minutes of oxygen injection time had passed. To give the tuyere maximum protection by keeping an accretion in position during oxidation it was necessary to attempt to keep the melt temperature a few degrees above the liquidus temperature. Rough estimation was possible using Figure 4.6.[44]

Table 4.1 summarises the experimental conditions used. When the oxygen was switched on to start refining in run C, the core and shroud blocked completely and the run had to be

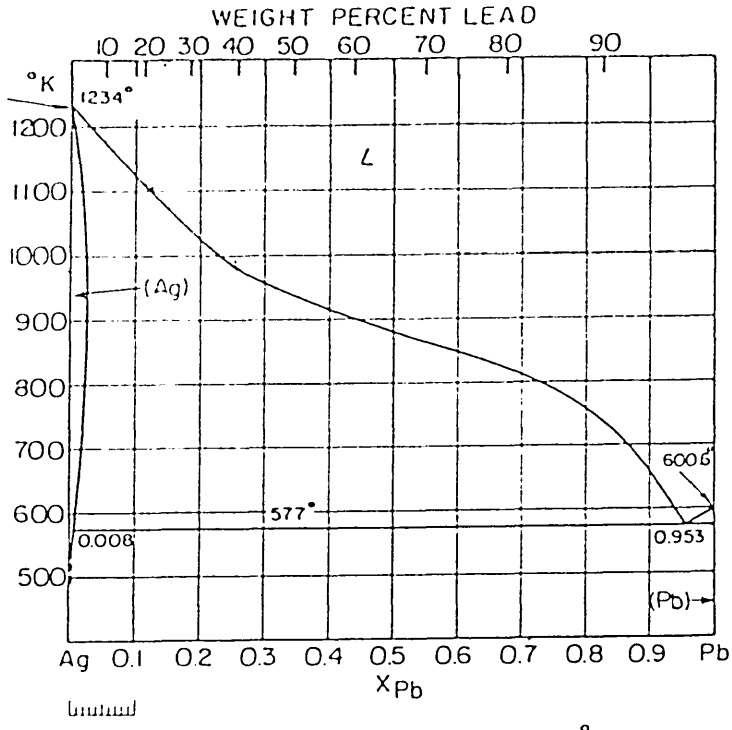

SILVER - LEAD SYSTEM, 1273°K

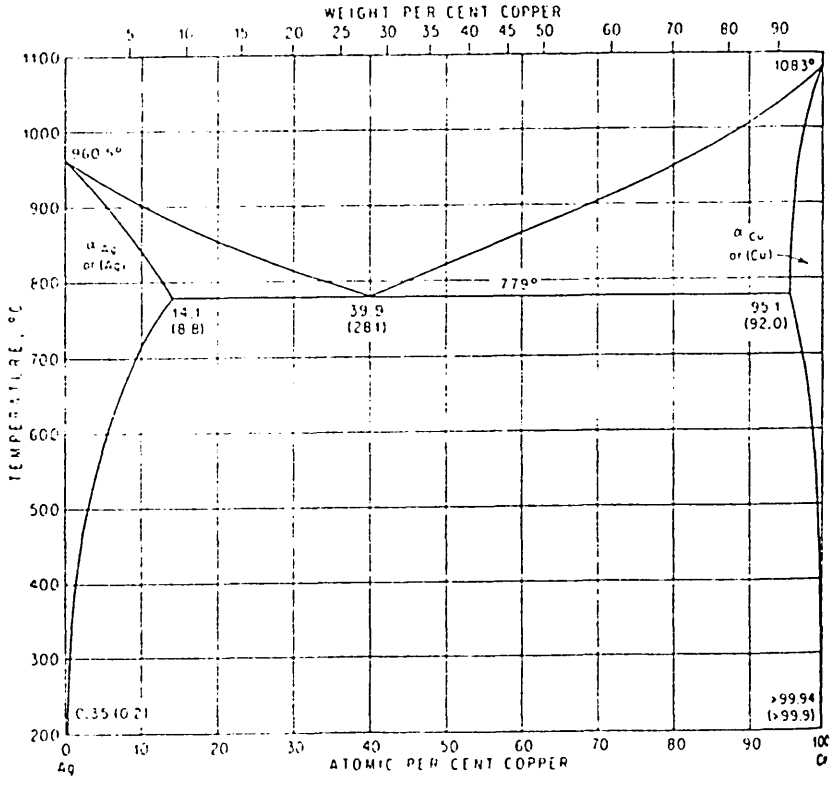

Fig.4.6 Silver-lead and silver-copper systems.

Table 4.1 Experimental conditions

Run	Conditions	Outcome
P	Core gas oxygen Constant pressure oxygen supply (4 bar) Constant pressure N_2 supply(2 bar) Pb-Ag melt only	Intermittent blocking of tuyere
A	Core gas oxygen Constant pressure O_2 supply(4 bar) Constant pressure N_2 supply(2 bar)	Successfully refined. Tuyere blocked at end of run.
B	Core gas oxygen Constant pressure O_2 supply(4 bar) Constant pressure N_2 supply (2 bar)	Success.
C	Core gas oxygen Constant flow O_2 supply (28 bar) Constant pressure N_2 supply (2 bar)	Tuyere blocked completely.
D	Core gas oxygen Constant flow O_2 supply (6 bar) Constant pressure N_2 supply (1.2 bar)	Success.
DD	Core gas oxygen : carried out in succession from run D Constant flow O_2 supply (10 bar) Constant pressure N_2 supply (1.2 bar)	Severe tuyere wear
E	Core gas 50% O_2, 50% N_2 Constant pressure core supply (2.5 bar) Constant pressure N_2 supply (1.2 bar)	Tuyere blocked Slow refining rate. Some tuyere wear.
F	Core gas oxygen Constant pressure O_2 supply Constant pressure N_2 supply (2 bar)	Accretion maintained, no wear.
H	Core gas oxygen Constant pressure O_2 supply (3.2 bar)	Accretion maintained, no wear.

abandoned as the tuyere could not be unblocked by raising the melt temperature.

Runs D and DD were carried out in sequence (using the same melt). The oxygen flow was initially set at 0.7 Nl/min. (6 bar regulator pressure) but the core began to block intermittently, so the flowrate was increased to 1.55 Nl/min. (10 bar regulator pressure) after 17 minutes of refining time. When sufficient time had elapsed for most of the lead to have been oxidized, an attempt was made to pour off the litharge slag whilst still injecting oxygen and nitrogen. Further charges of lead and copper were made and run DD was initiated. The same oxygen flowrate of 1.55 Nl/min. was maintained and the shroud pressure was again 1.2 bar.

Run E employed a core gas mixture of 50% oxygen and 50% nitrogen, this being a "weaker" refining gas. Constant pressure supplies were reinstated. At the initiation of O_2/N_2 refining at 2.53 bar regulator pressure the shroud and core flow blocked completely. The run was continued in order to investigate the extent of oxidation by atmospheric oxygen and induction stirring. Before and after the blockage occurred oxygen potential measurements were made in the melt using the oxygen probe (Appendix 3).

In runs F and H the conditions of the first runs (P, A and B) were repeated (constant pressure supplies of core oxygen and shroud nitrogen). For run F the oxygen supply pressure was set at 4 bar and the nitrogen to 2 bar. In run H the

shroud nitrogen supply pressure was set to 4.25 bar and the core oxygen to 3.2 bar. At the end of the refining time the litharge slag was poured off and further oxygen injection proceeded to investigate subsequent copper refining.

It was generally found that as a result of vigorous mixing conditions in the crucible, good separation of the slag and metal was not possible while the nitrogen necessary to maintain an open tuyere was passing through the melt. Attempts were made to pour off the slag first but these were not successful. In later runs the whole contents of the crucible were poured into a clay graphite pot and then smelted together in a gas-fired furnace to separate metal and slag.

The heating rate was measured when a steady temperature had been reached with a particular power input. The power was turned off and the resulting rate of decrease in temperature was a measure of the rate of previous heat input. The exothermic heat of oxidation was measured by noting the rate of temperature rise. The thermocouple, contained within the stainless steel sheath, could not be left in the melt due to the severe attack from the litharge. Generally four or five thermocouples were used in each run and operated by dipping them in the melt just long enough for the temperature to stabilize (about 30 seconds).

After each run the tuyeres were removed, sectioned and photographed to assess their performance in relation to the supply line pressure behaviour.

4.3 RESULTS AND THEIR INTERPRETATION

4.3.1 Impurity removal

The analyses for lead and copper in the silver are plotted in Figures 4.7 to 4.13 and tabulated along with oxygen flowrates in Table 4.2 for runs P to H respectively. The analyses were carried out at BRM by atomic absorption and some values were checked by titration at BRM. No attempt was made to weigh the slag as it was cast together with the silver and it contained eroded refractory material.

No foaming was observed at the end of the blow. Our results were different from Tait[6] in this respect, presumably because of the lower quantity of PbO slag formed.

The gaps in Table 4.2 for temperature measurements are due to persistent thermocouple failure.

Heat balance

Towards the end of each run, as the lead content decreased, so the heat generation rate decreased and the melting point rises following the liquidus in Figure 4.6. With no extra heat input some metal solidified around the top of the crucible giving rise to increased solute (Pb) concentration in the bath. This would account for some slightly high lead values at the end of each run.

To maintain the Ag-Pb-Cu melt at a constant temperature of

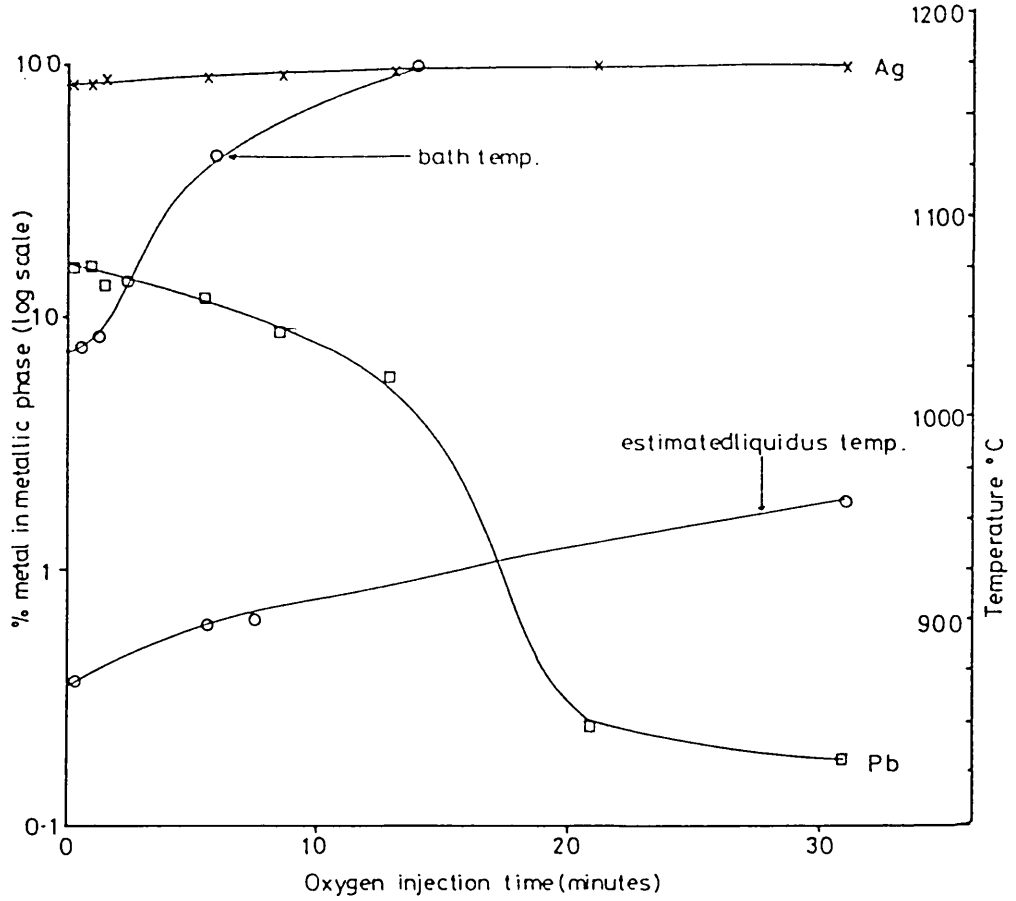

Fig.4.7 Melt content and temperature change - run P.

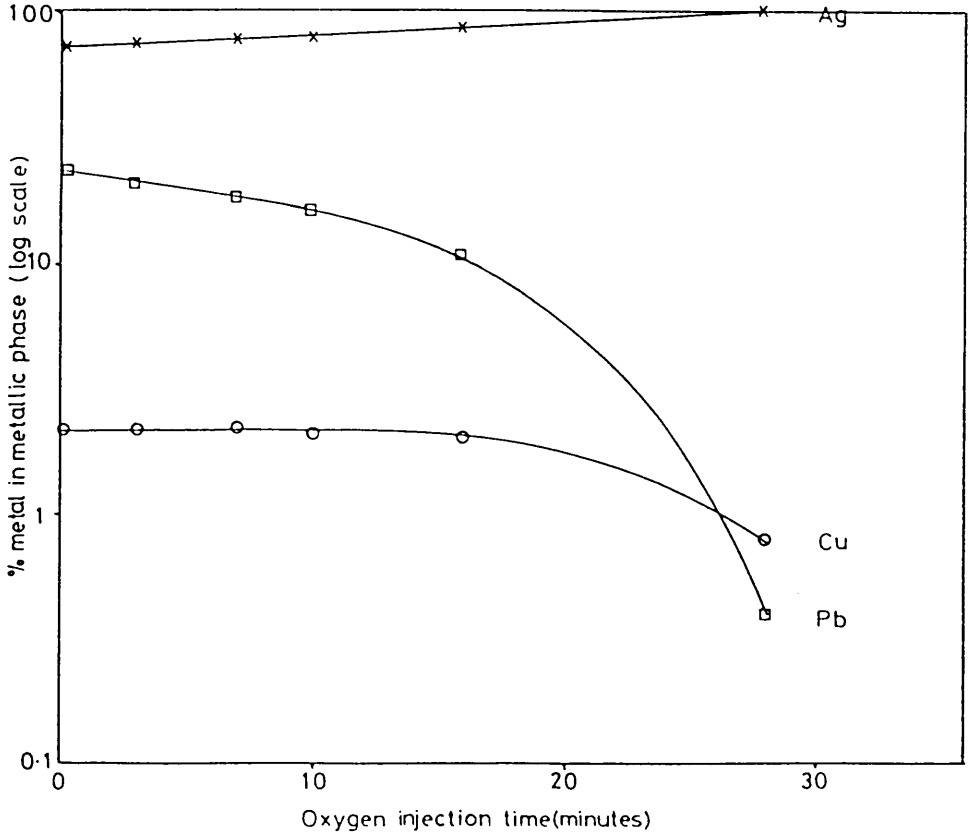

Fig.4.8 Melt content change - run A.

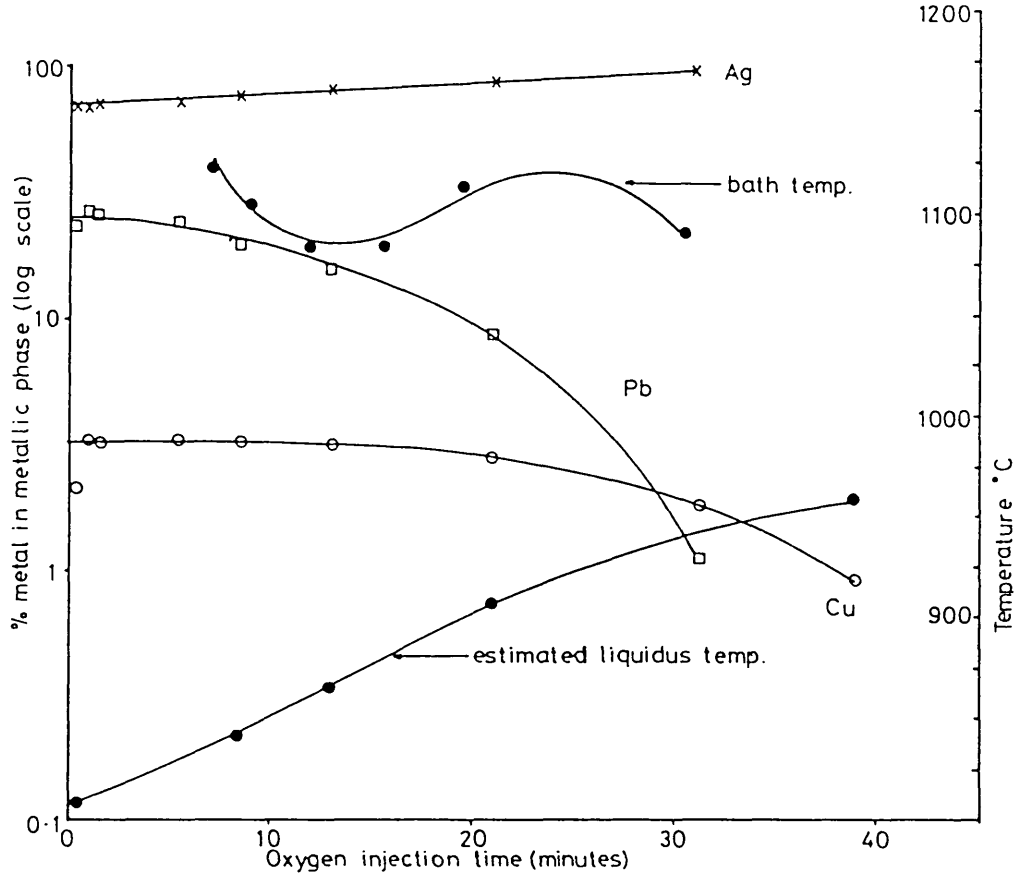

Fig.4.9 Melt content and temperature change - run B.

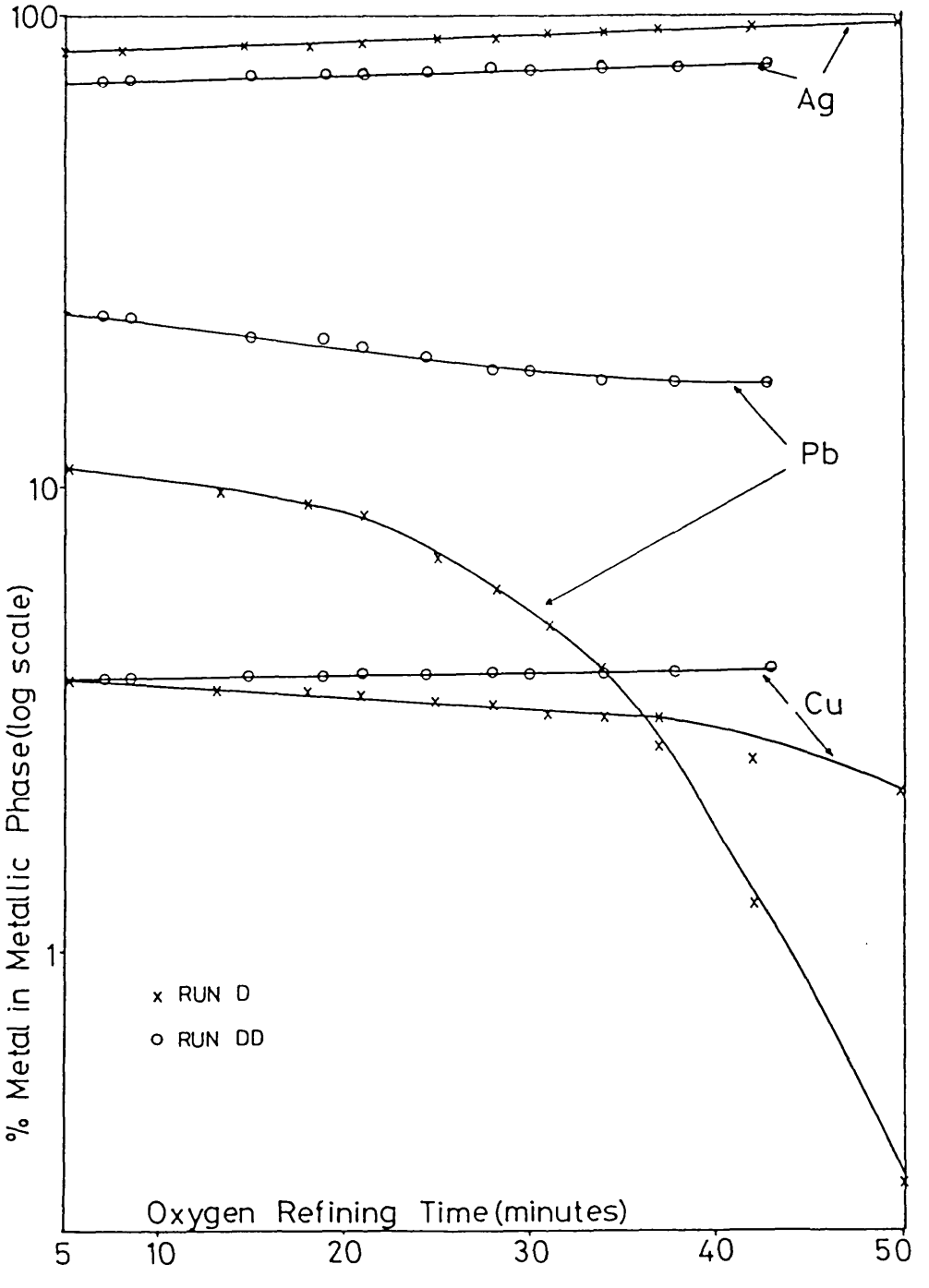

Fig.4.10 Melt content change - runs D, DD.

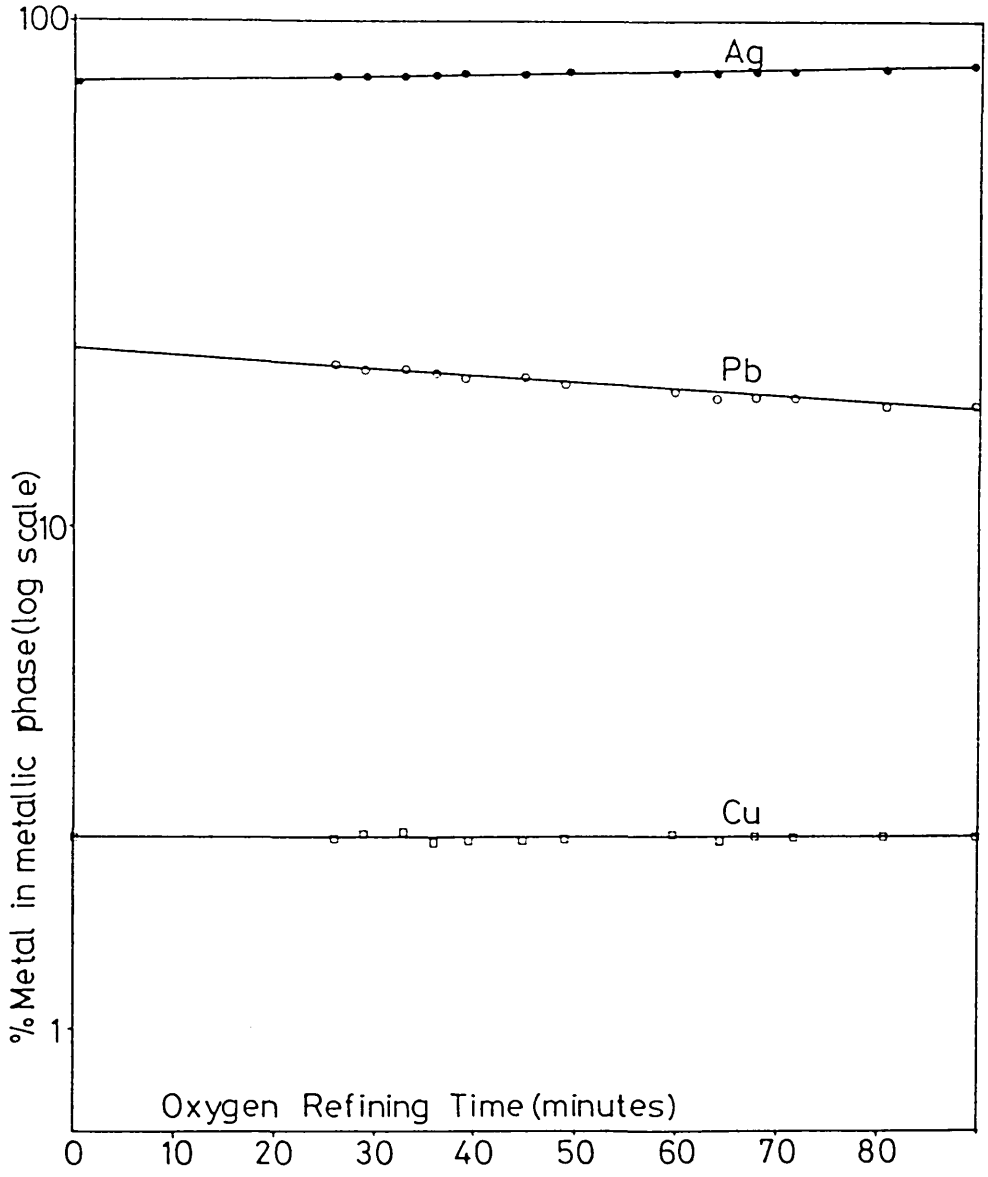

Fig.4.11 Melt content change - run E.

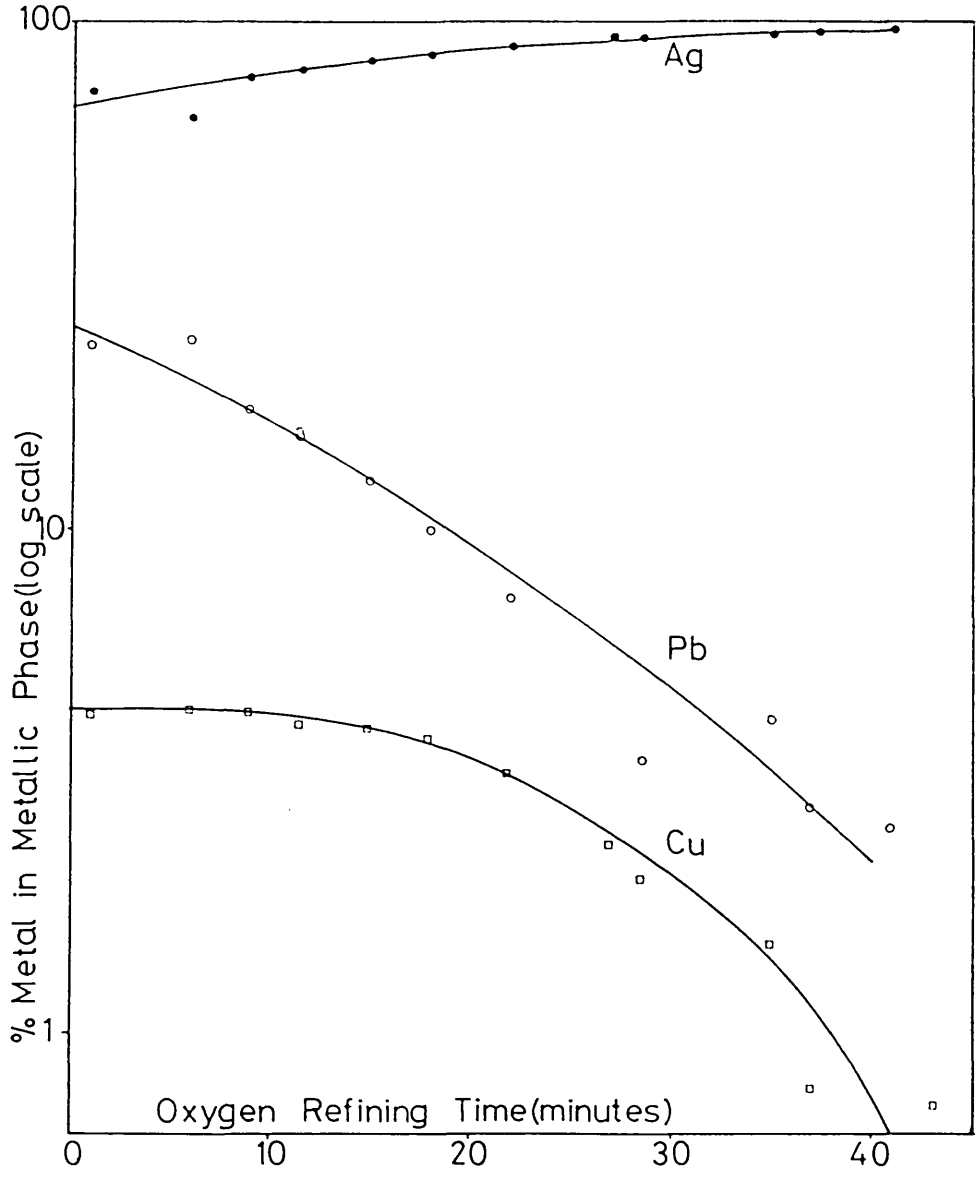

Fig.4.12 Melt content change - run F.

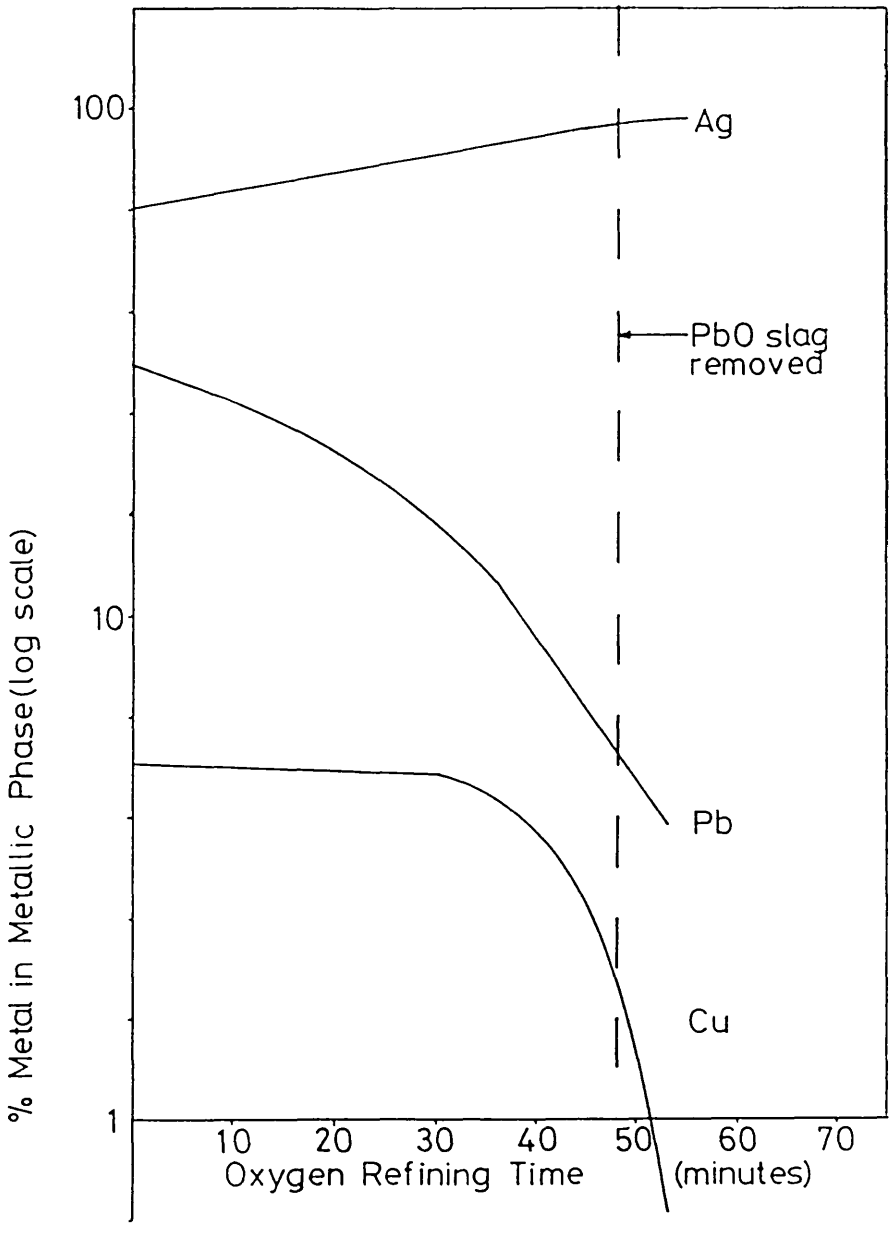

Fig.4.13 Melt content change - run H.

Table 4.2 Results

RUN	Time (min)	%Pb	%Cu	Balance %Ag	O_{O_2} Nl/m.
P	Initial charge	17.5	0	82.5	
	0	16	0.033	83.9	5.0
	1	16.2	0.034	83.8	5.0
	1.5	13.1	0.036	86.9	5.0
	5.5	12.0	0.034	87.9	4.91
	8.5	8.9	0.039	91	4.91
	13	5.9	0.038	94	4.92
	21	0.24	0.014	99.75	4.92
	31	0.18	0.013	99.8	4.5
	39	2.3	0.011	97.7	4.5
	Final agitated slag			7.1 Ag 2.54 metallics	
A	Initial charge	25.4	2.18	72.5	
	0	23.2	2.19	74.6	0.97
	3	22.4	2.24	75.4	10.16
	7	18.9	2.26	78.8	8.48
	10	16.8	2.13	81.1	8.48
	16	11.0	2.08	86.9	7.98
	28	0.4	0.78	98.8	8.52
B	Initial charge	24.9	2.19	72.9	
	1	26.7	3.34	69.9	3.52
	1.5	26.4	3.32	70.3	6.93
	5.5	24.3	3.31	72.4	7.39
	8.5	19.9	3.30	76.8	6.67
	13	16.0	3.50	80.5	7.52
	21	9.0	2.81	88.2	7.59
	31	1.13	1.89	96.9	7.39
	39	4.7	0.93	94.37	7.68

RUN	Time (mins)	%Pb	%Cu	Balance %Ag	O_{O_2} Nl/m.	Temp.
D	initial charge	13.8	3.99	82.2		
	1	12.9	3.87	83.23		
	4	11.9	3.90	84.2		
	8	10.9	3.82	85.3		960
	14.5	9.7	3.70	86.6		998
	18	9.2	3.64	87.7		1039
	21	8.7	3.58	87.72	0.656	1037
	25	7.0	3.45	89.55	1.1652	1037
	28	6.0	3.39	90.61	1.279	998
	31	5.1	3.27	91.73		998
	34	4.1	3.19	92.71		960
	37	2.8	3.2	94.0	1.549	936
	42	1.3	2.2	96.1		960
	50	0.3	2.2	97.5		960
DD	Initial charge	24.9	3.74	71.36		
	1	24.8	3.80	71.4		969
	3	23.6	3.84	72.6	1.37	998
	7	23.2	3.86	72.9	0.39	986
	8.5	23.0	3.88	73.1	2.61	975
	15	20.9	3.95	75.2	2.66	
	19	20.6	3.91	75.5		
	21	19.9	4.0	76.1		
	24.5	19.0	3.95	77.1		
	28	17.7	3.97	78.33		1091
	30	17.8	3.94	78.26		1037
	34	17.0	4.0	79.0	2.87	1039
	38	16.1	4.0	79.9		985
	43	16.1	4.1	79.8		

RUN	Time (mins)	%Pb	%Cu	Balance %Ag	O_2 Nl/m.	Temp.
E	Initial charge	22.8	2.44	74.7		
	0	20.8	2.38	76.8		830
	3	20.3	2.43	77.3		824
	7	20.4	2.46	77.1		924
	10	20.0	2.38	77.63		986
	13	19.5	2.35	78.2		1001
	19	19.5	2.39	78.1		912
	23	19.1	2.4	78.5		881
	34	18.4	2.43	79.2		874
	38	18.0	2.35	79.7		849
	42	17.8	2.39	79.81		
	46	17.4	2.4	80.2		947
	55	17.0	2.41	80.6		932
	64	17.2	2.40	80.4		936
	74	16.0	2.37	81.6		934
F	Initial charge	26.2	4.64	69.2		
	1	22.7	4.34	72.96	7.93	
	6	21.6	4.46	65.9	7.03	
	9	17.3	4.38	78.32	8.62	
	11.5	15.3	4.16	80.5		
	15	12.5	4.06	83.4		
	18	10.0	3.84	86.2	7.65	
	22	7.2	3.31	89.5		
	27	2.9	2.38	94.7		
	28	3.5	2.04	94.5	5.30	
	35	4.2	1.51	94.3	3.89	
H	Initial charge	31.6	5.1	63.3		824
	1.5	30.8	5.1	64.1	4.94	882
	4.25	29.4	5.0	65.6	4.94	906
	8	27.4	5.1	67.5	4.94	943
	12	25.6	5.1	69.3	4.53	964
	16	23.0	5.1	71.9	4.53	1024
	20	21.1	5.0	73.8	4.53	1001
	25	18.1	4.9	77.0	4.53	954
	27	17.2	4.9	77.9	4.12	
	29	15.9	4.8	79.3	4.12	914
	33.5	13.2	4.6	82.2		924
	36	11.6	4.3	84.1	6.18	
	38	10.2	4.3	85.5	8.96	924
	41.5	6.4	3.4	90.2	8.96	
	45	6.6	2.8	90.6	9.01	
	53	3.8	0.96	95.24	9.01	
	55	5.0	1.0	94	9.01	
	Solid product	0.33	1.0	98.7		

843°C in run F, before refining began, required a heat input rate of 2.5 kW. Of this amount it was estimated that about 3% was used in heating the nitrogen, 60% was conducted through the refractory and 37% was radiated to the atmosphere. The results are different to those reported in Section 4.1.2 because the crucible is smaller.

In run H a constant heat input rate was established before refining to keep the melt temperature steady. This same heat input rate was maintained for the following 16 minutes of refining; any temperature rise being due to exothermic heat of lead oxidation. An approximate heat balance was calculated from the measured data. The temperature during refining increased from 824°C to 1024°C in 16 minutes. During this period the lead content decreased from 31.6% to 23% which was the equivalent of 9.34 moles. Therefore 9.34 moles of lead oxide had formed and 4602 g of lead and 1075 g of copper remained. Taking into account the heat capacities of the melt constituents after 16 minutes the heat required was 2.04 MJ. The heat generated by oxidation of 9.34 moles of lead is calculated as 1.73 MJ. This rough balance between 2.04 MJ accumulated and 1.73 MJ from oxidation is quite satisfactory bearing in mind the crude nature of the experiments.

Slag analysis

Assuming that all reactions proceed to thermodynamic equilibrium, the silver content of the slag can be calculated to be 0.06 moles of Ag_2O per 1000g of slag (or 1.24% Ag). This compares with 9.65% measured after run P

(7.11% Ag + 2.54% as metallics) and indicates that the agitation in the bath was too violent to allow silver to settle from the slag into the metallic phase.

Some of the slag that was poured off from run D was allowed to settle in a crucible in the gas-fired furnace. The silver content of the slag was 2.29%. This is still higher than 1.24% expected from thermodynamic data, but is a great improvement over 9.65% measured from the agitated slag.

Oxygen utilization

Table 4.3 compares the approximate volumes of oxygen supplied to the melt with those required to oxidize the lead and copper. In runs D, DD, F and H, the oxygen utilization was always greater than 100%, presumably because some of the lead reacted with oxygen from the atmosphere. The oxygen volumes supplied were calculated from rotameter and pressure measurements and averaged between sample times. The volumes required to oxidise the lead were based on the metal sample analyses.

Melt oxygen potential

The most consistent oxygen probe results were obtained using air as the reference gas at an approximate flowrate of 100 ml/min. For run E, nitrogen was bubbled through a pure silver melt and an e.m.f. of 4mV was recorded corresponding to P_{O_2} = 0.176. This value was higher than expected and indicated that a nitrogen purge was not a particularly effective

Table 4.3 Oxygen utilization.

RUN	Volume of O_2 required for Pb refining (Nl) Q_R	Volume of O_2 supplied to melt (Nl) Q_s	Oxygen efficiency $Q_R/Q_s \times 100$
D	195	49.1	390
DD	208	55.8	370
F	322	312	103
H	491	329	150

method of silver melt deoxidation when the melt was in contact with air. When the 50/50 mixture of oxygen and nitrogen was passed through, an e.m.f. of +10 mV was measured, corresponding to a P_{O_2} = 0.299 atm.

When 25% lead and 4% copper were added to the melt, an e.m.f. of +300 mV was recorded, corresponding to a P_{O_2} = 2.3 x 10^{-6} atm.

No results are available for the P_{O_2} values during refining from any run because the stainless steel reference electrodes were always dissolved within one minute of being in contact with the lead oxide slag. Also the zirconia probes could not withstand the severe conditions caused by the violent bath agitation and corrosive slag attack. Thus many expensive tubes were broken.

4.3.2 Gas supply

Under constant pressure supply conditions of nitrogen injection into silver only, periodic variation of shroud pressure indicated when an accretion of frozen metal existed at the tuyere tip. If an accretion forms at any instant the gas pressure drop across it rises, causing a decrease in flowrate. This in turn leads to less cooling and as a result the accretion can melt back and the cycle repeats leading to a time-averaged steady flowrate (this is illustrated in Figure 4.14).

When lead and copper additions were made the pressure

dropped to a steady value, presumably because the accretion had "dissolved" due to the dramatic increase in melt superheat.

The constant-flow gas supply was installed because the exact amount of oxygen over a given time period could be easily computed and compared with that used during oxidation. During practice the performance was very unsatisfactory. The oxygen was supplied in "bursts" lasting about one minute each, and followed by a period of also one minute when very little or no gas flowed into the melt. Molten metal flowed into and partially blocked the tuyere resulting in oxygen accumulation in the gas lines with a rise in pressure. The reason for this is that the core blocked until the pressure behind it rose to a high enough value for the blockage to be blown out (along with some of the copper core tube). The pressure then decreased in the gas lines, the oxygen flowed rapidly and the core blocked again. The shroud flow continued steadily during the intermittent oxygen flow. The reasons for the intermittent blocking of the core by the oxygen flow are not fully understood.

Constant pressure supply proved to be easier to operate. Run H was especially successful when the shroud supply pressure was about 1 bar greater than the core supply.

4.3.3 Tuyere and refractory wear

The gas supply system and pressure conditions have a profound effect on tuyere performance and wear

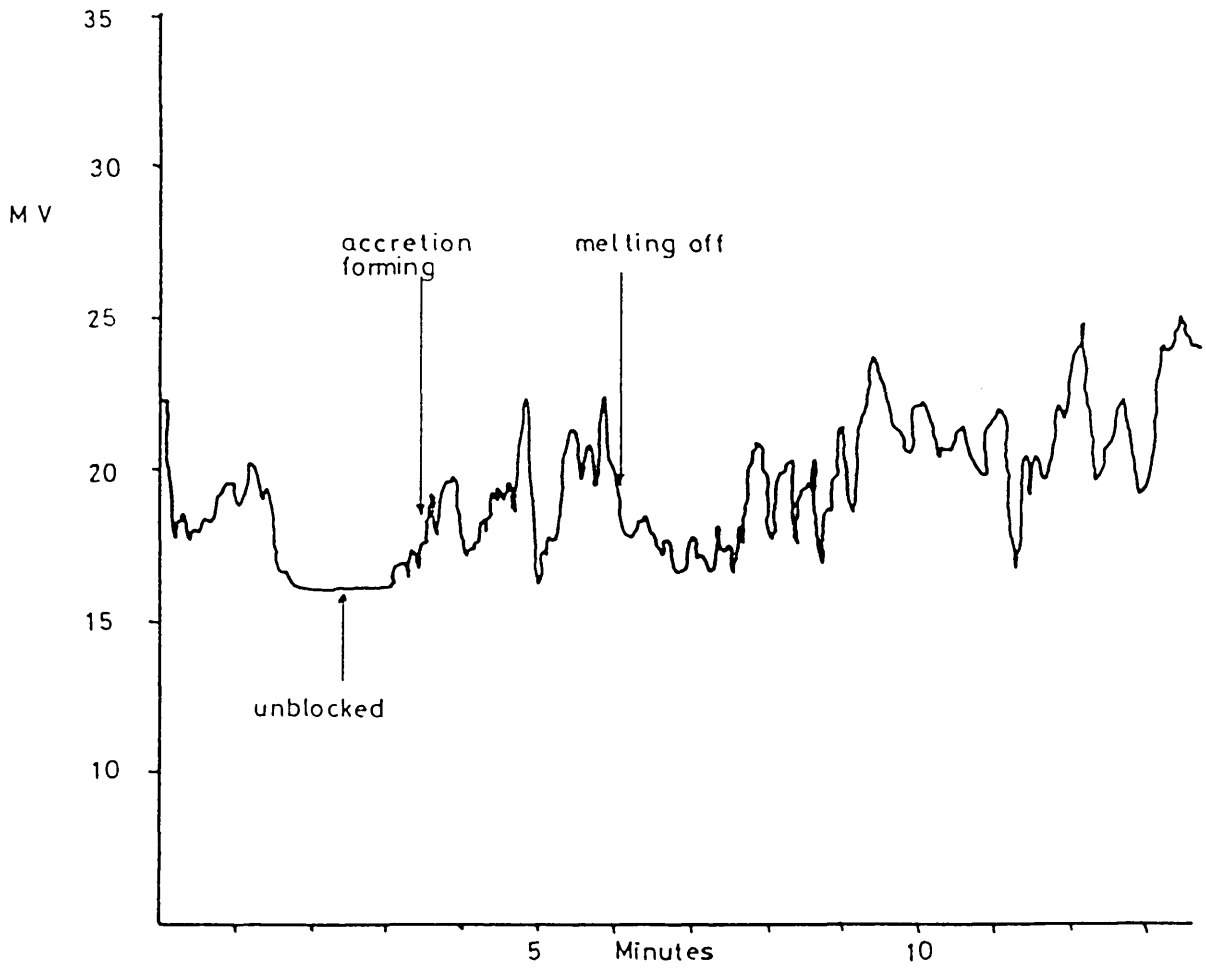

Fig.4.14 Pressure transducer output variation with time and accretion condition.

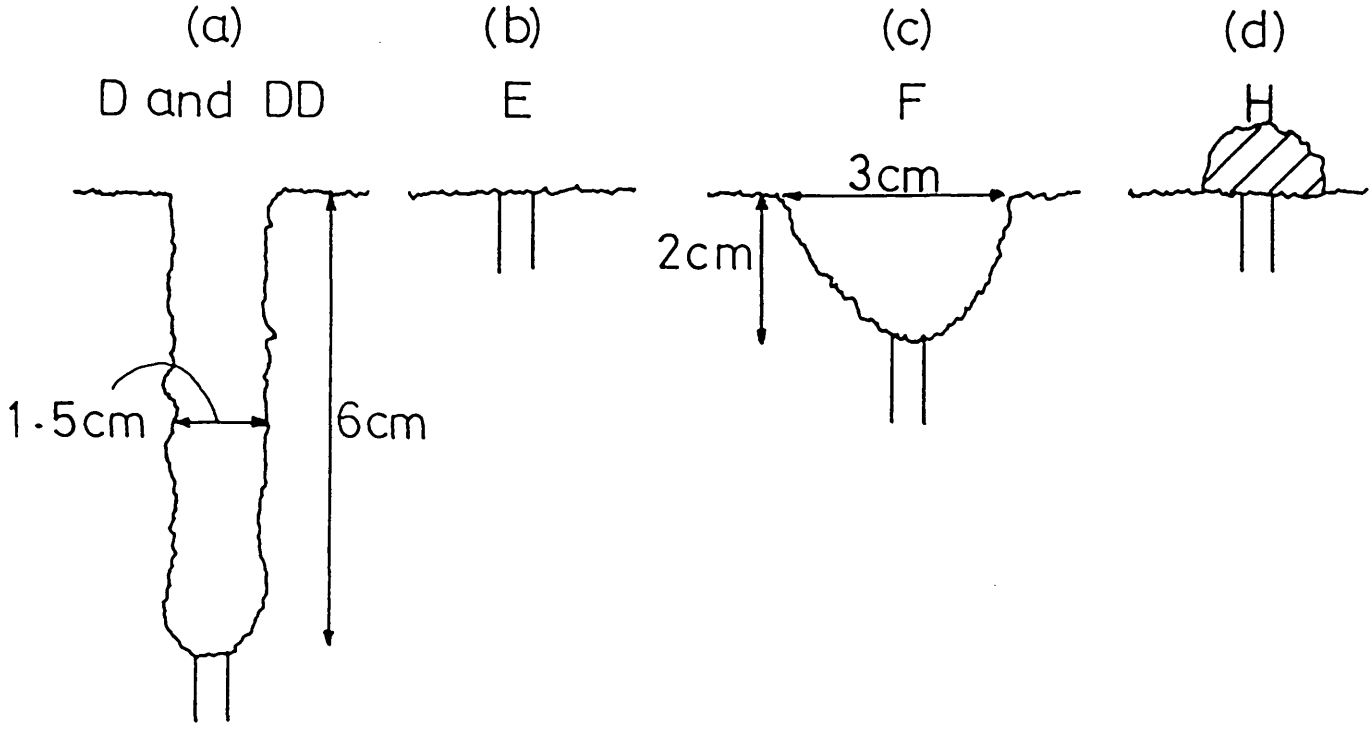

Fig.4.15 Tuyere refractory wear patterns observed after each run.

characteristics. Figure 4.15 shows the effect on tuyere wear of supply conditions. For constant flow supply (Figure 4.15a) the tuyere just "bores" backwards as if the shroud affords no protection at all. Figure 4.15b shows no erosion for run E, because previously to blocking the injected gases were effectively inert in molten silver. Operation without a protective accretion due to insufficient shroud cooling leads to severe cratering (4.15c). In run H (Figure 4.15d), where an accretion was formed and maintained, there was no apparent wear, despite a melt superheat of 220^{o}C at times.

At the end of the oxidation period the bath was almost pure silver and the superheat was low. If the same oxygen flowrate was maintained, the oxygen only served to cool the tuyere as no oxidation occurred, resulting in accretion formation which usually blocked the tuyere (core and shroud).

Figure 4.16 shows the sectioned tuyere tips after runs D, DD, E, F, and H. In runs D and DD (Figure 4.16a) the core has been dissolved back into the tuyere and the resulting cavity within the shroud walls has become partially blocked. Gas was still able to escape between the stainless steel walls and the solidified metal. In Figure 4.16b the core has again been dissolved back and completely blocked by the melt in run E. In run F there was no blockage because gas velocities were sufficient to prevent flooding. The overall tuyere length was reduced by 2 cm (Figure 4.16c). In Figure 4.16d, run H, an accretion still covered the end of the original length tuyere, although some of the stainless steel

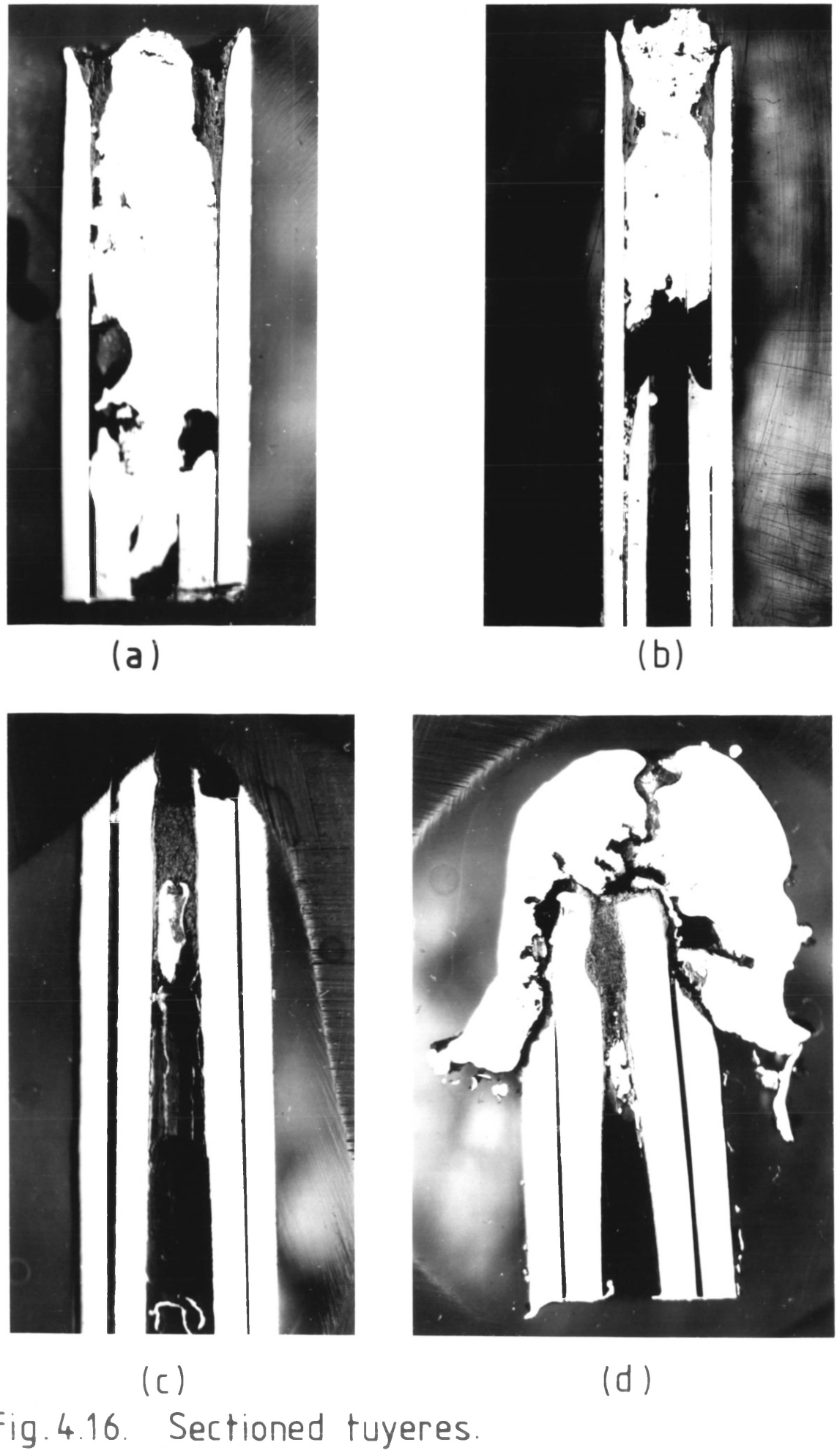

(a) (b)

(c) (d)

Fig. 4.16. Sectioned tuyeres.

shroud was dissolved. Both core and shroud gases were able to escape into the melt through the visible air passages in and around the accretion.

A great deal of slag-line attack on the sidewall above the tuyere was observed when using the low-grade alumina crucible for a set of preliminary runs. In addition, in the tuyere region a deep (12 mm) crater appeared after only one run.

The same refractory lining, Stein 1600, was used for all the remaining runs in this study without any problems. Localised erosion was confined to the wall behind the tuyere where there was a small depression of about 6.0 cm diameter by 6 mm deep. Similarly, about 6 mm of slag-line refractory was removed around the circumference.

After each tuyere was removed, a new one was cemented into place with castable Stein 1600.

4.4 DISCUSSION

4.4.1 Laboratory model

Lead and copper were oxidized out of the silver melt in one stage leaving silver of about 99% purity. For a 20 kg melt containing 5 kg of lead and 0.5 kg of copper complete cupellation took between 30 and 40 minutes, depending on the oxygen injection rate.

The quantity of silver in the slag was very high and indicated that a settling time should be allowed in the process, with the tuyere removed from the melt.

Overall oxygen balances, calculated by comparing the total amount of lead and copper oxidised with the best estimate of the total quantity of oxygen injected, give an indication of the oxygen utilisation efficiency. It appeared that all of the oxygen injected was used in oxidation. Further oxidation occurred by atmospheric oxygen.

During the refining period the exothermic heat generated balanced the heat losses until most of the lead had been oxidized. A scaled-up version of the model should therefore be able to operate autogenously.

The most successful runs in terms of resistance to tuyere and refractory attack were those carried out with a constant pressure supply. The best conditions were identified in run H where, despite increased splashing, resulting from a large shroud gas flowrate, the formation and maintenance of an accretion throughout the entire run completely eliminated wear in the tuyere region.

Oxygen potential measurements indicated that very high oxygen potentials occurred in liquid silver in contact with air, even when purging with nitrogen. When lead and copper were added to the melt, the resulting very low oxygen potential was similar to that predicted from the free energy diagram in Pb/PbO. The measured value is slightly higher

than that for Pb/PbO because lead activity is less than unity. Thermodynamic data predicts that for copper oxidation a higher P_{O_2} at 1000°C is required than for lead. When there is still a significant proportion of lead in the melt P_{O_2} is too low for copper oxidation. As refining proceeds the lead activity decreases to below a certain level and the P_{O_2} is able to rise sufficiently for copper oxidation to commence.

These results indicate that the use of borates or phosphates to remove copper will be fruitless in the presence of lead, unless all of the lead oxide slag can be removed initially.

4.4.2 Pilot-plant

Several aspects of the design of the pilot plant have been discussed in Section 4.1.3. Some information from this work will be useful in further design work of the tuyere.

The laboratory experiments were designed to be a one quarter scale model of a proposed process. The scaling criterion was simply to have the same flowrate per unit area of bath surface. On the basis of experimental data, pilot-plant conditions may now be related to those observed in the laboratory.

To obtain the required reaction rate the oxygen must be supplied at 180 Nl/m, giving a nominal velocity of 378 m/s through a 1/8"I.D. copper core. There will be a pressure drop of about 7 bar along a core of 0.7 m. To obtain adequate cooling the shroud nitrogen flowrate must be 30 Nl/m, a

nominal velocity of 78 m/s, using a shroud I.D. of 7.036 mm and a core O.D. of 6.426 mm, a gap of 0.305 mm. The resultant pressure drop along the shroud would be 40 psi in a tuyere 0.7 m long. Both shroud and core should be operated at constant pressure with the facility of at least a 10 bar supply on each line. Melt penetration back into the nozzle is likely to be very much less than for the model, as discussed by You et al.[46] and Collins[47].

If tuyere wear cannot be eliminated by any operational technique, cementing in new ones has been shown to be successful. Indeed replaceable porous plugs of pitch-bonded magnesia have been employed successfully in the steel industry[49]. A tapered refractory plug housing a tuyere would enable quick and simple replacement in the event of failure.

The suggested shape of the vessel to contain the 1.5 tonnes charge from the vacuum retort is shown in Figure 4.1. Refractory lining the vessel with chrome-magnesite bricks, although using the best material for the job[45], is difficult due to the vessel size. Stein 1600 castable has been shown at BRM to be reliable and is more convenient. The vessel is required to rotate through approximately 100^{o} to cater for the charging, blowing, settling and tapping stages.

An O_2/gas burner may be fitted to the top of the vessel or the hood as an external heat source for use in the final stages of refining or as a pre-heater.

4.5 CONCLUSIONS

1) Oxygen injection into silver-lead-copper melts was a very fast method of cupellation.

2) A successful technique of tuyere operation under constant pressure supply has been identified. The very best results, obtained in run H, involved maintaining a porous accretion at the tuyere tip. Other fairly successful runs (F,P,A,B) were also obtained.

3) Operating the tuyere under constant pressure with adequate shroud cooling minimized tuyere and refractory wear. Refractory erosion away from the tuyere was no problem.

4) Constant flow conditions caused excessive tuyere wear, despite obtaining successful reaction rates.

5) Copper removal was only possible if the melt oxygen potential rose above a certain level, corresponding to a low level of lead. Improved copper refining was possible if the lead oxide slag was removed at a late stage of the refining process and a flux added.

6) Oxygen utilization was over 100%, indicating that atmospheric oxygen takes part in the reactions.

7) The process should be autogenous with respect to heat if process time can be kept to below 3 hours.

4.6 FURTHER WORK

1) If the proposed cupellation time of three hours in the pilot-plant is exceeded for any reason, heat losses become important and alternative sources of heat must be provided. A novel way of achieving this would be to

switch over to natural gas injection in the shroud towards the end of the refining period. If twice as much oxygen as methane were injected, then a neutral gas would be produced by the reaction

$$CH_4 + 2O_2 = CO_2 + 2H_2O$$

By increasing the O_2/CH_4 ratio refining could proceed slowly, while decreasing the ratio would give a reducing gas which could be used to deoxidize the bath prior to casting (provided all the slag had been skimmed off). In this way silver scrap could be charged, using the heat of combustion for melting. Investigation of methane use as a shroud gas could produce some interesting results.

2) Some confirmatory work is still required to fully understand successful tuyere operation. This includes nozzle blockage problems, accretion formation, pressure drops in the tuyere, refractory wear and behaviour of different refractories (see Section 3.6).

3) A good reason for slag removal before the end of the refining period is to allow low levels of lead and copper to be obtained. The slag (containing between 2.3 - 9% Ag) would be recycled to the blast furnace. After this stage the effect of adding fluxes of borates or phosphates on further removal of lead and copper should be investigated. Slag settling also requires consideration.

CHAPTER 5

HEAT TRANSFER CALCULATIONS FOR PIPE-LIKE ACCRETION FORMATION AROUND A SUBMERGED GAS INJECTION TUYERE

CHAPTER 5

HEAT TRANSFER CALCULATIONS FOR PIPE-LIKE ACCRETION FORMATION AROUND A SUBMERGED ANNULAR GAS INJECTION TUYERE.

5.1 INTRODUCTION

In recent years, the widespread application of submerged gas injection in the metallurgical industry has led to an increasing interest in accretion formation around tuyeres. The growth of accretions is well known in copper converting. In the steel industry the formation and subsequent control of accretions is an important tuyere protection mechanism leading to successful operation of the Q-BOP, combined top and bottom blowing and the AOD processes. The accretions protect the refractory around the nozzle area from the high temperature reaction zone[4]. Sufficient cooling is achieved by introducing a coolant gas into a concentric nozzle surrounding a core tube supplying the reactive gas[1].

Factors responsible for tuyere and refractory protection are generally quoted as being the endothermic dissociation of the protective fluid and/or sensible heat required to raise the temperature of the dissociated products or inert gas up to the melt temperature. The main heat input to the accretion results from convection from metal flowing over the surface towards the ascending jet. In a bubbling regime (see Chapter 2) bubbles intermittently displace the liquid metal which washes across the accretion and refractory

surfaces, leading to rapid temperature fluctuations. These could contribute to the refractory erosion process by generating local, short term thermal stress variations[41].

5.2 Previous work

Earlier work on heat transfer calculations by Krivsky and Schuhmann[49] around a tuyere in a hypothetical copper converter was limited to the calculation of the temperature distribution in the refractory surrounding the tuyere. Their method involved using simple boundary conditions and the relaxation method. They concluded that the pronounced cooling effect of the tuyere could cause accretion formation. Their model did not consider the rise in gas temperature along the tuyere nor did they study accretion formation.

Denier, Grosjean and Zanetta[50] have made temperature measurements in the tubes constituting the tuyeres, in the surrounding refractory bricks and in the oxygen reaction zone. They also developed a model to describe the heat flow within the tuyere, and discussed the role of the shroud gas in limiting tuyere wear. Moore and Wraith[41] have developed a model for the case of rapid temperature fluctuation in and around an annular tuyere without an accretion as liquid metal washes across it and the refractory.

Accretions fall broadly into two extreme catagories. They are:-

(a) pipe-shaped accretions[4] with gas-flow channels predominantly up the centre and

(b) porous and fully capped[28], mushroom-like accretions with gas-flow channels spreading radially outwards from the tuyere exit.

Some work on the calculation of accretion shapes has been done by Ohguchi and Robertson[29,51] and Boxall et al[52]. These two mathematical models were based on pipe-like accretions from single tube nozzles, producing long slender shapes. Ohguchi and Robertson went further to produce a porous-accretion model in order to calculate shapes of fully capped, mushroom-like accretions. A rather simpler model has been proposed by Sahai and Guthrie[11] based on the heat balance between the heat removed by the gas, heat supplied by the hot metal and the heat required to solidify the metal. Their analysis, however, ignores the cooling of adjacent refractories and treats the accretion/refractory interface as adiabatic. Their results indicate that when using a hydrocarbon as the cooling shroud gas, about 60% of the maximum cooling capability is available for freezing an accretion.

5.3 Present approach

Calculations have been carried out to estimate the conditions under which pipe-shaped accretions occur and the shape of the accretion, by considering heat transfer both in

the refractory around the annular tuyere and in the molten metal. The increase in gas temperature with distance has been taken into account. The approach taken is similar to that of Ohguchi and Robertson[29]. Mechanisms of tuyere failure are discussed.

5.4 Modelling of heat transfer around a tuyere

A section of the cylindrical heat transfer zone is shown in figure 5.1, incorporating the cylindrical annular tuyere, the assumed path of injection gas in the liquid metal and the refractory around the tuyere. It is assumed that the jet of gas penetrating the liquid metal has the same effective diameter as that of the shroud tube internal diameter[11]. The actual paths of the gas in an accretion are of complicated shapes consisting of a multiplicity of minute holes expanding radially[4]. To account for this the value of the heat transfer coefficient for gas/metal was chosen higher than for gas/ refractory. . This aspect will be discussed in detail later.

The concept of a thermal boundary layer was introduced to account for heat transfer from hot liquid to solidified steel at the accretion/liquid steel interface. Beyond this layer it is assumed that the bulk liquid metal temperature is homogeneous due to strong agitation by injected gas. Thus a temperature gradient in the liquid metal exists only in the thermal boundary layer. The mean heat flux density (q_d)

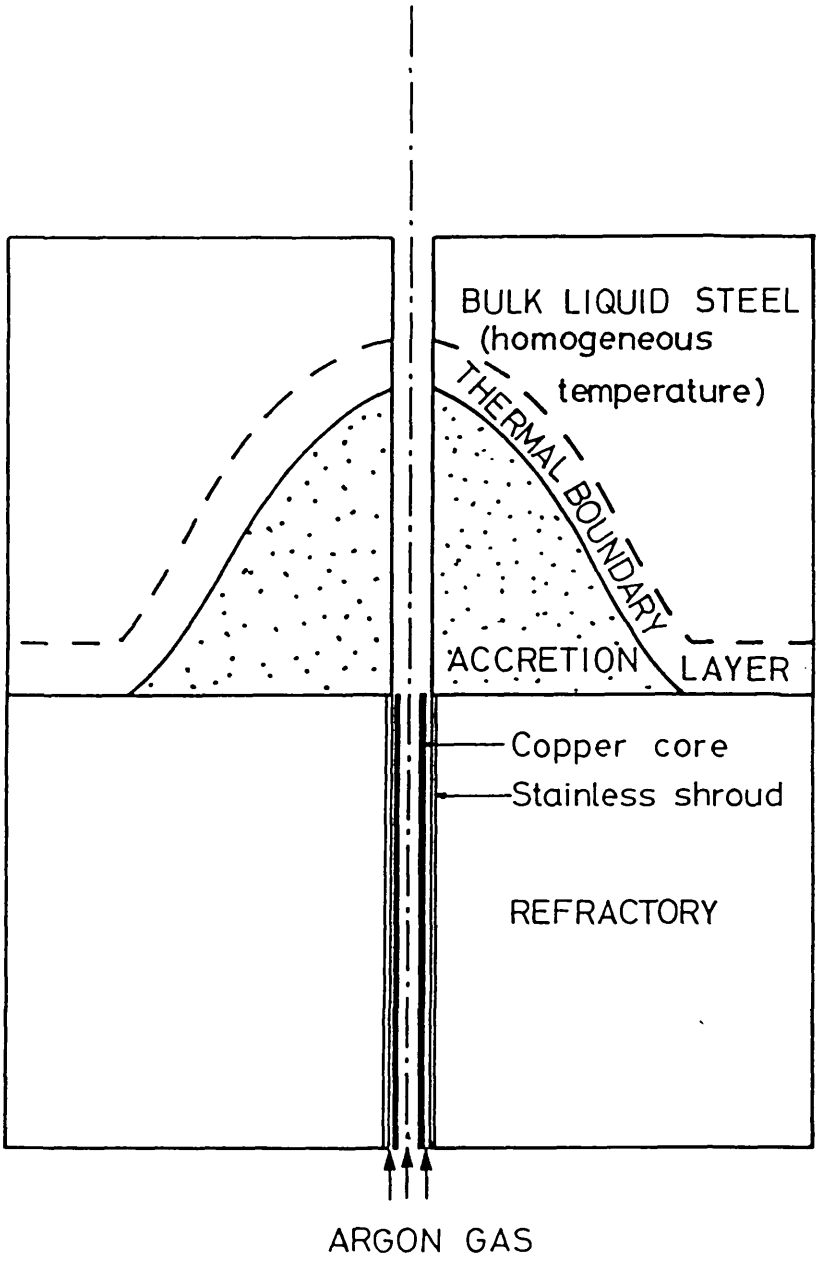

Fig.5.1 Heat transfer zone, incorporating the annular tuyere.

across the thermal boundary layer is expressed by

$$(q_d) = k_d \, \Delta T_s / R_d \qquad (5.1)$$

ΔT_s is the temperature difference between solidification temperature and bulk temperature (superheat), and k_d and R_d are respectively the thermal conductivity and thickness of the boundary layer.

In practice, it is very difficult to estimate the actual value of R_d, because it is locally altered with the shape of the accretion and the properties of fluid flow. In the present work a constant value of R_d was chosen, and the value of k_d was adjusted to obtain a particular value of q_d for given ΔT_s. A particular ratio of k_d/R_d is equivalent to assuming a particular value of heat transfer coefficient on a plane surface i.e.,

$$(q_d) = (k_d/R_d) \, \Delta T_s = h_1 \, \Delta T_s \qquad (5.2)$$

The assumption of constant R_d leads to higher fluxes at the surface when the accretion is strongly curved. Since this is probably the case, in practice it is not a bad assumption to use.

5.5 FORMULATION

1) Governing equation

The section of the cylindrical region in which heat transfer calculations are done is shown in Figure 5.2 and the detail

of the annular tuyere in Figure 5.3. By assuming axial symmetry, the governing heat transfer equation for liquid steel, solid steel and refractory in cylindrical coordinates with no internal heat generation becomes

$$(1/\alpha)\delta T/\delta t = \delta^2 T/\delta Z^2 + (1/r)\delta T/\delta r + \delta^2 T/\delta r^2 \qquad (5.3)$$

2) Gas temperature

The heat balance on the gas rising through the annulus in the refractory region can be described by

$$2\pi\Delta Z(h_{gov} r_7 (T_7 - T_{sho}) + h_4 r_4 (T_4 - T_{sho})) = \dot{m} C_p (T_{sh} - T_{sho}) \qquad (5.4)$$

where

$$h_{gov} = (1/h_7 + k_{sh}/t_s)^{-1}$$

and that within the core tube by

$$2\pi\Delta Z h_2 r_2 (T_2 - T_{co}) = \dot{m}_c C_p (T_c - T_{co}) \qquad (5.5)$$

Similarly, the heat balance for gas rising through the bore in the accretion is given by (see Figure 5.2)

$$2\pi\Delta Z h_{gs} r_6 (T_6 - T_{go}) = \dot{m} C_p (T_g - T_{go}) \qquad (5.6)$$

3) Boundary Conditions

The boundary conditions for the different regions are as follows

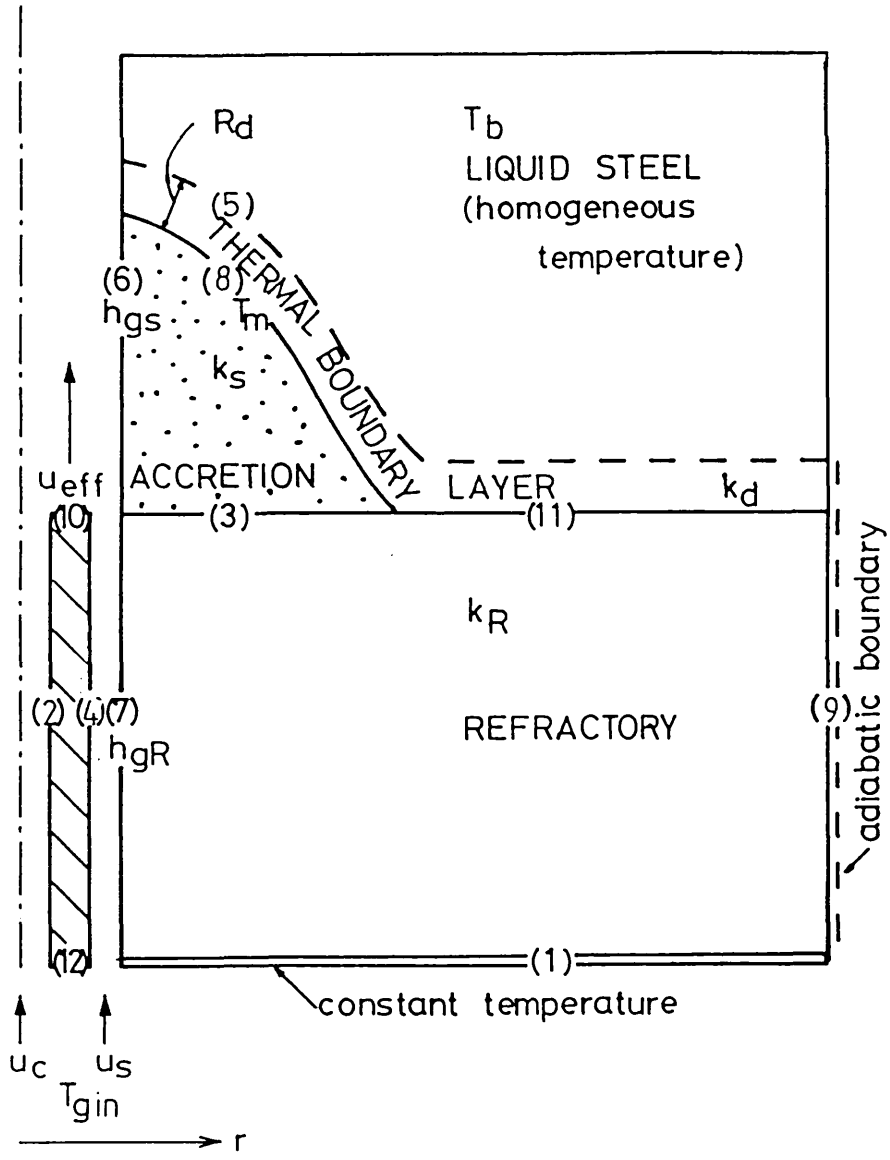

Fig.5.2 Section of cylindrical region for heat transfer calculations.

(a) Refractory shell (boundary (1) in Figure 5.2).

T = constant

(b) Side surface of cylindrical region to be calculated (boundary (9) in Figure 5.2).

This boundary is assumed to be thermally insulated

$$\delta T/\delta r = \emptyset \qquad (5.7)$$

(c) Interface between refractory and solid steel (boundary (3) in Figure 5.2)

$$(k_s \delta T/\delta Z)_s = (k_R \delta T/\delta Z)_R \qquad (5.8)$$

$$(T)_s = (T)_R$$

(d) Interface between liquid and solidified steel (boundary (8) in Figure 5.2)

$$(k_d \delta T/\delta Z)_l = (k_s \delta T/\delta Z)_s \qquad (5.9)$$

$$(T)_l = (T)_s = T_m \text{ (melting point)}$$

(e) Interface between bulk liquid and thermal boundary layer (boundary (5) in Figure 5.2)

$$T = T_b \text{ constant (bulk liquid temperature)} \qquad (5.10)$$

(f) Heat transfer boundary between accretion and gas

(boundary (6) in Figure 5.2)(see loop in Appendix 4)

$$h_{gs}(T_w-T_g) = k_s(\delta T/\delta r)_{r_o} \qquad (5.11)$$

(g) Heat transfer boundary between refractory and annulus gas(boundary (7) in Figure 5.2)

$$h_{gov}(T_w-T_g) = k_R(\delta T/\delta r)_{r_o} \qquad (5.12)$$

(h) Heat transfer boundary between annulus gas and outer core surface (boundary (4) in Figure 5.2)

$$2\pi\Delta Z(h_4 r_4(T_5-T_4)+F\epsilon\sigma r_7(T_7^4-T_4^4)) =$$

$$k_{core}\,\Delta Z(T_4-T_3)/\ln(r_4/r_3) \qquad (5.13)$$

(i) Heat transfer boundary between core gas and core tube (boundary (2) in Figure 5.2)

$$h_2(T_2-T_1) = k_{core}(\delta T/\delta r)r_2 \qquad (5.14)$$

(j) Heat transfer during mixing of core and annulus gas into accretion (boundary (1Ø) in Figure 5.2.)

$$(\dot{m}_c C_{pc}+\dot{m}_s C_{ps})T_{mean}=\dot{m}_c C_{pc} T_{gc}+\dot{m}_s C_{ps} T_{gs} \qquad (5.15)$$

(k) Interface between refractory and liquid steel (boundary (11) in Figure 5.2.)

$$(k_d \delta T/\delta Z)_1 = (k_R \delta T/\delta Z)_R \qquad (5.16)$$

$$(T)_1 = (T)_R$$

(1) Inlet gas temperature (boundary (12) in Figure 5.2.)

$$T_g = T_g \text{ in constant} \qquad (5.17)$$

5.6 CALCULATION AND DATA

For steady-state heat transfer calculation, Equation 5.3 may be modified to the following form to reduce computational labour. Replacing r by $X=\ln r$[53] equation 5.3 becomes

$$\delta^2 T/\delta Z^2 + e^{-2x} \delta^2 T/\delta x^2 = 0 \qquad (5.18)$$

By selecting a constant mesh interval ΔX in the X-direction, the logarithmic sub-division sets up a mesh with fine spacing close to the tuyere which expands with increasing X. Equation 5.18 was solved with the gas temperature equations by the successive over-relaxation method[54]. From Figure 5.3 and Equation 5.4 it can be seen that the shroud tube is accounted for in calculations by assuming that it is a resistance to heat flow from the refractory. The gas velocity is calculated assuming that the shroud tube internal diameter is r_7.

After each iteration the position of the thermal boundary layer was reset. The procedure for setting the thermal boundary layer of constant thickness is similar to the method used by Ohguchi[29] and is shown in Figure 5.4.

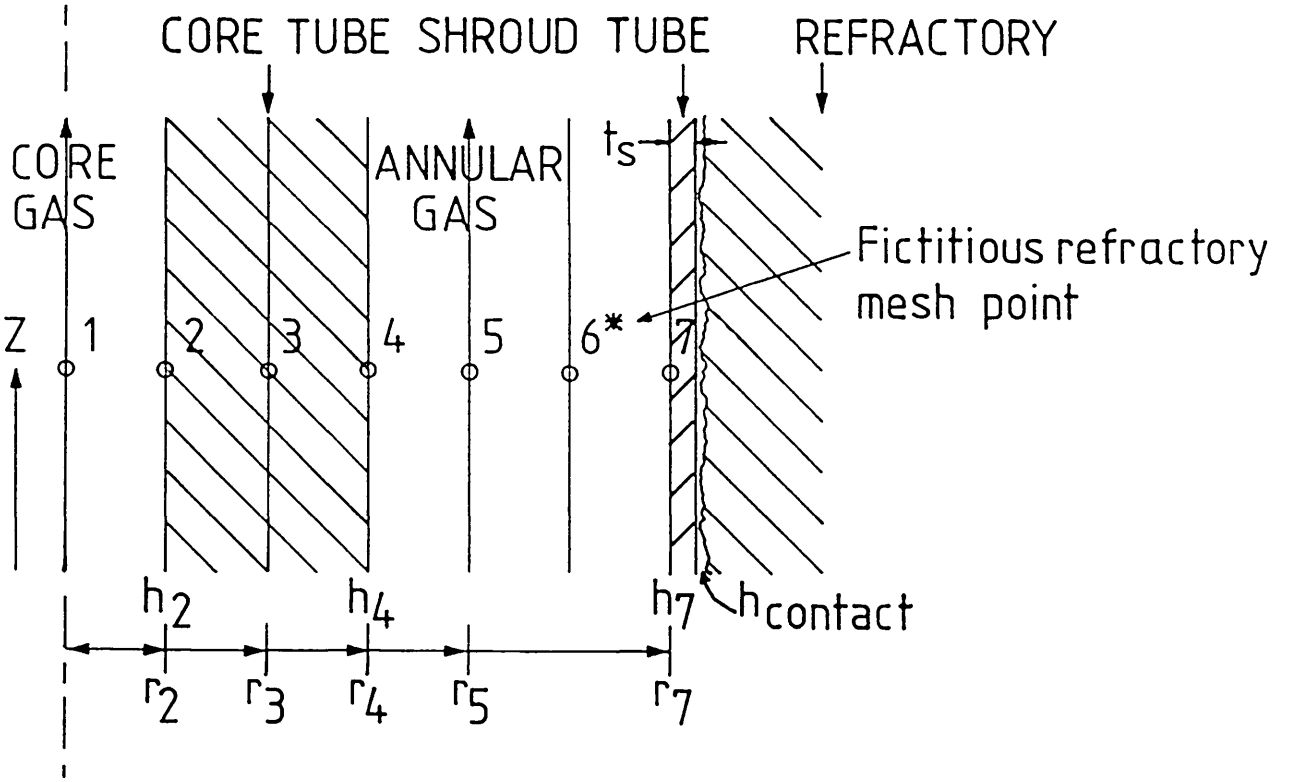

Fig.5.3 Mesh point representation of annular tuyere.

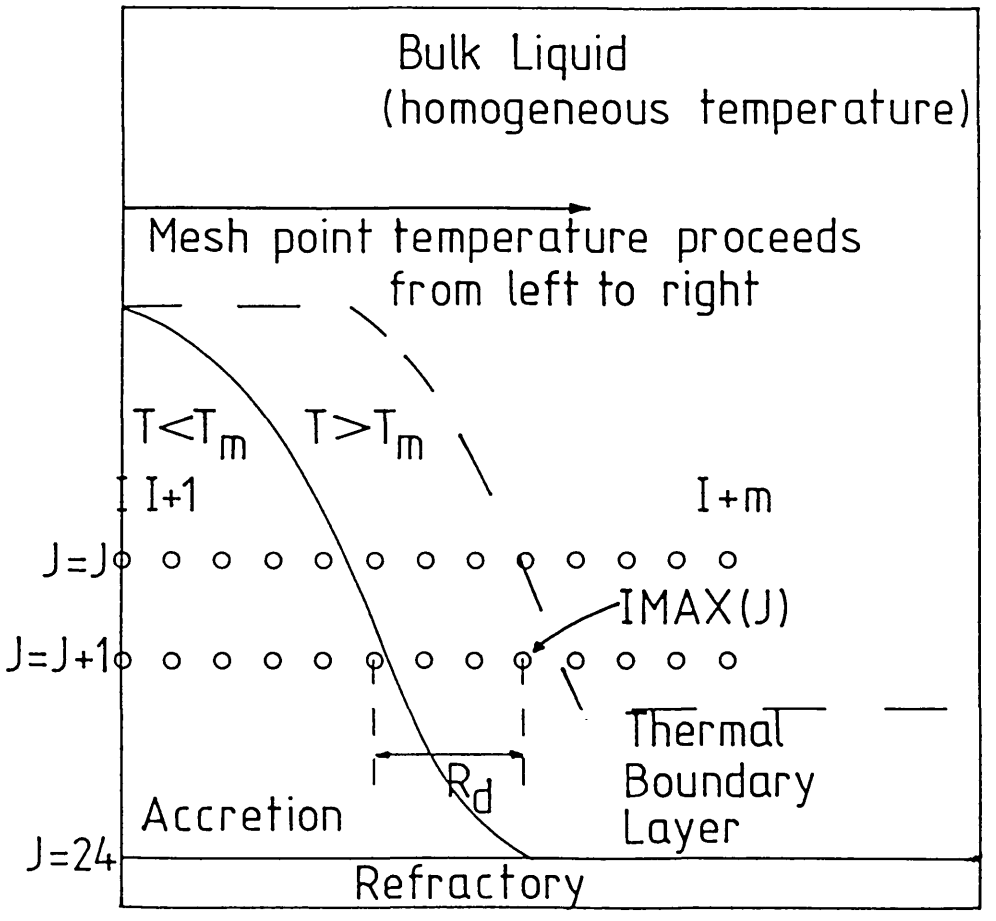

Fig.5.4 Resetting of thermal boundary layer.

Consider the mesh points lying immediately inside the solid/liquid interface. From each of these a line of length R_d is drawn horizontally into the bulk liquid. The mesh points of liquid steel falling within distance R_d are taken as those of the thermal boundary layer and the temperatures are calculated. Then, liquid steel mesh points of the rest of the area are regarded as those of the bulk liquid and are kept at constant temperature.

A computing flow chart for the solution of the accretion boundary problem is shown in Figure 5.5. In this we imagine an array of mesh points of mI columns by nJ rows where m = 35 and n = 24 in this programme. The direction of a sweep in any one iteration is from left to right, and when temperatures of all mesh points in one row have been calculated, relaxation of the next row begins at the left hand side. IMAX(J) specifies the position of the mesh point at a horizontal distance R_d from the accretion edge for a particular row, beyond which the bulk liquid temperature is homogeneous. When all the temperatures in a row have been calculated up to IMAX(J), relaxation of the next row immediately begins.

For the presentation of the fixed interface boundaries a general finite difference expression was used[53]. As an example mesh points and temperatures at the liquid or solid steel/refractory interface, where thermal conductivity and mesh point interval change, are shown in Figure 5.6, and i-1, i, i+1 etc. are the mesh point subscripts of

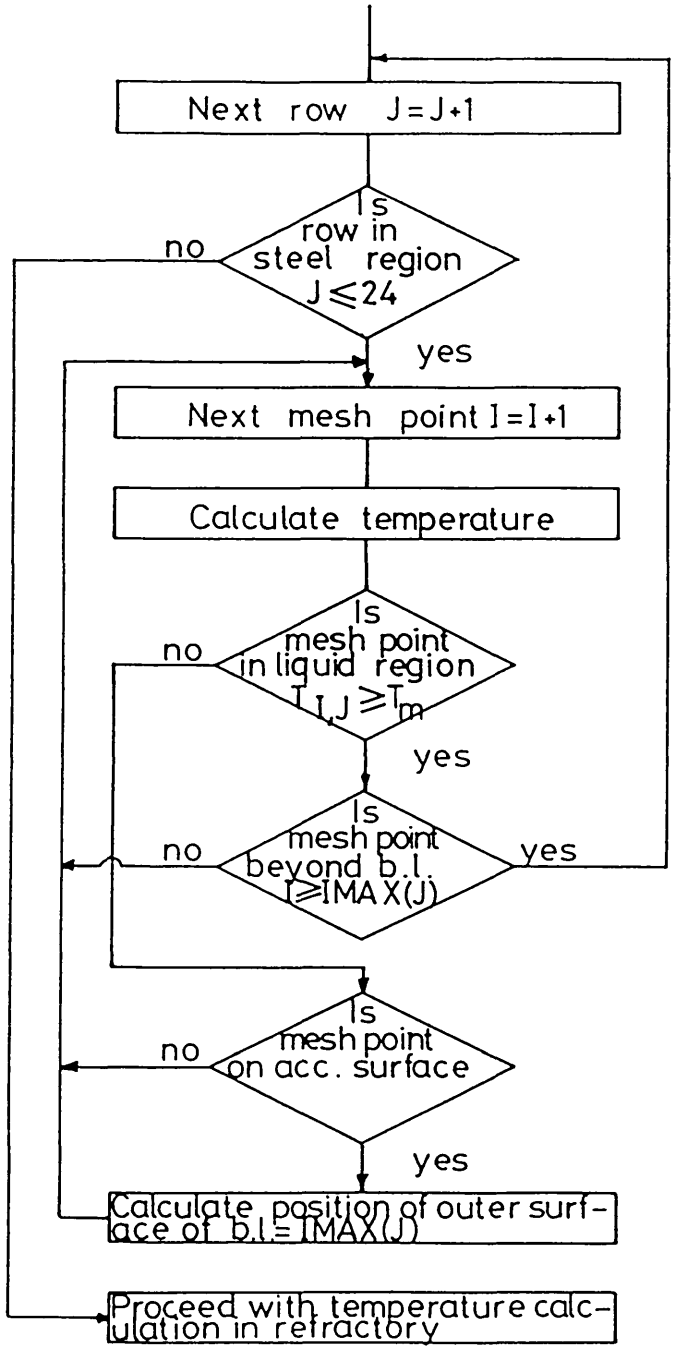

Fig.5.5 Flowchart indicating solution of moving accretion boundary problem.

Z-direction (ignoring those in the r-direction). In Figure 5.6 the right-hand side of the mesh point i is the steel region, which has thermal conductivity k_s and mesh interval ΔZ_s, and the left-hand side is the refractory region, which has thermal conductivity k_R and mesh interval ΔZ_R. T_i is the temperature of the mesh point at the interface. To calculate T_i, two fictitious temperatures (T^*_{i-1}, T^*_{i+1}) may be introduced. T^*_{i-1} is the fictitious steel temperature extended in the refractory region and T^*_{i+1} is the fictitious refractory temperature extended into the steel zone. Using these fictitious temperatures the boundary condition Equation 5.8 is expressed by the following central-difference equation,

$$k_s(T_{i+1}-T^*_{i-1})/2\,\Delta Z_s = k_R(T^*_{i+1}-T_{i-1})/2\,\Delta Z_R \qquad (5.19)$$

At mesh point i, two more difference equations derived from Equation 5.18 can be formed. One is the governing equation for steel temperatures T^*_{i-1}, T_i, T_{i+1}, and the other is for refractory temperatures T_{i-1}, T_i, T^*_{i+1}. Using these three equations the three unknown temperatures T^*_{i-1}, T_i, T^*_{i+1}, can be calculated.

The following mathematical modification was employed in the calculation of the thermal boundary layer to facilitate computation of the accretion boundary. Temperature and thermal conductivity of the boundary layer (T and k_d) are replaced by modified temperature θ and thermal conductivity k_s, which is chosen as equal to the value of solid steel. This is expressed as

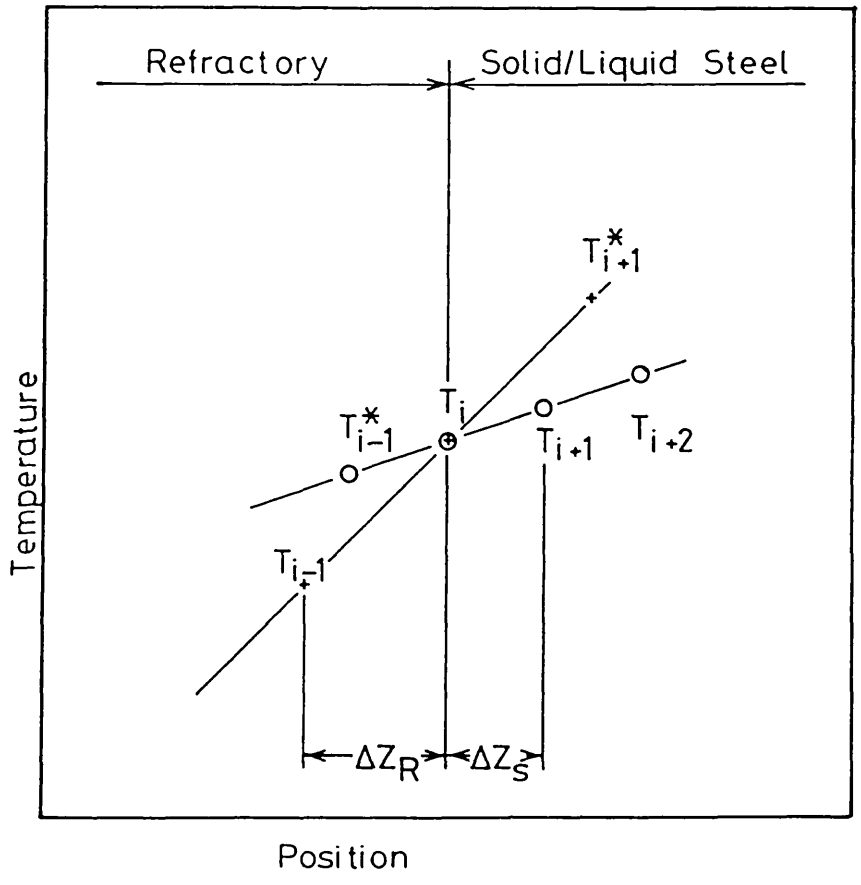

Fig.5.6 Finite difference representation of fixed interface.

$$(T,\ k_d) \longrightarrow (\theta,\ k_s)$$

in the liquid region where θ is defined by

$$\theta = T_m + (T - T_m) k_d / k_s \qquad (5.20)$$

This modification does not affect the governing equation and boundary conditions. For example, the left-hand side of Equation 5.8 or Equation 5.9 is

$$(k_d \delta T / \delta Z)_l = (k_d (\delta T / \delta \theta)(\delta \theta / \delta Z))_l = (k_s \delta \theta / \delta Z)_l$$

$$(T)_l = T_m = (\theta)_l$$

The advantage of this modification is that the accretion boundary problem (solid/liquid interface) can be simplified, because there is no discontinuity of gradient between solid steel temperature and modified liquid temperature and the solid/liquid boundary condition (Equation 5.9) is automatically satisfied. Actual computation was performed using the above modified temperature and thermal conductivity for temperature initialization. As the calculation progressed, if a θ value dropped to T_m or less, the temperature was replaced by T, calculated implicitly from equation 5.20. After convergence of the relaxation calculation the original temperatures were recalculated.

The heat transfer coefficient between core gas and core tube was estimated by the well known Colburn equation[37], which is

$$Nu = 0.023Re^{0.8}Pr^{0.33} \quad (5.21)$$

For the heat transfer coefficient from the outer wall of the core to the annulus gas[55], the form of Equation 5.21 is

$$Nu = 0.023Re^{0.8}Pr^{0.33}(r_7/r_4)^{0.45} \quad (5.22)$$

Similarly that for heat transfer from the inner shroud pipe wall to the annulus gas[56] is

$$h/u_o \rho C_p = 0.023Re^{-0.2}Pr^{-2/3} \quad (5.23)$$

In Equations 5.22 and 5.23 the characteristic length dimension is taken as the annular gap. Values of h_{gov} were updated every iteration. As the path of gas in the accretion actually consists of many narrow conduits the effective heat transfer coefficient in solid metal was chosen higher than that in the refractory zone. The value of h_{gs} adopted was generally three times greater than the value calculated for a single bore tuyere of the same diameter. The enhanced value has been shown by Ohguchi[29] to result in calculated accretion sizes of comparable dimensions to those actually observed in steel converters. No attempt was made to calculate the cooling effect due to expansion of the gas.

Material properties and typical gas injection conditions for the computation are presented in Tables 5.1 and 5.2 respectively. The thermal conductivity of the refractory is that of typical steelmaking brick (siliceous fireclay[57] or

medium alumina fireclay). Generally the values in Table 5.1 and Table 5.2 were used, unless specifically mentioned.

Constant material properties of argon gas were assumed for computation[58], though gas temperature was changing extensively along the tuyere length. Effectively the only temperature dependent variables in Equation 5.4, 5.5, or 5.6 are the h variables for convection, because the change of gas temperature does not affect mass flow rate per unit area at all, and the specific heat of argon gas is almost independent of temperature. The temperature dependence of h can be estimated by the use of Equation 5.21. Thus h values are proportional to the absolute temperature raised to the power of Ø.1 - a small effect.

The actual computation was done on the CDC Cyber 174 computer at Imperial College. The total number of mesh points for the finite difference representation was 35 x 5Ø, and a typical run consumed about 3ØØ seconds of computer time. The computer programme REFRAC9 is given in Appendix A.4.

Table 5.1 Material properties

Steel	k_s	29 W/mK
	T_m	1540°C
Refractory	k_R	1.3 W/mK
Copper core tube	k_{Cu}	385 W/mK
	OD	0.00794 m
	ID	0.00635 m
Stainless steel shroud tube	k_{sh}	30 W/mK
	OD	0.0127 m
	ID	0.0111 m
Argon gas at 727°C	ρ	0.49 kg/m^3
	C_p	519 J/kgK
	k_{Ar}	0.0427 W/mK
	μ	5.42 x 10^{-5} kg/ms
Methane gas at 728°C	ρ	0.96 kg/m^3
	C_p	2190 J/kgK
	k_{CH_4}	0.3135 W/mK
	μ	4.134 x 10^{-5} kg/ms
Oxygen gas at 727°C	ρ	0.389 kg/m^3
	C_p	909.2 J/kgK
	k_{O_2}	0.109 W/mK
	μ	7.109 x 10^{-5} kg/ms

Table 5.2 Gas injection conditions

Refractory thickness		25 cm
Outside temperature of refractory		200 ^{o}C
Superheat of liquid steel	ΔT_s	100 ^{o}C

$h_{contact}$	9510 W/m^{2}K
h_{gs}	1000 W/m^{2}K
R_d	3.0 cm
k_d	250.8 W/mK
h_l (= k_d/R_d)	8360 W/m^{2}K

5.7 RESULTS

The model was run under varying conditions of gas flowrate, superheat etc. in an attempt to establish the effect of shroud cooling on accretion size. Core oxygen flowrates per tuyere in the AOD described in Chapter 3 varied between zero and Ø.Ø35 m^3/s and argon in the shroud line between Ø.ØØ5 and Ø.Ø22 m^3/s. The zero oxygen flowrate in the core was used only in the reduction step.

The effect of changing the core gas flowrate is indicated in Figure 5.7 for an effective superheat of 5ØØ°C. The justification for such a high value during reactive gas injection is discussed in Section 5.8.5. For an increase in total gas flowrate the accretion grows. Values of h_{gs} were calculated using Equation 5.21 and then enhanced by a factor of three. The calculated accretion shapes are slender compared with those usually observed[28]. The reason is that the path of the gas is assumed to be in a pipe along the axis of the accretion, whereas actual accretions often have numerous divergent paths.

The increment of gas temperature is a few hundred degrees in the refractory. Despite the high superheat the model does not indicate that the temperature levels in the annular tuyere ever become high enough for melting of the copper tube under the conditions specified in the calculations shown in Figure 5.7. The mixed gas temperature rises more rapidly in the accretion because of a higher heat transfer coefficient between the gas and accretion. A very

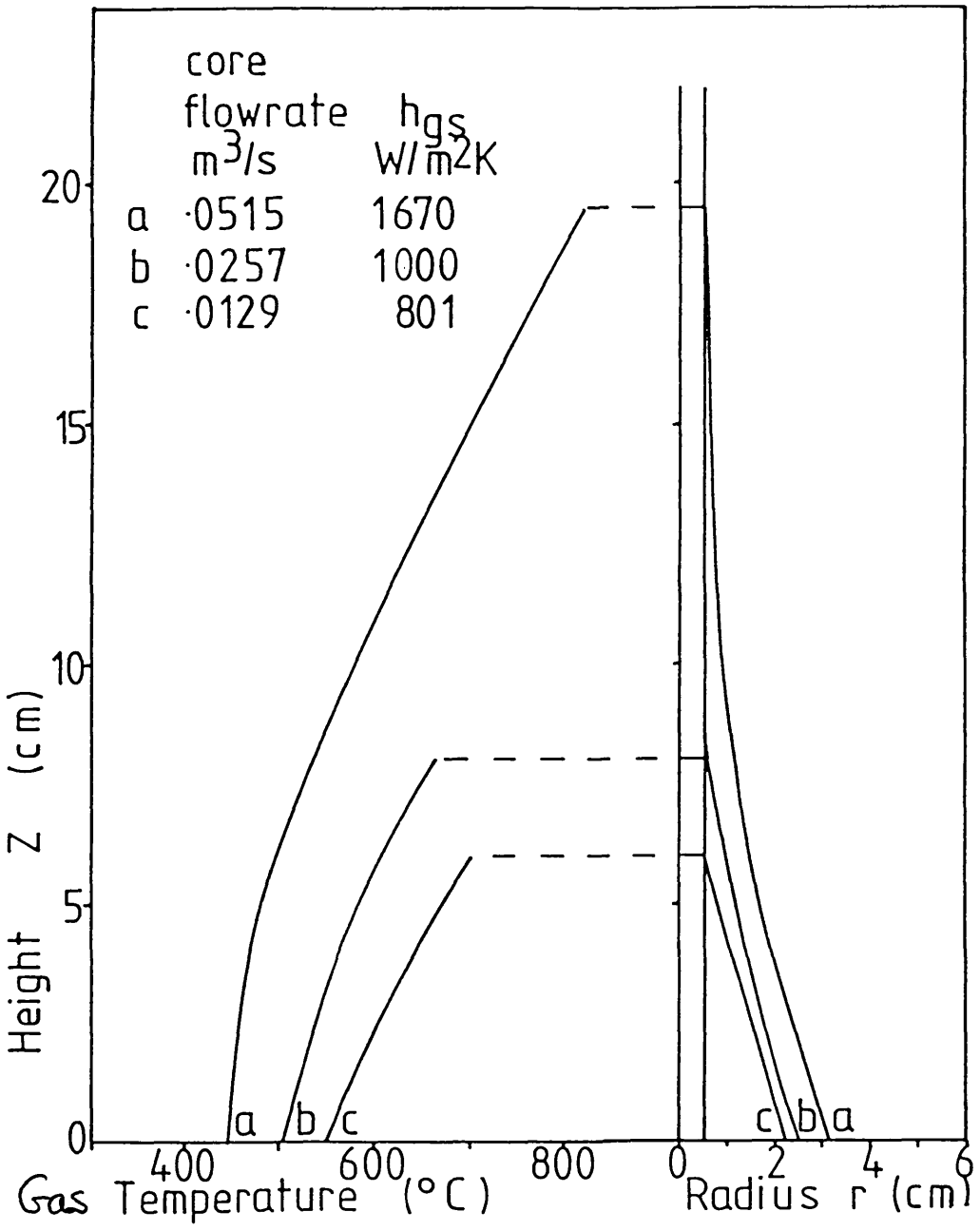

Fig.5.7 Effect of changing core gas flowrate.

Q_{sh} = 0.013 m^3/s ΔT_s = 500°C

interesting result of the calculations plotted in Figure 5.7 is that the gas temperature on escape from the accretion is very far below the melt temperature. This point is discussed in detail in Section 5.8.4.

The only case where true superheat can be used with any degree of realism is in the case where argon only is injected mainly through the shroud in the reduction step.

Figure 5.8 indicates the effect of melt superheat (ΔT_s) on accretion height, base radius and gas temperature at a total flowrate of $Q = 0.015\ m^3/s$, typical of the reduction step. The calculations imply that accretions will exist at very high superheats. It may again be noted that the gas temperatures at the tuyere tip are low at high superheats.

Figure 5.9 shows the variation of the accretion shape with the thermal conductivity of the refractory. The bottom radius increases with increase in thermal conductivity of the refractory due to the effect of greater heat removal through the refractory zone. The accretion height does not change. Thus under the conditions chosen heat transfer in the refractory zone does not influence accretion height.

Effect of gas/accretion heat transfer coefficient

If the number and size of channels was greater than estimated then the effective heat transfer coefficient might be different to that used earlier. It is therefore of interest to consider h_{gs} as a parameter in the model.

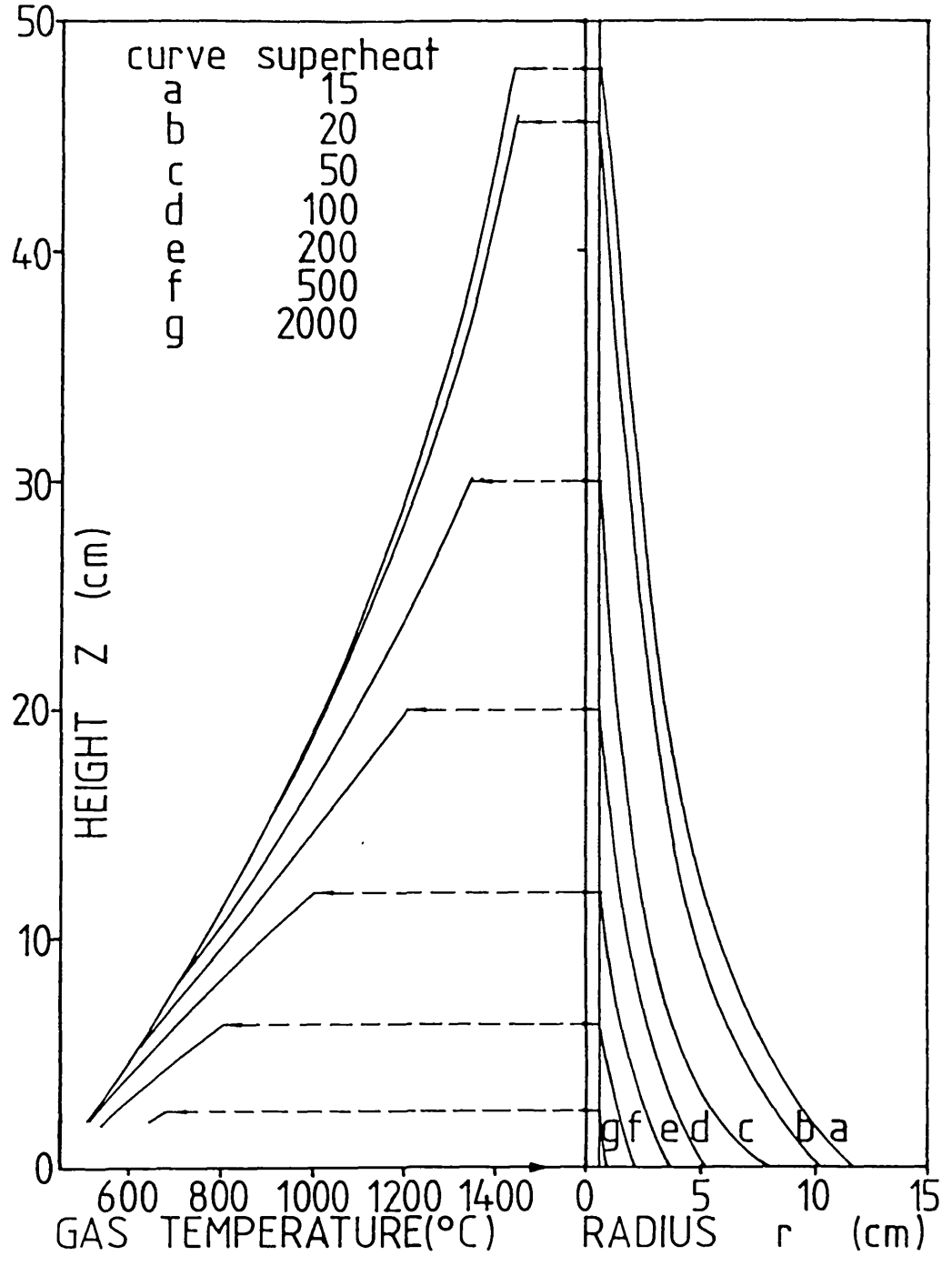

Fig.5.8 Variation of accretion shape and gas exit temperature with melt superheat (Q_{core} = Ø.ØØ2, Q_{sh} = Ø.Ø13 m^3/s).

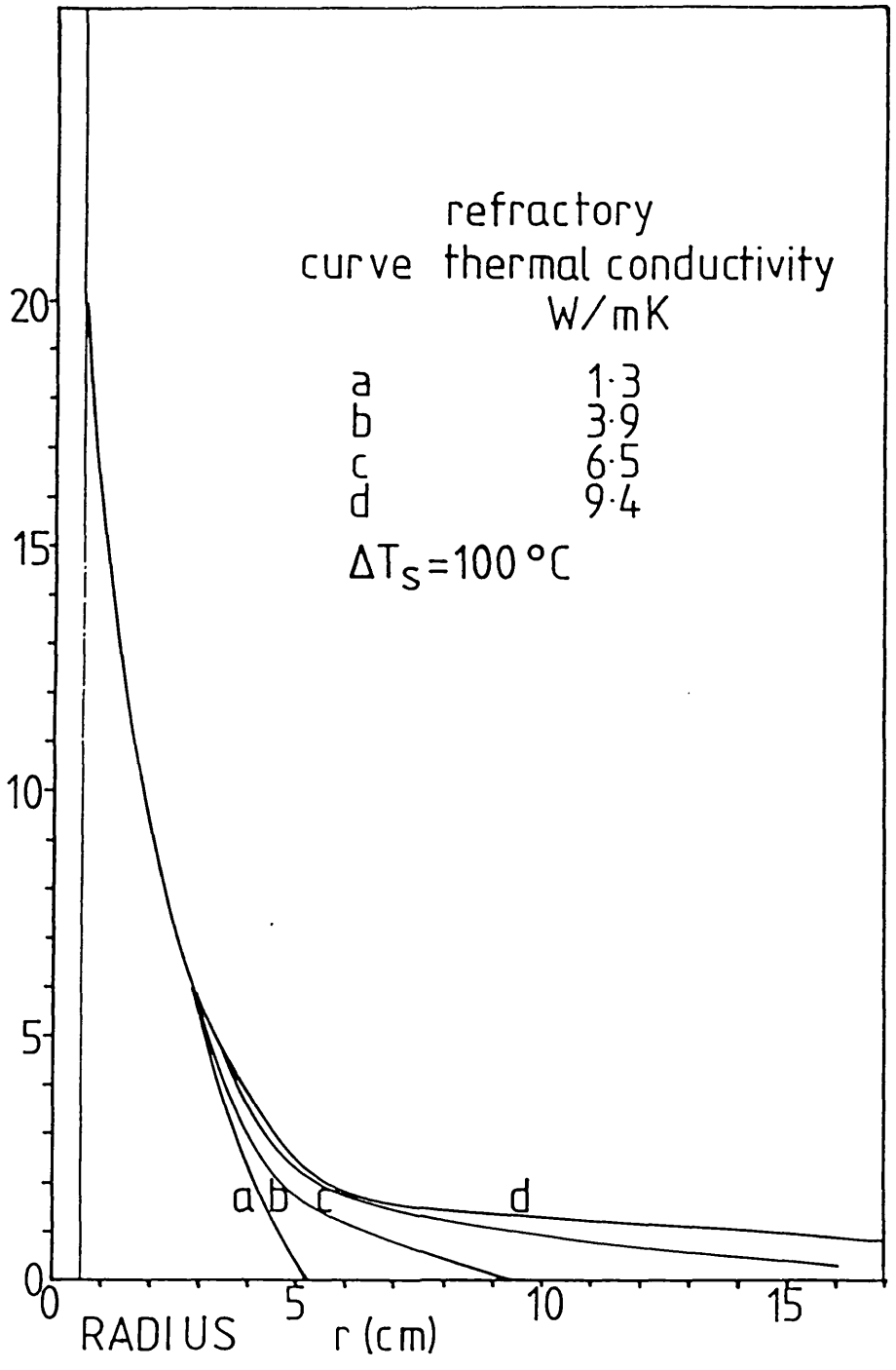

Fig.5.9 Variation of accretion shape with thermal conductivity of refractory (Q_{core} = 0.002, Q_{sh} = 0.013 m^3/s).

The effect of changing h_{gs} for the case of the reduction step is shown in Figure 5.10. The accretion height has a maximum value at h_{gs} of about 2000 W/m^2K. The gradient of the accretion height curve for lower h_{gs} values is quite steep. For h_{gs} values lower than about 100 W/m^2K no accretion is stable. For h_{gs} values above 1000 W/m^2K the accretion height changed only gadually. These results are discussed in Section 5.8.4.

For the case of a reactive gas, with a high effective superheat the calculated accretion height increased steadily with an increase in h_{gs}. The data are plotted in Figure 5.11.

Effect of accretion thermal conductivity

In the calculations presented earlier the thermal conductivity of solid steel was used for the accretion. The thermal conductivity of the accretion may be decreased by porosity and the presence of oxides. The accretion size calculated decreased with decrease in thermal conductivity (Figure 5.12).

Methane as a shroud gas

Calculations were performed wherein the inert shroud gas properties were those of methane. For the calculation, it was assumed that no gas cracking or other chemical reactions occurred. Figure 5.13 shows that methane is more effective in tuyere cooling by forming a slightly larger accretion

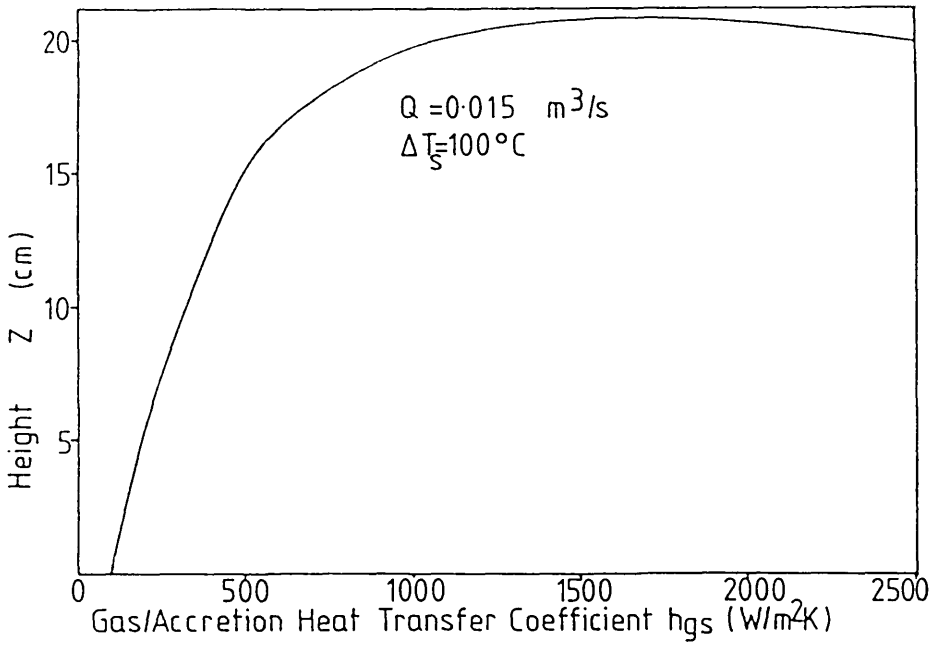

Fig.5.10 Effect of accretion/gas heat transfer coefficient variation on accretion height. Reduction step.

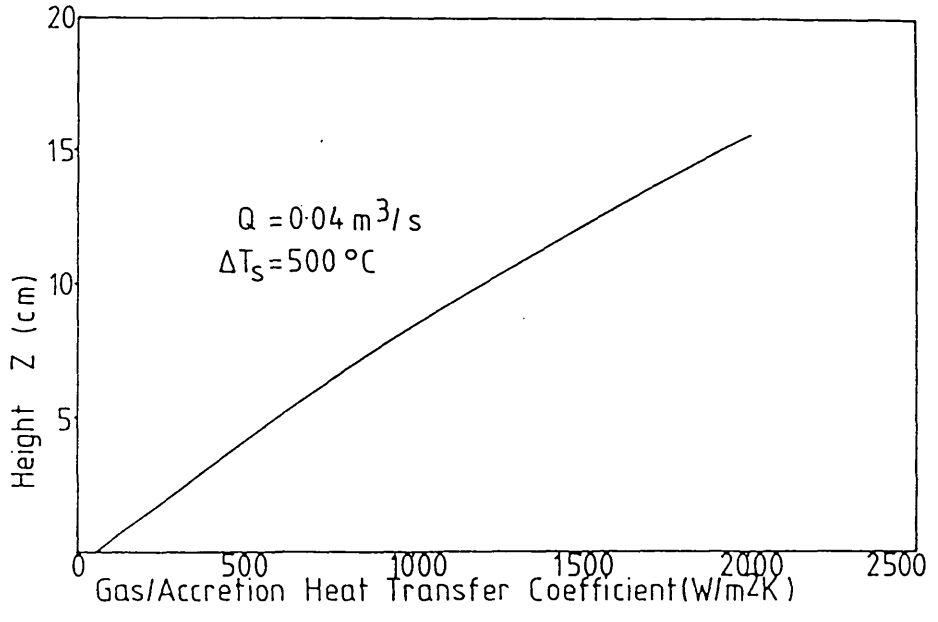

Fig.5.11 Effect of accretion/gas heat transfer coefficient variation on accretion height. Reactive gas.

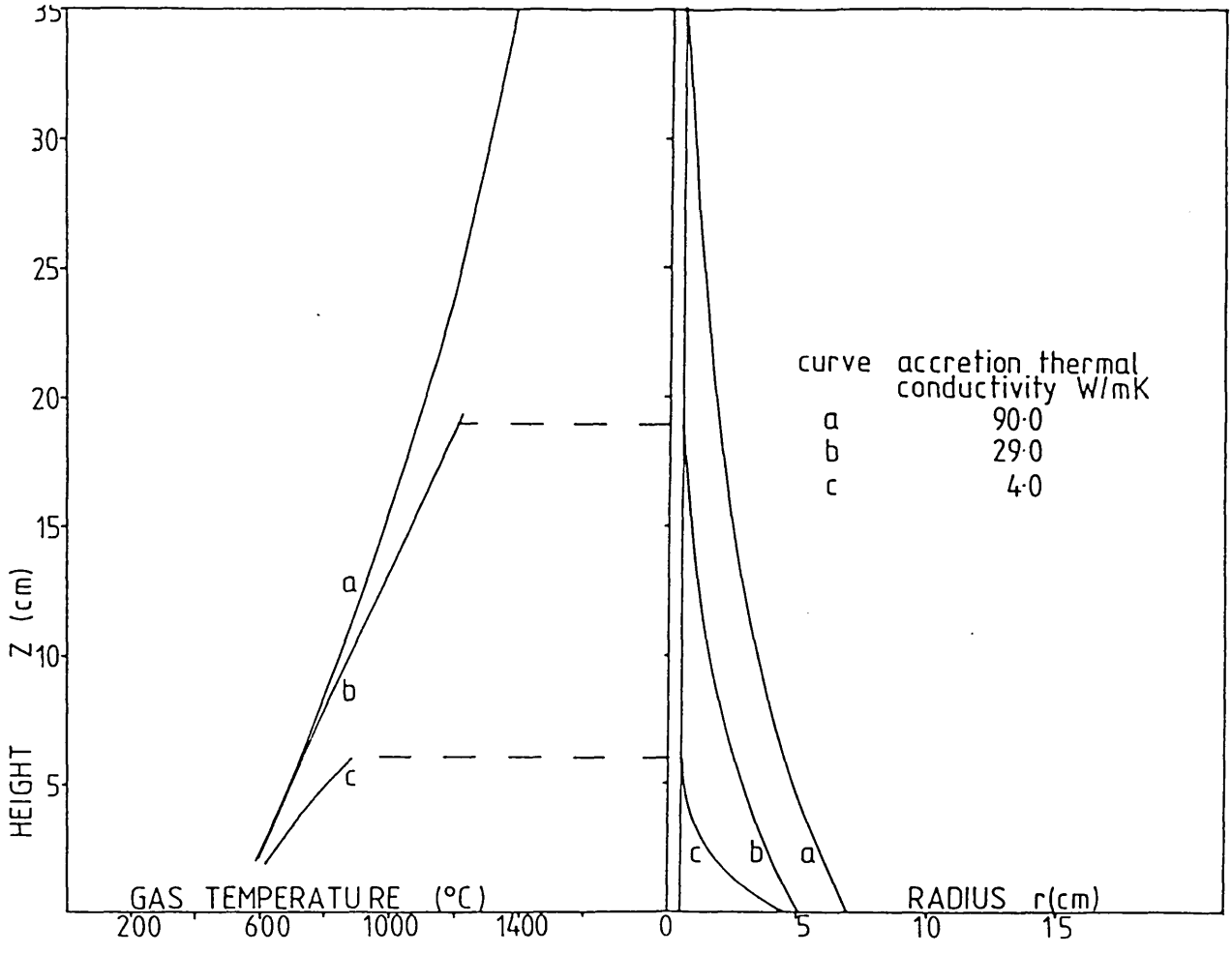

Fig.5.12 Variation of accretion shape and gas temperature with thermal conductivity of accretion.

than argon, due to the greater specific heat of this gas. The calculations were for an accretion of low k_{acc}.

Single tube tuyere configuration

Calculations were carried out wherein the annular tuyere was replaced by a single tube tuyere, of diameter equal to the ID of the shroud tube. Figure 5.14 shows that for the same total argon gas flowrate larger accretions are predicted even when the effective superheat is as high as 500°C. This was a surprising result. The gas in the annular tuyere removed more heat from the refractory therefore the gas entering the accretion was hotter than for the single tube tuyere. The hot gas could only remove a smaller amount of heat from the accretion before reaching its maximum temperature. The explanation of the occurrence of a maximum temperature of the outlet gas is given in Section 5.8.4.

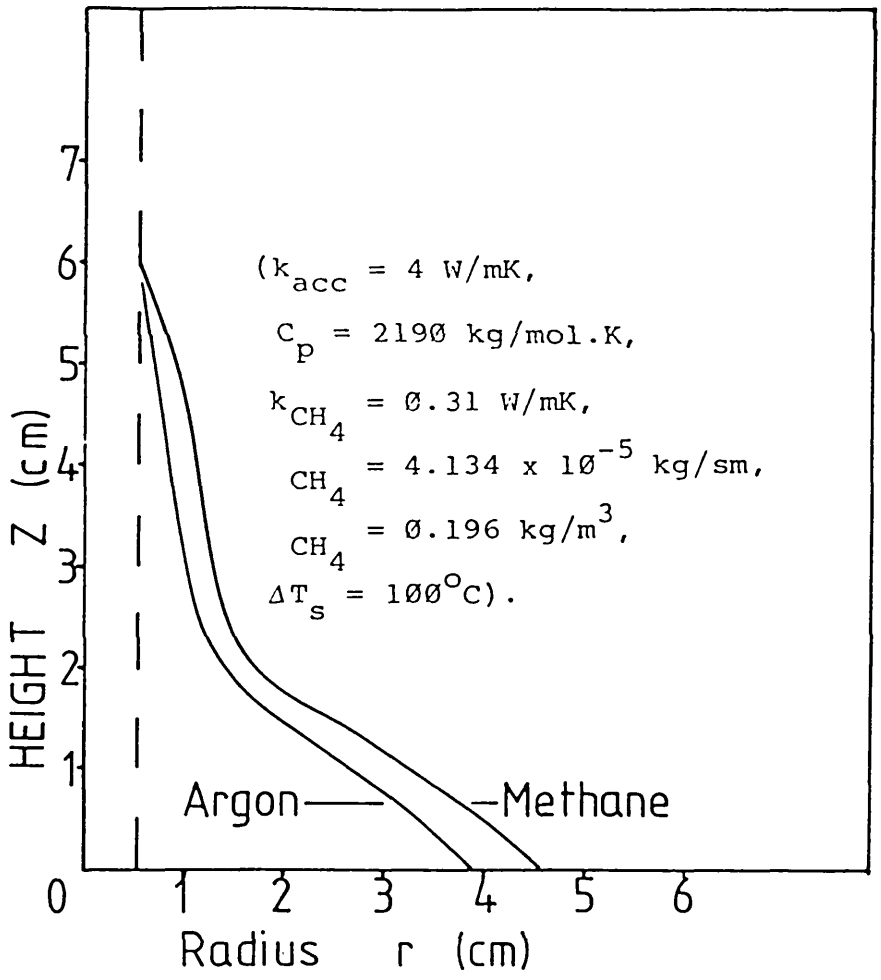

Fig.5.13 Variation of accretion shape with shroud gas properties

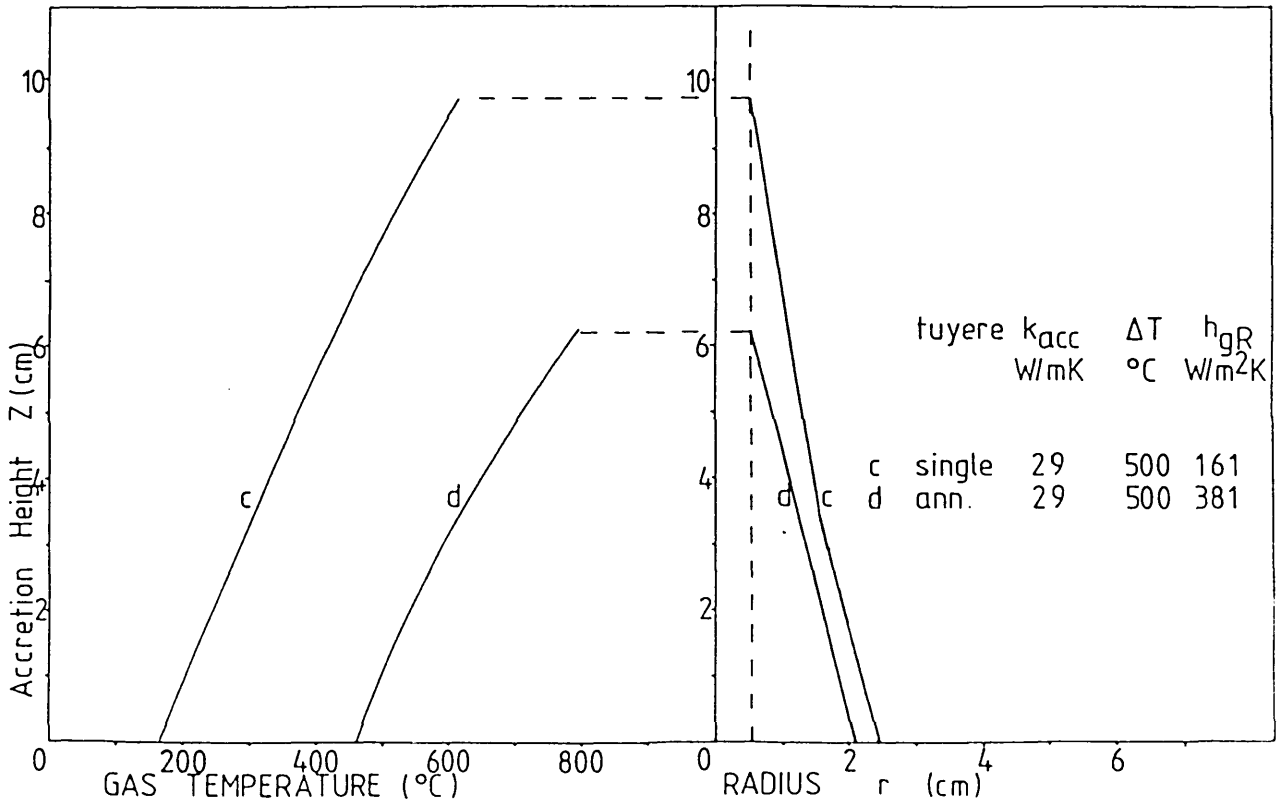

Fig.5.14 The effect of a single tube tuyere.

5.8 DISCUSSION

One of the main reasons for further developing the computer model of Ohguchi[29] was to include the annular tuyere with shroud gas flow. The calculations showed that cooling in the refractory had a relatively small effect on the accretion size and shape (Figure 5.9). The strong influence of the shroud flow observed in practice was not seen in the calculated results (Figure 5.14). This must mean that the phenomena associated with accretion growth at annular tuyeres were not being properly modelled. However since one of the main purposes of modelling is as a quantitative check on the way in which a process or device is assumed to operate the relative failure of the model served a useful purpose in forcing a reassessment of ideas about accretion formation.

5.8.1 Accretion Growth Model

In general the calculated accretion sizes were too large compared with actual observed accretions[11,28,59] at the same nominal superheat. No appreciable difference in accretion size could be obtained by decreasing the annular gap, although this is known to be an important factor in increasing tuyere cooling capability[50,59]. Indeed calculations on single tube tuyeres resulted in wider accretions being produced.

The inadequacy of the model in predicting realistic accretion shapes has led to further calculations representing accretion growth under extreme conditions.

The model predicts accretions to be present even at very high superheats (1000°C), and size is sensitive to the value chosen for accretion thermal conductivity. The lack of agreement between the known behaviour of accretions on shrouded tuyeres and the model results must be due to the fact that the assumptions used are incorrect.

5.8.2 Heat transfer in gas channel

The simplified heat transfer region shown in Figure 5.1 is not always accurate in representing accretion shape or the nature of its contact with the tuyere tubes. An actual accretion on the end of a tuyere is shown in Figure 4.16d and

schematically in Figure 5.15[28]. The accretion is not pipe-like consisting of solid steel, but closed off and porous. The cooling shroud gas escapes mainly through the pores and is alone responsible for freezing the accretion. At the top of the accretion the core gas has been able to burn out a pipe-like conduit resulting from exothermic oxidation reactions with little or no local shroud cooling. The heat generated close to the accretion can lead to substantial melting back. Radiation from a reacting surface may occur to the copper core tube through the conduit.

5.8.3 Growth mechanism

The bubble forming at the accretion tip is able to displace the liquid around the accretion Figure 5.16(b), so that at some stage the accretion may be completely surrounded by gas, Figure 5.16(c).

Accretions sometimes have a "layered" structure[11,28]. It is possible that accretions grow throughout the refining period, each layer forming as metal "washes" over the accretion between bubbles, Figure 5.16(d). This process may continue until the melting rate equals the freezing rate. In the calculations it was assumed that the accretion was continuously in contact only with bulk liquid.

5.8.4 Gas temperature

Figure 5. 17 compares the effects of melt superheat (ΔT_s),

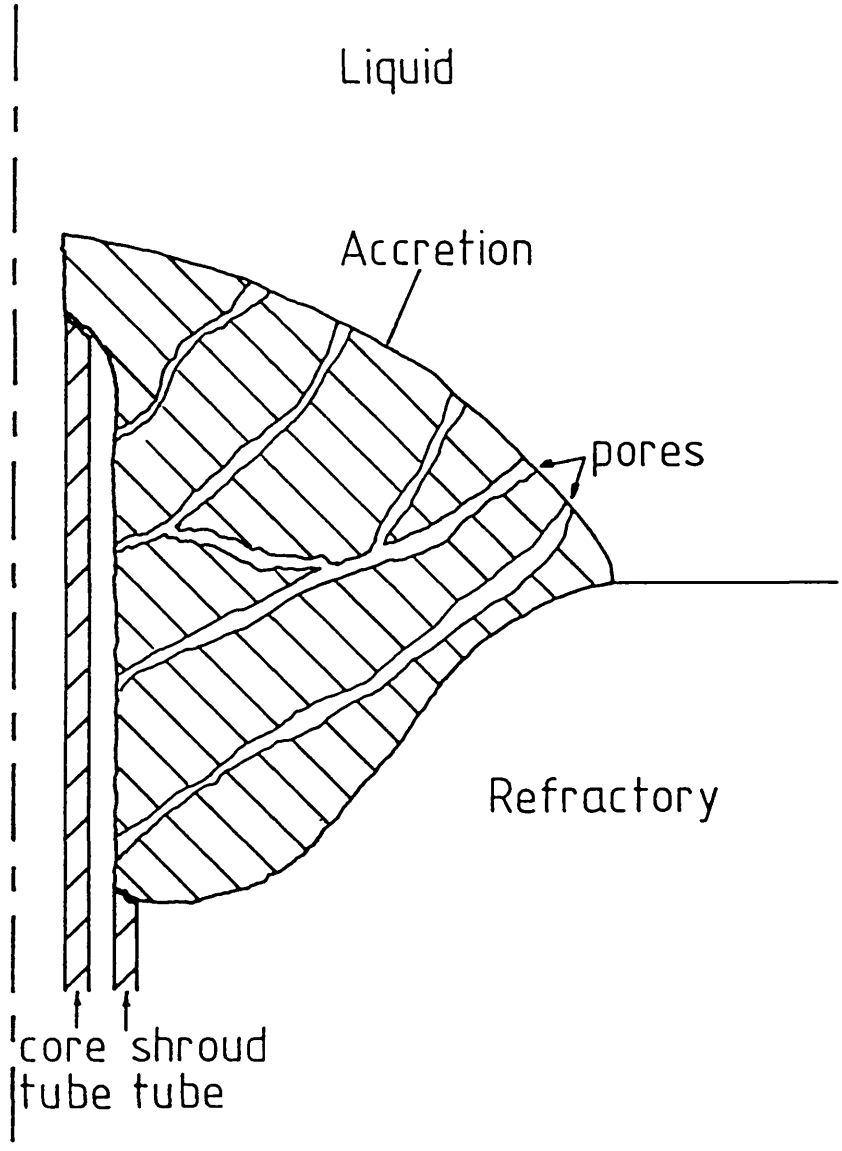

Fig.5.15 Schematic of accretion structure, after Nakamura et al.[28]

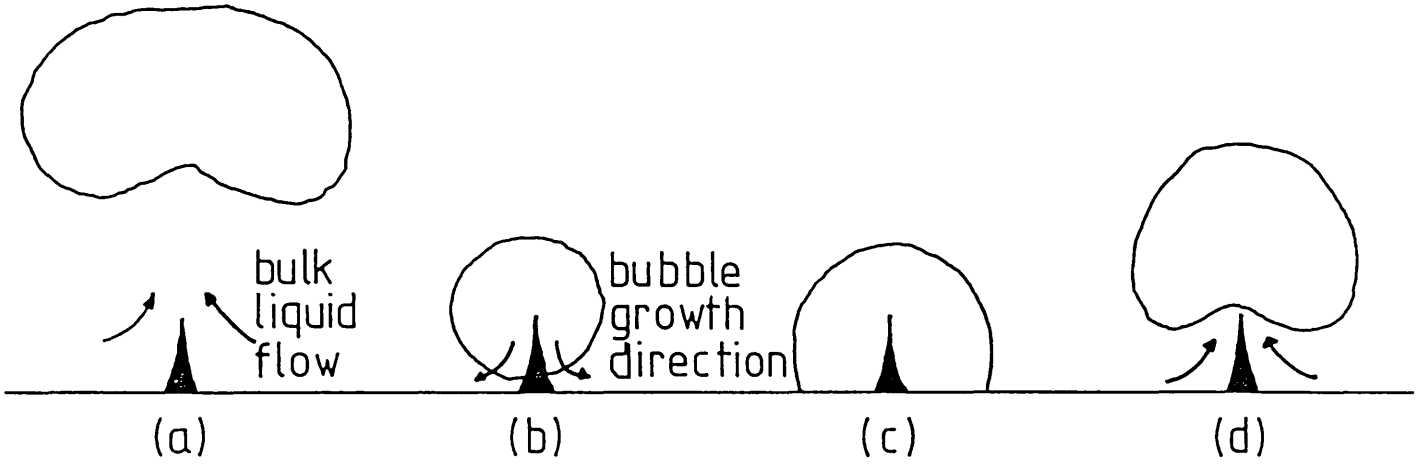

Fig.5.16 Schematic of bubble growth around a tuyere.

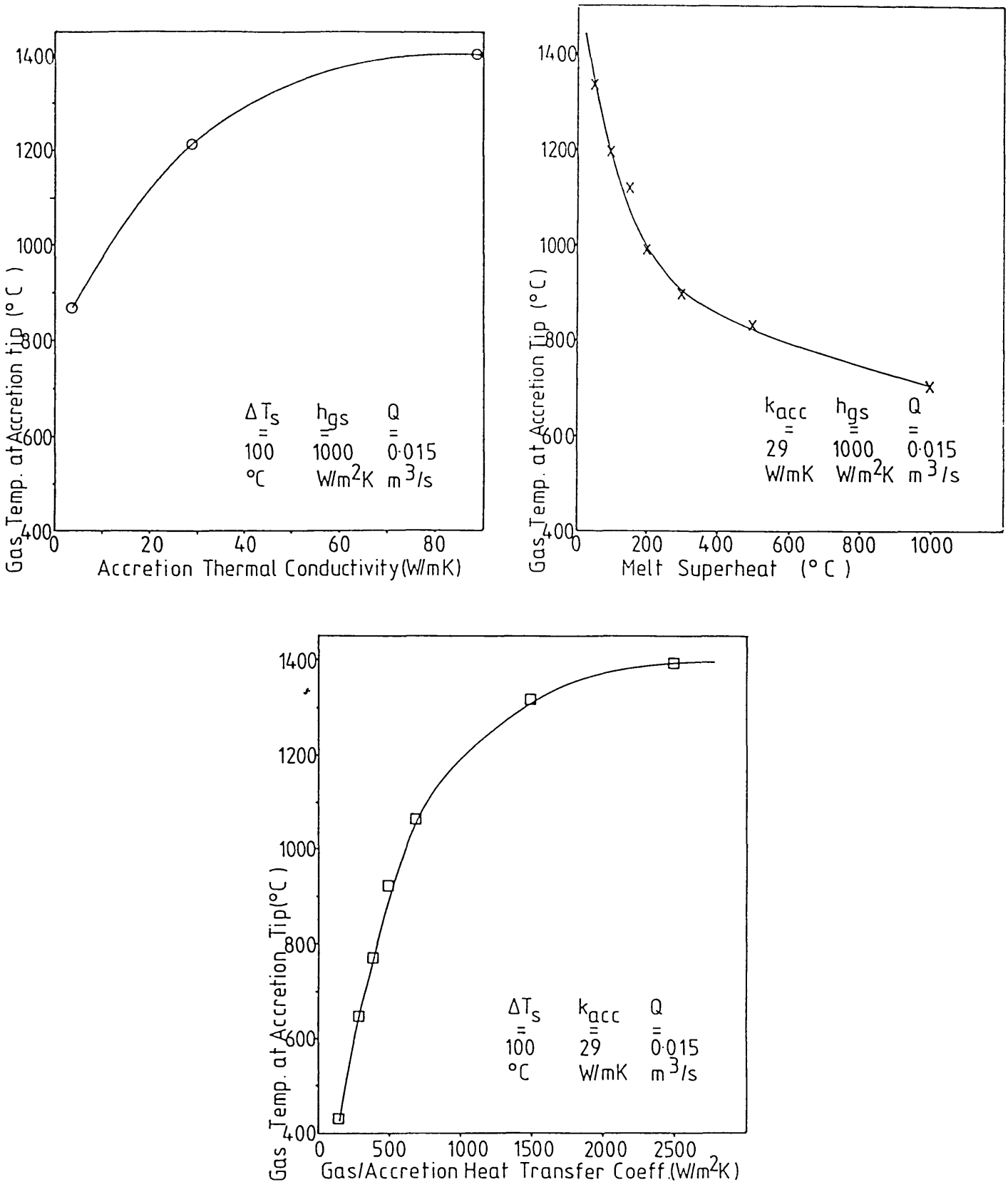

Fig.5.17 Effect of melt superheat, gas/accretion heat transfer coefficient and accretion thermal conductivity on gas exit temperature.

$$h_l \Delta T_s > (T_m - T_g) h_{gs} \qquad (5.27)$$

Equation 5.27 requires that for a constant ratio of liquid/gas heat transfer coefficients a rise in melt superheat causes the gas exit temperature to decrease. This leads to a twofold effect on decreasing accretion size. Firstly, the accretion melts back as a result of convective heat transfer from increased melt superheat. Secondly, the amount of heat removed by the gas is limited by the maximum temperature it is able to attain for a given superheat.

Accretion height was shown to be dependent on the value of gas/solid heat transfer coefficient. The h_{gs} values used in the calculations were three times greater than those required for single tubes to account for enhanced heat removal by the gas in a porous accretion. The shape of the curve in Figure 5.10 may be interpreted by rewriting Equation 5.27 as

$$T_g = T_m - (h_l \Delta T_s / h_{gs}) \qquad (5.28)$$

Assuming values of h_l and ΔT_s to be fixed, an increase of h_{gs} will lead to an increase of gas temperature at the accretion exit, resulting in a larger accretion.

In Figure 5.10 accretion height reaches a maximum value at a particular h_{gs} for the reduction step case

gas/accretion heat transfer coefficient (h_{gs}) and accretion thermal conductivity (k_{acc}) on the outlet gas temperature. The gas temperature increases with decreasing ΔT_s or increase in either k_{acc} or h_{gs}.

If, at a position close to the tuyere tip, it is assumed that the accretion surface is plane and heat flows to the gas uni-directionally perpendicular to the axis through an accretion of thickness τ, Figure 5.18, a heat balance can be taken at the accretion surface as

Heat convected to accretion surface = Heat conducted through accretion

$$h_l \Delta T_s = k_{acc}(T_m - T)/\tau \qquad (5.24)$$

and at the gas/accretion interface as

Heat convected to accretion surface = Heat removed by gas

$$h_l \Delta T_s = h_{gs}(T - T_g) \qquad (5.25)$$

Eliminating T in Equations (5.24) and (5.25) yields

$$\tau = (k_{acc}/h_l)((T_m - T_g)/\Delta T_s - (h_l/h_{gs})) \qquad (5.26)$$

Thus an increase in accretion thermal conductivity will result in a wider accretion (Figure 5.12). The accretion will disappear ($\tau = 0$) for the condition

when the gas exit temperature equals T_m. Below this h_{gs} value the gas emerges below T_m and accretions decrease in size - a large reduction in height occurring for a small decrease in h_{gs}. If a tuyere were to be operated from a gas supply regulated at constant pressure (see Chapter 3), marked variations in gas flowrate can occur due to intermittent partial blockage by accretions. This leads to cyclic variation of h_{gs} values, which in turn can ultimately result in the accretion growing and melting back at a similar frequency. If the pressure drop across the accretion momentarily increased (due to growth and/or partial blockage) then the gas flowrate and therefore h_{gs} would decrease. The accretion would then melt back and unblock until the gas flowrate increased sufficiently for h_{gs} to rise to a value appropriate for resumption of growth.

For the case of a higher gas flowrate and superheat the gradient of the height versus h_{gs} curve in Figure 5.11 is less steep and never reaches a maximum. Equation 5.38 implies that the gas exit temperature is therefore always less than T_m under the range of h_{gs} values considered. This results in smaller accretions, which is indeed the case and is shown in Figure 5.7.

It was surprising to note that the model generated larger accretions for single tube tuyeres. Annular tuyeres were more effective in removing heat from the refractory without producing larger accretions. In the model the temperature of the gas flowing into the accretion is therefore lower for a

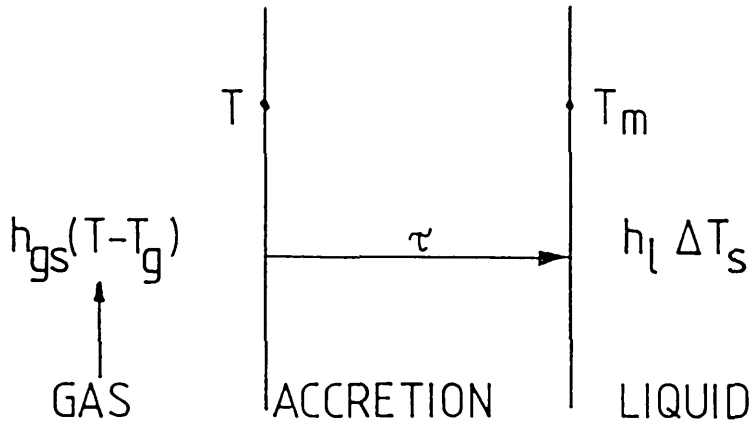

Fig.5.18 Simplified gas/accretion/molten metal heat transfer region.

single tube, resulting in a larger driving force for heat transfer from the accretion to the gas. Actual accretions are porous and little is known about the cooling effect of the gas in the pores.

5.8.5 Reactive Gas

Another important aspect not included in the calculations is the heat transfer between the accretion and the envelope of a reacting gas bubble. If a sufficient quantity of heat is radiated to the accretion at T_m the mean heat flux may be sufficiently high to reduce its size to below the value it would have if only in contact with liquid metal. The increased mean heat flux to the accretion can be represented in the calculations by including a higher effective superheat, ΔT_{seff}.

A reactive gas, such as oxygen, injected into liquid steel will start to react at the gas/liquid interface as soon as the bubble emerges into the liquid metal bath and heat of reaction will be evolved at the gas/liquid interface. Denier et al.[50] have measured ignition zone temperatures through a tuyere in a basic oxygen furnace using optical pyrometry at IRSID to be as high as 2245°C. This could be responsible for profound changes on accretion shapes, if present, due to radiation. Similar temperatures have been observed in the hot spot of LD converters, immediately under the oxygen jet(s).

Oxygen transport and heat transfer across gas/liquid interface

In this section the amount of oxygen transported across the gas/liquid interface and the resulting heat evolution rate are estimated for a growing bubble.

Oxygen transport

Figure 5.19 depicts the transient growth of an isolated gas bubble in molten iron at a bulk temperature of 1550^{o}C.

Assumptions

1) The growing bubble is spherical in shape and initially its diameter is equal to the orifice diameter.

2) The bubble detaches when its centre has moved up a distance equal to its radius after time t_d (= 0.1 sec).

3) The system remains at constant pressure.

4) Gas flowrate through the orifice remains constant.

5) Constant gas composition entering the bubble.

6) Rate of gas reaction is controlled by mass transfer in the gas phase.

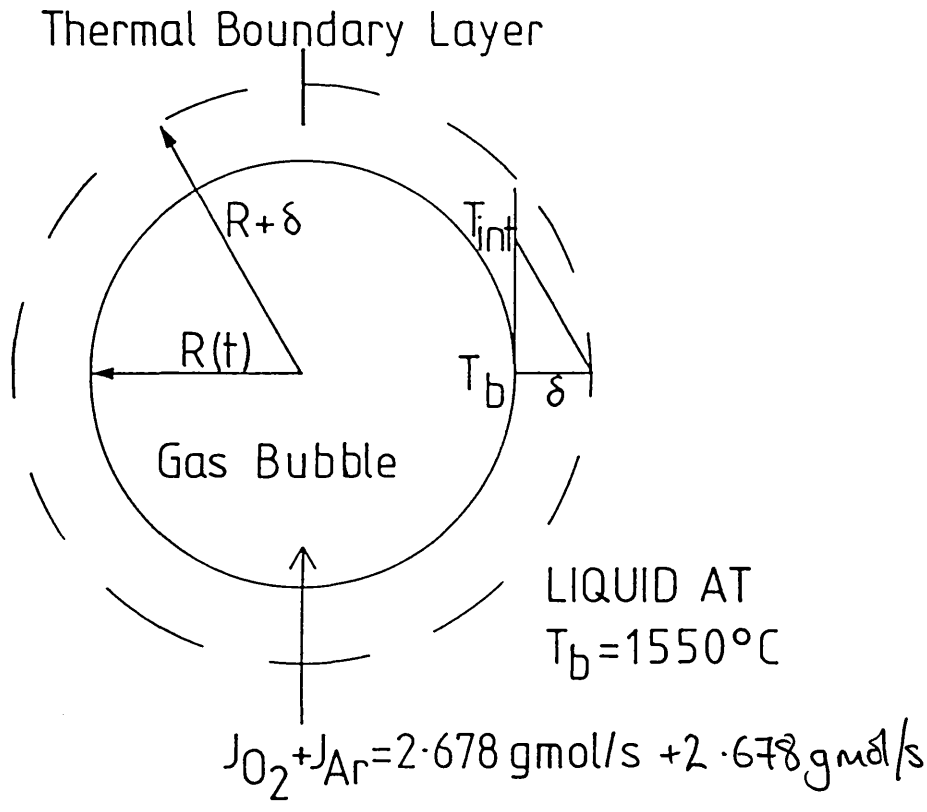

Fig.5.19 Transient growth of a gas bubble in molten iron.

7) Gas emerges into liquid steel at 1550°C.

The continuity equation is

Rate of change of total moles in bubble = Rate of gas mixture injection - Rate of reaction at gas/liquid interface

$$d/dt(V_b C_T) = J_{O_2} + J_{Ar} - k_g A C_T x_b \qquad (5.29)$$

For a spherical bubble Equation 5.29 can be written as

$$dR/dt = (J_{O_2} + J_{Ar})/(C_T 4\pi R^2) - k_g x_b \qquad (5.30)$$

A balance on the reactive component gives

Rate of accumulation of O_2 =
Rate of injection of O_2 - Rate of reaction of O_2

$$d/dt(V_b C_T x_b) = J_{O_2} - k_g A C_T x_b \qquad (5.31)$$

Substitution of Equation 5.30 into Equation 5.31 for dR/dt gives

$$dx_b/dt = 3J_{O_2}/4\pi R^3 C_T - 3k_g x_b/R +$$

$$3x_b(k_g x_b - (J_{O_2} + J_{Ar})/(C_T 4\pi R^2))/R \qquad (5.32)$$

Heat evolution at gas/liquid interface

Many investigations have been carried out in which pure oxygen has been suddenly contacted with liquid iron and iron alloys[60]. Results have shown that an oxide layer is formed immediately and that this layer is initially FeO.

Assuming that the reaction at the gas/liquid interface is indeed that of iron oxidation,

$$2Fe + O_2 = 2FeO$$

and that the heat of this reaction is $\Delta H_{1823} = 496$ kJ/mole[39] and the rate of oxygen transfer in the gas phase is rate controlling, then the heat flux density at any time during bubble growth is $k_g C_T x_b(t) \Delta H$ W/m^{2}s. A heat balance at the gas/liquid interface is

Heat generated by chemical reaction = Heat conducted into liquid steel + Heat radiated to accretion

$$k_g A_b x_b \Delta H C_T = A_b k_s (T_{int} - T_b)/\delta$$

$$+F \epsilon \sigma A_{acc} (T_{int}^4 - T_m^4) \qquad (5.33)$$

Assuming that the accretion is small compared to the bubble and is surrounded by it, Figure 5.16(c), the value of the radiation term in Equation 5.33 has been verified a posteriori to be less than 1% of the chemical heat generation term, even for large effective superheats, and can therefore be ignored.

Considering the heat flow into a thermal boundary layer of thickness δ to be uni-directional and normal to the bubble surface, a heat balance, ignoring heat radiated to the accretion, and assuming a linear temperature profile over a time interval dt, yields

Heat accumulated in thermal boundary layer = Chemical heat generation at gas/liquid interface

$$4\pi\rho C_p d/dt(R^2 \delta \Delta T/2) = 4\pi R^2(\dot{q}''_{ref} x_b) \qquad (5.34)$$

where $\dot{q}''_{ref} = \Delta H k_g C_T$

A balance on the chemical heat conducted into the thermal boundary layer gives

$$k(T_{int}-T_b)/\delta = k\Delta T/\delta = \dot{q}''_{ref} x_b \qquad (5.35)$$

Substituting for ΔT from Equation 5.35 into 5.34 and differentiating with respect to time and substituting the result into Equation 5.34 gives the following expression for the change in boundary layer thickness with time:-

$$d\delta/dt = (\alpha/\delta) - (\delta . dR/dt) - (\delta/2x_b)(dx_b/dt) \qquad (5.36)$$

where $\alpha = k/\rho C_p$

The temperature rise of the gas/liquid interface is evaluated by including the updated value of δ into the

implicit Equation 5.35.

Computed Results

Equations 5.31, 5.32, 5.34, and 5.36 have been solved simultaneously as an initial value problem by using Merson's form of the RUNGE - KUTTA method, to get bubble size, change of reactive gas concentration, thermal boundary layer width and interfacial temperature respectively for the period of bubble growth. The initial boundary conditions were

at $t = 0$, R = nozzle radius, $x_b = x_{bo}$,

$T_{int} = T_b$, $\delta = (\alpha 2\Delta t)^{1/2}$ for the first time step

The time intervals for the transient computation are initially very small(0.001 s) to ensure that the dR values are small enough when the growth rate is very large. However, after 0.01 s of bubble growth the time interval was increased to 0.01 s

At high gas flowrates, gas enters the growing bubble and circulates at high velocities, thus causing a high degree of turbulence. Values of mass transfer coefficients were taken as k_g = 100 and 300 cm/s. The former value is large compared to those normally reported and was used in the work of Nilmani[9]. The latter value represents an extreme case, although a value of k_g = 300 cm/s was obtained in the work on decarburisation kinetics by Sain and Belton[61]. They obtained their results by impinging a high velocity gas jet

onto a molten iron surface.

Figure 5.20 depicts R and x_b variation with time. For k_g = 300 cm/s the bubble radius is smaller because more oxygen will have reacted after a given time. As the bubble grows, oxygen reacts very fast for the higher k_g. The two curves in Figure 5.20 show appreciable differences in the final oxygen content at the time of bubble detachment, more oxygen having reacted in the k_g = 300 cm/s case. Good agreement is obtained with the results of Nilmani[9].

The temperature of the gas/liquid interface and thickness of the thermal boundary layer during bubble growth are shown in Figure 5.21. The interfacial temperature is higher at all times for k_g = 300cm/s and rises by 97°C at detachment because more oxygen has reacted than for the case of k_g = 100 cm/s when the interfacial temperature has risen by 54°C at detachment.

The effective superheat ΔT_{seff} is evaluated from the implicit expression

$$F \epsilon \sigma A_b (T_{int}^4 - T_m^4) = h_l A_{acc} \Delta T_{seff} \qquad (5.37)$$

and is plotted for bubble growth under conditions of k_g=100 cm/s and k_g = 300 cm/s in Figure 5.22. In the calculations the accretion size is assumed to be fixed and conical(15 cm high and 5 cm base radius) and the emissivity of the bubble surface has been assumed equal to 0.4. The effective

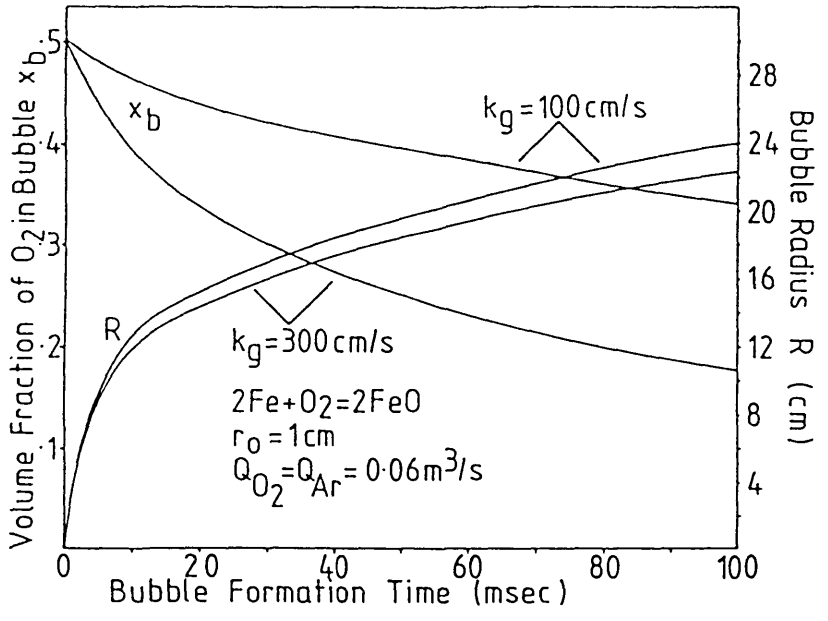

Fig.5.21 Variation in bubble radius and oxygen volume fraction during growth.

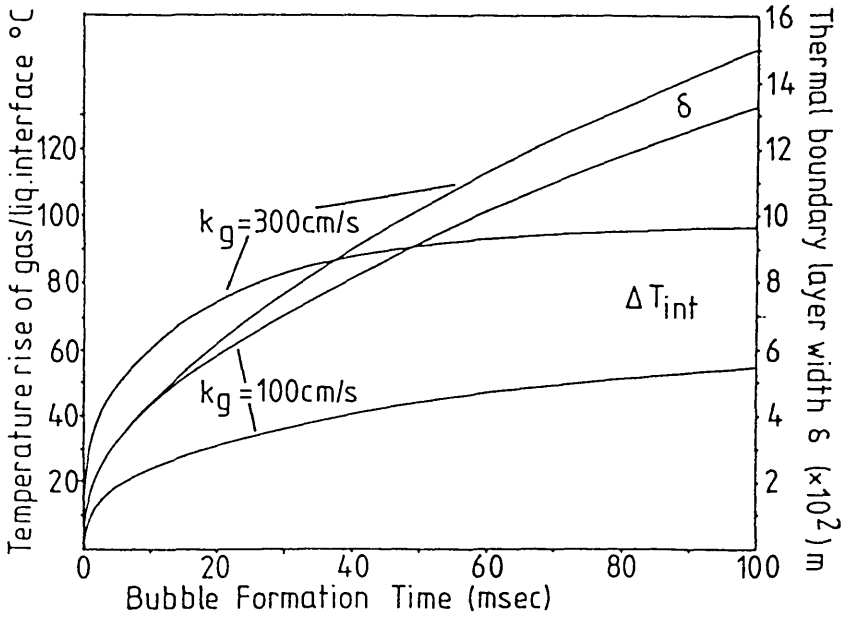

Fig.5.22 Gas/liquid interfacial temperature and thickness of thermal boundary layer thickness during bubble growth.

In Figure 5.22 the effective superheats are too high because FA_b in Equation 5.37 was made equal to A_b and increased with time.

Using a radiation network for two gray surfaces shows that the correct formula for the rate of radiation heat transfer (Q_{rad}) to the accretion is

$$Q_{rad} = (\epsilon_b A_{acc} / (\epsilon_b \quad (I-\epsilon_{acc})(\epsilon_b/\epsilon_{acc}) \quad (I-\epsilon_b)A_{acc}/A_b)) * (T_{int}^4 - T_m^4)$$

If ϵ_b and ϵ_{acc} were both 0.5 and $A_{acc} \ll A_b$ then the formula gives

$$Q_{rad} = (A_{acc}/2) \quad (T_{int}^4 - T_m^4)$$

Thus Q_{rad} should have been assumed constant.

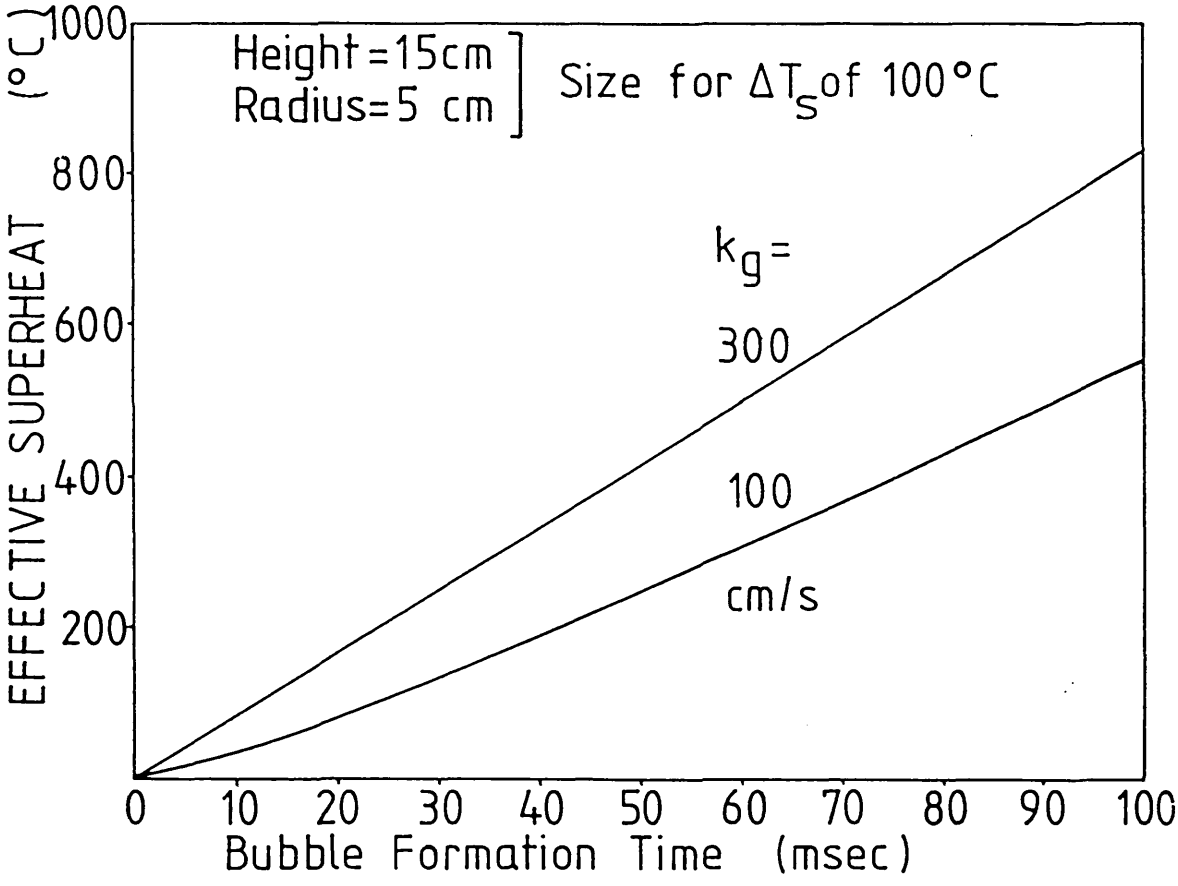

Fig.5.2 2 Effective superheat of gas/liquid interface radiating to accretion.

superheats rise almost linearly with time and at detachment are calculated to be as high as 820 and 550 ^{o}C for k_g = 300 cm/s and k_g = 100 cm/s respectively. During early stages of bubble growth when accretion size is large compared to the bubble a relatively large fraction of the chemical heat may be radiated to the accretion, lowering the calculated gas/liquid interfacial temperature. As the bubble grows this effect diminishes.

In general the calculated bubble surface temperature rise is lower than observed by Denier et al.[50]. However, good agreement is found between the effective superheats calculated during bubble growth and Denier's results, and certainly including superheat values of about 800^{o}C in the accretion formation calculations is not unreasonable.

The shortcomings of the above analysis are fairly obvious. The bubbles are not likely to be spherical but elliptical[15]. At high injection velocities bubbles tend to coalesce and form jets (see Chapter 2), thus altering bubble detachment time t_d. The injected gas will contain a fine dispersion of liquid metal droplets, thus increasing the surface available for reaction. Realistic values of mass transfer coefficient are required for energetic reactive gas injection before the above analysis can be carried out in a worthwhile fashion.

5.9 Tuyere failure mechanisms

The optimum accretion length is believed by the industry to be 20-50 mm (see Chapter 3)[31]. Anything smaller results in the point of maximum heat generation (oxygen input point) moving closer to the tuyere and brick, increasing the temperature of the tuyere. If the temperature of the tuyere tip exceeds the ignition temperature of either tube, it may burn back with disasterous effects on the surrounding refractory.

Another wear mechanism has been observed[51] even in the presence of an accretion. During accretion growth the temperature distribution in the refractory changes significantly due to the cooling caused by the gas flow. This must lead to considerable thermal stress in the refractory around the tuyere and may cause it to spall. Unprotected parts of the tuyere could be left protruding into the melt.

Moore and Wraith[41] have calculated the thermal gradients near the top of the refractory around the tuyere as the liquid washes across its surface. They found that the temperature changes rapidly with time and spalling in some refractories is very sensitive to this factor.

In tuyere manufacture some degree of eccentricity must usually be tolerated in the annulus. Analyses of eccentric annulus flows by Kays and Leung[62] have shown that eccentricity lowers the mean Nusselt number and introduces Nusselt number variation around the tuyere periphery. This

may lead to 'hot-spots' forming around and along the tuyere.

A further phenomenon leading to tuyere failure may be attributed to penetration of the melt into the tuyere during gas injection. This flooding or wetting has been investigated by Engh[63], Davis[25], You[46] and Messina[64] in single tube nozzles and by Collins in annular tuyeres[47], and has been seen to result in the melt freezing in or destroying the tuyere tubes. Liquid droplets in contact with oxygen in the core could oxidise with exothermic reaction heat being released. This could result in the tuyere tubes burning back if the ignition temperature is attained.

In single tube nozzle investigations Davis and Magny[25] have observed that when bubbles rise, liquid metal moves to fill the space formerly occupied by gas. If this liquid movement has a sufficient component of momentum directed up the nozzle, blocking may occur. From isothermal water model experiments on single tubes Engh et al.[63] postulate that small droplets may freeze before hitting the tuyere wall. Such droplets would not stick to the wall. Larger droplets may be molten when they hit the wall and some may freeze to it while others are blown back into the melt. Engh's model experiments give an indication of the number of droplets that could stick to the wall. Messina[64] has linked experimental observations of water ingress into single transparent tuyeres with minimum nitrogen purge flows required in the Q-BOP process.

Using mercury and molten pig iron over the full range of flowrates from bubbling to continuous jet systems You et al.[46] have confirmed the fact that more penetration of liquid into the nozzle occurs when the gas injection conditions are bubbly as opposed to jetting. As a rough guide their results yield the following relationship for maximum penetration depth (S_{max}) as a function of a modified Froude number for liquid penetration (N_{Fr_p}). In single tube vertically downward or upward nozzles

$$S_{max} = 4 \times 10^{-3} D (N_{Fr_p})^{-1/2} \qquad (5.38)$$

where $N_{Fr_p} = (u_o^2/gd_o)(\rho g/\rho l)^3$

Equation 5.38 is in good agreement with penetration depths measured in cut open industrial tuyeres (see Figure 4.16) and indicates that penetration may never be eliminated however high the gas velocity.

Working in aqueous systems with annular tuyeres Collins[47] has shown that wetting can be completely eliminated by providing adequate gas flow through the annulus. The ratio of shroud to core flow rate required to ensure 'dry' operation falls with decrease in size of annular gap.

The difficulty of combining fluid dynamic information on wetting behaviour of clean tuyeres with heat transfer information on accretion formation has led to some

pilot-scale investigations at BSC[47]. Successful operation of a nitrogen shrouded air tuyere discharging into molten steel depends on maintaining an accretion and in the event of a melt back still maintaining adequate flows to prevent blocking.

5.10 CONCLUSIONS

A model for heat transfer and accretion formation round an annular tuyere has been developed to calculate accretion shapes. The problem of calculating the location of the liquid/solid interface has been solved. The model ignored the effect of porosity in the accretion by assuming that the gas flows through a single pipe-like channel, along the accretion axis, of diameter equal to the ID of the shroud tube, with an enhanced value of the gas/accretion heat transfer coefficient.

The calculations took no account of gas bubbles flowing over the accretion but the effect of heat transfer from a radiating gas bubble interface was allowed for by including a larger effective superheat. The calculated accretion shapes were found to be slender and larger than actual accretions. The model was unsuccessful in demonstrating that larger accretions could be produced using an annular tuyere as opposed to a single one.

A finite difference formulation of the equations for the steady-state has been solved using a relaxation technique.

The results are summarized as follows,

1) Increasing the core gas flowrate causes the accretion to grow.

2) Accretion size increases inversely with the square root of the melt superheat. The gas leaves the accretion tip at lower temperatures for higher superheats.

3) Accretion height reaches a maximum for a particular value of gas/accretion heat transfer coefficient for a low superheat.

4) A decrease in the value of the effective accretion thermal conductivity results in a marked decrease in accretion size.

5) Reducing the shroud gap and/or increasing the shroud gas velocity leads to an insignificant change in accretion size at all values of the effective superheat. Indeed, a single tube tuyere produced a larger accretion.

6) Use of methane as a shroud gas results in the calculation of slightly larger accretions.

7) The calculated temperature increase in the reaction zone during bubble formation is lower than

experimental evidence would suggest. The calculated effective superheat, however, is sufficiently high to reduce accretion size to below the value it would have if only in contact with liquid metal. The actual value of ΔT_{seff} depends on the mass transfer coefficient. Further experimental investigations are required to determine realistic k_g values between reactive gas jets and liquid metals.

CHAPTER 6

SUMMARY AND CONCLUSIONS

CHAPTER 6

SUMMARY AND CONCLUSIONS

Aqueous modelling of the AOD injection process indicates that operation is in the bubbling regime. Large bubbles form close to the tuyere and break up into smaller bubbles on rising up the wall.

In order to minimize refractory erosion around the tuyere it would be better to inject gas at higher F_M/F_B. The effect would be to reduce lateral gas spread at the tuyere exit thus preventing the cyclic "washing" by bubbles over the refractory. The severe tuyere erosion patterns observed in the WSA converter occur when F_M/F_B = Ø.Ø8. Model studies using H_2 at the process flowrate predict that flow at the tuyere is bubbly and that the consequent gas and liquid motion makes a major contribution to the refractory erosion process. In studies concerning classification of gas behaviour injected through a submerged orifice several definitions of what jetting is and the conditions necessary to achieve it have been proposed.

Mori[21,22] defined jetting as the absence of gas spreading across the nozzle plane, and the necessary conditions as achieving sonic (or choked) nozzle velocities. This precise definition, however, is too restrictive as large gas envelopes can form away from the nozzle plane. Furthermore results from the present study show that bubbling occurs

even when the nozzle is choked. The particular mass flux density condition quoted by McNallan[23,24] as being necessary to achieve jetting was shown experimentally to be incorrect.

Results from the present work have shown that in vertically upward injection, in systems where the gas/liquid density ratio (ρ_g/ρ_l) is low (such as gas/metal systems), bubbles grow attached to the nozzle plane for F_M/F_B less than Ø.Ø7 or detached from it when F_M/F_B is greater than Ø.11. True gas in liquid jets, as defined by Themelis et al.[19], can only occur in systems of higher ρ_g/ρ_l (eg air/water). Therefore results from modelling gas injection behaviour close to the tuyere in refining processes with the air/water system should be treated with caution.

Nearly all submerged gas injection processes operate with accretions at the end of the tuyere. These may be porous or pipe-like. Their sizes and shapes have been observed to change from process to process and even from blow to blow in the AOD. Steady-state heat transfer calculations for pipe-like accretion formation have confirmed that accretions can grow purely as a result of cooling by the gas. Large values of the effective superheat were incorporated into the calculations to account for the exothermic heat that is generated when a reactive gas is injected. The unsteady-state rise in temperature between a reactive gas mixture and a bubble growing into molten iron was computed. It was shown to be approximately 1ØØ^{o}C, equivalent to an

effective superheat of 800°C because of the rapid heat transfer by radiation.

In the design of annular tuyeres factors relating to the cooling mechanisms, the manner of gas flow through porous accretions and the nature of contact between the tuyere and the accretion are extremely complex. The model therefore failed to prove the superior performance of narrow annular gap tuyeres compared to that of single tubes.

The pressure/flowrate characteristics of oxygen and air discharging through model accretions was studied in the laboratory. Results showed that for fairly "open" accretions (nA_h/A_p is greater than 0.6) the supply pressure, at a given mass flux density, remains roughly constant as the "openness" increases. Pressure monitoring of accretion "openness" is therefore difficult. Furthermore, since the tuyeres in the AOD operated under choking conditions, no changes in bubbling frequency arising from accretion formation can be detected by upstream pressure transducers. It is therefore impossible to make predictions concerning the state at the tuyere tip from pressure measurements upstream. The pressure pulse technique has, however, been successfully employed[18] in low injection velocity processes, such as copper and nickel converters, to measure bubbling frequency.

In studies on the removal of lead from lead-silver alloys (cupellation) submerged injection of oxygen through a

nitrogen shrouded tuyere into silver-lead-copper bullion was successful, and processing times were significantly quicker than for the traditional process. Further advantages of this alternative process technology applied at pilot-plant scale would be excellent oxygen utilization, less waste gas production, autogenous operation with respect to heat recovery from oxidation if processing time is kept to a minimum, and less precious metal is retained "in process". A successful experimental technique of operating the tuyere under a constant pressure supply with an adequate flow to ensure maintenance of a porous accretion at the tuyere tip has been identified. It was possible to assess the condition of the accretion by monitoring the supply pressure due to the fairly closed structure of the accretion (the AOD accretion was too "open" to record significant pressure changes).

APPENDIX 1

CHOKED FLOW AND JETS FROM CHOKED NOZZLES

APPENDIX 1

CHOKED FLOW AND JETS FROM CHOKED NOZZLES

A.1.1 INTRODUCTION

Very large bubbles form when gas is injected through large nozzles into liquids under low top pressure. The Davidson and Schuler[12] bubble volume is given by the expression

$$V_b = 1.378\ Q^{6/5} g^{-3/5} \qquad (2.1)$$

To keep bubble volume small enough in relation to the small tank described in Chapter 2, the nozzle diameter can be reduced, thus restricting the gas flowrate but not the high injection velocities. To cover the range of low top pressures used the required nozzle diameter was calculated to be Ø.15 mm.

In previous studies[15, 17, 18] concerning classification of submerged gas jet break up behaviour values of the Injection number were calculated by rewriting Equation 2.3 in terms of velocity, ie.

$$N_I = f(F_M/F_B) = C(u_o^2/d_o g)^{2/5}(\rho_g/\rho_l) \qquad (A.1.1)$$

where u_o is termed the "nominal velocity" and is equal to (Q/A_o).

Considering gas injection conditions with high driving pressures through small nozzles, values of u_o thus calculated may be many times greater than the actual velocities obtained. In the case of convergent nozzles, velocities can only be sonic in the nozzle. The momentum flowrate of the gas is therefore over estimated. The prime objective of this work is to measure jet momentum flowrates and velocities through different nozzle types and to develop a realistic model to predict the momentum flowrate of submerged gas jets.

Regarding the use of such small-scale nozzles, design and manufacture are important in limiting pressure and friction losses so that maximum injection velocities can be obtained. Therefore momentum and velocity measurements performed on gas jets discharging into the atmosphere will enable the optimum design and manufacturing techniques to be identified.

A.1.2 Previous work

Nozzles for producing supersonic jets[65] have a converging entrance leading to a section of minimum cross-section, or throat. The gas velocity at this point cannot exceed the speed of sound in the gas. Assuming the gas follows ideal gas laws and that the flow is frictionless and adiabatic, the flow rate is readily calculated (see Appendix A.2). From the throat, the gas expands through a diverging section, accelerating to supersonic velocities. The maximum velocity

attainable in the exit gas stream is determined by the ratio of nozzle driving pressure to the pressure at the nozzle exit and, for a given velocity, there exists an optimum ratio of throat area to exit area which permits the gas to expand to a pressure at the exit section equal to the surrounding pressure. These conditions imply that, ideally, a given nozzle design is restricted to one flowrate (or driving pressure).

The effect of exceeding the design flowrate is to produce an underexpanded jet[66]. Such a jet is at a pressure above ambient and will undergo further expansion with pressure wave formation after leaving the nozzle, with lowered efficiency in converting this additional pressure into momentum flowrate. Blowing below design flowrate produces an over-expanded jet. The jet exit pressure in this case is lower than ambient and the jet contracts upon leaving the nozzle, again with pressure wave formation and lowered efficiency of pressure conversion into momentum flowrate.

In the central core of the jet the supersonic velocity persists for a distance which depends on the exit velocity and finally decays until at some distance from the nozzle the entire jet is subsonic.
After this jet exits from the nozzle, it spreads at an angle of about 20^{o} with entrainment of the surrounding atmosphere.

Particles of fluid from the surroundings are then carried away by the jet so that the mass flow increases in a

downstream direction. Concurrently the jet spreads out and its velocity decreases, but the total momentum flowrate remains constant.

Early investigations by Anderson and Johns[65] have enabled a correlation of data defining the structure of the jet issuing from a nozzle driven at design conditions. Later Smith[67] found good agreement between their correlations and his model studies of free oxygen jets. Convergent-divergent nozzle design criteria are discussed by Foelsch[68] and Shapiro[69] who point out that such nozzles designed by the method-of-characteristics[69] should have carefully selected entrance profiles and contours and flat-wall boundary layer corrections.

Experimental investigations[71] measuring the decay of the centre line velocity in subsonic jets yield the following relationship

$$u_c/u_e = K(d_o/x) \qquad (A.1.2)$$

with K values lying between 6.2 and 8.6 for throat Reynolds number variation between 8×10^3 and 5×10^4 ($Re = Gu/\mu$).

The characteristics of jets normally impinging on to solid flat surfaces have received some attention, notably by Poreh and Cermak[72], (for a submerged water jet), and Bradshaw and Love[73] (for an air jet). Poreh and Cermak[72] concluded that in the neighbourhood of the stagnation point

the flow pattern was almost identical to that computed on the assumption of irrotational flow.

Bradshaw and Love[73] observed that the region of increased static pressure near the stagnation point is roughly hemispherical, with a radius slightly larger than that of the jet. The wall shear stress rises sharply from zero at the stagnation point to a maximum at one jet radius.

In a recent paper, Russell et al.[70] note that high operating pressure levels lead directly to nozzles of Ø.1 mm throat diameter for use in a gas dynamic laser. In this case machining and assembly tolerances are difficult and costly to meet. From their experiments they concluded that a nozzle comprising of a simple $1Ø^{o}$ conical expansion provided a reasonable compromise between boundary-layer and shock losses.

A.1.3 Present approach

In this study it was decided to follow up the simple design criteria of Russell et al.[70] and to manufacture several nozzles consisting of simple conical expansions of varying angles and lengths. Jet momentum flowrates for each nozzle were determined by measuring the force exerted by a hydrogen jet impinging on a flat plate. The centre line stagnation pressures were measured using a pitot-tube arrangement for jet velocity calculation. The influence of design and manufacture is discussed in relation to the increased

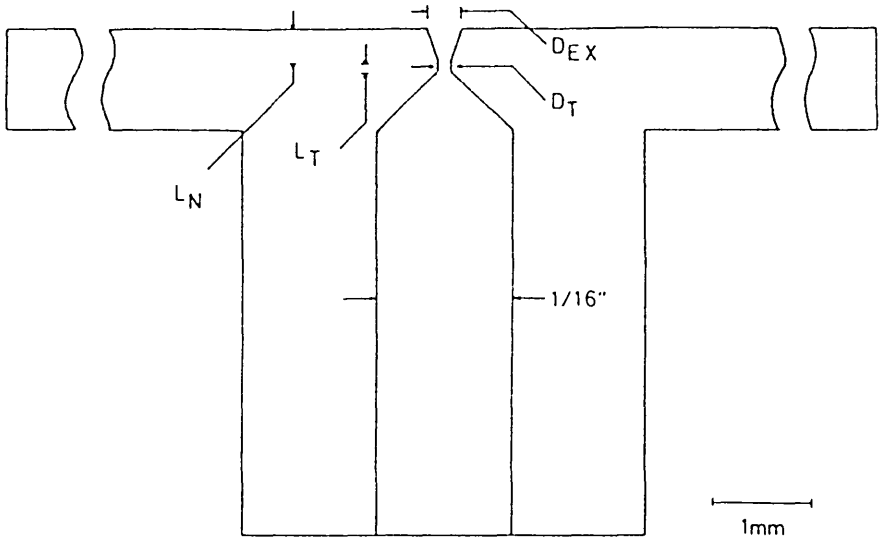

Fig.A.1.1 Simple replaceable convergent-divergent nozzle.

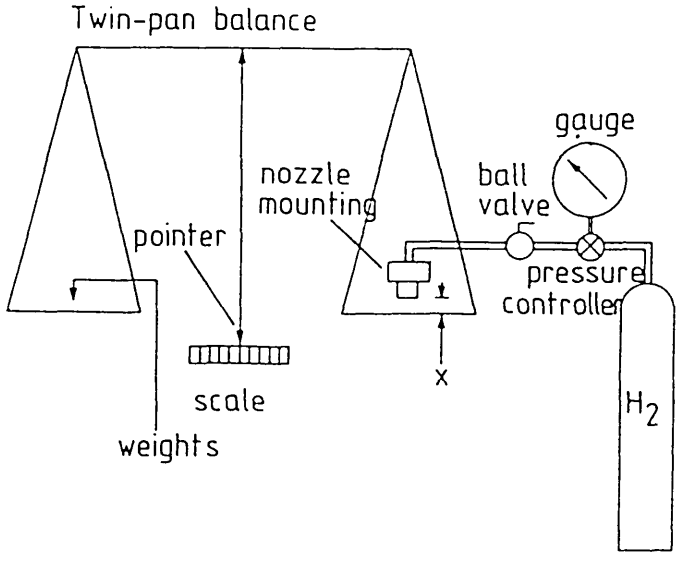

Fig.A.1.2 Momentum flowrate measurement apparatus.

friction from these small diameter nozzles.

A.1.4 Experimental apparatus nozzles

A simple convergent-divergent nozzle is shown in Figure A.1.1. The nozzle could be screwed into the assembly shown in Figure 2.7. The dimensions of the four nozzles investigated are summarized in Table A.1.1. The diameters (throat and exit) were checked during manufacture with an optical microscope. The exact length of the throat was uncertain because it was calculated from the difference in drilled depths which were difficult to measure accurately. Calibrations were made by connecting a rubber hose between the nozzle exit and a domestic gas meter and by measuring the volume flowrate at room temperature and pressure.

Jet momentum flowrate measurement

The force exerted on a flat plate by a normally impinging jet is equal to the rate of change of momentum flux in the jet direction[35], which is

$$F = \dot{m}u \qquad (A.1.3)$$

Measuring values of F enables the momentum flowrate of the gas jet to be calculated.

The gas jet was arranged to discharge vertically downwards from each individual nozzle onto the flat plate, as shown in

Table A.1.1 Nozzle dimensions

Nozzle	Type	Conical half angle	d_t	d_{ex}	Divergent length
			mm	mm	mm
2	C-D	7	.1736	.434	.904
3	C-D	10	.1736	.325	.46
4	C-D	15	.1736	.318	.305
6	C	0	.1736	.1736	.25

Table A.1.2 Nozzle flow characteristics

Nozzle	F_N x 10^5	C_D	h_L
2	1.512	.95	.115
3	1.274	.81	.524
4	1.408	.88	.3
6	1.371	.82	.473

where

$$Q_{STP} = F_N \cdot P_o \quad m^3/s \qquad F_N \text{ has units } m^4S/kg \qquad \text{(A.1.6)}$$

$$C_D = \text{Measured flow/frictionless adiabatic flow} \qquad \text{(A.1.7)}$$

$$h_L = (1/C_D)^2 - 1 = K_L + 4fl/2d \qquad \text{(A.1.8)}$$

Figure A.1.2. The flat plate was fixed on one pan of a mechanical twin-pan balance; combinations of weights varying between Ø.ØØ5 and 1Ø g were placed on the other pan. Gas flowrate was preset for each trial using the pressure controller.

Jet velocity measurement

If a gas jet originally at a pressure P is brought to rest in an open-ended tube (a pitot-tube) pointing into the jet, the speed of the gas jet can be deduced measuring the stagnation pressure using the expression

$$P_{stag}/P = (1 + (k-1)Ma^2/2))^{k/(k-1)} \qquad (A.1.4)$$

if the flow is subsonic.

If the jet is supersonic a shock-wave will lie upstream of the pitot-tube. Francis[66] alters Equation A.1.4 to the following form to account for shock formation.

$$P_{stag}/P = (((k+1)((k+1)Ma^2/2)^k)/(2(kMa^2+1)-(k+1)))^{1/(k-1)} \qquad (A.1.5)$$

By measuring values of P_{stag} and P, the undisturbed pressure (atmospheric in this case), then Ma can be deduced from either Equation A.1.4 or A.1.5.

Centreline stagnation pressure measurements were made on

nozzle 6 - a simple convergent nozzle of throat diameter Ø.1736 mm, shown in Figure A.1.3. The pitot tube, pressure recording equipment and gas supply apparatus are shown in Figure A.1.4. The pitot tube was securely mounted on a carriage which was adjustable in all 3 dimensions, and aligned parallel to the flow direction. A small misalignment, however, does not introduce any serious error[35].

The gas jet discharged vertically upwards and flowrate was set by adjusting the pressure controller. The pressure transducer output was monitored on a chart-recorder.

A.1.5 Experimental Procedure

Jet momentum flowrate measurement

The nozzle exit was positioned a short distance (x) above the flat plate. A small gas flow was established by opening the ball valve. Weights were added to the balancing pan, while in the locked position, until, on unlocking, the pointer was maintained at zero on the scale. The total weight was recorded. In all cases measurements could be made up to + or - Ø.ØØ5 g, an accuracy of better than 1%. The gas flowrate was then increased (usually by 1Ø bar on the supply pressure) and the balancing procedure repeated up to a supply pressure of 1ØØ bar ($Q = 15 \times 1Ø^{-3}$ m^3/s at STP). The nozzle to flat plate separation (x) was increased in small increments up to 5Ø mm.

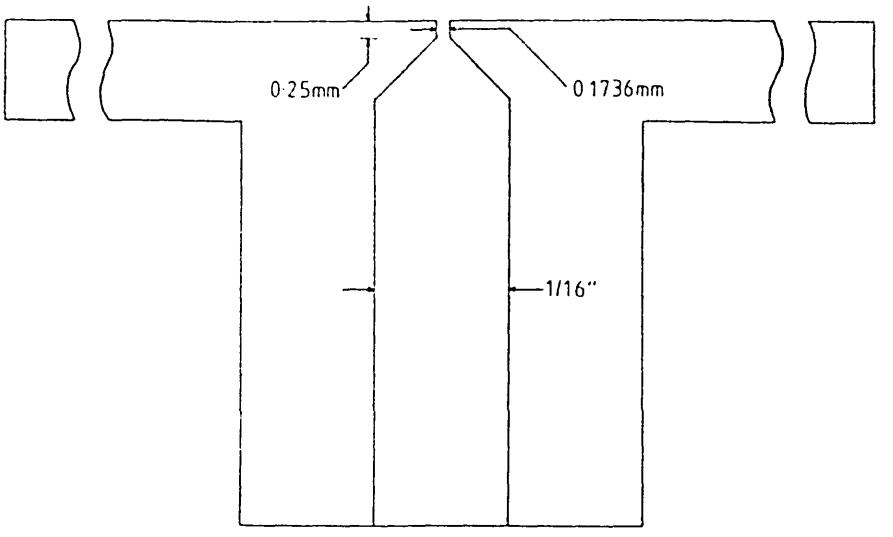

Fig.A.1.3 Nozzle 6 - convergent type.

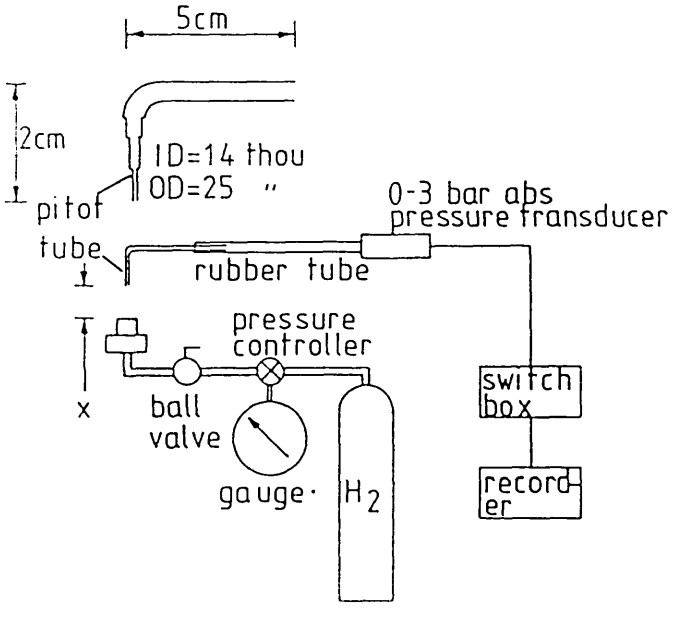

Fig.A.1.4 Jet velocity measurement apparatus.

Jet velocity measurement

The jet centre line velocities were identified by monitoring the transducer output for a maximum when adjusting the two screws to move the pitot tube in the horizontal plane. Measurements were taken on increasing the nozzle to pitot tube separation (x).

A.1.6 Results and interpretation

Flow calibration

A plot of mass flux density ($G = \dot{m}/A_t$) against supply pressure (P_{sup}) for each nozzle is given in Figure A.1.5 and compared with the theoretical performance for frictionless adiabatic flow (Equation A.2.6) through a nozzle. Nozzle flow characteristics are given in Table A.1.2.

Deviations of nozzle performance from ideality can be explained in terms of the overall head loss (h_L) across the nozzle. Since the entry profiles of each nozzle were similar (by virtue of manufacture and direct observation) then values of K_L must be similar and less than Ø.12 (nozzle 2). Losses due to friction in the remaining sections of the nozzles must account for h_L values in excess of Ø.12. Increased friction losses may arise from longer or narrow nozzle throats, exit profile and surface finish. The results show no correlation between the effect of increased friction and nozzle length or divergent angle (in contradiction to

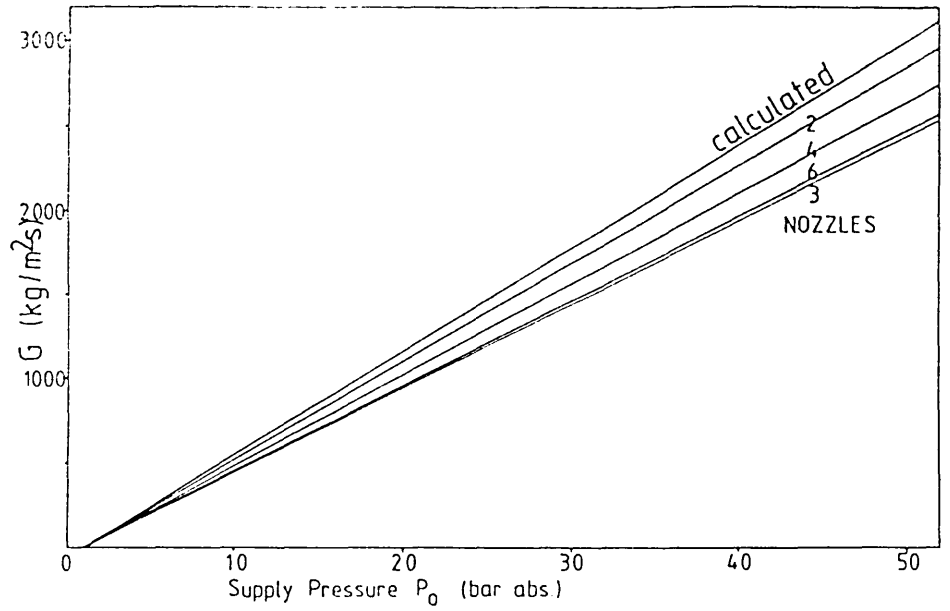

Fig.A.1.5 Nozzle gas flow calibration.

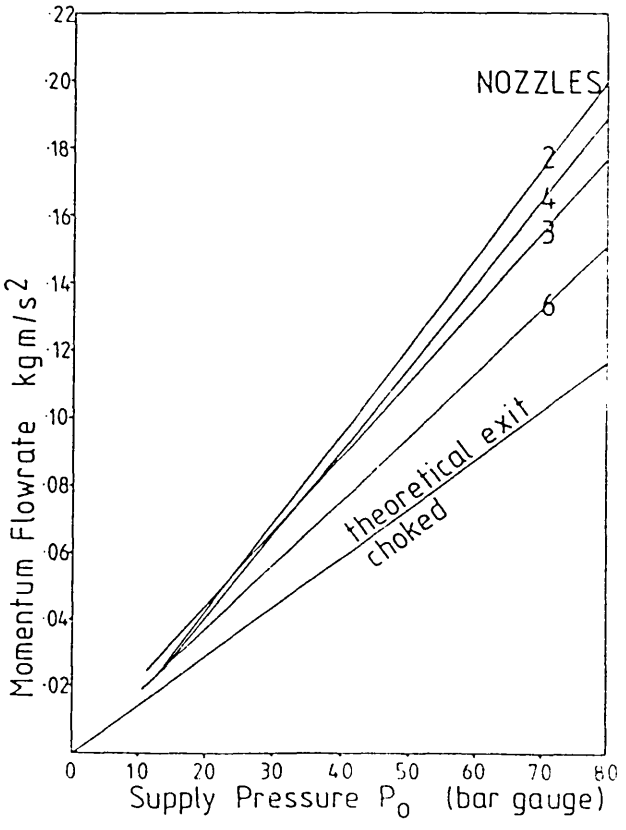

Fig.A.1.6 Comparison of momentum flowrate for each nozzle at x = 10 mm.

the work of Russell et al.[70]. Therefore deviations from ideality can be attributed to imperfections resulting from manufacture, easily outweighing advantages of careful design.

Jet momentum flowrate

Values of the force measured by the balance 10 mm downstream of the nozzle are plotted against supply pressure in Figure A.1.6 for each nozzle and compared to theoretical adiabatic frictionless flow through a nozzle. The theoretical force is evaluated using the impulse-momentum principle[35], which states that the momentum flowrate at the nozzle exit is

$$F_M = \dot{m}_e u_e \qquad \text{(A.1.3)}$$

Referring to Appendix 2, the mass flowrate is calculated from Equation A.2.6, and the velocity is deduced from Equation A.2.1. In all cases the measured momentum flowrate is greater than predicted at the nozzle exit. The measured force (F_M) plotted against supply pressure as a function of nozzle to flat plate separation (x) is plotted for nozzle 6 in Figure A.1.7. Measured values are greater than those predicted and increase with increasing x, in contradiction to the principle of momentum conservation of a discharging jet. Wakelin[71] has reported similar increases of up to 10 % in subsonic jets. This is either due to the momentum of gas entrained into the radial wall jet produced on the plate or the result of an upward velocity vector in the gas

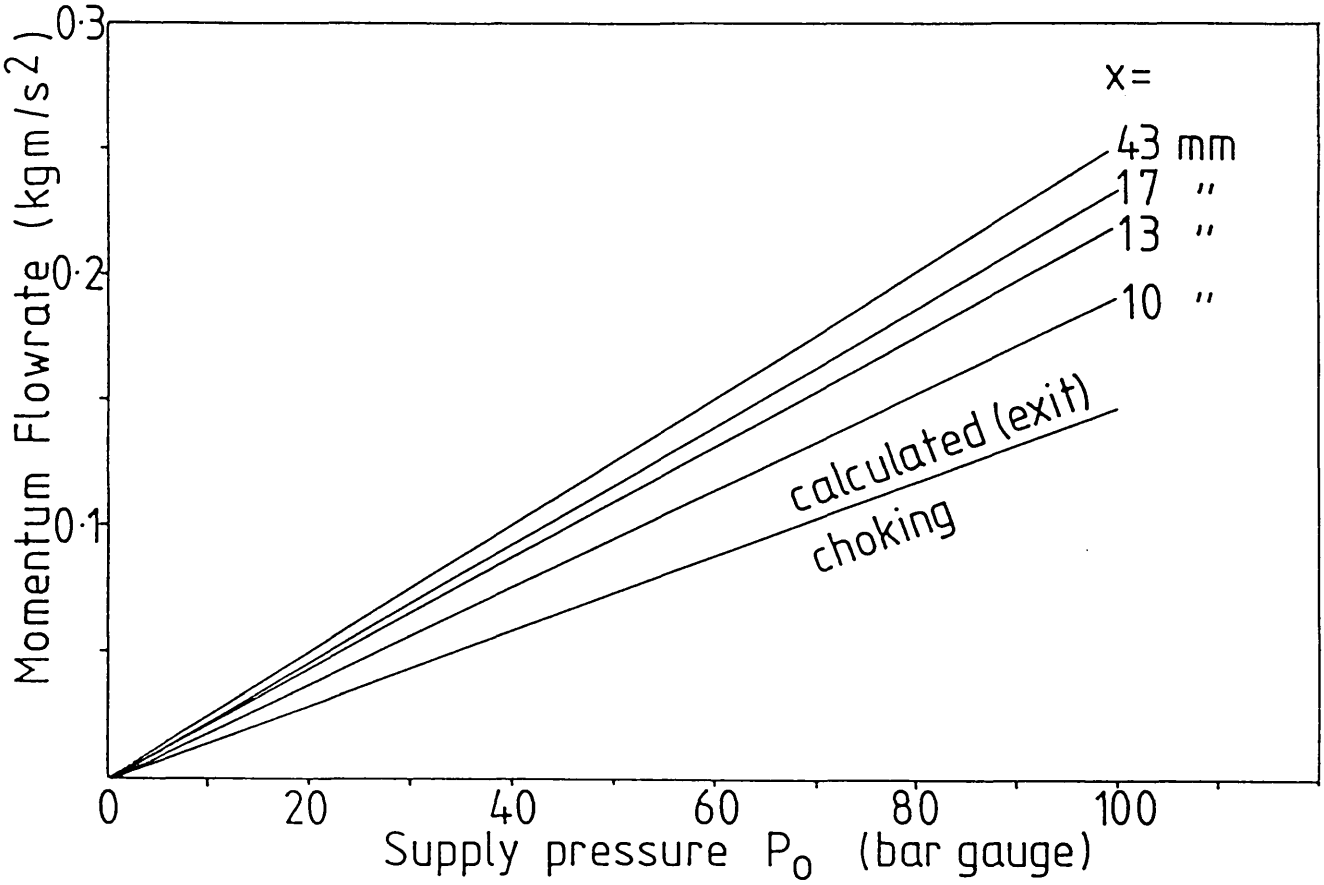

Fig.A.1.7 Momentum flowrate variation with supply pressure as a function of nozzle to plate separation.

departing from the area of impingement. Such an upward vector has been indicated by Bradshaw and Love[73] and Wakelin[71] showed that only a small upward velocity would be necessary.

Nozzle 2 was the most successful at converting the driving pressure into force, although none of the diverging angles showed an optimum performance at a particular pressure ratio. The 10^{o} nozzle was not as successful as that reported by Russell et al.[70].

Jet velocity measurements

Due to unpredictable values of momentum flowrate in relation to design criteria and the fact that the flat-plate impinging method indicated a momentum flowrate increase along the jet axis, it was decided to focus attention on the simple convergent only design of nozzle 6, Figure A.1.3. Stagnation pressure and calculated jet Mach number are plotted against dimensionless distance (x/d_o) from the nozzle exit in Figure A.1.8. Centre line velocity decreases rapidly away from the nozzle and is less for a lower driving pressure. Supersonic velocities extend to between 15 and 35 nozzle diameters downstream of the nozzle. Mach numbers as high as 1.8 were calculated for the highest flowrate 5 nozzle diameters from the nozzle exit.

The decay of the centre line velocity obeys Equation A.1.2 up to values of x/d_o of 200. Values of (u_c/u_e) are plotted

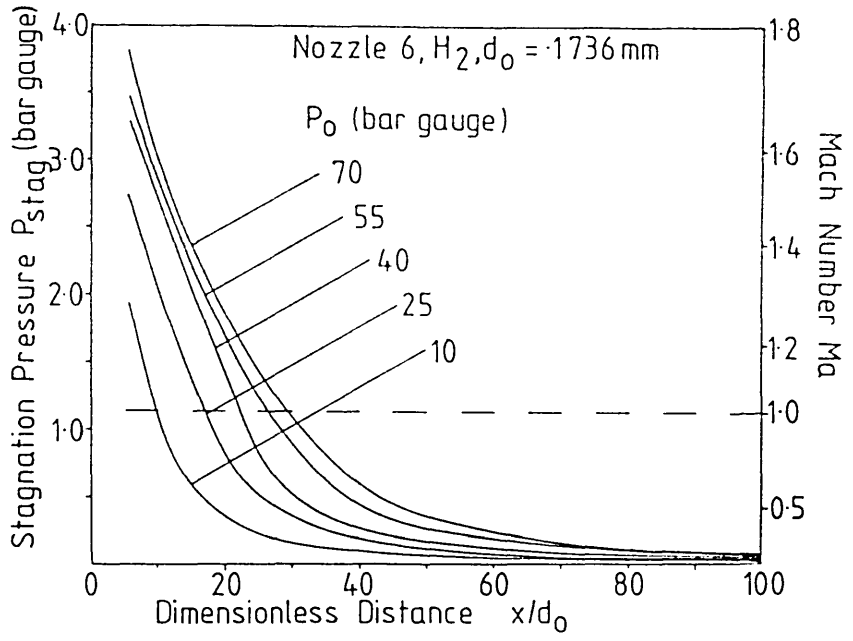

Fig.A.1.8 Centre line stagnation pressure and Mach number versus dimensionless distance as a function of supply pressure.

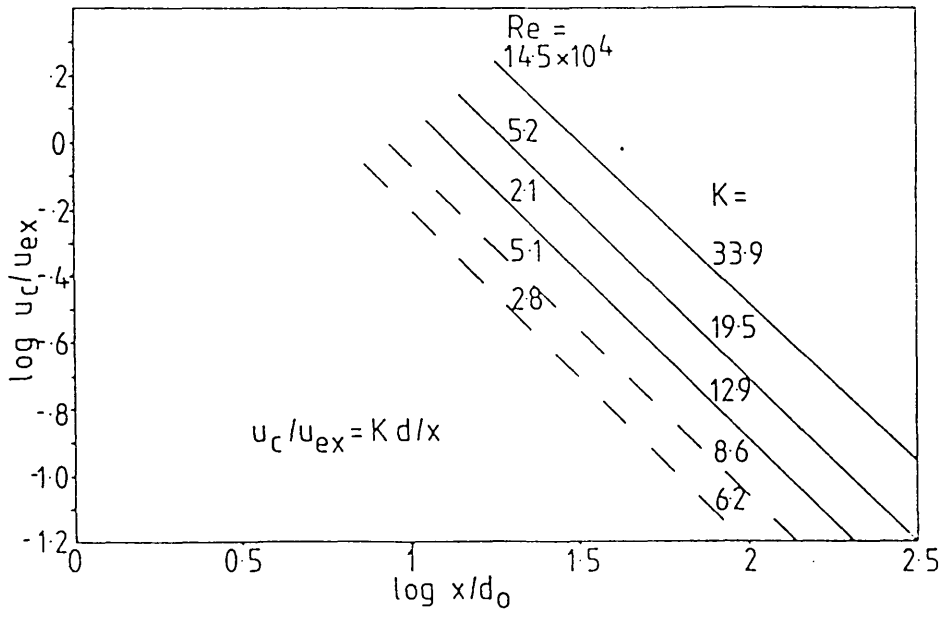

Fig.A.1.9 Decrease in jet centre line velocity with distance from nozzle.

against (x/d_o) values in Figure A.1.9 and compared with those obtained in a previous study[71]. K values vary with the throat Reynolds number. For Re = 2.1×10^4 to 14.5×10^4 K varies from 12.9 to 33.9. This variation is greater than observed previously.

A.1.7 Discussion

Nozzle design

Experimental investigations relating to the flow characteristics of jets discharging from convergent-divergent and convergent only nozzles were inconclusive in classifying optimum nozzle design criteria. The impingement technique employed to measure jet momentum flowrate was unsatisfactory because the results implied that momentum flowrate increased along the jet axis, which is impossible. The nozzle with a diverging angle of 7^o resulted in the highest measured force but the results did not indicate a trend leading to an optimum flowrate for a given diverging angle. Indeed the differences in individual nozzle performances could be attributed to intrinsic faults arising from manufacturing nozzles on such a small scale. Imperfect surface finish and sharp edges cause large friction losses.

Velocity measurements carried out on the simple convergent nozzle indicated the supersonic velocities persisted for a short distance downstream of the nozzle and that the centre line velocity decays in the expected manner. The pressure

variations with distance from the nozzle reported by Aoki[27] for a choked nozzle were not observed.

A.1.8 Choked submerged gas jet phenomena

Jet velocity measurements from a small throat diameter convergent nozzle operating under a high pressure driving force indicate that sonic or just above velocities are obtained for a few nozzle diameters along the jet axis. Calculation of the momentum flowrate is performed therefore by assuming that the gas is choked at the nozzle exit and that the principle of momentum conservation is obeyed along the jet. The gas momentum flowrate at the nozzle exit is

$$F_M = u_e \dot{m} = \dot{m}^2 / A_o \rho_e \qquad (A.1.9)$$

Mass flowrate ($\dot{m}$) is known from calibration and the gas velocity at the nozzle exit (u_e) is assumed to be sonic. The resulting value of F_M is a lower bound value because the injected gas has not fully expanded at the nozzle exit. Subsequent expansion occurs in all forward directions making the actual value of F_M very difficult to evaluate theoretically.

A plot of the calculated jet Froude number (u_e^2/dg) and gas/liquid density ratio (ρ_{gd}/ρ_l) is given in Figure A.1.10 for convergent and convergent-divergent nozzles discharging into water driven by a supply pressure of 100 bar (g). The gas flow is assumed to be frictionless and adiabatic. As

ρ_{gd}/ρ_l decreases (decrease in pressure) there is a sharp rise in Froude number up to choking conditions where $(P_2/P_1)_c$ = Ø.528 (see Appendix 2). Considering the case of a convergent nozzle, conditions become choked at the throat and no increase in gas flowrate is possible by further reducing the downstream pressure, resulting in a maximum Froude number. The nozzle delivers an under-expanded jet. To obtain the highest possible values of N_{Fr} with high pressure driving forces the nozzle exit profile must diverge in such a way that the gas jet is able to expand exactly to the ambient pressure at the nozzle exit. In order to satisfy this condition for the plot, it is assumed that the radius increases with decreasing downstream pressure in Figure A.1.1Ø. The theoretical supersonic gas velocity at the nozzle exit (u_e) can be deduced from Equation A.2.1. The N_{Fr} increases at a lower rate for $(P_2/P_1)_c$ is greater than Ø.528. Lines of constant F_M/F_B are also plotted on Figure A.1.1Ø. The plot of F_M/F_B versus ρ_{gd}/ρ_l is given in Figure A.1.11. With decreasing ρ_{gd}/ρ_l the F_M/F_B value rapidly reaches a maximum and then decreases relatively slowly. It is therefore difficult to obtain high values of F_M/F_B (and jetting) even at high values of N_{Fr} if the downstream pressure is very low.

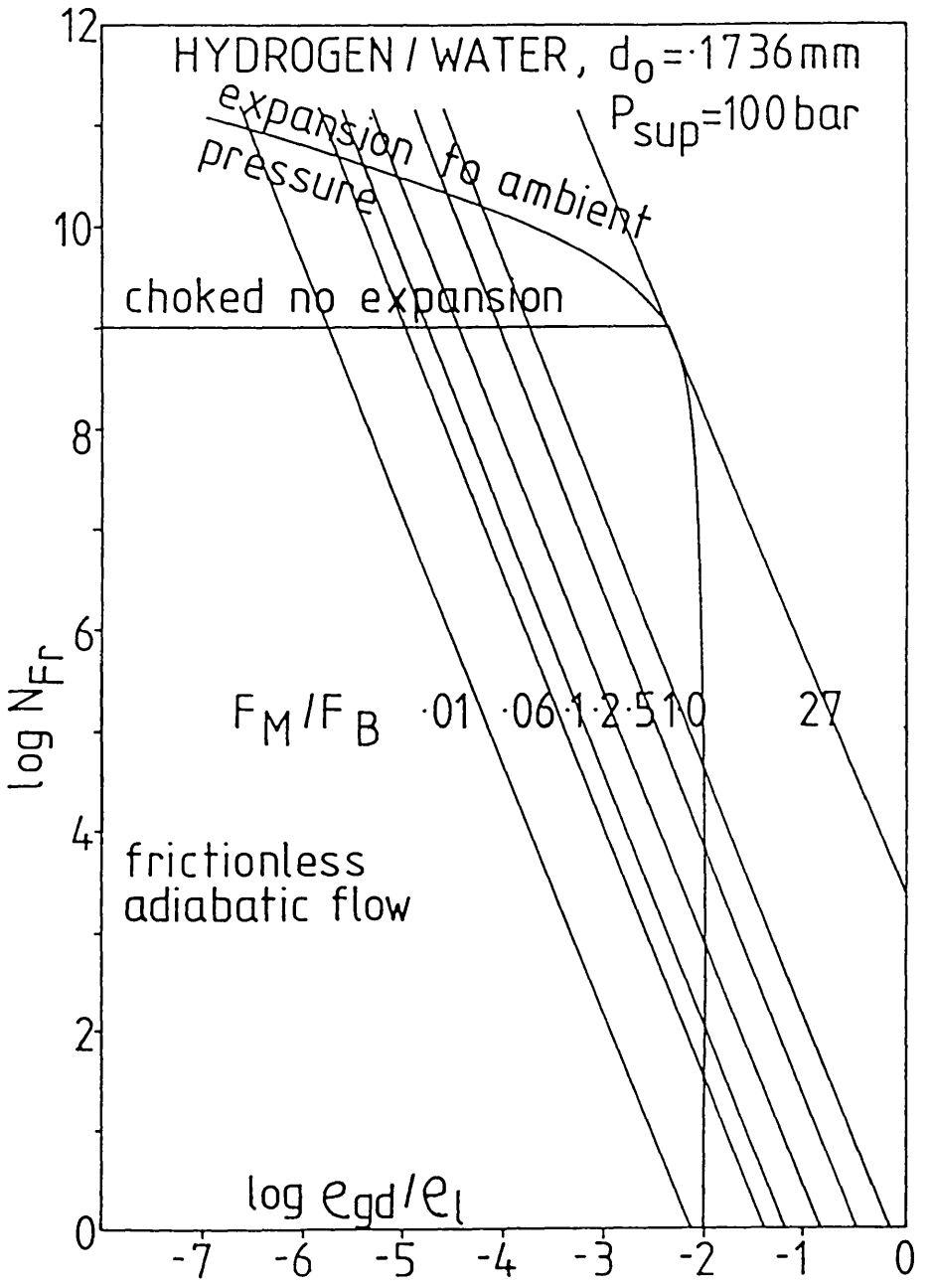

Fig.A.1.10 Froude number versus gas/liquid density ratio assuming adiabatic and frictionless flow through a small nozzle.

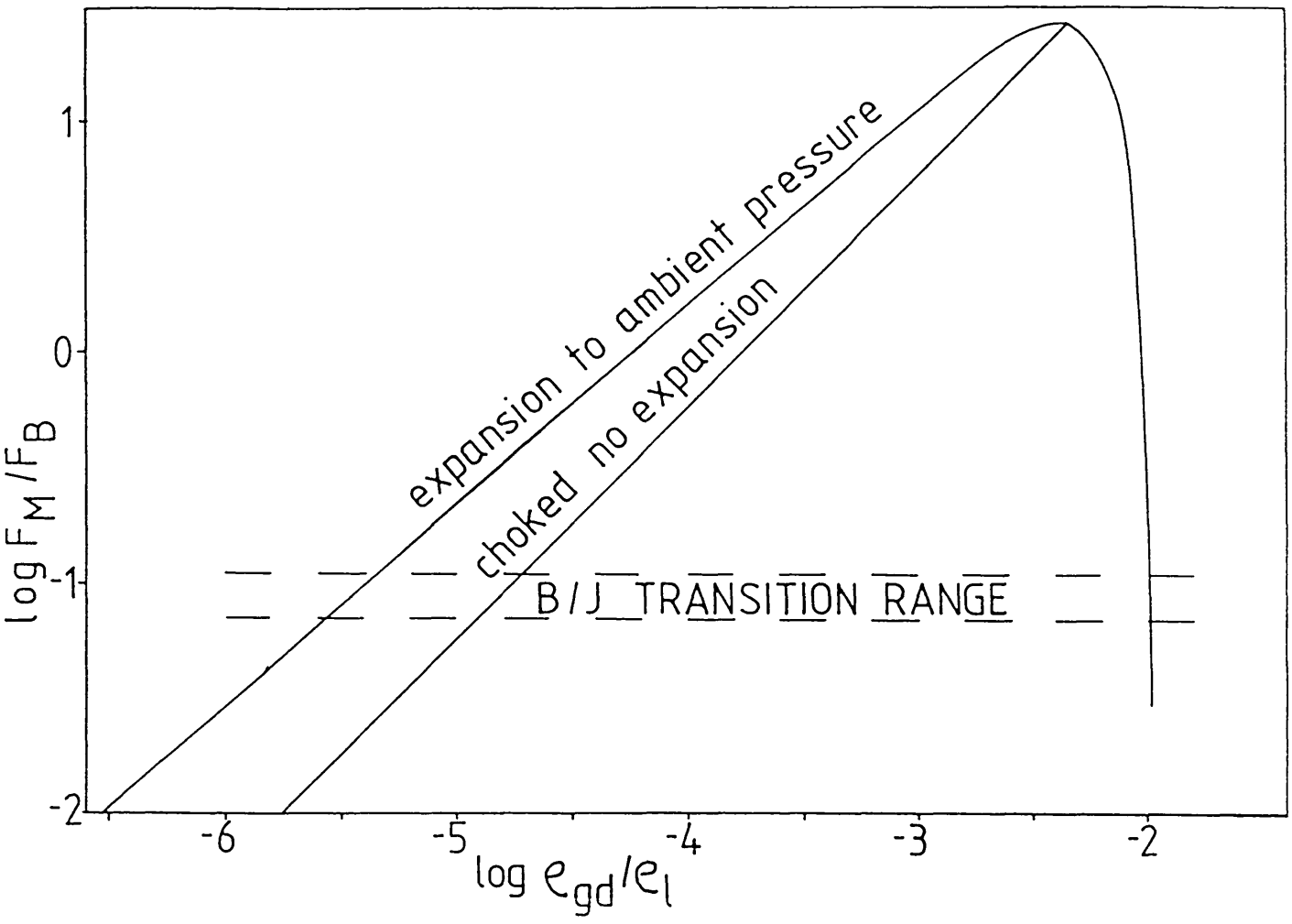

Fig.A.1.11 Ratio of momentum to buoyancy force variation with ratio of gas/liquid density for convergent-divergent and convergent nozzles.

APPENDIX 2

NOZZLE METERING

APPENDIX 2

A.2.1 NOZZLE METERING

Nozzles placed at the ends of pipelines as metering devices are generally termed flow nozzles. They depend for their operation on the fact that the gas flows through them under choked conditions. Once calibrated, a particular driving pressure will enable the flowrate to be calculated, independently of the downstream pressure.

Convergent metering nozzle

Figure A.2.1 depicts schematically the nozzle employed in this work. Considering frictionless flow of a compressible gas through a convergent nozzle into a downstream pressure P_d, integration of Euler's equation gives

$$Ma_t^2 = (2/k-1)((P_d/P_o)^{(k-1)/k} \qquad (A.2.1)$$

Supersonic velocities are not expected because there are no divergent sections.

If the pressure difference (P_o-P_d) is large enough to produce a sonic velocity, this exists at the throat and $Ma_t=1$. Substituting this value into Equation A.2.1 and solving for (P_d/P_o), the result is designated as the critical pressure ratio,

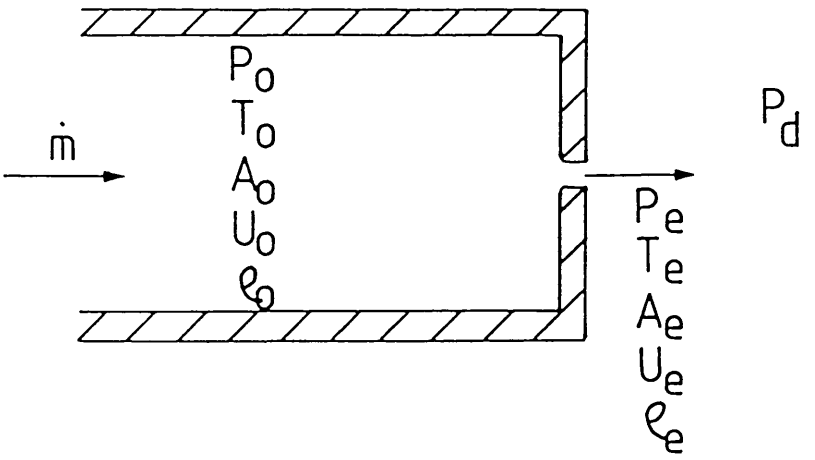

Fig.A.2.1 Convergent metering nozzle.

$$(P_d/P_o)_c = (2/(k+1))^{k/(k-1)} \qquad (A.2.2)$$

Thus if the sonic velocity is attained by the fliud, the absolute pressure P_t, in the throat section is in fixed ratio to the absolute pressure P_o and is therefore independent of P_d and the nozzle is said to choked. Sonic velocity is not attained unless the pressure difference (P_o-P_d) is large enough. For ratios of (P_d/P_o) above the critical, pressures P_d and P_t are the same. For ratios below this P_t is greater than P_d.

In fluid metering the mass flowrate is usually computed. For the ratio (P_d/P_o) greater than the critical, the mass flowrate is given as

$$\dot{m} = A\ u \qquad (A.2.3)$$

Substituting the velocity, calculated from

$$C_pT_o + u_o^2/2 = C_pT_t + u_t^2/2 \qquad (A.2.4)$$

and the isentropic relationship $(P_t/P_o) = (\rho_t/\rho_o)^k$ into Equation (A.2.3) gives

$$\dot{m}/A_t = P_o/(T_o)^{1/2}(2k/(R(k-1))$$

$$x \quad ((P_t/P_o)^{2/k}-(P_t/P_o)^{(k+1)/k})^{1/2} \qquad (A.2.5)$$

If (P_d/P_o) is less than critical, the ratio

$$(P_d/P_o) = (2/(k+1))^{k/k-1}.$$

Equation A.2.8 becomes

$$\dot{m}/A_t = P_o/(T_o)^{1/2}(((k/R)(2/k+1)^{(k+1)/(k-1)})^{1/2} \qquad (A.2.6)$$

The final term is a characteristic constant of gas. Mass flowrate is directly proportional to supply pressure (P_o) and independent of downstream pressure (P_d). Thus flowrate calculation is simple and makes a choked nozzle of known proportions ideal for flow metering.

APPENDIX 3

OXYGEN CONTENT IN THE MELT

APPENDIX 3

A.3 OXYGEN CONTENT IN THE MELT

Monitoring of oxygen concentration in the melt was achieved by using the solid electrolyte probe which was magnesia-stabilised zirconia[74] as shown in Figure A.3.1. Gas of known oxygen partial pressure (usually pure oxygen or air) was passed through a small stainless steel tube into the reference side of the probe. E.m.f. for this system is given by

$$E = (RT/4F)\log \frac{(P_{O_2} \text{ in Ag bath})}{(P_{O_2} \text{ in reference tube})} \qquad (A.3.1)$$

for the reaction

$$\emptyset_2 + 4e^- \rightleftharpoons 2O^{2-}$$

where E = E.M.F. (volts)

R = Universal gas constant (8.314 J/mol.K)

T = Absolute temperature (K)

F = Faraday's constant (96500 coulombs/mol.)

When air is used in the reference electrode, the P_{O_2}, which will be fixed, has been calculated assuming that air is made up of $\emptyset.21\ O_2$ and $\emptyset.79\ N_2$.

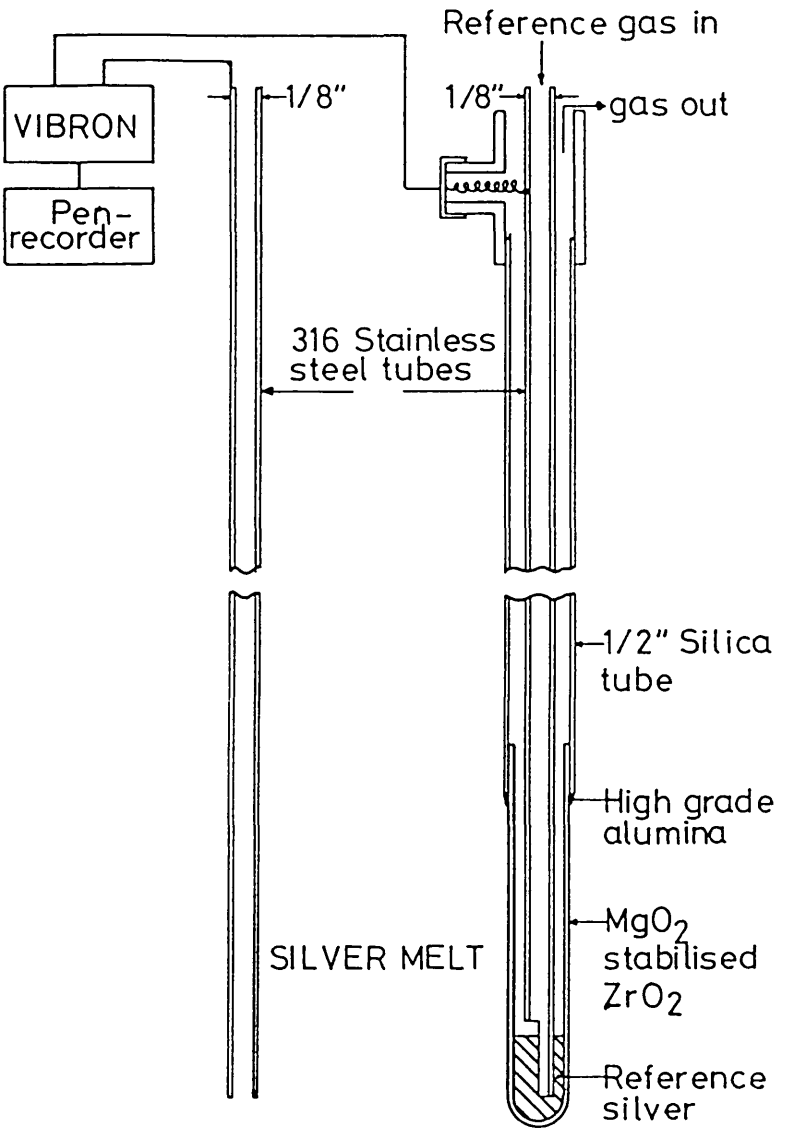

Fig.A.3.1 The oxygen probe.

APPENDIX 4

FORTRAN PROGRAM REFRAC9

```
      PROGRAM REFRAC9(DATA1,OUTPUT,TAPE5=DATA1,TAPE6=OUTPUT)
C*****************************************************************
      COMMON/COEFFS/TWA,TGA,RHOS,QCORE,QSHROUD,RSEVEN,RFOUR,RTWO,HTWO,
     +HFOUR,RHOC
      COMMON/COEFFS/CPS,CPC,TO,TGO,HSEVEN,DR,HCONT,KSHROUD
      COMMON/RES/NI,DXN,DZN,TS,TN,TE,TW,TCENT,TNEW,ALPHA
      COMMON/DATA/TOL,KS,KR,KD,HGS,COREID,COREOD,SHROID,TSUP,KCORE
      REAL KS,KR,KD,KCORE,KSHROUD
      DIMENSION T(40,55),ARN(40),AZ(55),IMAX(40)
      READ(5,*)TOL,QCORE,QSHROUD,COREID,COREOD,SHROID,TSUP,KCORE
      READ(5,*)KS,KR,KD,HGS,DR,HCONT,KSHROUD
      RREF=0.02718
      DZS=0.02
      DZR=0.01
      DZSN=DZS/RREF
      DZRN=DZR/RREF
      DX=0.002718
      DXN=DX/RREF
      RD=0.03
      RDN=RD/RREF
      NWIDE=16
      NHIGH=5
      RHOC=0.49
      RHOS=0.49
      CPC=519.
      CPS=519.
      QCORE=RHOC*QCORE
      QSHROUD=RHOS*QSHROUD
      RTWO=COREID/2.
      RFOUR=COREOD/2.
        RSEVEN=SHROID/2.
      RTHREE=RTWO+((RFOUR-RTWO)/2.)
C
      RTUYN=RSEVEN/RREF
      RTD=DXN
      TGO=30.
      TR=200.
      TM=1540.
      TSURF=1533.
      TB=TM+TSUP
      TO=TM-TGO
      TGON=0.0001
      TRN=(TR-TGO)/TO
      TSURFN=(TSURF-TGO)/TO
      TBN=(TB-TGO)/TO
      TMN=(TM-TGO)/TO
C DIMENSIONLESS VALUES
C CONDUCTIVITIES
      FR=KR/KCORE
      FS=KS/KCORE
      FD=KD/KS
CRELAXATION FACTOR/4
      ALPHA=.5-3.14159/2.8284*SQRT(1./NWIDE**2.+1./NHIGH**2.)
C
C*****************************************************************
C INITIALIZE MESH POINT VALUES
      DO 10 I=1,36
C RADIAL POSITION
      ARN(I)=RTUYN-1.+(EXP(DXN*FLOAT(I-7)))
      DO 20 J=1,24
      AZ(J)=50.-(2.*FLOAT(J))
C NODE AT BL
      IMAX(J)=INT(7.+(ALOG(RDN/RTUYN)/DXN))
C LIQ TEMPS
      T(I,J)=(TBN-TMN)*FD+TMN
   20 CONTINUE
C REFRACTORY TEMPS
      DO 30 J=25,51
      T(I,J)=TSURFN-((TSURFN-TRN)/25.)*(FLOAT(J)-25.)
      AZ(J)=FLOAT(25-J)
   30 CONTINUE
   10 CONTINUE
C GAS TEMPS
      DO 40 I=1,6,1
      DO 41 J=1,51
      T(I,J)=TGON
   41 CONTINUE
   40 CONTINUE
C
C*****************************************************************
      DPIS=2.*3.14159*DZSN/KCORE
      DPJ=ALOG(RFOUR/RTHREE)
      DPK=ALOG(RTHREE/RTWO)
      HKC=GSHROUD*CPS/(KCORE*RREF)
      HKF=KCORE*DZRN/(KCORE*DPJ)
      HKG=3.14159*((RFOUR**2.)-(RTWO**2.))/(0.005*RREF)
      HKH=KCORE/(KCORE*DPK)
      HKI=DZRN*HKH
      HKK=GCORE*CPC/(KCORE*RREF)
      HKN=HKC+HKK
      HKM=DPIS*HGS*RSEVEN
      HKO=HGS*2.*DXN/KCORE
C
CCOMPUTE T(I,J) VALUES BY G-S SOR METHOD,END WHEN MAX CHANGE
```

```
CLESS THAN TOL.
      DO 50 K=1,1000
      TO1=T(7,22)
      TO2=T(7,29)
      TO3=T(1,24)
      TO4=T(25,25)
      TO5=T(30,15)
      DO 70 J=1,24
      DO 71 I=7,35
C LIQ+PIPE GAS TEMP RELAXATION
      TSHR=T(5,25)
      TCORE=T(1,25)
      TMEAN=((GCORE*TCORE)+(GSHROUD*TSHR))/(GCORE+GSHROUD)
      IF(J.EQ.24) T(1,J+1)=TMEAN
C GAS TEMP PIPE
      T(1,J)=T(1,J+1)+((HKM/HKN)*(T(7,J+1)-T(1,J+1)))
C FICT. REFRACTORY TEMP. EXTENDED INTO PIPE BORE
      T(6,J)=T(8,J)-(HKO*(T(7,J)-T(1,J)))
      TS=T(I,J+1)
      IF(J.EQ.1)T(I,J-1)=(TBN-TMN)*FD+TMN
      TN=T(I,J-1)
      TE=T(I+1,J)
      TW=T(I-1,J)
      TCENT=T(I,J)
      NI=I
      DZN=DZSN
      CALL UPDATE
      T(I,J)=TNEW
      IF(T(I,J).LE.1.)T(I,J)=(T(I,J)-1.)/FD+1.
      IF(T(I,J).GE.1.) GOTO 150
      IF(TE.GE.1..AND.TW.LT.1.)GOTO 75
      GOTO 71
C LIQ/REFRACTORY RELAXATION IN BL
  150 IF(J.GE.22)GOTO 71
C NO. OF NODES TO BL EDGE
       IF(I.GE.IMAX(J))GOTO 70
      GOTO 71
   75 RTD=ARN(I)
      RBLN=RTD*RDN
      IMAX(J)=INT(7.+(ALOG(RBLN/RTUYN)/DXN))
   71 CONTINUE
   70 CONTINUE
C
      DPIR=2.*3.14159*DZRN/KCORE
C
      DO 72 I=7,35
      DO 72 J=25,50
C REFRACTORY AND TUYERE GAS RELAXATION
      TWA=T(7,J)
      TGA=T(5,J)
      CALL HTCOEFF
C
      HKA=DPIR*HSEVEN*RSEVEN
      HKB=DPIR*HFOUR*RFOUR
      HKJ=DPIR*HTWO*RTWO
      HKL=HSEVEN*2.*DXN/KCORE
      HKP=DPIR*0.4*RSEVEN*(TO**3.)*.00000005669
C FICT. REFRACTORY TEMP EXTENDED INTO TUYERE
      T(6,J)=T(8,J)-(HKL*(T(7,J)-T(5,J)))
C GAS TEMPS
      T(5,J)=T(5,J+1)+((HKA/HKC)*(T(7,J+1)-T(5,J+1)))+((HKB/HKC)*(T(4,J+
     +1)       -T(5,J+1)))
      T(4,J)=((HKB*T(5,J))+(HKP*(T(7,J)**4.))+(HKF*T(3,J)))/(HKB+HKF
     ++(HKP*T(4,J)))
C
      IF(J.EQ.25)T(3,J-1)=T(1,J-1)
      RESID=((HKF*T(4,J))+(HKG*(T(3,J-1)+T(3,J+1)))+(HKI*T(2,J)))-(T(3,J
     +)        *(HKF+(2.*HKG)+HKI))
      T(3,J)=T(3,J)+(RESID/(HKF+(2.*HKG)+HKI))
      T(2,J)=((HKI*T(3,J))+(HKJ*T(1,J)))/(HKI+HKJ)
      T(1,J)=T(1,J+1)+(HKJ/HKK)*(T(2,J+1)-T(1,J+1))
CINITIAL GAS TEMPS
      IF(J.EQ.50)THEN
      T(1,J)=TGON
      T(2,J)=TGON
      T(3,J)=TGON
      T(4,J)=TGON
      T(5,J)=TGON
      ENDIF
CFURNACE OUTER SHELL REMAINS AT 200
      IF(J.EQ.50)GOTO 65
CADIABATIC RHS BOUNDARY
      IF(I.EQ.35)T(I+1,J)=T(I-1,J)
      TS=T(I,J+1)
      TN=T(I,J-1)
      TE=T(I+1,J)
      TW=T(I-1,J)
      TCENT=T(I,J)
      NI=I
      DZN=DZRN
      CALL UPDATE
      T(I,J)=TNEW
      TINT=T(I,24)
      IF(TINT.GE.1.)TINT=(TINT-1.)/FD+1.
      T(I,25)=((0.5*FS*TINT)+(FR*T(I,26)))/((FS*0.5)+FR)
   65 T(I,50)=TRS
   72 CONTINUE
```

```
C
C*****************************************************************
CCONVERGENCE TEST
      IF(ABS(T(30,15)-T05).GE.TOL)GOTO50
      IF(ABS(T(25,25)-T04).GE.TOL)GOTO50
      IF(ABS(T(1,24)-T03).GE.TOL)GOTO50
      IF(ABS(T(7,29)-T02).GE.TOL)GOTO50
      IF(ABS(T(7,22)-T01).GE.TOL)GOTO50
      GOTO 80
   50 CONTINUE
C*****************************************************************
C*****************************************************************
      WRITE(6,102)
      GOTO 90
   80 WRITE(6,104)K
   90 WRITE(6,100)ALPHA
C
      DO158 I=1,35
      DO158 J=1,24
  158 IF(T(I,J).GE.1.) T(I,J)=(T(I,J)-1.)/FD+1.
C WRITE OUT DIMENSIONLESS VALUES
      CALL WRITEIT
       WRITE(6,105)
  105 FORMAT(//25X,"RADIAL POSITION")
      WRITE(6,103)(ARN(I),I=7,27,1)
  103 FORMAT(//8X,5HZCM  ,3X,5HTGC  ,5HTCORE,4H TGA,21F5.2)
       WRITE(6,106)(AZ(J),(T(I,J),I=1,7,2),(T(I,J),I=8,27,1),J=1,50)
  106 FORMAT(6X,F5.1,4X,24F5.3)
      WRITE(6,109)(ARN(I),I=28,35)
  109 FORMAT(//8X,5HZCM  ,3X,9F5.2)
      WRITE(6,110)(AZ(J),(T(I,J),I=28,35),J=1,50)
  110 FORMAT(6X,F5.1,4X,8F5.3)
C
C CONVERT TO REAL DIMENSIONS
      DO 170 I=1,35
      DO 170 J=1,50
      T(I,J)=T(I,J)*TO+TGO
      ARN(I)=ARN(I)*RREF*100.
  170 CONTINUE
C
C WRITE REAL VALUES
      WRITE(6,107)(ARN(I),I=7,27,1)
  107 FORMAT(//8X,5HZCM  ,3X,5HTGC  ,5HTCORE,4H TGA,21F5.1)
      WRITE(6,108)(AZ(J),(T(I,J),I=1,7,2),(T(I,J),I=8,27,1),J=1,50)
  108 FORMAT(6X,F5.1,4X,24F5.0)
      WRITE(6,111)(ARN(I),I=28,35)
  111 FORMAT(//8X,5HZCM  ,3X,9F5.1)
      WRITE(6,112)(AZ(J),(T(I,J),I=28,35),J=1,50)
  112 FORMAT(6X,F5.1,4X,8F5.0)
C
  104 FORMAT(//2X,I3,21H ITERATIONS WERE USED)
  100 FORMAT(/27H USING RELAXATION FACTOR OF,F5.3)
  102 FORMAT(//52HTOLERANCE TO END COMPUTATION NOT MET IN 1000 CYCLES.
     +    /31H LAST ROUND ON CALCULATIONS IS-)
      STOP
      END
C
C ****************************************************************
      SUBROUTINE HTCOEFF
      COMMON/COEFFS/TWA,TGA,RHOS,QCORE,QSHROUD,RSEVEN,RFOUR,RTWO,HTWO,
     +HFOUR,RHOC
      COMMON/COEFFS/CPS,CPC,TO,TGO,HSEVEN,DR,HCONT,KSHROUD
      REAL KGA,KGC,KSHROUD
C HRAD
      EMISS=0.78
      SIGMA=0.00000005669
      TAVE=((TWA+TGA)/2.)*TO+TGO
      HRAD=EMISS*SIGMA*(TAVE**3.)
C HCONV
      KGA=0.0427
      KGC=0.0427
      VISCA=0.0000542
      VISCC=0.0000542
      UA=QSHROUD/(3.14159*((RSEVEN**2.)-(RFOUR**2.)))
      UCORE=QCORE/(3.14159*(RTWO**2.))
      REA=(RHOS*UA*(RSEVEN-RFOUR))/VISCA
      PRA=(CPS*VISCA/KGA)
      HCONV=0.023*(REA**(-0.2))*(PRA**(-0.667))*UA*RHOS*CPS
C EFFECTIVE H OF SHROUD TUBE
      HEFF=KSHROUD/DR
      UINV=1./HCONV+(1./HEFF)+(1./(HRAD+HCONT))
      HSEVEN=1./UINV
      HFOUR=0.023*KGA/(RSEVEN-RFOUR)*(REA**0.8)*(PRA**0.4)
     +        *((RSEVEN/RFOUR)**0.45)
      REC=(RHOC*UCORE*2.*RTWO)/VISCC
      PRC=CPC*VISCC/KGC
      HTWO=0.023*KGC/(2.*RTWO)*(REC**0.8)*(PRC**0.33)
      RETURN
      END
C ****************************************************************
```

```
      SUBROUTINE UPDATE
      COMMON/RES/NI,DXN,DZN,TS,TN,TE,TW,TCENT,TNEW,ALPHA
      AXN=EXP(-(2.*DXN*FLOAT(NI-7)))
      FACTOR=2.*(AXN/(DXN**2.)+(1./(DZN**2.)))
      RESID=((TS+TN)/(DZN**2.))+(AXN*(TE+TW)/(DXN**2.))-(TCENT*FACTOR)
      TNEW=TCENT+'ALPHA*RESID/FACTOR)
      RETURN
      END
C
      SUBROUTINE WRITEIT
      COMMON/COEFFS/TWA,TGA,RHOS,QCORE,QSHROUD,RSEVEN,RFOUR,RTWO,HTWO,
     *HFOUR,RHOC
      COMMON/COEFFS/CPS,CPC,TO,TGO,HSEVEN,DR,HCONT,KSHROUD
      COMMON/DATA/TOL,KS,KR,KD,HGS,COREID,COREOD,SHROID,TSUP,KCORE
      WRITE(6,113)QCORE,QSHROUD
      WRITE(6,114)COREID,COREOD,SHROID,DR
      WRITE(6,115)TSUP
      WRITE(6,116)KCORE,KS,KR,KD,KSHROUD
      WRITE(6,117)HGS,HCONT
  113 FORMAT(6X,"QCORE=",F7.6,2X,"QSHROUD=",F7.6,"CUB.M/S")
  114 FORMAT(6X,"CORE ID=",F7.6,"M",2X,"CORE OD=",F7.6,"M",2X,
     *"SHROUD ID=",F8.6,"M",2X,"WALL=",F7.6,"M")
  115 FORMAT(6X,"MELT SUPERHEAT=",F5.1,"DEG.C")
  116 FORMAT(6X,"CONDUCTIVITIES IN W/M.K"/"KCORE=",F5.1,2X,"KMELT=",F9.2,
     *     2X,"KREFRAC=",F5.1,2X,"KBL=",F5.1,2X,"KSHROUD=",F5.1)
  117 FORMAT(6X,"HGS=",F7.1,2X,"HCONT=",F7.1,"W/SQ.M.K")
      RETURN
      END
```

List of symbols

A	Constant
A_{acc}	Accretion surface area
A_b	Bubble surface area during growth
A_c	Area open to core gas flow
A_h	Area of hole in artificial accretion
A_o	Cross-sectional area of nozzle exit
A_p	Cross-sectional area of pipe
A_s	Area open to shroud gas flow
A_t	Cross-sectional area of nozzle throat
C	Constant
C_D	Discharge coefficient
C_p	Specific heat at constant pressure
C_{pc}	Specific heat of core gas
C_{ps}	Specific heat of shroud gas
C_T	Molar concentration of oxygen
d_e	Exit diameter
d_o	Nozzle diameter
d_t	Throat diameter
f	Friction factor
F_N	Constant for each nozzle
F	View factor
F_B	Force due to jet momentum
F_M	Force due to jet buoyancy
g	Acceleration due to gravity
G	Mass flux density
G_h	Mass flux density in hole in artificial accretion

G_p	Mass flux density in tuyere core pipe
h	Heat transfer coefficient
h_{gov}	Overall refractory/annular gas h value
h_{gs}	Gas/accretion h value
h_l	Liquid metal/accretion h value
h_L	Head loss
IMAX(J)	Mesh point at R_d from accretion edge
$J_{O_2,Ar}$	Molar flowrate of oxygen, argon
k	Adiabatic exponent
K	Constant
k_{acc}	Thermal conductivity of accretion
k_{core}	Thermal conductivity of core tube
k_d	Thermal conductivity of thermal boundary layer
k_g	Mass transfer coefficient for oxygen bulk flow
k_R	Thermal conductivity of refractory
k_s	Thermal conductivity of molten iron
k_{sh}	Thermal conductivity of shroud tube
K_e	Varies with bubble shape
K_L	Entry loss coefficient
K_{Lh}	Entry loss coefficient of artificial accretion hole
l	Length of pipe
$\dot{m}$	Mass flowrate
$\dot{m}_c$	Mass flowrate of core gas
$\dot{m}_e$	Mass flowrate of of gas at nozzle exit
$\dot{m}_s$	Mass flowrate of shroud gas
M	Virtual mass of bubble

$\dot{M}$	Momentum flowrate
Ma	Mach number
Ma_e	Mach number at nozzle exit
n	Normal ordinate
n	Number of holes in artificial accretion
N_{Fr}	Froude number
N_{Fr}'	Modified Froude number
$N_{Fr\ p}$	Froude number for liquid penetration
N_I	Injection number
Nu	Nusselt number
P	Pressure
P_d	Downstream pressure
P_e	Exit pressure
P_o	Supply pressure
P_2	Pressure just downstream from abrupt contraction
P_{stag}	Stagnation pressure
Pr	Prandtl number
Q	Volume flowrate
q_d	Mean heat flux density across thermal boundary layer
$\dot{q}''_{ref}$	Heat flux density across bubble surface for pure oxygen bubble
r	Radius - cylindrical coordinate
r_o	Radius of nozzle
R	Bubble radius during growth
R	Engineering gas constant
Re	Reynolds number
R_d	Width of thermal boundary layer

s	Displacement of bubble origin
S_{max}	Maximum penetration depth
t	Time
t_d	Time to bubble detachment
t_s	Thickness of shroud tube wall
T	Temperature
T_b	Bulk liquid temperature
T_c	Core tube temperature
T_{co}	Core tube upstream temperature
T_d	Downstream gas temperature
T_e	Exit temperature
T_g	Gas temperature in accretion
T_{gc}	Core gas temperature
T_{gs}	Shroud gas temperature
T_{go}	Upstream gas temperature in accretion
T_i	Mesh point temperature, finite difference representation
T^*_i	Fictitious mesh point temperature in finite difference representation
T_{int}	Gas/liquid interfacial temperature
T_l	Liquid temperature
T_m	Melting point
T_{mean}	Mean temperature of mixing core and shroud gas at tuyere exit
T_o	Upstream temperature
T_s	Steel temperature
T_{sh}	Shroud tube temperature
T_{sho}	Shroud tube upstream temperature
T_w	Gas/accretion interfacial temperature

u	Gas velocity
u_c	Jet centre line velocity
u_e	Gas velocity at nozzle exit
u_o	Nominal velocity
u_t	Gas velocity at nozzle throat
V_b	Bubble volume
x	Distance downstream of nozzle
X	$\ln r$
x_b	Oxygen volume fraction in gas mixture
x_{bo}	Initial oxygen volume fraction
Z	Height - cylindrical coordinate

Greek symbols

α	Thermal diffusivity
δ	Width of thermal boundary layer of growing bubble
ΔF	Number of frames between two frames of interest
ΔN	Number of frames between two consective starts of timing mark
ΔP	Pressure loss
Δt	Time interval between two frames
ΔT_s	Melt superheat ($T_b - T_m$)
ΔX	Mesh interval in radial direction
ΔZ	Mesh interval in height direction
ϵ	Emissivity
Φ	Diameter
θ	Modified temperature in liquid region

ρ_e	Gas density at nozzle exit
ρ_g	Gas density
ρ_{gd}	Gas density downstream of nozzle
ρ_l	Liquid density
ρ_2	Gas density just downstream of abrupt contraction
σ	Stefan's constant
τ	Radial width of accretion

REFERENCES.

1. R.D.Pehlke, "Steelmaking - the jet age", Met. Trans. B., 11B, (1980), p.539.

2. Anon., "Q-Bop Steelmaking", I & SM, Dec.(1975), p.29.

3. F.S.Death, "Past Present and Future of AOD Refining", I & SM, (1975), p.30.

4. J.C.C.Leach, A.Rodgers and G.Sheehan, "Operation of the AOD Process in BSC", I & SM, No.3, (1978), p.107-120.

5. O.Haida, K.Nakanishi and T.Emi, "Recent Progress in Ladle Metallurgy in Japan with Emphasis Placed on the Application of Injection Technology", Scaninject II Conference, Lulea, (1980), p.2.1-2.25.

6. R.Tait et al., "The Cupellation of Lead-Copper-Silver Bullion by the Bottom Injection of Oxygen", Gas Injection into Liquid Metals Conference, Dept. of Metallurgy and Engineering Materials, University of Newcastle upon Tyne, April (1979).

7. G.A.Irons and R.I.L.Guthrie "Bubble Formation at Nozzles in Pig Iron", Met. Trans. B., 9B, (1978), p.101-110.

8. G.N.Oryall and J.K.Brimacombe, "The Physical Behaviour of a Submerged Gas Jet Injected Horizontally into a Liquid Metal", Met. Trans. B., 7B, (1976), p.391.

9. M.Nilmani, Ph.D Thesis, Dept. of Metallurgy and Materials Science, Imperial College, London, (1978).

10. S.Ohguchi and D.G.C.Robertson, "Formation of Porous Accretions Around Tuyere During Gas Injection", I & SM, 10, (1983), p.15.

11. Y.Sahai and R.I.L.Guthrie, "The Formation and Growth of

Thermal Accretions in Bottom Blown/Combination Blown Steelmaking Operations", I & SM, April (1984),p.34.

12. J.F.Davidson and B.O.G.Schuler, "Bubble Formation at an Orifice in an Inviscid Liquid", Trans. Inst. Chem. Engrs., (1960), 38, p.335-342.

13. A.E.Wraith, "Gas Lancing in Metal Refining: an Air-Water Model Study", Advances in Extractive Metallurgy and Refining, IMM, London, (1971), p.1-14.

14. A.E.Wraith and M.E.Chalkley, "Tuyere Injection for Metal Refining", Advances in Extractive Metallurgy, IMM Symposium, London (1977), p.27-33.

15. M.E.Chalkley and A.E.Wraith, "Gas Dispersion From a Tuyere in Mercury: Application of Tuyere Pressure Analysis", IMM Trans. C., Dec.(1978), p.266-271.

16. M.Nilmani and D.G.C.Robertson, "Model Studies of Gas Injection at High Flowrates by use of Water and Mercury", IMM Trans. C., April (1979), C.42-53.

17. L.R.Farias,Ph.D Thesis, Dept. of Metallurgy and Materials Science, Imperial College, (1982).

18. E.O.Hoefele and J.K.Brimacombe, "Flow Regimes in Submerged Gas Injection", Met. Trans. B., 10B, (1979), p.631.

19. N.J.Themelis, P.Tarassoff and J.Szekely, "Gas Liquid Momentum Transfer in a Copper Converter", Trans. AIME, 245, (1969), p.2425-2433.

20. E.T.Turkdogan, "Reflexions on Research in Pyrometallurgy and Metallurgical Chemical Engineering", IMM Trans. C., 83c, (1974), p.67-81.

21. K.Mori and M.Sano, "Interactions Between Injected Bubbles and Liquid Metals", Scaninject I Conference,

Lulea, (1977), p.D9:1-8.

22. K.Mori, Y.Ozawa and M.Sano, "A Direct Observation of Interactions of Gas Jets with Liquid Metal at a Submerged Orifice", Met. Trans. B., 10B, Dec.(1979), p.679 and 680.

23. M.J.McNallan and T.B.King, "Fluid Dynamics of Vertical Submerged Gas Jets in Liquid Metal Processing Systems", Met. Trans. B., 13B, (1982), p.165.

24. R.P.Singh and M.J.McNallan, "Fluid Dynamics and Mass Transfer in Submerged Gas-Particle Jets", Met. Trans. B., 14B, (1983), p.425.

25. K.G.Davis and J.G.Magny, "Blocking in Horizontal Nozzles During Injection of Gas into Liquid Cast Iron", Metals Technology, (1979), p.1.

26. K.Mori, M.Sano and T.Sato, "Size of bubbles Formed at Single Nozzle Immersed in Molten Iron", Transactions ISIJ, 19, (1979), p.553-558.

27. T.Aoki et al., "Characteristics of SG Jets and a New Bottom Blowing Tuyere", Injection Phenomena in Extraction and Refining Conference, Dept. of Metallurgy and Engineering Materials, Univ. of Newcastle upon Tyne, April (1982), p.A1-36.

28. H.Nakamura, T.Emi et al., "Solidified Iron (Mushroom) Around Tuyeres of the Q-BOP", Tetsu-to-Hagane, 67, (1981), p.S873.

29. S.Ohguchi and D.G.C.Robertson, "Heat Transfer Calculations for Accretion Formation Around a Tuyere During Submerged Gas Injection into Molten Steel", Conference on Injection Phenomena in Extraction and Refining, Dept. of Metallurgy and Engineering

Materials, Univ. of Newcastle upon Tyne, April (1982), p.J1.

30. N.B.Ballal and A.Ghosh, "A Water Model Study of Bottom-Blown Oxygen Steelmaking Processes", Met. Trans. B., 12B, Sept.(1981), p.525.

31. Private Communication, Wiggin Steel and Alloys, Birmingham, (1982).

32. R.H.Perry et al., "Chemical Engineers' Handbook", Fourth Edition, McGraw-Hill, (1950), 5-27.

33. L.Farias and D.G.C.Robertson, "Analysis of Pressure Traces in Submerged Injection Systems", Injection Phenomena in Extraction and Refining Conference, Dept. of Metallurgy and Engineering Materials, Univ. of Newcastle upon Tyne, April (1982), p.E1-25.

34. P.Collins and A.E.Wraith, "Dynamic Pressure Response in the Core flow of an Annular Tuyere", Injection Phenomena in Extraction and Refining Conference, Dept. of Metallurgy and Engineering Materials, Univ. of Newcastle upon Tyne, April (1982), p.H1-13.

35. J.K.Vennard and R.L.Street, "Elementary Fluid Mechanics", Fifth Edition, Wiley, London, (1976).

36. J.C.Hunsaker and B.G.Rightmire, "Engineering Applications of Fluid Mechanics", McGraw-Hill, New York, (1947).

37. C.O.Bennett and J.E.Myers, "Momentum, Heat and Mass Transfer", Second Edition, McGraw-Hill, London, (1974).

38. H.L.Langhaar, "Steady Flow in the Transition Length of a Straight Tube", ASME, J. Appl. Mech., 9, (1942), p.A55-58.

39. O.Kubaschewski, E.L.Evans and C.B.Alcock,

"Metallurgical Thermochemistry", Fourth Edition, Oxford Pergamon Press, (1967).

40. A.A.Bustos, G.G.Richards, N.B.Gray and J.K.Brimacombe, "Injection Phenomena in Non-Ferrous Processes", Met. Trans. B., 15B, March (1984), p.77.

41. P.Moore and A.E.Wraith, "Mathematical Modelling of the Refractory Temperature Fluctuations Generated Locally by Bubble Formation at an Annular Tuyere", Conference on Injection Phenomena in Extraction and Refining, Dept. of Metallurgy and Engineering Materials, Univ. of Newcastle upon Tyne, April (1982), p.L1.

42. Private Communication - Britannia Refined Metals, Northfleet, Kent.

43. V.Jung, "Recovery of Precious Metals From Lead Bullion", J. Metals, Oct.(1981), p.42.

44. Metals Handbook, Vol.8, Metallography,structures and phase diagrams, 8 th Edition, Am. Soc. for Metals, 1973, p.253-255.

45. Private Communication - Britannia Refined Metals - Minutes of Meeting, June 1983.

46. B.D.You et al., "Study on the Bubble Formation and Penetration of the Melt into the Nozzle During the Injection of Gas with or without Powder", Scaninject III Conference, Lulea, (1983), p.10:1.

47. P.Collins,"Isothermal Model Studies of the Flooding Characteristics of Plain and Annular Tuyeres", Conference on Injection Phenomena in Extraction and Refining, Dept. of Metallurgy and Engineering Materials, Univ. of Newcastle upon Tyne, April (1982), p.D1

48. B.E.Grabner, "Installation and Wear Behaviour of Porous Plugs with Directed Porosity in LD-Vessels and Ladles", Scaninject III Conference, Lulea, June 1983, p.8-23.

49. W.A.Krivsky and R.Schuhman, "Heat Flow and Temperature Distribution Around a Copper Converter Tuyere", Trans. AIME 215, (1959), p.82.

50. G.Denier, J.C.Grosjean and H.Zanetta, "Heat Transfer in Tuyeres for Oxygen Bottom-Blowing Conveters", I & SM, 7, (1980), p.123.

51. S.Ohguchi, Ph.D Thesis, Dept. of Metallurgy and Materials Science, Imperial College, London, (1983).

52. G.Boxall et al., "Modelling and Visualization of Tuyere Accretion Growth", Conference on Injection Phenomena in Extraction and Refining, Dept. of Metallurgy and Engineering Materials, Univ. of Newcastle upon Tyne, (1982), p.B1.

53. D.R.Croft and D.G.Lilley, "Heat Transfer Calculations Using Finite Difference Equations", Applied Science Publishers Limited, London, (1977).

54. G.D.Smith, "Numerical Solution of Partial Differential Equations", Oxford University Press, Second Edition, (1978).

55. J.H.Wiegand, "Discussion on Annular Heat Transfer Coefficients for Turbulent Flow", Trans. Am. Inst. Chem. Engrs., 41, (1945), p.147.

56. E.N.Sieder and G.E.Tate, "Heat Transfer and Pressure Drop of Liquids in Tubes", Ind. and Eng. Chem., 28, No. 12, (1936), p.1429.

57. G.H.Geiger and D.R.Poirier, "Transport Phenomena in Metallurgy", Addison-Wesley Publishing Company, (1973).

58. "Handbook of Chemistry and Physics", Ed. R.C.Weast, CRC Press Inc., 63rd Edition, Florida, (1982).

59. C.J.Dobson, L.Farias, and D.G.C.Robertson, "Tuyere Gas Pressure Analysis at Wiggin Steel and Alloys", Internal Report, Dept. of Metallurgy and Materials Science, Imperial College, London, (1982).

60. D.G.C.Robertson, Phd Thesis, University of New South Wales, Australia, (1968), p.74.

61. D.R.Sain and G.R.Belton, "The Influence of Sulphur on Interfacial Reaction Kinetics in the Decarburization of Liquid Iron by Carbon Dioxide", Met. Trans. B., 9B, (1978), p.403.

62. W.M.Kays and E.Leung, "Heat Transfer in Annular Passages - Hydrodynamically Developed Turbulent Flow with Arbitrarily Prescribed Heat Flux", Int. J. Heat Mass Transfer, 6, (1963), p.537.

63. T.A.Engh et al., "Model Studies of Clogging in Tuyeres and lances", Scand. J, Metallurgy, 5, (1976), p.21.

64. C.J.Messina, "Minimum Gas Flows for Protecting Submerged Tuyeres During Furnace Rotation", Steelmaking Proceedings, Pittsburgh, 65, (1982), p.221.

65. A.R.Anderson and F.R.Johns, "Characteristics of Free Supersonic Jets Exhausting into Quiescent Air", Jet Propulsion, 25, (1955), p.13.

66. J.R.D.Francis, "A Textbook of Fluid Mechanics for Engineering Students", Third Edition,. Edward Arnold (Publishers) Limited, London, (1969).

67. G.C.Smith, "Multiple Jet Oxygen Lances - Theoretical Analysis and Correlation with Practice", Journal of

Metals, (1966), p.846.

68. K.Foelsch, "The Analytical Design of an Axially Symmetric Laval Nozzle for a Parallel and Uniform Jet", J. Aero. Sci., (1949), p.161.

69. A.H.Shapiro, "The Dynamics and Thermodynamics of Compressible Fluid Flow", The Ronald Press Company, New York, (1953).

70. D.A.Russell et al., "Screen Nozzles for Gas Dynamic Lasers", AIAA J., 13, No.5, (1975), p.593.

71. D.H.Wakelin, Phd Thesis, Dept. of Metallurgy and Materials Science, Imperial College, London, (1966).

72. M.Poreh and J.E.Cermak, "Flow Characteristics of a Circular Submerged Jet Impinging Normally on a Smooth Boundary", Proc. Sixth Mid-West Conference on Fluid Mechanics, (1959), p.198.

73. P.Bradshaw and E.M.Love, "The Normal Impingement of a Circular Air Jet on a Flat Surface", N.A.C.A. Report No.3205, Sept.(1959).

74. S.Mizoguchi, Ph.D Thesis, Department of Metallurgy and Materials Science, Imperial College, 1972, p.52.